Synthesis and Activation of Gold and Bimetallic Clusters for Catalysis

A Thesis Submitted to the College of

Graduate Studies and Research

In Partial Fulfilment of the Requirements

For the Degree of Doctor of Philosophy

In the Department of Chemistry

University of Saskatchewan

Saskatoon

By

Atal Shivhare

Permission to Use

In presenting this thesis in partial fulfilment of the requirements for a Postgraduate degree from the University of Saskatchewan, I agree that the Libraries of this University may make it freely available for inspection. I further agree that permission for copying of this thesis in any manner, in whole or in part, for scholarly purposes may be granted by the professor or professors who supervised my thesis work or, in their absence, by the Head of the Department or the Dean of the college in which my thesis work was done. It is understood that any copying or publication or use of this thesis or parts thereof for financial gain shall not be allowed without my written permission. It is also understood that due recognition shall be given to me and to the University of Saskatchewan in any scholarly use which may be made of any material in my thesis.

Requests for permission to copy or to make other use of material in this thesis in whole or part should be addressed to:

Head of the Department of Chemistry

University of Saskatchewan

Saskatoon, Saskatchewan (S7N 5C9)

Canada

Abstract

This thesis investigates the synthesis and activation of highly monodisperse $Au_{25}(SR)_{18}^-$ clusters and bimetallic clusters (AuAg and AuPd) protected with various stabilizers for reduction and hydrogenation catalytic reactions. The first chapter is the introduction chapter, which summarizes the literature involving monolayer protected Au clusters, atomically precise Au clusters, bimetallic clusters, X-ray absorption spectroscopy, research objectives, and organization and scope. The second chapter describes the synthesis of $Au_{25}(SR)_{18}^-$ clusters protected with various thiolate stabilizers for nitrophenol reduction catalysis using $NaBH_4$ as a reducing agent. This chapter also describes the stability of these clusters under reaction conditions using UV-Vis spectroscopy and MALDI mass spectrometry. The third chapter details the synthesis of carboxylic acid-protected Au_{25} clusters using a $NaBH_4$ purification strategy. Here, the knowledge obtained in the second chapter regarding the exceptional stability of $Au_{25}(SR)_{18}^-$ clusters in the presence of $NaBH_4$ was used to isolate carboxylic acid protected Au_{25} clusters from a polydisperse reaction mixture. The fourth chapter describes the synthesis and activation of mesoporous carbon supported $Au_{25}(SR)_{18}^-$ clusters for nitrophenol reduction catalysis. Here, thermal removal of thiolate stabilizers led to the enhancement in the catalytic activity at low calcination temperatures; however, at higher calcination temperatures activity dropped as particle sintering was observed. Activation of these clusters on mesoporous carbon support was followed by TEM and X-ray absorption spectroscopy. The fifth chapter describes the thermal and chemical removal of thiolate stabilizers from supported $Au_{25}(SC_8H_9)_{18}^-$ clusters. Here, the removal of thiolate stabilizers and subsequent growth of Au_{25} clusters was followed by TEM and EXAFS spectroscopy. The sixth and seventh chapters describe the synthesis of AuPd and AuAg bimetallic clusters using $Au_{25}(SR)_{18}^-$ clusters as precursors and their characterization using UV-Vis spectroscopy, transmission electron microscopy, and X-ray absorption spectroscopy. Here, AuPd bimetallic clusters were thermally and chemically treated, which resulted in the formation of AuPd bimetallic nanoparticles with segregated Pd atoms on the surface. AuPd bimetallic nanoparticles were used for the selective hydrogenation catalysis of allyl alcohol. The last chapter of this thesis includes final conclusions and possible avenues for future work.

Acknowledgements

I would like to acknowledge my supervisor Dr. Robert W. J. Scott for his valuable guidance throughout my Ph.D. program. I would also like to thank my advisory committee members, Drs. Ian Burgess, Matthew Paige, and Jafar Soltan for their valuable suggestions throughout my project, Daniel M. Chevrier from Dalhousie University for helping me with EXAFS data fittings, and Dr. Mark S. Workentin and Dr. Mahdi Hesari from University of Western Ontario for assisting me with the purification of $Au_{25}(SC_8H_9)_{18}^-$ clusters.

My sincere thanks to University of Saskatchewan and Department of Chemistry for giving an opportunity to continue my Ph.D. research. Funding for this project was provided by the Natural Sciences and Engineering Research Council of Canada (NSERC)

Also, my sincere thanks to all past and present Scott Group members.

DEDICATIONS

I would like to dedicate this thesis to my family members and my supervisor Dr. Robert W. J. Scott.

TABLE OF CONTENTS

CHAPTER 1

List of Figures

151

List of Tables

List of Schemes

List of Equations

List of Abbreviations

ATP	Adenosine Triphosphate
ADP	Adenosine Diphosphate
AIE	Aggregation Induced Emission
CLS	Canadian Light Source
CN	Coordination Number
DNA	Deoxyribonucleic Acid
DFT	Density Functional Theory
ESI-MS	Electro-Spray Ionization Mass Spectrometry
EXAFS	Extended X-ray Absorption Fine Structure
FT	Fourier Transform
fcc	Face Centered Cubic
HOMO	Highest Occupied Molecular Orbital
HRTEM	High Resolution Transmission Electron Microscopy
HXMA	Hard X-ray MicroAnalysis
IR	Infrared Spectroscopy
LUMO	Lowest Unoccupied Molecular Orbital
MPCs	Monolayer Protected Clusters
MBA	Mercaptobenzoic Acid
MALDI-MS	Matrix Assisted Laser Desorption Ionization Mass Spectrometry
11-MUA	11-Mercaptoundecanoic Acid
16-MHA	16-Mercaptohexadecanoic Acid
MS	Mass Spectrometry

NMR	Nuclear Magnetic Resonance
NADP	Nicotinamide Adenine Dinucleotide Phosphate
NHE	Standard Hydrogen Electrode
NSERC	National Sciences and Engineering Research Council of Canada
QY	Quantum Yield
SG	Glutathione
SPR	Surface Plasmon Resonance
SEC	Size Exclusion Chromatography
SXRMB	Soft X-ray Microcharacterization Beamline
THF	Tetrahydrofuran
TOAB	Tetraoctylammonium Bromide
TGA	Thermogravimetric Analysis
TOF	Turnover Frequency
XAS	X-ray Absorption Spectroscopy
XANES	X-ray Absorption Near Edge Structure
XPS	X-ray Photoelectron Spectroscopy

1.0 Introduction

Metallic gold had long been considered inactive for catalysis until the seminal discovery by Haruta *et al*. showing that well dispersed Au nanoparticles on oxide supports can act as catalysts for low temperature CO oxidation reactions.[1] Since then, a large number of research articles have been published showing the use of supported Au nanoparticles for a variety of chemical transformations.[2-5] Investigations on the origin of catalytic activity from supported Au nanoparticles catalysts reveal that various factors such as 1) nanoparticle size, 2) activation of substrates at the nanoparticle-support interface, 3) presence of water, and 4) charge transfer from support to nanoparticles can be responsible for the observed catalytic activity.[6] A widely accepted belief has been that a decrease in Au nanoparticles size will lead to the enhancement in the catalytic activity because of higher surface to volume ratio and higher number of under-coordinated surface sites. These observations have been mainly based on polydisperse Au nanoparticles and therefore obviate the study of exact structure-property relationships.

Brust, Schiffrin and co-workers in 1994 reported the synthesis of Au monolayer protected clusters (Au MPCs) via a two phase method using a phase transfer catalyst. These clusters were found to be relatively monodisperse in nature and could be size-tuned by changing the amount of thiolate stabilizers used in the synthesis.[7] Later, other groups reported the synthesis of atomically-precise Au clusters by modifying the synthesis protocol reported by Brust and Schiffrin, often by changing to a single phase solvent such as tetrahydrofuran (THF). These atomically precise Au clusters are highly monodisperse in nature and the number of Au atoms and thiolate stabilizers present in these clusters can be determined by mass spectrometry.[8] Because of their high monodispersity, these clusters have been used by various groups in order to study the size and structure related catalytic properties of Au nanocatalysts.[9]

This section begins with the synthesis, characterization, and applications of Au MPCs. Subsequently, atomically-precise Au and bimetallic clusters, their applications, and characterization using X-ray absorption spectroscopy are described. Finally, the objectives of this thesis, as well as it's organization and scope are discussed.

1.1 Au Monolayer Protected Clusters (Au MPCs)

Au MPCs are Au clusters protected with a monolayer of organic stabilizers.[10] In this thesis Au MPCs are divided into two categories. The first category includes polydisperse Au monolayer protected clusters and the second category includes highly monodisperse, atomically-precise Au monolayer protected clusters.

1.1.1 Synthesis of Polydisperse Au MPCs

The first successful synthesis of polydisperse Au MPCs was reported by Brust, Schiffrin and co-workers, which is commonly known as the bi-phasic protocol for the synthesis of Au MPCs.[7] According to this protocol, first the $HAuCl_4$ salt was transferred from aqueous solution to toluene using tetraoctylammonium bromide (TOAB) as the phase-transfer reagent. In the second step, Au(III) in toluene reacted with dodecanethiolate stabilizers to putatively form Au(I) thiolate polymers. Finally, the Au(I) was reduced by adding an excess of $NaBH_4$.

$$AuCl_4^- \text{ (water)} + \text{TOAB (toluene)} \longrightarrow TOA^+AuCl_4^- \text{ (toluene)} \qquad (1)$$

$$TOA^+AuCl_4^- \text{ (toluene)} + RSH \longrightarrow (\text{-}Au^ISR\text{-})_n \text{ (polymer)} \qquad (2a)$$

$$TOA^+AuCl_4^- \text{ (toluene)} + 2\,RSH \longrightarrow TOA^+AuCl_2^- + RSSR + 2HCl \qquad (2b)$$

$$(\text{-}Au^ISR\text{-})_n + BH_4^- \longrightarrow Au_n(SR)_m \qquad (3)$$

Scheme 1.1. Synthesis of Au MPCs using bi-phasic protocol.

This eventually leads to the formation of Au MPCs, as shown in Scheme 1.1. The as-prepared Au MPCs were found to be stable and can be repeatedly isolated from and redissolved in common organic solvents without any decomposition.[11] Subsequent studies suggested that a wide range of different thiolates can be used in the same protocol.[12-14] This method turned out to be somewhat useful in controlling the size of various MPCs by simply changing the amount of thiolate stabilizers used.[15-20]

Shortly afterwards, another synthesis protocol was reported. According to this protocol, the entire reaction was carried out in a one-phase system. Here Au salt was mixed with p-mercaptophenol in methanol, and to the resulting mixture, $NaBH_4$ was added carefully in small portions.[21] The advantage of one-phase protocol over bi-phasic protocol was to be able to use thiolate stabilizers protected with polar functional groups, and to avoid the use of TOAB and other phase transfer agents that are difficult to remove from the final reaction product.

To be able to control the size distribution of the final product, many groups have tried to identify the metal ion precursor prior to the addition of $NaBH_4$. The widely accepted belief until 2010 was that Au(III) salt reacts with thiolate stabilizers and forms $[Au(I)SR]_n$ polymers (Scheme 1.1, 2a), which upon reduction convert into Au MPCs.[2,10] This long-standing view was recently challenged by Lennox and co-workers.[22] They showed that in the bi-phasic protocol, the actual metal ion precursor species was $[NR_4][AuX_2]$ complex and not $[Au(I)SR]_n$ polymers (Scheme 1.1, 2b). The $[NR_4][AuX_2]$ complex was formed after the addition of alkanethiols to the $[NR_4][AuX_4]$ complex. In this reaction, alkanethiols were oxidized to disulfides, and Au^{3+} was reduced to Au^+. The stoichiometry of the reaction and the formation of disulfide was confirmed by ^1H NMR and Raman spectroscopy. Data showed that after the addition of 2 equiv. of alkanethiols, $[NR_4][AuX_4]$ was completely converted to $[NR_4][AuX_2]$ (Scheme 1.1, 2b) with the concomitant formation of disulfides. Furthermore, this study suggested that while tetraoctylammonium metal complexes were the precursors for bi-phasic protocols, insoluble $[Au(I)SR]_n$ polymers were the precursors for one-phase protocol, and this polymer precursor was also formed in bi-phasic synthesis if water was present in the reaction mixture.

In order to further delineate the mechanism of Au MPCs formation in bi-phasic systems, Tong and co-workers studied the formation of Au-S bond after the addition of $NaBH_4$ to $[NR_4][AuX_2]$ complexes.[23] They found using various spectroscopic techniques that $[NR_4][AuX_2]$ complexes form reverse micelles in toluene with water molecules trapped inside the micelle. After the addition of $NaBH_4$ to $[NR_4][AuX_2]$ complexes, first Au^+ gets reduced inside the micelle and then the thiol stabilizers diffuses through the micelle and attaches to the Au surface resulting in the formation of MPCs.

1.1.2 Synthesis of Atomically-Precise Monolayer Protected Au Clusters

Atomically-precise Au clusters (<2 nm in diameter) are highly monodisperse, relatively stable, structurally well-defined, ligand protected Au clusters with a definite number of Au atoms.[11] These clusters have also been termed as molecular clusters because of their small sizes, which leads to the quantization of energy levels and hence the appearance of molecule-like optical properties.[8] Atomically-precise Au clusters, because of their monodispersity and well-established structures are an important class of materials in order to study the size and structure related properties of Au nanomaterials.[9]

The synthesis of atomically-precise Au clusters has been non-trivial compared to conventional Au monolayer protected clusters (Au MPCs), as it involves the optimization of reaction conditions in such a way that only certain sized clusters are obtained. In some cases, tedious post synthetic extraction steps are involved in order to isolate specific Au clusters from a crude mixture.

1.1.2.1 Synthesis of Alkyl and Aryl Thiolate Protected Atomically-Precise Au Clusters

Two widely used strategies are reported in the literature for the synthesis of alkane-thiolate and aryl-thiolate protected, atomically-precise Au clusters, namely, a size focusing strategy and a ligand based etching strategy.[24-25] The underlying principle behind both these strategies is the same and involves the decomposition of unstable (larger) clusters through etching, leaving behind only stable atomically-precise Au clusters in solution.

The size focusing strategy involves the exposure of polydisperse Au MPCs to air for 4-5 days until stable atomically precise Au clusters are obtained, which can be observed by UV-Vis absorption spectroscopy and mass spectrometry. The first successful high-yield synthesis of atomically precise $Au_{25}(SR)_{18}^-$ clusters using size focusing strategy was reported by Jin and co-workers.[26] According to this synthesis, $HAuCl_4$ in water was first phase transferred to toluene using TOAB. Subsequently, the Au salt in toluene was cooled and then reduced by adding excess of cold $NaBH_4$ in the presence of thiol stabilizers. The resulting crude mixture started to show peaks characteristic of small Au clusters (step-like features), which upon further stirring under air for 4-5 days converted to monodisperse $Au_{25}(SR)_{18}^-$. Dass *et al.* showed using mass spectrometry that as-synthesized crude mixture contained Au clusters ranging from Au_{25} to Au_{102}, which upon further stirring slowly converted to monodisperse Au_{25} clusters.[27] The role of TOAB in this bi-phasic protocol was earlier thought to be only a phase-transfer reagent, which was essential in order to phase-transfer Au salt from water to toluene. However, later studies suggested that tetraoctylammonium bromide was necessary to stabilize $Au_{25}(SR)_{18}^-$ clusters by providing tetraoctylammonium (TOA^+) ions which can stabilize negatively charged $Au_{25}(SR)_{18}^-$ clusters in solution.[28-29] Our group has also reported that bromide ions from TOAB acts as oxidation promotor of-Au MPCs.[30] Decomposition of all unstable Au MPCs will lead to the formation of highly stable $Au_{25}(SR)_{18}^-$ clusters. The critical role of the solvent in size focusing strategy was reported for $Au_{144}(SR)_{60}$ clusters.[31] While toluene and THF were shown to be suitable for the synthesis of

$Au_{25}(SR)_{18}^-$ clusters, methanol was found to be suitable for the synthesis of $Au_{144}(SR)_{60}$ clusters.[31] Although, single phase methods using THF and methanol are available, the majority of these methods still use TOAB. The exact role of the solvent in these syntheses is not clear, however several groups have suggested that the choice of solvent is essential in controlling the initial distribution of Au MPCs in the polydisperse mixture, which eventually convert into atomically precise Au clusters through size focusing.[32-33]

Ligand-based etching strategies are also common, and have been used by various groups in order to synthesize a variety of atomically-precise Au clusters.[34-40] According to this strategy, a polydisperse Au MPC mixture is treated with a large excess of thiol stabilizers at higher temperatures. This results in the decomposition of all unstable Au clusters, leaving behind only stable, atomically-precise Au clusters. Whetten *et al*. first reported the thermal etching of hexanethiolate-protected, polydisperse Au clusters in the presence of dodecanethiol at 70°C.[25] Analysis of the reaction mixture at various after certain time intervals using mass spectrometry, optical spectroscopy, and X-ray diffraction revealed the formation of small clusters. Based on the formation of $Au_n(SR)_m$ oligomers upon etching as shown by mass spectrometry, they suggested that $[Au(I)SR]_n$ polymers could be the possible byproduct of the etching reaction, which is responsible for the decrease in size. Formation of $[Au(I)SR]_n$ polymers was also supported by the appearance of a white byproduct during the etching reaction, which, they ascribed to labelled a Au(I) thiolate polymer. Subsequently this concept has been used in the synthesis of various ligand-protected, atomically-precise Au clusters. For example, Pradeep *et al*. reported the synthesis of glutathione (SG) protected Au_{25} clusters through the etching of polydisperse $Au_n(SG)_m$ clusters at 55°C in water.[41] Jin *et al*. reported the synthesis of dodecanethiolate protected $Au_{38}(SR)_{24}$ clusters through the etching of polydisperse $Au_n(SR)_m$ clusters in a two phase (acetone + water) system at 80°C.[38] Here, $Au_n(SR)_m$ clusters dissolved in water, were treated with excess of dodecanethiol dissolved in acetone. The etching reaction took place at the interface of acetone and water, and after a few hours, all the clusters were transferred to the acetone layer. Characterization of the acetone layer by UV-Vis spectroscopy and mass spectrometry showed the formation of dodecanethiolate protected $Au_{38}(SR)_{24}$ clusters. Qian *et al*. reported the synthesis of $Au_{144}(SCH_2CH_2Ph)_{60}$ clusters through the etching of polydisperse $Au_n(SCH_2CH_2Ph)_m$ clusters in toluene at 80°C for 24 hours.[42] Mass spectrometric characterization of the starting polydisperse mixture showed several distinct peaks of ~34, 31.9, 29, 25.8, and 7.4 kDa, while after etching only one peak at ~34 kDa representative of $Au_{144}(SCH_2CH_2Ph)_{60}$ clusters was seen.[42] The effect of different solvents on the synthesis of $Au_{38}(SR)_{24}$ clusters through ligand based etching strategies was explored by Jin *et al*.[33] They found that the solvent seems to affect the size distribution of initially formed polydisperse mixture, which subsequently affects the outcome of the reaction after etching. They used two different solvents, methanol and acetone in order to synthesize polydisperse Au MPCs as starting precursors for etching. Polydisperse Au MPCs mixtures synthesized in methanol and acetone were characterized using mass spectrometry. Mass spectrometry showed the formation of $Au_{38}(SR)_{24}$ and larger clusters in the case of acetone, and $Au_{38}(SR)_{24}$ and sub-Au_{38} clusters in the case of methanol. These Au MPC precursors were then subjected to etching in toluene-ethanol mixture at 80^{o}C for 40 hours in the presence of large excess of phenylethanethiol as etchant. The MPCs which were originally synthesized in acetone gave higher yields of $Au_{38}(SR)_{24}$ clusters than MPCs which were synthesized in methanol.

Both size focusing and ligand-based etching approaches have their advantages in terms of synthesizing specific sizes Au clusters. However, there is still a need to systematically study the effect of various reaction parameters such as choice of solvent, reaction temperature, time of etching, and the amount of etchant (thiol) used in order to fully realize the true potential of these strategies.

1.1.2.2 Synthesis of Functional Thiolate-Protected Atomically-Precise Au Clusters

Synthesis of atomically-precise Au clusters which have functional groups on the thiolate group is extremely challenging and there are few examples described in the literature. Pradeep *et al*. reported an indirect route, in which they attempted to substitute glutathione ligands with 3-mercapto-2-butanol, N-acetyl glutathione at room temperature in water as a solvent.[43] An attempt to synthesize Au_{25} clusters directly using these ligands did not lead to a successful outcome. Data suggested only partial substitution of glutathione ligands with the aforementioned ligands, and repeated attempts to completely substitute glutathione ligands on the surface of Au_{25} clusters were unsuccessful. Synthesis of $Au_{102}(p\text{-MBA})_{44}$ has been reported, however; it involves a series of complex post-synthetic steps in order to extract Au_{102} clusters from the crude mixture.[44]

Recently, Xie and co-workers reported a novel, high yield synthesis of carboxylic acid and amine terminated thiolate protected Au_{25} clusters.[45] In this synthesis, NaOH was introduced into the reaction mixture before the addition of $NaBH_4$. Addition of NaOH was hypothesized to decrease the reducing strength of $NaBH_4$, and increase the etching ability of free thiols present in the reaction mixture. Under weakly reducing and enhanced etching conditions, equilibrium was established between forward (reduction) and backward (etching) reactions, leading to the formation of thermodynamically stable, ligand protected Au_{25} clusters. Salient features of the synthesis were two-fold: 1) this synthesis protocol was able to accommodate a wide range of functional thiols with different chain lengths, and 2) yield of resulting thiolate protected Au_{25} clusters was ~90%.In another study, use of a weak reducing agent for the synthesis of $Au_{25}(SR)_{18}^-$ clusters has also been reported by the same group. They showed that CO instead of more conventional $NaBH_4$ can be used as mild reducing agent in order to synthesize atomically precise $Au_{25}(SR)_{18}^-$ clusters.[46]

Our group has also reported the synthesis of 11-mercaptoundecanoic acid and 16-hexadecanoic acid protected Au_{25} clusters. The results of this study are discussed elsewhere (Chapter 3).

1.1.3 Characterization

The presence of both inorganic (cluster core) and organic (organic stabilizers) moieties allow for the characterization of these MPCs using a variety of characterization techniques. The following techniques have been used very frequently in order to characterize Au MPCs.

1.1.3.1 UV-Vis spectroscopy

UV-Vis absorption features of Au MPCs have been found to be sensitive to the average cluster size. Au clusters above 2 nm in diameter exhibit a surface plasmon resonance (SPR) band at ~550 nm wavelength.[47] The intensity of this SPR band depends on the cluster size. For example, Murray and co-workers showed that the intensity of SPR band decreases and eventually disappears for smallest cluster giving a featureless absorption spectrum.[11] Clusters smaller than ~2 nm in diameter do not support a SPR band and start to show step-like absorption features in their absorption spectra because of HOMO-LUMO transitions.[47] The position of HOMO-LUMO absorption bands varies with the cluster size and hence can be used in order to identify a particular-sized cluster. For example; in the case of $Au_{25}(SR)_{18}^-$ clusters, three main absorption features are observed.[28] The major peak at ca. 1.7 eV is attributed to the HOMO-LUMO transition and other two minor peaks at ca. 2.6-3.3 eV are attributed to the transition from HOMO to LUMO+1 and LUMO+2, and HOMO-5 to LUMO transitions (Figure 1.1).

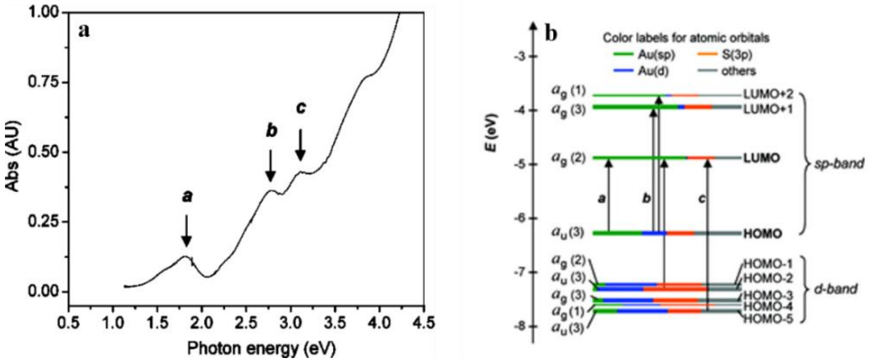

Figure 1.1 (a) Step-like UV-Vis absorption features of $Au_{25}(SR)_{18}^-$ clusters and (b) orbital level energy diagram for a model compound; $Au_{25}(SH)_{18}^-$. (Reprinted with permission from reference 28. Copyright (2008) American Chemical Society)

1.1.3.2 HRTEM and TGA analysis

High resolution transmission electron microscopy (HRTEM) in conjunction with thermogravimetric analysis (TGA) has been used in order to characterize the average number of thiolate stabilizers present on the surface and the average number of metal atoms present in the core. Using this information, the average molecular formula for Au MPCs can be determined.[25] For example, Murray and co-workers calculated the average molecular formula for 1-dodecanethiolate-protected Au MPCs using TEM and thermogravimetric analysis (TGA).[48] The number of Au atoms in one cluster can be calculated using the formula below (Equation 1.1).

$$\mathrm{n} = \frac{4\pi R^3 N_a}{3V_g} \qquad \textbf{(1.1)}$$

Here n is the number of atoms per cluster, R is the nanoparticle radius, Na is the avogadro number and V_g is the molar volume of Au. The number of ligands in one cluster (N) can be calculated using Equation 1.2:

$$\mathrm{N} = (\mathrm{n} \times \mathrm{AW} \times \mathrm{wt\%of\,ligand})/(\mathrm{MW} \times \mathrm{wt\%of\,Au}) \qquad \textbf{(1.2)}$$

Here, AW is the atomic weight of Au, and MW is the molecular weight of one thiolate ligand. The Diameter of Au cluster can be obtained from TEM analysis and wt% of ligand can be calculated from TGA analysis. Using this information average molecular formulae for Au MPCs have been calculated.

1.1.3.3 NMR

Nuclear magnetic resonance (NMR) analysis of Au MPCs has been done by various groups in order to compare between various core sizes, and to differentiate between the thiolate stabilizers attached to the surface of Au core and free excess alkanethiols in solution.[11,49] ^{1}H and ^{13}C NMR resonances of thiolates on Au MPCs are relatively broadened compared to free thiols. This broadening has been attributed to several factors such as, spin-spin relaxing, distribution in chemical shifts because of various Au-SR bonding sites and a gradient in chain packing density from near surface to terminus.[12,50] Broadening in ^{1}H and ^{13}C NMR resonances has been found to be directly correlated with the size of Au MPCs, where sharper peaks were observed with a decrease in cluster size.[11-12] NMR spectroscopy has also been used to confirm the Au-SR linkage for thiolate stabilizers with multiple coordination sites.[49] Methylene groups close to Au surface are broadened compared to methylene groups further away from Au surface. This is because of the dense, solid-like packing of methylene groups near Au surface. This may lead to fast spin-relaxation from dipolar interaction and thereby broaden the width of NMR peak. Whereas methylene groups further away from the Au surface experience freedom of motion similar to dissolved species. Based on this, for a ligand molecule with multiple coordination sites, the NMR peak width of specific hydrogen atoms on the thiolate can be used to identify the point of linkage.[11]

1.1.3.4 Mass Spectrometry

Recently mass spectrometry has been used by various groups in order to study the composition and charge state of Au MPCs. Using mass spectrometry, the composition of various Au MPCs has been established.[51-52] Two types of mass spectrometry have been commonly used; matrix assisted laser desorption ionization mass spectrometry (MALDI-MS) and electro-spray ionization mass spectrometry (ESI-MS). Unlike MALDI-MS, ESI-MS has usually been considered to be a soft technique, and fragmentation of clusters during analysis can be significantly minimized using this technique.[53-57] ESI-MS has also been demonstrated to be useful in studying the charge state of atomically precise Au clusters. For example, Tracy *et al*. showed using ESI-MS that $Au_{25}(SR)_{18}^{-}$ clusters are negatively charged.[57] While in negative ion ESI-MS mode, $Au_{25}(SR)_{18}^{-}$ clusters show an intense molecular ion peak, and addition of metal salts is necessary in positive ion mode in order to generate positive charge on these clusters. Metal ions bind with these clusters and develop positive charge, which can be analyzed in positive ESI-MS mode. The use of ESI-MS is limited to samples which either carry charge with them or can be charged by either metal ion addition or through ligand functionalization. MALDI-MS has been shown to be useful for characterizing neutral clusters. However, it can lead to significant fragmentation of clusters under investigation.[58] It is important to minimize the laser intensity to suppress the fragmentation of clusters under investigation. However, extra care is needed since this can also suppress the molecular ion peak signal.[58] Using MALDI-MS, various neutral clusters such as Au_{38}, Au_{24}, Au_{144}, etc. have been analyzed and their molecular compositions have been assigned.[59-60]

1.1.3.5 Single Crystal X-ray Diffraction

Single crystal X-ray diffraction has been used to study the atomic structure of various Au MPCs. The first successful use of single crystal X-ray diffraction was shown by Kornberg and co-workers in the characterization of p-mercaptobenzoic protected Au_{102} clusters.[44] Subsequently, this technique has been used to characterize the atomic structure of various Au MPCs, such as Au_{25}, Au_{38}, Au_{144}, etc.[8] Use of this technique, however, is limited to only those clusters which can produce single crystals; thus samples need to be ultra-monodisperse.

X-ray single crystal studies of atomically precise Au clusters suggest that these clusters are made up of highly symmetrical Au core and $[-Au(I)SR-]_n$ "staple motifs". These oligomeric units attach to the Au core via the sulphur atoms, resulting in the formation of a core-shell type structure (Figure 1.2).[8]

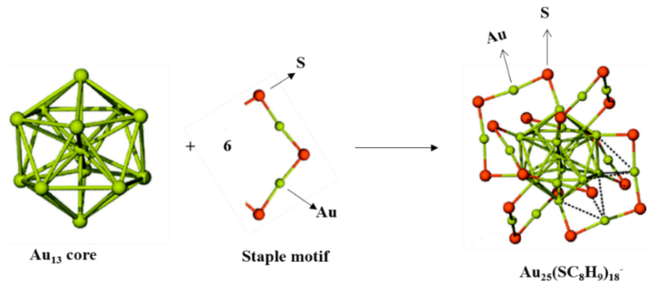

Figure 1.2 Crystal structure of $Au_{25}(SC_8H_9)_{18}^-$ cluster showing Au_{13} icosahedron core protected with 6 staple motifs. Reprinted (adapted) with permission from (29). Copyright (2008) American Chemical Society.

The length and the number of these oligomeric units vary from cluster to cluster. The first crystal structure study of an atomically precise Au_{102}(p-MBA)$_{44}$ cluster was published by Kornberg *et al*. and showed that Au_{102}(p-MBA)$_{44}$ clusters are made up of an 80 Au atom core and 22, –S-Au-S- staples which were attached to the Au_{80} core via sulphur atoms.[44] Subsequently, various other groups have reported similar types of bonding arrangements in different sized Au clusters. For example, Murray *et al*. reported the crystal structure of $Au_{25}(SC_8H_9)_{18}^-$ clusters.[29] These clusters are made up of an Au_{13} icosahedron core and 6 V-shaped –S-Au-S-Au-S- staple motifs. These clusters were found to carry a negative charge, which is balanced by the tetraoctylammonium ion (TOA^+) originally used in the synthesis. A crystal structure study of $Au_{38}(SC_8H_9)_{24}$ clusters suggested that these clusters are made up of Au_{23} prolate shaped core and three monomeric (-S-Au-S-) and six dimeric (-S-Au-S-Au-S-) staple motifs.[61] Here, Au_{23} core can be viewed as the fusion of two Au_{13} icosahedron cores by sharing one triangular plane of the icosahedron, resulting in the loss of a Au_3 unit. The crystal structure of [$Au_{24}(SCH_2Ph\text{-}^tBu)_{20}$] shows that two Au_4 tetrahedron units join together through two triangular faces of tetrahedron forming the Au_8 core.[62] This Au_8 core is further protected with four tetrameric $Au_4(SR)_5$ staple motifs forming the $Au_{24}(SR)_{20}$ cluster. Likewise, there are many other clusters reported in the literature with an unique core-shell structure.[8]

A major question which arises from these studies is what determines the stability of these clusters with different sizes and shapes? The most widely accepted theory in order to explain the stability of these clusters has been the super-atom theory.[63] According to this theory, Au clusters with a total number of valence electrons of 2, 8, 18, 34, 48, 58, 92, etc. are stable because they have closed electronic shells. The total number of valence electrons in a Au cluster can be expressed by the following equation 1.3.

$$N^* = N \times V_a - L - Z \text{ formula.} \qquad \textbf{(1.3)}$$

Here, N is the total number of Au atoms, V_a is the number of valence electrons per Au atom, L is the number of ligands, and Z is the charge on the Au cluster. Based on this formula, for $Au_{25}(SC_8H_9)_{18}^-$ clusters, the total number of valence electrons can be expressed as 25 x 1 – 18 + 1 = 8. Here, 8 represents the total number of valence electrons in $Au_{25}(SC_8H_9)_{18}^-$ clusters and therefore these clusters follow the super-atom stability concept as mentioned before. Using this formula, the stability of several clusters such as, $Au_{102}(SR)_{44}$ and $Au_{38}(SR)_{20}$ can also be explained.

However, there are numerous other clusters such as, $Au_{144}(SR)_{60}$, $Au_{24}(SR)_{20}$, $Au_{30}(SR)_{18}$, $Au_{40}(SR)_{24}$ and $Au_{44}(SR)_{28}$, the stability of which cannot be explained by using super-atom theory, and alternative explanations are needed in order to explain the stability of these clusters.

1.1.4 Applications

Because of the presence of Au core and surface monolayers, Au MPCs have been used for various applications such as sensing, catalysis, and photocatalysis. Sensing applications are based on the surface plasmon resonance band of the Au core and the ability to attach various monolayers with different functional groups. The second and third applications are based on the ability to tune Au MPC sizes and therefore the HOMO-LUMO band gap in order to study the size and electronic structure dependent catalytic and photocatalytic properties of Au nanocatalysts.

1.1.4.1 Sensing

Au MPCs have been used for the sensing of heavy metal ions, small molecules, and biological molecules. Metal ion sensing is typically based on the incorporation of metal ion binding sites into the monolayers. The binding of metal ions to these monolayers changes the intensity and the position of SPR band. For example, Hupp and co-workers reported that 11-mercaptoundecanoic acid-protected Au MPCs were able to coordinate with heavy metal ions such as Pb^{2+}, Hg^{2+}, and Cd^{2+}.[64] This resulted in the change in color of Au MPCs because of aggregation and therefore change in SPR band position. The selectivity towards different metal ions has been studied by various groups by modifying the monolayer on the surface of Au MPCs which would selectively bind to particular metal ion. Researchers have also reported that the sensitivity of detection can be significantly enhanced through metal-ion induced aggregation. Aggregation of Au MPCs leads to multifold enhancement in the detection limit compared to single Au clusters because of plasmon dipole coupling.[65-67]

Au MPCs with metallated monolayers (monolayers appended with metal ions) have been used for small molecules, DNA, and protein detection. Metal ions complexed with the functional groups of monolayers can act as binding sites for various compounds. For example, Yuan and co-workers reported the detection of bis-phosphorylated peptides using Au MPCs appended with dipicolylamine·Zn^{2+} complexes. The detection mechanism was based on red-to-blue color change of the Au MPCs solution because of the coordination of peptides with the metal ions complexed with surface monolayer, which resulted in MPC aggregation.[68] Gunnlaugsson and co-workers reported that Au MPCs with thiol monolayers complexed with Eu^{3+} were ideal candidates for the detection of phosphate and carboxylate containing molecules such as ATP, ADP, NADP or coumaric and pantothenic acid. The detection mechanism was based on luminescence quenching upon coordinating phosphate and carboxylate containing molecules with Eu^{3+}.[69] William and co-workers functionalized Au MPCs with Ru^{2+}-polypyridyl complexes. The resulting water soluble systems were found to have high affinity for salmon testes DNA.[70]

1.1.4.2 Catalysis

Au MPCs have been widely used for a variety of catalytic reactions mainly because of the ability to tune their sizes and the steric bulk of the monolayers. The catalytic activity of these MPCs has been found to be influenced by two main factors. First is the size of these MPCs which is directly correlated with the electronic structure and the number of low-coordinated surface atoms. Second is the accessibility of the cluster surface to substrate molecules which can be tuned by modifying the steric bulk of the capping ligands. Our group has recently shown that the catalytic activity of Au MPCs protected with different chain length thiolate stabilizers was directly related to the steric bulk of these stabilizers.[71] The highest activity for p-nitrophenol reduction was found in the case of least bulky stabilizers and catalytic activity decreased as the chain length of the stabilizers was increased. Jin and co-workers found that the catalytic activity of Au_{25} clusters protected with glutathione and captopril stabilizers for p-nitrobenzaldehyde hydrogenation was directly related to the steric bulk of these stabilizers. Captopril-stabilized Au_{25} clusters, because of the smaller steric bulk of captopril compared to glutathione, showed higher catalytic activity.[72] Mandal and co-workers studied the effect of chain length on the catalytic activity of Au MPCs for the reduction of p-nitrophenol, and the redox reaction between potassium ferricyanide and sodium thiosulfate. They established a direct correlation between the chain length of the stabilizers and catalytic activity.[73]

In a classic example, Jin and co-workers studied the size and structure dependent catalytic activity of atomically precise Au clusters for the chemoselective hydrogenation of 4-nitrobenzyldehyde.[74] Here, various Au clusters, such as Au_{15}, Au_{18}, Au_{25}, and Au_{38} protected with different thiolate stabilizers were used as catalysts and the resulting catalytic activity was correlated with the sizes and structures of these clusters. Zhu *et al.* studied styrene oxidation to benzaldehyde, styrene epoxide, and acetophenone using $Au_{25}(SR)_{18}$, $Au_{38}(SR)_{24}$, and $Au_{144}(SR)_{60}$ clusters as catalysts, and found that with an increase in cluster size the catalytic activity decreased.[75] Lie *et al*. studied the effect of Au cluster size on cyclohexane oxidation to cyclohexanol and cyclohexanone. They deposited various sized glutathione-protected Au clusters (Au_{10}, Au_{18}, Au_{25}, Au_{39}, and Au_{85}) on hydroxyapatite supports followed by calcination at 300°C in order to remove thiol stabilizers. The highest catalytic activity was observed for Au_{39} clusters and further increases in size led to decreases in the catalytic activity.[76] Wu *et al*. studied the activation of $Au_{25}(SR)_{18}^-$ clusters supported on various oxide supports for CO oxidation reactions.[77] Mild thermal activation of $Au_{25}(SR)_{18}^-/CeO_2$ under O_2 atmosphere was reported to be necessary in order to activate these clusters for catalysis. A mechanistic investigation on the origin of catalytic activity showed that thiol stabilizers block the active sites for catalysis. After thermal treatment at 473 K, removal of thiol stabilizers was observed with a concomitant enhancement in CO oxidation. Data suggested that catalysis took place at the interface of $Au_{25}(SR)_{18}^-$ clusters and CeO_2 support. While O_2 activation took place on CeO_2 support, CO was hypothesized to be activated by cationic Au sites generated after thiol stabilizers removal. Menard *et al*. reported the effect of thermal vs. ozone activation of $Au_{13}[PPh_3]_4[S(CH_2)_{11}CH_3]_4$ clusters deposited on TiO_2 support for the CO oxidation reaction.[78] Clusters activated via ozone treatment were found to catalyze CO oxidation at much lower temperature than clusters activated via thermal treatment. This was attributed to the significant growth in cluster size after thermal activation, whereas ozone treatment led to only minor growth in cluster size.

1.1.4.3 Photocatalysis

Au clusters, because of the presence of a HOMO-LUMO transition in the visible energy range, higher exited state lifetime, solubility in both polar and non-polar solvents, and relatively higher stability have been used as photocatalysts for several applications.[79-84] The advantages of using Au clusters have been to be able to tune their HOMO-LUMO band gap by tuning their sizes and the ability to tune their solubility by modifying the surface functionality.

Recently, Jin *et al*. showed that $Au_{25}(SC_8H_9)_{18}^-$ clusters were able to generate singlet oxygen ($^1O_2$) species upon exposure to visible light. These species was found to be responsible for the selective catalytic oxidation of organic sulfides to sulfoxides.[79] The optical band of $Au_{25}(SR)_{18}^-$ clusters (~1.3 eV) is larger than the energy of $^1O_2$ (~0.97 eV), which can allow for efficient energy transfer to $^3O_2$.[79] The efficiency of $^1O_2$ production as a function of cluster size was also studied. $Au_{25}(SR)_{18}^-$ clusters were reportedly found to produce $^1O_2$ much more efficiently than $Au_{38}(SR)_{24}$ clusters.[79] The reason behind this was the lower HOMO-LUMO gap of $Au_{38}(SR)_{24}$ clusters (~0.9 eV) compare to $^1O_2$, such that efficient electron transfer was not possible. Yu *et al*. reported the photocatalytic activity of $Au_{25}(SR)_{18}^-$ clusters supported on TiO_2 supports for methyl orange degradation.[80] TiO_2 has long been used as photocatalyst; however, it absorbs light mainly in the ultra-violet (UV) range, which limits the application of TiO_2 in photocatalytic applications because of the lack of absorption in visible range due to its large band gap (~3.2 eV). Yu *et al*. reported that a Au_{25}-TiO_2 composite material was an excellent catalyst for visible light driven photocatalytic degradation of methyl orange. Here, under visible light irradiation, $Au_{25}(SR)_{18}^-$ clusters generated exited electrons and holes. The exited photoelectrons were injected into the conduction band of TiO_2, while the leftover hole in the $Au_{25}(SR)_{18}^-$ clusters then reacted with O_2 forming $^1O_2$, which subsequently reacted with the dye molecule.[81] Lee *et al*. reported that the photocatalytic activity of ZnO-Au composites was found to increase with an increase in the size of Au cluster.[82] Here, an increase in cluster size was found to affect the rate of electron transfer from ZnO to the Au clusters, which subsequently affected the photocatalytic activity of the ZnO-Au composite material for the photobleaching of thionine. Size- and electronic structure-dependent photocatalytic activity of various Au MPCs was studied by Kamat and co-workers for the photocatalytic reduction of methyl viologen.[85] The photocatalytic activity of different sized glutathione protected Au MPCs was found to be directly correlated with the ligand-to-metal charge-transfer lifetime. The photocatalytic activity trend showed increasing photocatalytic reduction yields with decreasing cluster sizes, $Au_{25} < Au_{18} < Au_{15} < Au_{10-12}$.

1.2 Bimetallic Clusters

Bimetallic clusters can be defined as structurally well-characterized and highly monodisperse clusters (typically <2 nm in diameter) made up of two different metal components.[86-88] These clusters, owing to their well-characterized structures offer an opportunity to systematically study the effect of mixing two metal components on the physicochemical properties of resulting bimetallic species.[89-92]

1.2.1 Synthesis of Bimetallic Clusters

Bimetallic clusters have been mainly synthesized by using two strategies, namely, co-reduction strategies and post synthetic treatment strategies.

Co-reduction strategies typically involve the mixing of two metal salts in the presence of stabilizers followed by the addition of a reducing agent. The resulting crude mixture is then subjected to either thiol induced etching in order to synthesize the most stable bimetallic species or a purification step in which different sized bimetallic clusters are separated using either solvent extraction or chromatographic separation.[87,90,93-104] Formation of bimetallic clusters using this strategy have been reported to be influenced by several factors such as the redox potentials of the two metal components, their atomic radii, and the interaction between the metals and stabilizers.

In a classic example, Negishi *et al*. reported the synthesis of $Au_{25-x}Ag_xL_{18}$ bimetallic clusters, where x varied from 0 to 11.[93] Here, Au and Ag have similar atomic radii (~1.44 Å), which makes it easier to incorporate Ag within Au clusters.[95] However, the difference in redox potentials of Au ($AuCl_4^-$/Au: ca. 1V) and Ag (Ag^+/Ag: ca. 0.8 V) may lead to a separation of Ag and Au phases after the addition of reducing agent.[105] Negishi *et al*. overcame this challenge by using the difference in binding affinity of thiol stabilizers with Au and Ag metals,[93] as the thiol stabilizers have a higher binding affinity with Au than with Ag.[105] This can significantly reduce the redox potential difference between Au and Ag and therefore ensure the formation of bimetallic species. Xie *et al*. also reported the synthesis of mixed thiolate protected $Au_{25-x}Ag_xL_{18}$ bimetallic clusters.[45] Here, different ratios of hydrophobic and hydrophilic thiols were used in order to synthesize mixed thiolate-protected AuAg bimetallic clusters. It should be noted that the incorporation of both hydrophobic and hydrophilic stabilizers on the cluster surface can be challenging because of the difference in solubility between two different stabilizers, and difference in binding affinity with the two different metal components. These issues were mitigated by the incorporation of NaOH into the reaction mixture during the addition of $NaBH_4$. NaOH was proposed to diminish the reducing strength of $NaBH_4$.[106] Under these weakly reducing conditions, both stabilizers were found to be incorporated on the surface of the bimetallic clusters. In addition to $Au_{25-x}Ag_xL_{18}$ bimetallic clusters, $Au_{144-x}Ag_xL_{60}$ and $Au_{38-x}Ag_xL_{24}$ bimetallic clusters have also been synthesized. Unlike $Au_{25-x}Ag_xL_{18}$ clusters, $Au_{144-x}Ag_xL_{60}$ and $Au_{38-x}Ag_xL_{24}$ clusters were synthesized through post-synthetic thiol etching treatments of as-synthesized MPC polydisperse mixtures at elevated temperatures.[88,96] This is similar to the method used to make monometallic $Au_{38}(SR)_{24}$ clusters, where the synthesis of Au_{38} clusters requires post-synthetic thiol etching.[38]

$Au_{25-x}Cu_xL_{18}$ bimetallic clusters were synthesized by Negishi *et al.*.[97] It should be noted that unlike Ag, Cu has much lower atomic radius (1.28 Å) than Au (1.44 Å), and also the redox potential of Cu (Cu^{2+}/Cu: ca. 0.34 V) is much lower than Au (Au^{3+}/Au: ca. 1 V).[105] Based on this, it can be envisioned that the incorporation of Cu with Au might be challenging. Characterization of the resulting bimetallic clusters showed that, unlike $Au_{25-x}Ag_xL_{18}$ bimetallic clusters, $Au_{25-x}Cu_xL_{18}$ could only accommodate a maximum of 5 Cu atoms.[97] This was attributed to the difference in atomic radii and redox potentials between Au and Cu. Instability of the resulting AuCu bimetallic clusters because of the difference in above mentioned physical parameters was also shown by Gottlieb *et al.*[87] Here, they found dealloying of as synthesized $Au_{25-x}Cu_xL_{18}$ bimetallic clusters into stable monometallic $Au_{25}L_{18}^-$ clusters after a certain period of incubation. Kurashige *et al.* showed that more than 5 Cu atoms can be incorporated with Au in the resulting $Au_{25-x}Cu_xL_{18}$ bimetallic species by changing the bond strength of the thiol stabilizers.[99] They used selenolate stabilizers instead of thiolate stabilizers and found that up to 9 Cu atoms could be incorporated with Au. This was attributed to the enhanced binding strength of the selenolate ligands with Au and Cu metals, which imparts an extra stabilizing effect on the resulting bimetallic species.

Several groups have also reported the synthesis of $Au_{24}ML_{18}$ (M = Pd, Pt) bimetallic clusters.[90,104,107-109] Interestingly, only one hetero atom was found to be incorporated in the Au clusters, regardless of the initial metal salt ratio. The reason behind this anomaly could be the higher stability of resulting $Au_{24}ML_{18}$ bimetallic clusters compared to $Au_{25-x}M_xL_{18}$ bimetallic clusters.[102,109] Structural studies using x-ray single crystal spectroscopy and DFT calculations suggest that Pd or Pt atoms were incorporated inside the Au_{13} core of the Au_{25} cluster. Theoretical studies suggest that the incorporation of one Pd atom into the Au_{13} core of Au_{25} cluster would stabilize resulting bimetallic clusters more than the incorporation of more than one Pd atoms.[109]

While the co-reduction strategy has been used in order to incorporate different numbers of hetero atoms within Au cluster, it usually suffers from low yields of the resulting bimetallic clusters. This is because of the tedious post-synthetic separation steps involved in order to isolate specific bimetallic clusters from the crude mixture. For example, Jin and co-workers reported the synthesis of $PtAu_{24}(SR)_{18}$ clusters.[90] These clusters were synthesized using co-reduction strategy and isolated from crude mixture using size exclusion chromatography (SEC). The yield of these clusters was reported to be ca. 5%.

Post-synthetic strategies typically involve the reaction between as-synthesized monometallic thiolate-protected Au clusters and metal salts resulting in the formation of bimetallic clusters.[110-113] Murray *et al*. first reported the use of post-synthetic strategy in the synthesis of $Au_{25-x}M_xL_{18}$ (M = Ag, Cu, and Pb) bimetallic clusters via the reaction between $Au_{25}L_{18}^-$ clusters and metal salts.[111] They proposed that the reaction proceeded through a galvanic exchange between $Au_{25}L_{18}^-$ clusters and the metal ions. Here, the metal ions were reduced by exchanging electrons with the negatively charged Au clusters and the reduced metal atom was found to be incorporated into the resulting bimetallic species. Using this method, metal atoms have been usually found to be incorporated into the Au core. However, Wu and co-workers showed that reduced Ag atoms form adducts with Au_{25} clusters and proposed using DFT calculations that two Ag atoms were directly bonded with the Au_{13} core.[113]

Contrary to the co-reduction strategy, post-synthetic strategies are relatively similar in nature, as it involves the treatment of monometallic Au clusters with desired metal ions. Also, using post-synthetic strategies, in theory higher yields of the resulting bimetallic clusters can be obtained, as it does not involve any post-synthetic step in order to isolate bimetallic clusters from the crude mixture.

1.2.2 Structural Studies of Bimetallic Clusters

References suggest that the structure of bimetallic clusters can be viewed as core-shell type structures. Here, as for pure Au clusters, the metal core is protected by $(\text{-S-M-S-M-S-})_n$ type staple motifs. Studies suggest that hetero metal atoms could either become the part of core resulting in the formation of a mixed metal core or could become the part of staple motifs.[101-106] Detailed characterization of these clusters using EXAFS spectroscopy is described elsewhere (Section 1.3.3.4).

A crystal structure study of $Au_{24}PdL_{18}$ bimetallic clusters shows that the central Au atom from the Au_{13} icosahedron core of Au_{25} clusters was replaced by one Pd atom resulting in the formation of $Au_{25}PdL_{18}$ bimetallic clusters.[107-109,49] Theoretical studies suggest that the positioning of Pd atom at the center of the icosahedral core could lead to the enhancement in the interaction energy between central Pd atom and the surrounding $Au_{24}L_{18}$ core, and the replacement of central Au atom with Pd increases the thermodynamic stability of the resulting bimetallic cluster.[114] Tsukuda and co-workers also carried out extended X-ray absorption fine structure (EXAFS) analysis on these bimetallic clusters and found that the Pd-Au coordination number value after fitting was 12, and no Pd-S contribution was observed, further supporting a structure where Pd was incorporated at the center of the icosahedron core.[115] Jin and Zhang's groups subsequently predicted a similar structure for $PtAu_{24}L_{18}$ bimetallic clusters using EXAFS spectroscopy; EXAFS data also supported the fact that Pt atoms replaced the Au atom in the center of the Au_{13} icosahedron core.[103]

Yamazoe *et al*. studied the structure of $Au_{25-x}Ag_xL_{18}$ and $Au_{25-x}CuL_{18}$ bimetallic clusters using EXAFS spectroscopy.[116] Here, unlike the case for Pd atoms above, Ag and Cu atoms were found to be incorporated on the surface of the Au core. EXAFS data suggested that Ag atoms were incorporated on the surface of the Au_{13} core and Cu atoms were incorporated into the staple motifs. Incorporation of Ag on the surface of Au_{13} core was also predicted by the density functional theory (DFT) calculations. According to DFT, the lower surface energy of Ag(111) (1.25 J m^{-2}) compared to Au(111) (1.55 J m^{-2}) and similar atomic radii of Ag (1.45 Å) and Au (1.44 Å) atoms favor the incorporation of Au and Ag together on the surface.[117-118] Incorporation of Cu into the surface staple motifs was, however, not predicted by DFT calculations. This is because of the much higher surface energy of Cu(111) (1.83 J m^{-2}) compared to Au(111), which should favor the incorporation of Cu inside the Au_{13} core as in the case of Pd.[118] Later studies of $Au_{38-x}Ag_xL_{24}$ and $Au_{144-x}Ag_xL_{60}$ clusters also supported the incorporation of Ag atoms on the surface of Au core.[88,96] These theoretical findings in the case of AuAg bimetallic clusters were subsequently substantiated by the first successful crystallization and x-ray single crystal analysis of $Au_{25-x}Ag_xL_{18}$ bimetallic clusters by Dass and co-workers.[119] Data showed that the 12 Au atoms surrounding the central Au atom of 13 atom icosahedron core were substituted by Ag atoms in the resulting bimetallic clusters. X-ray single crystal analysis in the case of mixed ligand-protected (phosphine and thiolate) $Au_{13}Cu_x$ (X = 2, 4, 8) clusters suggested that an intact Au_{13} icosahedron core was protected with thiolate stabilizers directly and by phosphine ligands through Cu atoms. Here, as suggested by the earlier EXAFS study, Cu atoms did not become the part of Au_{13} core and preferred to stay in surface ligand motifs.[100]

It should be noted that the structure of bimetallic clusters with similar metal compositions obtained using two different strategies mentioned above could be different. For example, $Au_{24}AgL_{18}$ bimetallic clusters prepared through a co-reduction strategy were shown to have Ag atoms incorporated on the surface of Au_{13} core.[116] On the other hand, synthesis of AuAg bimetallic clusters through a postsynthetic strategy led to the formation of an $Au_{25}Ag_2L_{18}$ adduct. Here two Ag atoms were found to form an adduct with the Au_{13} core.[113]

1.2.3 Applications of Bimetallic Clusters

Bimetallic clusters, owing to the atomic level understanding of their structures, have been used in order to elucidate the systemic changes in physicochemical properties after mixing two metal components.

1.2.3.1 Photoluminescence

As mentioned previously, metal clusters (Au and Ag), because of their small sizes (<2 nm) can show a HOMO-LUMO gap.[47] Because of this, metal clusters show strong photoluminescence, and this property of metal clusters has been utilized in several applications such as metal sensing, biological imaging, and biological detection.[121-123] Recently, successful synthesis of structurally well-characterized bimetallic metal nanoclusters (<2 nm in size) have prompted the scientific community to study their structure dependent photoluminescence responses.

Jin *et al*. reported that upon substituting 13 Au atoms from rod shaped $[Au_{25}(PPh_3)_{10}(SC_2H_4Ph)_3Cl_2]^{2+}$ clusters by 13 Ag atoms, strong enhancement in the photoluminescence was observed.[124] Monometallic Au_{25} clusters showed only weak luminescence (QY = 0.1%) which upon substitution with 13 Ag atoms was increased to 40.1% in the resulting $Ag_{13}Au_{12}$ bimetallic cluster. Photoluminescence data suggested that substitution by up to 12 Ag atoms only led to very small enhancement in the photoluminescence (QY = 0.21%); however, after substitution with 13th Ag atom, photoluminescence increased dramatically to 40.1%. Here, the number and the position of substituted Ag atoms were characterized using mass spectrometry and X-ray single crystal spectroscopy. Dou *et al*. reported that $Au_{18}L_{14}$ monometallic clusters, upon treatment with Ag^+ started to show huge enhancement in the photoluminescence (QY = 6.8%) compared to monometallic $Au_{18}L_{14}$ clusters with very weak photoluminescence (QY = 0.37%).[125] Data suggested that Ag atoms were incorporated into the staple motifs of Au_{18} clusters, leading to dramatically increased emission, which they termed as aggregation-induced emission (AIE). Appearance of photoluminescence because of the incorporation of Ag^+ in to the staple motifs was substantiated by a control experiment. Here, they treated bimetallic clusters with cysteine, which preferentially reacted with Ag and turned off the photoluminescence. Products before and after the addition of cysteine were characterized by mass spectrometry and X-ray photoelectron spectroscopy, which again pointed towards the incorporation of Ag^+ into the staple motifs. Negishi *et al*. synthesized a series of $Au_{25-x}Ag_xL_{18}$ bimetallic clusters and studied the effect of Ag doping on photoluminescence.[93] Data suggested that Ag doping took place on the surface of the Au_{13} icosahedron core and a modulation in the emission wavelength was observed with doping. Pradeep and coworkers synthesized $Ag_7Au_6L_{10}$ bimetallic clusters starting with Ag_6 or Ag_7 monometallic clusters as precursors.[110] Here AgAu bimetallic clusters were shown to have a 10 fold enhancement in the emission intensity compared to monometallic Ag clusters.

1.2.3.2 Catalysis

Bimetallic nanoparticles have improved activity and selectivity for several chemical transformations compared to their monometallic constituents.[126] Improved activity and selectivity have been mainly attributed to two factors, namely ligand and ensemble effects. Ligand effects arise because of the modification in electronic structure upon mixing two metal components.[127] Ensemble effects arise from the particular surface arrangements of both metal components. In practical terms, it becomes very difficult to isolate these two effects because of the polydispersity of the bimetallic nanoparticles, and therefore the realization of the full potential of bimetallic nanoparticles for catalytic applications is challenging.

Bimetallic clusters are a new class of materials, and have the potential to address above mentioned issues because of their well-defined structures. In bimetallic clusters, the catalytically active component can be incorporated either on the surface or inside the core and thereby can help to elucidate structure/property relationships that result in improved catalytic activity and selectivity upon mixing two metal components.

Toshima *et al*. synthesized AuPd bimetallic clusters through galvanic exchange between Pd_{147} clusters and Au^{3+} ions. Au atoms in bimetallic clusters found to be atomically dispersed on the surface of Pd cluster. These bimetallic clusters were found to have much higher catalytic activity for glucose oxidation reactions than their larger counterparts.[89] Due to the presence of atomically well-dispersed Au atoms on the surface and results obtained from X-ray photoelectron spectroscopy, the high catalytic activity was attributed to the electronic effect as a result of the charge transfer from Pd to Au. Jin and coworkers synthesized $PtAu_{24}L_{18}$ bimetallic clusters and used them for styrene oxidation reactions.[90] Here, bimetallic clusters were found to have much higher catalytic activity (90.8% conversion) and selectivity (89.9% for benzaldehyde) for styrene oxidation reaction compared to monometallic $Au_{25}L_{18}$ clusters, which showed only 58.9% conversion and 54.0% selectivity towards benzaldehyde. It should be noted that in these bimetallic clusters Pt was incorporated inside the 13 atom icosahedron core. Since Pt is not in direct contact with styrene, the enhancement in catalytic activity and selectivity is likely caused by the electronic perturbation of the surface atoms after Pt incorporation. Similarly, Tsukuda and coworkers showed that $PdAu_{24}L_{18}$ bimetallic clusters were more active for benzyl alcohol oxidation reaction than monometallic $Au_{25}L_{18}^-$ clusters. Here Pd was also incorporated inside the 13 atom icosahedron core, and hence catalytic activity was attributed the modulation in electronic structure upon Pd incorporation.[128]

1.3 X-ray Absorption Spectroscopy

X-ray absorption spectroscopy is a branch of spectroscopy in which X-ray photons over the energy range of 100 eV to 100 keV are used to characterize crystalline or amorphous materials in bulk or nanoscale form. Absorption of X-rays by a material takes place based on the Lambert-Beer law. According to the Lambert-Beer law, if a photon of intensity I_o is incident on the sample then the transmitted intensity of the photon (I_t) can be defined as follows (Equation 1.4).

$$I_t\,(t) = I_o e^{-\mu(E)t}. \qquad \textbf{(1.4)}$$

Here, μ(E) is the frequency dependent absorption coefficient. When the energy of the photon equals or exceeds the binding energy of the core electron then a sharp increase in absorption coefficient takes place, as shown in Figure 1.3. Above the absorption edge, any energy higher than binding energy is converted into the kinetic energy of the photoelectron and the absorption coefficient will continue to decrease with increase in photon energy. The absorption coefficient is a smooth function of photon energy and varies approximately as follows (Equation 1.5).

$$\mu(E) \sim dZ^4/mE^3 \qquad \textbf{(1.5)}$$

Here, d represents the target density, Z represents atomic number, and m represents mass. Ejection of the photoelectron simultaneously creates a core-hole. This hole gets filled by an electron from higher energy state after a short time period of the order of 10^{-15} seconds and the corresponding energy difference is released through fluorescence X-rays or Auger electron emission.[129] In this section, spectroscopic techniques related to only absorption of photons such as X-ray absorption near edge structure (XANES) spectroscopy, and extended X-ray absorption fine structure (EXAFS) spectroscopy are discussed.

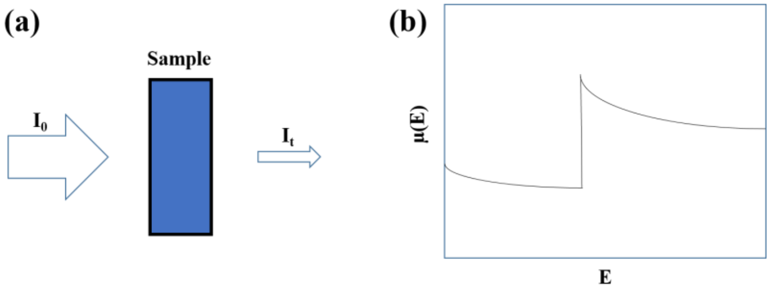

Figure 1.3 (a) Schematic of an incident and transmitted X-ray beam and (b) absorption coefficient as a function of photon energy around the absorption edge.

1.3.1 X-ray Absorption Near Edge Structure (XANES) Spectroscopy

XANES spectroscopy deals with the region within ~50 eV of the absorption edge which is characterized by the transition of a photoelectron to an unoccupied bound state (Figure 1.4). This region is divided in to three parts. The first part is the pre-edge which is caused by the electronic excitation to empty bound states. The second part is the absorption-edge, which is caused by the excitation of a photoelectron to the continuum. And, third part is caused by the multiple scattering of photoelectron ejected at low kinetic energy.[129] Two types of absorption edges are commonly used in this thesis; K-edge and L-edge. K-edges result from the excitation of an electron from 1s orbital (which have allowed transitions to p orbitals), while the L-edges represents the excitation of an electron from a 2s or 2p orbital. XANES features are sensitive to the oxidation states of absorbing atom and the coordination environments around the absorbing atom.[129] Higher oxidation states can leads to the increase in absorption edge (white line intensity) and also shift the absorption edge to the higher energy range.[122-126] XANES features are also useful in explaining the charge transfer phenomenon from or towards the absorbing atom. For instance, in the case of AuPd alloy bimetallic nanoparticles, charge transfer takes place from Pd to Au.[130-133] This charge transfer leads to higher white line intensity in the case of Pd L_3-edge (which probes the $2p_{3/2}$ to 4d transition) and reduced white line intensity in the case of Au L_3-edge, which probes the $2p_{3/2}$ to 5 transition.

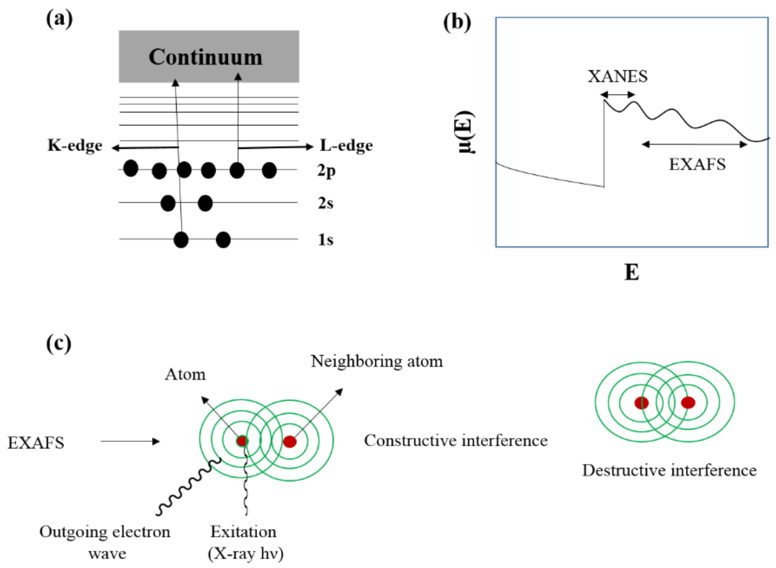

Figure 1.4 (a) Excitation of an electron to empty bound state, (b) absorption coefficient as a function of photon energy including EXAFS features, and (c) schematic depiction of constructive and destructive interferences.

1.3.2 Extended X-ray Absorption Fine Structure Spectroscopy (EXAFS)

EXAFS refers to the oscillatory features in the X-ray absorption spectrum ~30 eV past the absorption edge. These features arise because of the scattering of the created photoelectron from the atoms surrounding the absorbing atom. These scattered photoelectron waves interacts with the outgoing photoelectron wave to produce both constructive and destructive interferences, which eventually results in EXAFS oscillations in the X-ray absorption spectrum (Figure 1.4). Since EXAFS features originate because of the presence of neighboring atoms around the absorber, it is therefore dependent on the atomic arrangement around the absorbing atom. It contains information about the bond distance, coordination number, and thermal and structural disorder of atoms around a particular atomic species. EXAFS does not require long range order and thus amorphous materials also exhibit EXAFS oscillations.[129]

1.3.2.1 EXAFS equation

EXAFS refers to the extended features in the X-ray absorption spectrum ~30 eV past the absorption edge. Figure 1.5a shows the L_3-edge X-ray absorption spectrum of $Au_{25}(SC_8H_9)_{18}^-$ clusters supported on mesoporous carbon support ($Au_{25}(SC_8H_9)_{18}^-$/carbon). Figure 1.5b is the extracted EXAFS signal from L_3-edge absorption spectrum from this spectrum in k-space (i.e. wavenumber space), with the y axis multiplied by k^2 in order to increase the magnitude of the signal at high k values.

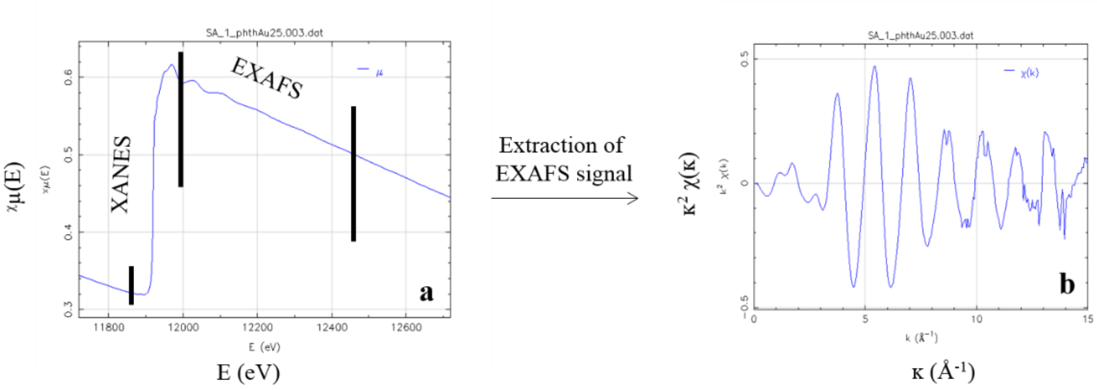

Figure 1.5 (a) L_3-edge x-ray absorption spectrum of $Au_{25}(SC_8H_9)_{18}^-$/carbon and (b) extraction of the EXAFS signal in k-space from the X-ray absorption spectrum.

The EXAFS fine structure function $\chi(E)$ is described as:

$$\chi(E) = (\mu(E) - \mu_0(E))/(\Delta\,\mu_0(E)) \quad \textbf{(1.6)}$$

Here, $\mu(E)$ is measured absorption coefficient, $\mu_o(E)$ is smooth background function representing the absorption of an isolated atom, and $\Delta\mu_o(E)$ represents the jump in the absorption $\mu(E)$ at the threshold energy E_o. Because of the wave-nature of the photoelectron, the EXAFS function (χ) can be written as a function of wavenumber (k) (Equation 1.7):

$$k = \sqrt{(2m_e(E - E_0)/\hbar^2)} \quad \textbf{(1.7)}$$

Here, m_e represents the electron mass, and ħ represents Planck constant divided by 2.

The EXAFS signal can be fourier transformed back into *R*-space, as shown in Figure 1.6. *R*-space data show various bonding pairs present in $Au_{25}(SC_8H_9)_{18}^-$ clusters.

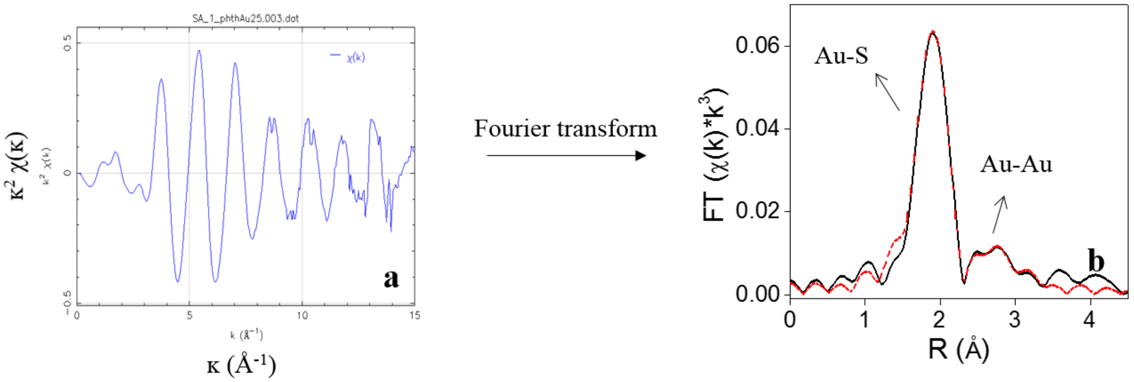

Figure 1.6 (a) EXAFS signal of $Au_{25}(SC_8H_9)_{18}^-$/carbon in k-space and (b) Fourier transformation of the EXAFS signal form k-space to *R*-space.

The EXAFS function can be expressed as a sum over the scattering contributions arising from the various scattering paths (Equation 1.8).[116]

$$\chi(k) = \sum_j S_0^2\, N_j \frac{|f_j(k)|}{kR_j^2}\, e^{-2R_j/\lambda(k)} e^{-2\sigma_j^2 k^2} \text{x}\, sin\, [2kR_j + \delta_c\,(k) + \delta_j\,(k)] \qquad \textbf{(1.8)}$$

Here, j represents the paths with same kind of scattering atom and same path length. S_0^2 represents the amplitude reduction factor. N_j represents the coordination number or the degeneracy of a particular scattering path, and $f_j(k)$ represents the scattering amplitude. The term $e^{-2R_j/\lambda(k)}$ accounts for the increasing decay of the photoelectron wave with increasing distance R_j. The term $e^{-2\sigma_j^2 k^2}$ accounts for the k dependent dampening of the EXAFS wave. Here σ is the disorder parameter (Debye-Waller parameter). Atoms in a given coordination shell do not have the same distance from the absorber. This is because the vibration of atoms from their mean position (thermal disorder) or structural variation in bond distance (static disorder). This results in the dampening of EXAFS wave with increasing k. The potential of the absorbing and scattering atom leads to a phase shift of the photoelectron wave represented by $\delta_c\,(k)$ and $\delta_j\,(k)$. This eventually appears in the sine function of the EXAFS wave.[134] A model can be used to fit EXAFS signal using above equation. Here, scattering amplitude and phase shift are calculated from the model, and amplitude reduction factor is calculated from the reference. Using the EXAFS equation, structural parameters such as, coordination number (N_j), distance between absorbing and scattering atom (R_j), disorder parameter (σ), and energy shift (E_0) can be calculated.

1.3.3 Characterization of Au and Bimetallic Clusters using X-ray Absorption Spectroscopy

XANES spectroscopy is typically used to characterize the oxidation state of metals and the coordination environments around the absorbing atom, therefore the main focus of this section will be on the characterization of Au and bimetallic clusters using EXAFS spectroscopy. As EXAFS spectroscopy is sensitive to the type and number of the surrounding atoms around the absorber and the distance between absorber and neighboring atoms, it has been used very extensively in order to characterize atomically-precise Au and bimetallic clusters.

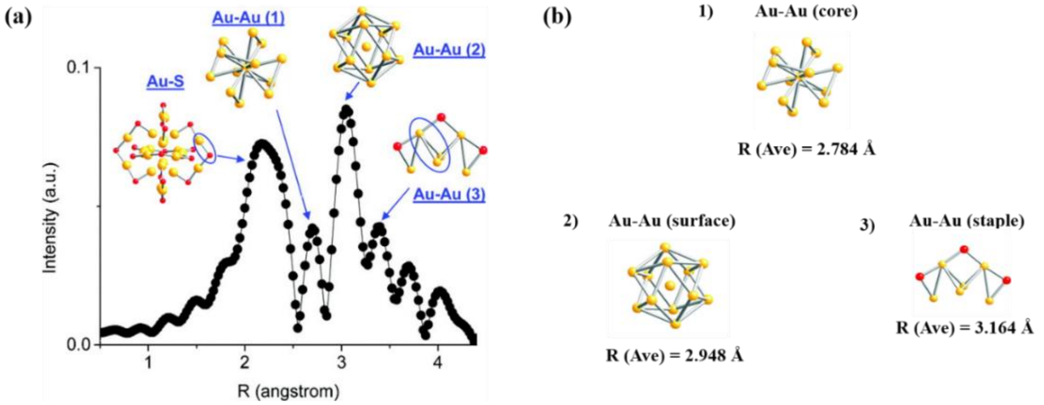

Figure 1.7 (a) Simulated FT-EXAFS from $Au_{25}(SR)_{18}^{-}$ clusters (b) different Au-Au bonding pairs present within Au_{25} cluster. Reprinted with adaptions with permission from (135). Copyright (2011) American Chemical Society.

1.3.3.1 EXAFS Characterization of $Au_{25}(SC_8H_9)_{18}$ Clusters

Zhang and coworkers *et al*. first reported the successful characterization of $Au_{25}(SC_8H_9)_{18}$ clusters using EXAFS spectroscopy.[135] Based on single crystal data reported by Jin and coworkers and Murray and coworkers,[28-29] $Au_{25}(SC_8H_9)_{18}^{-}$ clusters are made up of a 13 Au atoms icosahedron core and 6 V-shaped –S-Au-S-Au-S- staple motifs (as seen in Figure 1.5).

The staple motifs attach to the Au_{13} icosahedron core on Au_3 triangular planes forming the Au_{25} cluster. There are three different first-shell Au-Au bonding pairs present within Au_{25} cluster. The first Au-Au bonding pair represents the bonding between the central Au atom of the Au_{13} icosahedron and the 12 surface Au atoms of the core, and 6 short Au-Au pairs present on the surface of icosahedron with an average bond distance of 2.78 Å. The second Au-Au pair represents the larger distance Au-Au pairs present on the surface of the Au_{13} icosahedron with a bond distance of 2.95 Å. The third and last Au-Au bonding pair represents the bonding between surface Au atoms in the Au_{13} core and staple Au atoms (Figure 1.5).

The EXAFS spectrum of $Au_{25}(SC_8H_9)_{18}^-$ clusters shows four different peaks in R-space (Figure 1.5a). The first peak at ~ 2Å represents the Au-S contribution and three small peaks from ~ 2.5-3.8Å represent different Au-Au contributions as mentioned above (Figure 1.5b). X-ray single crystal data of $Au_{25}(SC_8H_9)_{18}^-$ clusters show four Au-Au bonding pairs instead of three. Surface Au atoms of Au_{13} core have two different Au-Au bonding pairs. Au-Au pairs directly below staple motifs are slightly squeezed (ca. 2.81 Å) compared to other Au-Au pairs (ca. 2.96 Å) on the surface. However, such a small difference between the bond distance values of squeezed Au-Au pairs and Au(central)-Au(surface) pairs is difficult to discriminate by FT-EXAFS, thus only three Au-Au boning pairs are observed in FT-EXAFS. In order to fit the EXAFS data, the coordination numbers for all three Au-Au bonding arrangements can be calculated theoretically, and can be fixed in order to fit bond distances, disorder parameters, and energy shifts of the Au clusters.[134] The amplitude reduction factor is usually obtained from Au foil, as it is common practice to determine the amplitude reduction factor for a model metal foil and use that information while fitting samples containing that metal.

1.3.3.2 EXAFS Characterization of $Au_{38}(SC_8H_9)_{24}$ Clusters

MacDonald *et al*. reported the EXAFS characterization of $Au_{38}(SC_8H_9)_{24}$ clusters.[136] Based on the single crystal structure reported by Jin and co-workers,[61] the $Au_{38}(SC_8H_9)_{24}$ cluster is made up of two face-fused Au_{13} icosahedron cores through the Au_3 triangular planes resulting in the formation of a Au_{23} prolate core. This Au_{23} core is capped with three monomeric (-S-Au-S-) and 6 dimeric (-S-Au-S-Au-S-) staple motifs resulting in the formation of the $Au_{38}(SC_8H_9)_{24}$ cluster. Based on the crystal structure data, bond lengths between the central atom of either unit of Au_{23} dimeric core and first-shell Au atoms range from 2.76 to 2.84 Å. Au-Au bond distances at the exterior of the Au_{23} core is 2.76-3.08 Å. Each exterior Au atom in the staple motifs has one shorter Au-Au bond distance (3.04-3.12 Å) to the biicosahedron and two longer ones (3.18-3.29 Å) to the other two Au atoms of Au_3 plane it is capping. The Au-S bond distance in the staple motifs is *ca.* 2.30 Å. EXAFS spectra of $Au_{38}(SC_8H_9)_{24}$ clusters in R space shows three major first shell peaks. The first peaks represents the Au-S contributions and two minor peaks represent the Au-Au contributions. The first Au-Au peak represents the Au-Au bonding between the central Au atom and surface Au atoms, and the second Au-Au peak represents the surface Au-Au bonding pairs. Based on this, the coordination number values for each Au-Au and Au-S bonding environments was calculated and fixed while fitting the EXAFS data. Based on X-ray single crystal data, the $Au_{38}(SR)_{24}$ cluster also has higher shell Au-Au bonding pairs but the EXAFS spectrum in R-space did not show significant Au-Au contributions at higher R-ranges.

Similarly, many other monometallic clusters such as $Au_{36}(SR)_{24}$, $Au_{28}(SR)_{20}$, and $Au_{102}(SR)_{44}$ have also been analyzed using EXAFS spectroscopy.[133-135] It should be noted that the prior knowledge of crystal cluster structure is extremely important in order to carry out precise EXAFS fittings, and therefore EXAFS is mainly used in order to study the structure and stability of these clusters under various chemical environments.

1.3.3.3 EXAFS Characterization of $[Au_{25-x}(SR)_{18}M_x]$(M = Ag, Cu) Bimetallic Clusters

Mass spectrometry suggests that atomic doping of Ag or Cu atoms takes place in Au_{25} clusters, but it does not tell anything about the possible structure of the resulting bimetallic cluster. Theoretically, three possible sites within the Au_{25} cluster are available for doping by Ag or Cu atoms. The first site is the central Au atom of the Au_{13} icosahedron core which can be replaced by Ag or Cu atoms. The second site would be the surface of Au_{13} icosahedron core, and third site would the staple motifs of the Au_{25} cluster, where Au atoms from these staple motifs can be replaced by Ag or Cu atoms. Based on these three doping sites model structure can be generated, and structural parameters and theoretical coordination number values around doped Ag or Cu atoms for different doping sites can be calculated. For example; in the case of first doping site, there would be 12 Au atoms surrounding the central Ag or Cu atom, and there would be no Ag-S or Cu-S bonding. In the case of second doping site, there would be 6 Au atoms surrounding the Ag or Cu atoms and these atoms would further be bonded with 1 S atom. In the case of third doping site, there would be no Au atom directly bonded with Ag or Cu atoms; however, these atoms would be bonded with two S atoms. Yamazoe *et al*. found in the case of $Au_{25-x}Ag_xL_{18}$ bimetallic clusters that Ag K-edge EXAFS data after fitting shows Ag-S coordination number of 1, and a first shell Ag-Ag coordination number of 3.4(9).[116] This means that the second doping site where Ag atoms were doped on the surface of Au_{13} icosahedron core is the most probable structure. In the case of Cu K-edge, EXAFS fitting by Yamazoe *et al*. gave a first shell Cu-S coordination number of 2.4(2) and no Cu-Au contribution was observed. This suggests that Cu atoms were substituted into the staple motifs of Au_{25} clusters.[108]

1.3.3.4 EXAFS Characterization of $Au_{24}Pd(SR)_{18}$ Bimetallic Clusters

Based on the arguments made above on the structure of bimetallic clusters, the structure of $Au_{24}Pd(SR)_{18}$ clusters synthesized using co-reduction methodology was shown to have Pd atoms doped in the center of the Au_{13} icosahedron core. Pd K-edge EXAFS spectrum of these bimetallic clusters showed only one peak in R-space located at ~2.5 Å. This peak was attributed to the Pd-Au bonding contribution. Pd-Au coordination number value after fitting was 10.7 (9), which again suggested the replacement of central Au atom with Pd atom resulting in the formation of $Au_{24}Pd(SR)_{18}$ bimetallic cluster.[115,103] EXAFS analysis of $Au_{24}Pt(SR)_{18}$ clusters synthesized using co-reduction methodology has also been also reported. However, because of the Pt-thiolate impurity present in the sample, exact correlation between the EXAFS coordination numbers and structure was not possible and thus is not discussed here.

1.3.3.5 EXAFS Study of the Activation of Atomically-Precise Au Clusters for Catalysis

EXAFS has also been shown to be useful in studying the activation of atomically-precise Au clusters for various catalytic reactions. For example, Tsukuda and co-workers studied the thermal activation of $Au_{25}(SR)_{18}^-$ clusters supported on porous carbon nanosheets for benzyl alcohol oxidation reactions.[137] Correlation of catalyst structure after various calcination temperatures with catalytic activity and selectivity using EXAFS spectroscopy showed that removal of thiol stabilizers via calcination was directly correlated with the conversion. The highest conversions were observed at 500°C with the complete removal of thiol stabilizers. However, incomplete removal of thiol stabilizers at 450°C resulted in maximum selectivity for benzaldehyde. This was attributed to the presence of residual thiols as observed by EXAFS spectroscopy, thus the oxidizing ability of Au was minimized and thus overoxidation into benzoic acid or benzyl benzoate was prevented. Jin and co-workers studied the activation of CeO_2 supported $Au_{25}(SR)_{18}^-$ clusters for CO oxidation catalysis using EXAFS and other spectroscopic techniques.[77] They found that while intact clusters were inert for CO oxidation, partial removal of thiol stabilizers at 150°C from the interface between the CeO_2 support and Au clusters led to the activation of CO on exposed Au atoms. Zhang *et al*. studied the activation of $Au_{38}(SR)_{24}$ clusters supported on Al_2O_3 and CeO_2 supports for cyclohexane oxidation reactions.[138] Clusters supported on CeO_2 supports were found to be more active and selective for ketones and alcohols than clusters supported on Al_2O_3 supports. Clusters supported on CeO_2 supports were found to be partially oxidized at 300^{o}C calcination. This was also observed in the EXAFS fitting with the appearance of Au-O contribution at 300^oC calcination temperatures. The highest catalytic activity and selectivity observed at 250^{o}C was attributed to the removal of thiol stabilizers as shown by EXAFS spectroscopy. Kumar and co-workers studied styrene-oxidation catalysis using biicosahedral $[Au_{25}(PPh_3)_{10}(SC_{12}H_{25})_5C_{l2}]$ and $Au_{25}(SC_8H_9)_{18}$ clusters as catalysts.[139] Both these catalysts were found to show higher conversion after calcination at 200^{o}C under vacuum. While higher conversion was attributed to the removal of thiolate stabilizers after calcination, higher selectivity towards benzaldehyde was attributed to the decrease in d-band hole population due to thiolate removal. Our group has also reported the study of the activation of mesoporous carbon supported $Au_{25}(SR)_{18}^-$ clusters using TEM and EXAFS spectroscopy. The results of this study are discussed in Chapter 4.

1.4 Research Objectives

Atomically precise Au clusters have recently emerged as an important class of materials because of their well-defined structures and high monodispersity. While these clusters offer an opportunity to systematically study the size- and structure-related physicochemical properties of Au nanomaterials, the use of these clusters for several important applications such as catalysis, sensing, and drug carriers has been limited mainly due to the lack of the proper understanding of their stability under experimental conditions. The first research objective was to study the effect of steric bulk of thiol stabilizers on the catalytic activity of alkanethiolate and arylthiolate protected $Au_{25}(SR)_{18}$ clusters for 4-nitrophenol reduction catalysis. Here, $Au_{25}(SR)_{18}$ clusters were chosen mainly because of the availability of the synthesis protocol which leads to the high yield of these clusters. Para-nitrophenol reduction with sodium borohydride was used as a model catalytic reaction as it allows one to follow the kinetics of the reaction by simply following the UV-Vis spectral features during reduction reaction. The results of this study are documented in Chapter 2.

In the literature, the synthesis of $Au_{25}(SR)_{18}$ clusters protected with alkane and aryl thiolates is well-documented. However, not many studies have been done on $Au_{25}(SR)_{18}^-$ clusters protected with functional groups terminated thiolate stabilizers such as –COOH, $-NH_2$ etc. It should be noted that the functional groups terminated thiolate stabilizers can allow for the further functionalization of these clusters with biological molecules such as amino acids for biological applications. The second research objective was to synthesize 11-mercaptoundecanoic acid and 16-mercaptohexadecanoic acid protected $Au_{25}(SR)_{18}^-$ clusters. The synthesis was based on isolating the $Au_{25}(SR)_{18}$ clusters from a polydisperse reaction mixture using a $NaBH_4$ purification strategy which was developed based on results from Chapter 2. The results of this study are reported in Chapter 3.

Supported Au nanoparticles have been shown to have high catalytic activity for various catalytic reactions. However, because of the polydispersity of these nanoparticles, correlation of structure-property relationships becomes challenging. Atomically-precise Au clusters have recently emerged as model compounds in order to study the structure-related catalytic properties of Au nanocatalysts. The third part of research objectives was to synthesize supported $Au_{25}(SC_8H_9)_{18}^-$ clusters, use these clusters for catalysis, and to study the structure dependent catalytic activity using TEM and EXAFS spectroscopy. Here, $Au_{25}(SC_8H_9)_{18}$ clusters were immobilized on mesoporous carbon supports and these supported clusters were characterized using X-ray absorption spectroscopy. Stability of these clusters was studied under various calcination temperatures using TEM and EXAFS spectroscopy and finally an attempt was made to correlate the structure of these clusters with the catalytic activity for the 4-nitrophenol reduction reaction. The results of this study are documented in Chapter 4.

Thiolate protected $Au_{25}(SR)_{18}$ clusters immobilized on support materials have been mainly activated by removing thiolate stabilizers at elevated temperatures for various catalytic applications. The thermal activation step usually leads to the sintering of these clusters and thereby affects the catalytic activity (Chapter 4, deactivation of catalyst). The fourth part of research objectives involves the exploration of alternative mild chemical activation routes in order to activate supported $Au_{25}(SC_8H_9)_{18}^-$ clusters with minimal growth in cluster size. In Chapter 5 of this thesis, the use of BH_4^- reducing agents on the activation of Al_2O_3 supported $Au_{25}(SC_8H_9)_{18}$ clusters (removal of thiol stabilizers from the surface of these clusters) has been described. Here, the resulting structural changes and growth in cluster size after thermal and BH_4^- treatments were studied using TEM and EXAFS spectroscopy.

Recently, there have been many reports suggesting the formation of highly monodisperse bimetallic clusters using $Au_{25}(SR)_{18}$ clusters as precursors. Bimetallic clusters with fixed metal composition have been deemed important as they offer an opportunity to systematically study the effect of the addition of two metal components on the physicochemical properties of resulting bimetallic clusters. These bimetallic clusters have been mainly synthesized by simply reacting $Au_{25}(SR)_{18}^-$ clusters with desired metal ions in stoichiometric proportions. The resulting bimetallic clusters have been mainly characterized by using mass spectrometry. While mass spectrometry gives us information about the composition, it gives very little information about the structure of resulting bimetallic clusters. The fifth part of research objectives involves the investigation of the reaction between $Au_{25}(SC_8H_9)_{18}$ clusters with Pd^{2+} and Ag^+ ions using *in situ* X-ray absorption spectroscopy. Here the difference in reactivity between $Au_{25}(SC_8H_9)_{18}^-$ clusters with Pd^{2+} and Ag^+ ions was studied using TEM, UV-Vis, and XAS, and based on the data, an attempt was made to elucidate the possible structure of the resulting bimetallic clusters. The results of this study are documented in Chapter 6.

AuPd bimetallic nanoparticles have been reported to have improved catalytic activity and selectivity for various industrially important reactions. Improved activity and selectivity have been mainly attributed to two effects namely, ensemble effects and ligand effects. While ligand effects are attributed to the modification in the electronic structure upon mixing two metal components, the ensemble effect arises because of the presence of a particular ensemble of active metal components on the surface of bimetallic nanoparticles. Practically, it becomes really challenging to isolate these effects because of the ill-defined structures of AuPd bimetallic nanoparticles and therefore realization of the full potential of these bimetallic nanoparticles becomes challenging. The sixth part of research objective deals with the synthesis of AuPd bimetallic nanoparticles using highly monodisperse $Au_{25}(SC_8H_9)_{18}$ clusters as starting precursors. The resulting bimetallic nanoparticles were characterized using TEM and EXAFS spectroscopy and based on these spectroscopic data, their structures were elucidated. Finally, these bimetallic nanoparticles were used for allyl alcohol hydrogenation catalysis and an attempt was made in order to study the relationship between their structures and catalytic activity.

1.5 Organization and Scope

This Ph.D. thesis describes the synthesis and activation of Au and bimetallic clusters for various catalytic reactions and the use of X-ray absorption spectroscopy in order to follow the synthesis and activation process. It is divided into eight chapters. Chapter 2, 3, and 4 are near-verbatim copies of articles published in different journals with minor formatting changes. Chapter

5, 6, and 7 are near-verbatim copies of submitted manuscripts. At the beginning of each chapter, a brief summary has been provided of the chapter including (1) where the manuscript was published or to be submitted, (2) what my contributions were to the work contained in the chapter/manuscript, and (3) summarize the chapter and briefly indicated how it fits into the thesis as a whole.

Chapter 2 describes the study of the effect of the bulkiness of thiolate stabilizers on the catalytic activity of $Au_{25}(SR)_{18}^-$ clusters and the stability of these clusters under reaction conditions. Chapter 3 describes the synthesis of 11-mercaptoundecanoic acid and 16-mercaptohexadecanoic acid protected Au_{25} clusters using $NaBH_4$ purification strategy. Here, the knowledge obtained in Chapter 2 on the stability of $Au_{25}(SR)_{18}^-$ clusters in solution was used to isolate Au_{25} clusters from a polydisperse reaction mixture. Chapter 4 describes the study of the thermal activation of mesoporous carbon supported $Au_{25}(SC_8H_9)_{18}$- clusters for 4-nitrophenol reduction reaction. Here, TEM and EXAFS spectroscopy were used in order to study the structure-catalytic activity relationship. Chapter 5 describes the activation of Al_2O_3 supported $Au_{25}(SC_8H_9)_{18}$ clusters using thermal and chemical treatments of supported clusters. Here, the resulting structural changes were followed by using TEM and EXAFS spectroscopy. Chapter 6 describes the synthesis of AuPd and AgAg bimetallic clusters using $Au_{25}(SC_8H_9)_{18}^-$ clusters as precursors. X-ray absorption spectroscopy was used in order to follow the reaction between $Au_{25}(SC_8H_9)_{18}^-$ clusters and Pd^{2+} and Ag^+ ions and the structure of the resulting bimetallic clusters was elucidated by using TEM, *in situ* XANES and EXAFS spectroscopic studies. Chapter 7 describes the synthesis of AuPd bimetallic nanoparticles with isolated atomic-Pd sites on the surface using AuPd bimetallic clusters described in Chapter 6 as starting precursors. Here, TEM and EXAFS spectroscopy were used to follow the structure of AuPd bimetallic nanoparticles. Finally, in Chapter 8, a final summary, outlook, and future work is presented.

1.6 References

1. Haruta, M.; Kobayashi, T.; Sano, H.; Yamada, N., Novel Gold Catalysts for the Oxidation of Carbon-Monoxide at a Temperature Far Below 0-Degrees-C. *Chem. Lett.* **1987,** (2), 405-408.

2. Ketchie, W. C.; Murayama, M.; Davis, R. J., Promotional effect of hydroxyl on the aqueous phase oxidation of carbon monoxide and glycerol over supported Au catalysts. *Top. Catal.* **2007,** *44* (1-2), 307-317.

3. Prati, L.; Rossi, M., Gold on carbon as a new catalyst for selective liquid phase oxidation of diols. *J. Catal.* **1998,** *176* (2), 552-560.

4. Carrettin, S.; McMorn, P.; Johnston, P.; Griffin, K.; Hutchings, G. J., Selective oxidation of glycerol to glyceric acid using a gold catalyst in aqueous sodium hydroxide. *Chem. Commun.* **2002,** (7), 696-697.

5. Alshammari, H.; Miedziak, P. J.; Davies, T. E.; Willock, D. J.; Knight, D. W.; Hutchings, G. J., Initiator-free hydrocarbon oxidation using supported gold nanoparticles. *Catal. Sci. Technol.* **2014,** *4* (4), 908-911.

6. Min, B. K.; Friend, C. M., Heterogeneous Gold-Based Catalysis for Green Chemistry: Low-temperature CO Oxidation and Propene Oxidation. *Chem. Rev.* **2007**, *107* (6), 2709-2724.

7. Brust, M.; Walker, M.; Bethell, D.; Schiffrin, D. J.; Whyman, R., Synthesis of Thiol-Derivatized Gold Nanoparticles in a 2-Phase Liquid-Liquid System. *J. Chem. Soc. Chem. Comm.* **1994,** (7), 801-802.

8. Jin, R. C., Atomically precise metal nanoclusters: stable sizes and optical properties. *Nanoscale* **2015,** *7* (5), 1549-1565.

9. Li, G.; Jin, R. C., Atomically Precise Gold Nanoclusters as New Model Catalysts. *Accounts. Chem. Res.* **2013,** *46* (8), 1749-1758.

10. Templeton, A. C.; Wuelfing, M. P.; Murray, R. W., Monolayer protected cluster molecules. *Accounts. Chem. Res.* **2000,** *33* (1), 27-36.

11. Hostetler, M. J.; Wingate, J. E.; Zhong, C. J.; Harris, J. E.; Vachet, R. W.; Clark, M. R.; Londono, J. D.; Green, S. J.; Stokes, J. J.; Wignall, G. D.; Glish, G. L.; Porter, M. D.; Evans, N. D.; Murray, R. W., Alkanethiolate gold cluster molecules with core diameters from 1.5 to 5.2 nm: Core and monolayer properties as a function of core size. *Langmuir* **1998,** *14* (1), 17-30.

12. Terrill, R. H.; Postlethwaite, T. A.; Chen, C. H.; Poon, C. D.; Terzis, A.; Chen, A. D.; Hutchison, J. E.; Clark, M. R.; Wignall, G.; Londono, J. D.; Superfine, R.; Falvo, M.; Johnson, C. S.; Samulski, E. T.; Murray, R. W., Monolayers in three dimensions: NMR, SAXS, thermal, and electron hopping studies of alkanethiol stabilized gold clusters. *J. Am. Chem. Soc.* **1995,** *117* (50), 12537-12548.

13. Johnson, S. R.; Evans, S. D.; Brydson, R., Influence of a terminal functionality on the physical properties of surfactant-stabilized gold nanoparticles. *Langmuir* **1998,** *14* (23), 6639-6647.

14. Porter, L. A.; Ji, D.; Westcott, S. L.; Graupe, M.; Czernuszewicz, R. S.; Halas, N. J.; Lee, T. R., Gold and silver nanoparticles functionalized by the adsorption of dialkyl disulfides. *Langmuir* **1998,** *14* (26), 7378-7386.

15. Templeton, A. C.; Chen, S. W.; Gross, S. M.; Murray, R. W., Water-soluble, isolable gold clusters protected by tiopronin and coenzyme A monolayers. *Langmuir* **1999,** *15* (1), 66-76.

16. Quiros, I.; Yamada, M.; Kubo, K.; Mizutani, J.; Kurihara, M.; Nishihara, H., Preparation of alkanethiolate-protected palladium nanoparticles and their size dependence on synthetic conditions. *Langmuir* **2002,** *18* (4), 1413-1418.

17. Pengo, P.; Polizzi, S.; Battagliarin, M.; Pasquato, L.; Scrimin, P., Synthesis, characterization and properties of water-soluble gold nanoparticles with tunable core size. *J. Mater. Chem.* **2003,** *13* (10), 2471-2478.

18. Imahori, H.; Kashiwagi, Y.; Hanada, T.; Endo, Y.; Nishimura, Y.; Yamazaki, I.; Fukuzumi, S., Metal and size effects on structures and photophysical properties of porphyrin-modified metal nanoclusters. *J. Mater. Chem.* **2003,** *13* (12), 2890-2898.

19. Zelakiewicz, B. S.; de Dios, A. C.; Tong, Y. Y., C-13 NMR spectroscopy of C-13(1)-labeled octanethiol-protected Au nanoparticles: Shifts, relaxations, and particle-size effect. *J. Am. Chem. Soc.* **2003,** *125* (1), 18-19.

20. Canepa, M.; Fox, M. A.; Whitesell, J. K., The influence of core size on electronic coupling in shell-core nanoparticles: gold clusters capped with pyrenoxylalkylthiolate. *Photoch. Photobio. Sci.* **2003,** *2* (11), 1177-1180.

21. Brust, M.; Fink, J.; Bethell, D.; Schiffrin, D. J.; Kiely, C., Synthesis and Reactions of Functionalized Gold Nanoparticles. *J. Chem. Soc. Chem. Comm.* **1995,** (16), 1655-1656.

22. Goulet, P. J. G.; Lennox, R. B., New Insights into Brust-Schiffrin Metal Nanoparticle Synthesis. *J. Am. Chem. Soc.* **2010,** *132* (28), 9582-9584.

23. Li, Y.; Zaluzhna, O.; Xu, B. L.; Gao, Y. A.; Modest, J. M.; Tong, Y. J., Mechanistic Insights into the Brust-Shiffrin Two-Phase Synthesis of Organo-chalcogenate-Protected Metal Nanoparticles. *J. Am. Chem. Soc.* **2011,** *133* (7), 2092-2095.

24. Jin, R. C.; Qian, H. F.; Wu, Z. K.; Zhu, Y.; Zhu, M. Z.; Mohanty, A.; Garg, N., Size Focusing: A Methodology for Synthesizing Atomically Precise Gold Nanoclusters. *J. Phys. Chem. Lett.* **2010,** *1* (19), 2903-2910.

25. Schaaff, T. G.; Whetten, R. L., Controlled etching of Au : SR cluster compounds. *J. Phys. Chem. B* **1999,** *103* (44), 9394-9396.

26. Zhu, M.; Lanni, E.; Garg, N.; Bier, M. E.; Jin, R., Kinetically controlled, high-yield synthesis of Au_{25} clusters. *J. Am. Chem. Soc.* **2008,** *130* (4), 1138-1139.

27. Dharmaratne, A. C.; Krick, T.; Dass, A., Nanocluster Size Evolution Studied by Mass Spectrometry in Room Temperature $Au_{25}(SR)_{18}$ Synthesis. *J. Am. Chem. Soc.* **2009,** *131* (38), 13604-13605.

28. Zhu, M.; Aikens, C. M.; Hollander, F. J.; Schatz, G. C.; Jin, R., Correlating the crystal structure of A thiol-protected Au_{25} cluster and optical properties. *J. Am. Chem. Soc.* **2008,** *130* (18), 5883-5885.

29. Heaven, M. W.; Dass, A.; White, P. S.; Holt, K. M.; Murray, R. W., Crystal structure of the gold nanoparticle $[N(C_8H_{17})_4][Au_{25}(SCH_2CH_2Ph)_{18}]$. *J. Am. Chem. Soc.* **2008,** *130* (12), 3754-3755.

30. Dasog, M.; Scott, R. W. J., Understanding the oxidative stability of Au MPCs in the presence of halids ions under ambient conditions. *Langmuir* **2007,** *23* (6), 3381-3387.

31. Qian, H. F.; Jin, R. C., Ambient Synthesis of $Au_{144}(SR)_{60}$ Nanoclusters in Methanol. *Chem. Mater.* **2011,** *23* (8), 2209-2217.

32. Liu, C.; Li, G.; Pang, G. S.; Jin, R. C., Toward understanding the growth mechanism of $Au_n(SR)_m$ nanoclusters: effect of solvent on cluster size. *RSC Adv.* **2013,** *3* (25), 9778-9784.

33. Qian, H. F.; Zhu, Y.; Jin, R. C., Size-Focusing Synthesis, Optical and Electrochemical Properties of Monodisperse $Au_{38}(SC_2H_4Ph)_{24}$ Nanoclusters. *ACS Nano* **2009,** *3* (11), 3795-3803.

34. Nimmala, P. R.; Dass, A., $Au_{99}(SPh)_{42}$ Nanomolecules: Aromatic Thiolate Ligand Induced Conversion of $Au_{144}(SCH_2CH_2Ph)_{60}$. *J. Am. Chem. Soc.* **2014,** *136* (49), 17016-17023.

35. Jupally, V. R.; Dass, A., Synthesis of $Au_{130}(SR)_{50}$ and $Au_{130-x}Ag_x(SR)_{50}$ nanomolecules through core size conversion of larger metal clusters. *Phys. Chem. Chem. Phys.* **2014,** *16* (22), 10473-10479.

36. Nimmala, P. R.; Jupally, V. R.; Dass, A., Core Size Conversion: Route for Exclusive Synthesis of Au_{38} or Au_{40} Nanomolecules. *Langmuir* **2014,** *30* (9), 2490-2497.

37. Zeng, C. J.; Liu, C. Y.; Pei, Y.; Jin, R. C., Thiol Ligand-Induced Transformation of $Au_{38}(SC2H_4Ph)_{24}$ to $Au_{36}(SPh\text{-}t\text{-}BU)_{24}$. *ACS Nano* **2013,** *7* (7), 6138-6145.

38. Qian, H. F.; Zhu, M. Z.; Andersen, U. N.; Jin, R. C., Facile, Large-Scale Synthesis of Dodecanethiol-Stabilized Au_{38} Clusters. *J. Phys. Chem. A* **2009,** *113* (16), 4281-4284.

39. Qian, H. F.; Liu, C.; Jin, R. C., Controlled growth of molecularly pure $Au_{25}(SR)_{18}$ and $Au_{38}(SR)_{24}$ nanoclusters from the same polydispersed crude product. *Sci. China. Chem.* **2012,** *55* (11), 2359-2365.

40. Crasto, D.; Dass, A., Green Gold: $Au_{30}(S\text{-}t\text{-}C4H9)_{18}$ Molecules. *J. Phys. Chem. C* **2013,** *117* (42), 22094-22097.

41. Muhammed, M. A. H.; Ramesh, S.; Sinha, S. S.; Pal, S. K.; Pradeep, T., Two Distinct Fluorescent Quantum Clusters of Gold Starting from Metallic Nanoparticles by pH-Dependent Ligand Etching. *Nano Res.* **2008,** *1* (4), 333-340.

42. Qian, H. F.; Jin, R. C., Controlling Nanoparticles with Atomic Precision: The Case of $Au_{144}(SCH_2CH_2Ph)_{60}$. *Nano Lett.* **2009,** *9* (12), 4083-4087.

43. Shibu, E. S.; Muhammed, M. A. H.; Tsukuda, T.; Pradeep, T., Ligand exchange of $Au_{25}SG_{18}$ leading to functionalized gold clusters: Spectroscopy, kinetics, and luminescence. *J. Phys. Chem. C* **2008,** *112* (32), 12168-12176.

44. Jadzinsky, P. D.; Calero, G.; Ackerson, C. J.; Bushnell, D. A.; Kornberg, R. D., Structure of a thiol monolayer-protected gold nanoparticle at 1.1 angstrom resolution. *Science* **2007,** *318* (5849), 430-433.

45. Yuan, X.; Zhang, B.; Luo, Z. T.; Yao, Q. F.; Leong, D. T.; Yan, N.; Xie, J. P., Balancing the Rate of Cluster Growth and Etching for Gram- Scale Synthesis of Thiolate- Protected Au_{25} Nanoclusters with Atomic Precision. *Angew. Chem., Int. Edit.* **2014,** *53* (18), 4623-4627.

46. Yu, Y.; Luo, Z.; Yu, Y.; Lee, J. Y.; Xie, J., Observation of cluster size growth in CO-directed synthesis of $Au_{25}SR_{18}$ nanoclusters. *ACS Nano* **2012**, 6 (9), 7920-7927.

47. Qian, H. F.; Zhu, M. Z.; Wu, Z. K.; Jin, R. C., Quantum Sized Gold Nanoclusters with Atomic Precision. *Accounts. Chem. Res.* **2012,** *45* (9), 1470-1479.

48. Hou, W. B.; Dasog, M.; Scott, R. W. J., Probing the Relative Stability of Thiolate- and Dithiolate-Protected Au Monolayer-Protected Clusters. *Langmuir* **2009,** *25* (22), 12954-12961.

49. Shivhare, A.; Wang, L. S.; Scott, R. W. J., Isolation of Carboxylic Acid-Protected Au-25 Clusters Using a Borohydride Purification Strategy. *Langmuir* **2015,** *31* (5), 1835-1841.

50. Badia, A.; Gao, W.; Singh, S.; Demers, L.; Cuccia, L.; Reven, L., Structure and Chain Dynamics of Alkanethiol-Capped Gold Colloids. *Langmuir* **1996,** *12* (5), 1262-1269.

51. Negishi, Y.; Nobusada, K.; Tsukuda, T., Glutathione-protected gold clusters revisited: Bridging the gap between gold(I)-thiolate complexes and thiolate-protected gold nanocrystals. *J. Am. Chem. Soc.* **2005,** *127* (14), 5261-5270.

52. Whetten, R. L.; Khoury, J. T.; Alvarez, M. M.; Murthy, S.; Vezmar, I.; Wang, Z. L.; Stephens, P. W.; Cleveland, C. L.; Luedtke, W. D.; Landman, U., Nanocrystal gold molecules. *Adv. Mater.* **1996,** *8* (5), 428-433.

53. Dass, A., Mass Spectrometric Identification of $Au_{68}(SR)_{34}$ Molecular Gold Nanoclusters with 34-Electron Shell Closing. *J. Am. Chem. Soc.* **2009,** *131* (33), 11666-11667.

54. Jupally, V. R.; Kota, R.; Dornshuld, E. V.; Mattern, D. L.; Tschumper, G. S.; Jiang, D-E.; Dass, A., Interstaple Dithiol Cross-Linking in $Au_{25}(SR)_{18}$ Nanomolecules: A Combined Mass Spectrometric and Computational Study. *J. Am. Chem. Soc.* **2011,** *133* (50), 20258-20266.

55. Nimmala, P. R.; Dass, A., $Au_{36}(SPh)_{23}$ Nanomolecules. *J. Am. Chem. Soc.* **2011,** *133* (24), 9175-9177.

56. AbdulHalim, L. G.; Kothalawala, N.; Sinatra, L.; Dass, A.; Bakr, O. M., Neat and Complete: Thiolate-Ligand Exchange on a Silver Molecular Nanoparticles *J. Am. Chem. Soc.* **2014,** *136* (45), 15865-15868.

57. Tracy, J. B.; Crowe, M. C.; Parker, J. F.; Hampe, O.; Fields-Zinna, C. A.; Dass, A.; Murray R. W., Electrospray Ionization Mass Spectrometry of Uniform and Mixed Monolayer Nanoparticles: $Au_{25}[S(CH_2)_2Ph]_{18}$ and $Au_{25}[S(CH_2)_2Ph]_{18-x}(SR)_x$. *J. Am. Chem. Soc.* **2007,** *129* (51), 16209-16215.

58. Dass, A.; Stevenson, A.; Dubay, G. R.; Tracy, J. B.; Murray, R. W., Nanoparticle MALDI-TOF Mass Spectrometry without Fragmentation: $Au_{25}(SCH_2CH_2Ph)_{18}$ and Mixed Monolayer $Au_{25}(SCH_2CH_2Ph)_{18-x}(L)_x$. *J. Am. Chem. Soc.* **2008,** *130* (18), 5940-5946.

59. Toikkanen, O.; Ruiz, V.; Ronnholm, G.; Kalkkinen, N.; Liljeroth, P.; Quinn, B. M., Synthesis and Stability of Monolayer-Protected Au_{38} Clusters. *J. Am. Chem. Soc.* **2008,** *130* (33), 11049-11055.

60. Qian, H.; Jin, R., Ambient Synthesis of $Au_{144}(SR)_{60}$ Nanoclusters in Methanol. *Chem. Mater*. **2011**, *23*(8) 2209-2217.

61. Qian, H. F.; Eckenhoff, W. T.; Zhu, Y.; Pintauer, T.; Jin, R. C., Total Structure Determination of Thiolate-Protected Au-38 Nanoparticles. *J. Am. Chem. Soc.* **2010,** *132* (24), 8280-8281.

62. Das, A.; Li, T.; Li, G.; Nobusada, K.; Zeng, C. J.; Rosi, N. L.; Jin, R. C., Crystal structure and electronic properties of a thiolate-protected Au_{24} nanocluster. *Nanoscale* **2014,** *6* (12), 6458-6462.

63. Walter, M.; Akola, J.; Lopez-Acevedo, O.; Jadzinsky, P. D.; Calero, G.; Ackerson, C. J.; Whetten, R. L.; Gronbeck, H.; Hakkinen, H., A unified view of ligand-protected gold clusters as superatom complexes. *P. Natl. Acad. Sci. USA* **2008,** *105* (27), 9157-9162.

64. Kim, Y. J.; Johnson, R. C.; Hupp, J. T., Gold nanoparticle-based sensing of "spectroscopically silent" heavy metal ions. *Nano Lett.* **2001,** *1* (4), 165-167.

65. Obare, S. O.; Hollowell, R. E.; Murphy, C. J., Sensing strategy for lithium ion based on gold nanoparticles. *Langmuir* **2002,** *18* (26), 10407-10410.

66. Russell, L. E.; Pompano, R. R.; Kittredge, K. W.; Leopold, M. C., Assembled nanoparticle films with crown ether-metal ion "sandwiches" as sensing mechanisms for metal ions. *J. Mater. Sci.* **2007,** *42* (17), 7100-7108.

67. Choi, I.; Song, H. D.; Lee, S.; Yang, Y. I.; Kang, T.; Yi, J., Core-Satellites Assembly of Silver Nanoparticles on a Single Gold Nanoparticle via Metal Ion-Mediated Complex. *J. Am. Chem. Soc.* **2012,** *134* (29), 12083-12090.

68. Zhang, S. H.; Wang, J.; Han, L. A.; Li, C. G.; Wang, W.; Yuan, Z., Colorimetric detection of bis-phosphorylated peptides using zinc(ii) dipicolylamine-appended gold nanoparticles. *Sensor Actuat. B-Chem.* **2010,** *147* (2), 687-690.

69. Massue, J.; Quinn, S. J.; Gunnlaugsson, T., Lanthanide luminescent displacement assays: The sensing of phosphate anions using Eu(III)-cyclen-conjugated gold nanoparticles in aqueous solution. *J. Am. Chem. Soc.* **2008,** *130* (22), 6900-6901.

70. Elmes, R. B. P.; Orange, K. N.; Cloonan, S. M.; Williams, D. C.; Gunnlaugsson, T., Luminescent Ruthenium(II) Polypyridyl Functionalized Gold Nanoparticles; Their DNA Binding Abilities and Application As Cellular Imaging Agents. *J. Am. Chem. Soc.* **2011,** *133* (40), 15862-15865.

71. Dasog, M.; Hou, W.; Scott, R. W. J., Controlled growth and catalytic activity of gold monolayer protected clusters in presence of borohydride salts. *Chem. Commun.* **2011,** *47* (30), 8569-8571.

72. Li, G.; Jiang, D. E.; Kumar, S.; Chen, Y. X.; Jin, R. C., Size Dependence of Atomically Precise Gold Nanoclusters in Chemoselective Hydrogenation and Active Site Structure. *ACS Catal.* **2014,** *4* (8), 2463-2469.

73. Biswas, M.; Dinda, E.; Rashid, M. H.; Mandal, T. K., Correlation between catalytic activity and surface ligands of monolayer protected gold nanoparticles. *J. Colloid. Interf. Sci.* **2012,** *368*, 77-85.

74. Li, G.; Jiang, D. E.; Kumar, S.; Chen, Y. X.; Jin, R. C., Size Dependence of Atomically Precise Gold Nanoclusters in Chemoselective Hydrogenation and Active Site Structure. *ACS Catal.* **2014,** *4* (8), 2463-2469.

75. Zhu, Y.; Qian, H. F.; Zhu, M. Z.; Jin, R. C., Thiolate-Protected Au-n Nanoclusters as Catalysts for Selective Oxidation and Hydrogenation Processes. *Adv. Mater.* **2010,** *22* (17), 1915-1920.

76. Liu, Y. M.; Tsunoyama, H.; Akita, T.; Xie, S. H.; Tsukuda, T., Aerobic Oxidation of Cyclohexane Catalyzed by Size-Controlled Au Clusters on Hydroxyapatite: Size Effect in the Sub-2 nm Regime. *ACS Catal.* **2011,** *1* (1), 2-6.

77. Wu, Zili.; Jiang, D-E.; Mann, A. K. P.; Mullins, D. R.; Qiao, Z-A.; Allard, L. F.; Zeng, C.; Jin, R.; Overbury, S. H., Thiolate Ligands as a Double-Edged Sword for CO Oxidation on CeO_2 Supported $Au_{25}(SCH_2CH_2Ph)_{18}$ Nanoclusters. *J. Am. Chem. Soc.* **2014,** *136* (16), 6111-6122.

78. Menard, L. D.; Xu, F.; Nuzzo, R. G.; Yang, J. C., Preparation of TiO2-Supported Au Nanoparticle Catalysts from a Au13 Cluster Precursor: Ligand Removal Using Ozone Exposure Versus a Rapid Thermal Treatment. *J. Catal.* **2006**, *243*(1), 64-73.

79. Kawasaki, H.; Kumar, S.; Li, G.; Zeng, C. J.; Kauffman, D. R.; Yoshimoto, J.; Iwasaki, Y.; Jin, R. C., Generation of Singlet Oxygen by Photoexcited $Au_{25}(SR)_{18}$ Clusters. *Chem. Mater.* **2014,** *26* (9), 2777-2788.

80. Yu, C. L.; Li, G.; Kumar, S.; Kawasaki, H.; Jin, R. C., Stable $Au_{25}(SR)_{18}/TiO_2$ Composite Nanostructure with Enhanced Visible Light Photocatalytic Activity. *J. Phys. Chem. Lett.* **2013,** *4* (17), 2847-2852.

81. Kauffman, D. R.; Alfonso, D.; Matranga, C.; Li, G.; Jin, R. C., Photomediated Oxidation of Atomically Precise $Au_{25}(SC_2H_4Ph)_{18}^-$ Nanoclusters. *J. Phys. Chem. Lett.* **2013,** *4* (1), 195-202.

82. Lee, J.; Shim, H. S.; Lee, M.; Song, J. K.; Lee, D., Size-Controlled Electron Transfer and Photocatalytic Activity of ZnO-Au Nanoparticle Composites. *J. Phys. Chem. Lett.* **2011,** *2* (22), 2840-2845.

83. Stamplecoskie, K. G.; Kamat, P. V., Size-Dependent Excited State Behavior of Glutathione-Capped Gold Clusters and Their Light-Harvesting Capacity. *J. Am. Chem. Soc.* **2014,** *136* (31), 11093-11099.

84. Stamplecoskie, K. G.; Chen, Y. S.; Kamat, P. V., Excited-State Behavior of Luminescent Glutathione-Protected Gold Clusters. *J. Phys. Chem. C* **2014,** *118* (2), 1370-1376.

85. Stamplecoskie, K. G.; Kamat, P. V., Size-Dependent Excited State Behavior of Glutathione-Capped Gold Clusters and Their Light-Harvesting Capacity. *J. Am. Chem. Soc.* **2014,** *136* (31), 11093-11099.

86. Fields-Zinna, C. A.; Crowe, M. C.; Dass, A.; Weaver, J. E. F.; Murray, R. W., Mass Spectrometry of Small Bimetal Monolayer-Protected Clusters. *Langmuir* **2009,** *25* (13), 7704-7710.

87. Gottlieb, E.; Qian, H. F.; Jin, R. C., Atomic-Level Alloying and De-alloying in Doped Gold Nanoparticles. *Chem-Eur. J.* **2013,** *19* (13), 4238-4243.

88. Kumara, C.; Dass, A., AuAg alloy nanomolecules with 38 metal atoms. *Nanoscale* **2012,** *4* (14), 4084-4086.

89. Zhang, H. J.; Watanabe, T.; Okumura, M.; Haruta, M.; Toshima, N., Catalytically highly active top gold atom on palladium nanocluster. *Nat. Mater.* **2012,** *11* (1), 49-52.

90. Qian, H. F.; Jiang, D. E.; Li, G.; Gayathri, C.; Das, A.; Gil, R. R.; Jin, R. C., Monoplatinum Doping of Gold Nanoclusters and Catalytic Application. *J. Am. Chem. Soc.* **2012,** *134* (39), 16159-16162.

91. Le Guevel, X.; Trouillet, V.; Spies, C.; Li, K.; Laaksonen, T.; Auerbach, D.; Jung, G.; Schneider, M., High photostability and enhanced fluorescence of gold nanoclusters by silver doping. *Nanoscale* **2012,** *4* (24), 7624-7631.

92. Niihori, Y.; Kurashige, W.; Matsuzaki, M.; Negishi, Y., Remarkable enhancement in ligand-exchange reactivity of thiolate-protected Au-25 nanoclusters by single Pd atom doping. *Nanoscale* **2013,** *5* (2), 508-512.

93. Negishi, Y.; Iwai, T.; Ide, M., Continuous modulation of electronic structure of stable thiolate-protected Au-25 cluster by Ag doping. *Chem. Commun.* **2010,** *46* (26), 4713-4715.

94. Kauffman, D. R.; Alfonso, D.; Matranga, C.; Qian, H. F.; Jin, R. C., A Quantum Alloy: The Ligand-Protected $Au_{25-x}Agx(SR)_{18}$ Cluster. *J. Phys. Chem. C* **2013,** *117* (15), 7914-7923.

95. Dou, X. Y.; Yuan, X.; Yao, Q. F.; Luo, Z. T.; Zheng, K. Y.; Xie, J. P., Facile synthesis of water-soluble $Au_{25-x}Ag_x$ nanoclusters protected by mono- and bi-thiolate ligands. *Chem. Commun.* **2014,** *50* (56), 7459-7462.

96. Kumara, C.; Dass, A., $(AuAg)_{144}(SR)_{60}$ alloy nanomolecules. *Nanoscale* **2011,** *3* (8), 3064-3067.

97. Negishi, Y.; Munakata, K.; Ohgake, W.; Nobusada, K., Effect of Copper Doping on Electronic Structure, Geometric Structure, and Stability of Thiolate-Protected Au_{25} Nanoclusters. *J. Phys. Chem. Lett.* **2012,** *3* (16), 2209-2214.

98. Dharmaratne, A. C.; Dass, A., $Au_{144-x}Cu_x(SC_6H_{13})_{60}$ nanomolecules: effect of Cu incorporation on composition and plasmon-like peak emergence in optical spectra. *Chem. Commun.* **2014,** *50* (14), 1722-1724.

99. Kurashige, W.; Munakata, K.; Nobusada, K.; Negishi, Y., Synthesis of Stable CunAu25-n Nanoclusters (n = 1-9) using Selenolate Ligands. *Chem. Commun.* **2013,** *49* (48), 5447-5449.

100. Yang, H. Y.; Wang, Y.; Lei, J.; Shi, L.; Wu, X. H.; Makinen, V.; Lin, S. C.; Tang, Z. C.; He, J.; Hakkinen, H.; Zheng, L. S.; Zheng, N. F., Ligand-Stabilized $Au_{13}Cu_x$ (x=2, 4, 8) Bimetallic Nanoclusters: Ligand Engineering to Control the Exposure of Metal Sites. *J. Am. Chem. Soc.* **2013,** *135* (26), 9568-9571.

101. Yang, H.; Wang, Y.; Yan, J.; Chen, X.; Zhang, X.; Häkkinen, H.; Zheng, N., Structural Evolution of Atomically Precise Thiolated Bimetallic $[Au_{12+n}Cu_{32}(SR)_{30+n}]^{4-}$ (n = 0, 2, 4, 6) Nanoclusters. *J. Am. Chem. Soc.* **2014,** *136* (20), 7197-7200.

102. Negishi, Y.; Kurashige, W.; Niihori, Y.; Iwasa, T.; Nobusada, K., Isolation, structure, and stability of a dodecanethiolate-protected Pd_1Au_{24} cluster. *Phys. Chem. Chem. Phys.* **2010,** *12* (23), 6219-6225.

103. Christensen, S. L.; MacDonald, M. A.; Chatt, A.; Zhang, P.; Qian, H. F.; Jin, R. C., Dopant Location, Local Structure, and Electronic Properties of $Au_{24}Pt(SR)_{18}$ Nanoclusters. *J. Phys. Chem. C* **2012,** *116* (51), 26932-26937.

104. Negishi, Y.; Igarashi, K.; Munakata, k.; Ohgake, W.; Nobusada, K., Palladium Doping of Magic Gold Cluster $Au_{38}(SCH_4Ph)_{24}$: Formation of $Pd_2Au_{36}(SC_2H_4Ph)_{24}$ with Higher Stability than $Au_{38}(SC_2H_4Ph)_{24}$. *Chem. Commun.* **2012**, *48* (5), 660-662.

105. *CRC Handbook of Chemistry and Physics*, CRC Press, Cleveland, OH, 91, 2010.

106. Kreevoy, M. M.; Hutchins, J. E., H_2bh_3 as an Intermediate in Tetrahydridoborate Hydrolysis. *J. Am. Chem. Soc.* **1972,** *94* (18), 6371-6376.

107. Bruma, A.; Negreiros, F. R.; Xie, S.; Tsukuda, T.; Johnston, R. L.; Fortunelli, A.; Li, Z. Y., Direct atomic imaging and density functional theory study of the $Au_{24}Pd_1$ cluster catalyst. *Nanoscale* **2013,** *5* (20), 9620-9625.

108. Niihori, Y.; Matsuzaki, M.; Pradeep, T.; Negishi, Y., Separation of Precise Compositions of Noble Metal Clusters Protected with Mixed Ligands. *J. Am. Chem. Soc.* **2013,** *135* (13), 4946-4949.

109. Kacprzak, K. A.; Lehtovaara, L.; Akola, J.; Lopez-Acevedoa, O.; Hakkinen, H., A density functional investigation of thiolate-protected bimetal $PdAu_{24}(SR)_{18}^z$ clusters: doping the superatom complex. *Phys. Chem. Chem. Phys.* **2009,** *11* (33), 7123-7129.

110. Udayabhaskararao, T.; Sun, Y.; Goswami, N.; Pal, S. K.; Balasubramanian, K.; Pradeep, T., Ag_7Au_6: A 13-Atom Alloy Quantum Cluster. *Angew. Chem., Int. Edit.* **2012,** *51* (9), 2155-2159.

111. Choi, J. P.; Fields-Zinna, C. A.; Stiles, R. L.; Balasubramanian, R.; Douglas, A. D.; Crowe, M. C.; Murray, R. W., Reactivity of $[Au_{25}(SCH_2CH_2Ph)18]^{1-}$ Nanoparticles with Metal Ions. *J. Phys. Chem. C* **2010,** *114* (38), 15890-15896.

112. Wu, Z. K., Anti-Galvanic Reduction of Thiolate-Protected Gold and Silver Nanoparticles. *Angew. Chem., Int. Edit.* **2012,** *51* (12), 2934-2938.

113. Yao, C. H.; Chen, J. S.; Li, M. B.; Liu, L. R.; Yang, J. L.; Wu, Z. K., Adding Two Active Silver Atoms on Au_{25} Nanoparticle. *Nano. Lett.* **2015,** *15* (2), 1281-1287.

114. Jiang, D. E.; Dai, S., From Superatomic $Au_{25}(SR)_{18}^-$ to Superatomic $M@Au_{24}(SR)_{18}^q$ Core-Shell Clusters. *Inorg Chem* **2009,** *48* (7), 2720-2722.

115. Negishi, Y.; Kurashige, W.; Kobayashi, Y.; Yamazoe, S.; Kojima, N.; Seto, M.; Tsukuda, T., Formation of a $Pd@Au_{12}$ Superatomic Core in $Au_{24}Pd_1(SC_{12}H_{25})_{18}$ Probed by ^{197}Au Mossbauer and Pd K-Edge EXAFS Spectroscopy. *J. Phys. Chem. Lett.* **2013,** *4* (21), 3579-3583.

116. Yamazoe, S.; Kurashige, W.; Nobusada, K.; Negishi, Y.; Tsukuda, T., Preferential Location of Coinage Metal Dopants (M = Ag or Cu) in $[Au_{25-X}M_X(SC_2H_4Ph)18]^-$ (x similar to 1) As Determined by Extended X-ray Absorption Fine Structure and Density Functional Theory Calculations. *J. Phys. Chem. C* **2014,** *118* (43), 25284-25290.

117. Rossi, G.; Ferrando, R.; Rapallo, A.; Fortunelli, A.; Curley, B. C.; Lloyd, L. D.; Johnston, R. L., Global optimization of bimetallic cluster structures. II. Size-matched Ag-Pd, Ag-Au, and Pd-Pt systems. *J. Chem. Phys.* **2005,** *122* (19).

118. Rapallo, A.; Rossi, G.; Ferrando, R.; Fortunelli, A.; Curley, B. C.; Lloyd, L. D.; Tarbuck, G. M.; Johnston, R. L., Global optimization of bimetallic cluster structures. I. Size-mismatched Ag-Cu, Ag-Ni, and Au-Cu systems. *J. Chem. Phys.* **2005,** *122* (19).

119. Kumara, C.; Aikens, C. M.; Dass, A., X-ray Crystal Structure and Theoretical Analysis of $Au_{25-x}Ag_x(SCH_2CH_2Ph)_{18}^-$ Alloy. *J. Phys. Chem. Lett.* **2014,** *5* (3), 461-466.

120. Malola, S.; Hakkinen, H., Electronic Structure and Bonding of Icosahedral Core-Shell Gold-Silver Nanoalloy Clusters $Au_{144-x}Ag_x(SR)_{60}$. *J. Phys. Chem. Lett.* **2011,** *2* (18), 2316-2321.

121. Sun, H. T.; Sakka, Y., Luminescent metal nanoclusters: controlled synthesis and functional applications. *Sci. Technol. Adv. Mat.* **2014,** *15* (1).

122. Green, T. D.; Yi, C. Y.; Zeng, C. J.; Jin, R. C.; McGill, S.; Knappenberger, K. L., Temperature-Dependent Photoluminescence of Structurally-Precise Quantum-Confined $Au_{25}(SC_8H_9)_{18}$ and $Au_{38}(SC_{12}H_{25})_{24}$ Metal Nanoparticles. *J. Phys. Chem. A* **2014,** *118* (45), 10611-10621.

123. Lin, C. A. J.; Lee, C. H.; Hsieh, J. T.; Wang, H. H.; Li, J. K.; Shen, J. L.; Chan, W. H.; Yeh, H. I.; Chang, W. H., Synthesis of Fluorescent Metallic Nanoclusters toward Biomedical Application: Recent Progress and Present Challenges. *J. Med. Biol. Eng.* **2009,** *29* (6), 276-283.

124. Wang, S. X.; Meng, X. M.; Das, A.; Li, T.; Song, Y. B.; Cao, T. T.; Zhu, X. Y.; Zhu, M. Z.; Jin, R. C., A 200-fold Quantum Yield Boost in the Photoluminescence of Silver Doped Ag_xAu_{25-x} Nanoclusters: The 13th Silver Atom Matters. *Angew. Chem., Int. Edit.* **2014,** *53* (9), 2376-2380.

125. Luo, Z. T.; Yuan, X.; Yu, Y.; Zhang, Q. B.; Leong, D. T.; Lee, J. Y.; Xie, J. P., From Aggregation-Induced Emission of Au(I)-Thiolate Complexes to Ultrabright Au(0)@Au(I)-Thiolate Core-Shell Nanoclusters. *J. Am. Chem. Soc.* **2012,** *134* (40), 16662-16670.

126. Sankar, M.; Dimitratos, N.; Miedziak, P. J.; Wells, P. P.; Kiely, C. J.; Hutchings, G. J., Designing bimetallic catalysts for a green and sustainable future. *Chem. Soc. Rev.* **2012,** *41* (24), 8099-8139.

127. Gao, F.; Goodman, D. W., Pd-Au bimetallic catalysts: understanding alloy effects from planar models and (supported) nanoparticles. *Chem. Soc. Rev.* **2012,** *41* (24), 8009-8020.

128. Xie, S. H.; Tsunoyama, H.; Kurashige, W.; Negishi, Y.; Tsukuda, T., Enhancement in Aerobic Alcohol Oxidation Catalysis of Au_{25} Clusters by Single Pd Atom Doping. *ACS Catal.* **2012,** *2* (7), 1519-1523.

129. Schnohr, C. S.; Ridgway, M. C., X-Ray Absorption Spectroscopy of Semiconductors. *Springer Series in Optical Science* 190.

130. Maclennan, A.; Banerjee, A.; Hu, Y. F.; Miller, J. T.; Scott, R. W. J., In Situ X-ray Absorption Spectroscopic Analysis of Gold-Palladium Bimetallic Nanoparticle Catalysts. *ACS Catal.* **2013,** *3* (6), 1411-1419.

131. Maclennan, A.; Banerjee, A.; Scott, R. W. J., Aerobic Oxidation of Alpha,Beta-Unsaturated Alcohols using Sequentially-Grown AuPd Nanoparticles in Water and Tetraalkylphosphonium Ionic Liquids. *Catal. Today* **2013,** *207*, 170-179.

132. Balcha, T.; Strobl, J. R.; Fowler, C.; Dash, P.; Scott, R. W. J., Selective Aerobic Oxidation of Crotyl Alcohol Using AuPd Core-Shell Nanoparticles. *ACS Catal.* **2011,** *1* (5), 425-436.

133. Liu, F.; Wechsler, D.; Zhang, P., Alloy-Structure-Dependent Electronic Behavior and Surface Properties of Au-Pd Nanoparticles. *Chem. Phys. Lett.* **2008,** *461* (4-6), 254-259.

134. Gaur, A.; Shrivastava, B. D.; Nigam, H. L., X-ray Absorption Fine Structure (XAFS) Spectroscopy. *Proc. Indian. Natn. Sci. Acad.* **2013**, 921-966.

135. MacDonald, M. A.; Chevrier, D. M.; Zhang, P., The Structure and Bonding of $Au_{25}(SR)_{18}$ Nanoclusters from EXAFS: The Interplay of Metallic and Molecular Behavior. *J. Phys. Chem. C* **2011,** *115* (31), 15282-15287.

136. MacDonald, M. A.; Zhang, P.; Chen, N.; Qian, H.; Jin, R., Solution-Phase Structure and Bonding of $Au_{38}(SR)_{24}$ Nanoclusters from X-ray Absorption Spectroscopy. *J. Phys. Chem. C* **2011,** *115* (1), 65-69.

137. Yoskamtorn, T.; Yamazoe, S.; Takahata, R.; Nishigaki, J.; Thivasasith, A.; Limtrakul, J.; Tsukuda, T., Thiolate-Mediated Selectivity Control in Aerobic Alcohol Oxidation by Porous Carbon-Supported Au_{25} Clusters. *ACS Catal.* **2014**, *4* (10), 3696-3700.

138. Zhang, B.; Kaziz, S.; Li, H.; Hevia, M. G.; Wodka, D.; Mazet, C.; Bürgi T.; Barrabés, N., Modulation of Active Sites in Supported $Au_{38}(SC_2H_4Ph)_{24}$ Cluster Catalysts: Effect of Atmosphere and Support Material. *J. Phys. Chem. C* **2015,** *119* (20), 11193-11199.

139. Liu, J.; Krishna, K. S.; Losovyj, Y. B.; Chattopadhyay, S.; Lozova, N.; Millerm J. T.; Spivey, J. J.; Kumar, C. S. S. R., Ligand-Stabilized and Atomically Precise Gold Nanocluster Catalysis: A Case Study for Correlating Fundamental Electronic Properties with Catalysis. *Chem. A Euro. J.* **2013**, *19* (31), 10201-10208.

CHAPTER 2

2. Stable and Recyclable Au_{25} Clusters for the Reduction of 4-Nitrophenol

This work has been published in *Chemical Communications*. $Au_{25}(L)_{18}^-$ clusters protected with various alkane and aryl thiols were synthesized and used as catalysts for the 4-nitrophenol reduction reaction. The catalytic activity was found to increase with decrease in the steric bulk of thiol stabilizers. Stability of these clusters under experimental conditions was studied using UV-Vis spectroscopy and mass spectrometry. These clusters were shown to preserve their structural integrity during catalysis and found to be more stable than their larger counterparts ($Au_{\sim 180}$). A recyclability study in the case of $Au_{25}(SC_6H_{13})_{18}^-$ clusters show that these clusters can be isolated after one catalytic cycle and reused again.

This work has been published in *Chem. Commun.* **2013,** *49* (3), 276-278. The author would like to acknowledge the contributions of Stephen J. Ambrose, Dr. Haixia Zhang, and Dr. Randy W. Purves for assisting in the collection of mass spectrometry data, and Dr. Mark S. Workentin and Dr. Mahdi Hesari for assisting in the purification of $Au_{25}(SR)_{18}^-$ clusters. The author's contributions to this article include: synthesis of various monolayer-protected Au_{25} clusters, catalysis experiments, characterization of the catalysts before and after catalysis, kinetic study of the catalysis, and in the preparation of the manuscript. The manuscript was revised by Dr. Robert Scott prior to publication.

Stable and Recyclable Au_{25} Clusters for the Reduction of 4-Nitrophenol

Atal Shivhare,[a] Stephen J. Ambrose,[b] Haixia Zhang,[b] Randy W. Purves,[ab] Robert W. J. Scott[*a]

Department of Chemistry, University of Saskatchewan, 110 Science Place, Saskatoon,
Saskatchewan, Canada

2.1 Abstract

Thiol-stabilized $Au_{25}L_{18}$ monolayer protected clusters (MPCs) were found to be active for the reduction of 4-nitrophenol. Results suggest that these MPCs are stable catalysts and do not lose their structural integrity during the catalytic process. High stability under the reaction conditions enables the recyclability of these MPCs.

2.2 Introduction

Advances in the synthesis of ultrasmall, monodisperse gold monolayer protected clusters (MPCs) in high yields have led scientists towards understanding their fundamental physical and chemical properties.[1,2] Recent single crystal studies of $Au_{102}L_{44}$ and $Au_{25}L_{18}$ MPCs have shown the presence of highly symmetrical gold cores surrounded by Au-thiolate staple motifs containing alternating Au and S atoms, in which the core is directly connected to the terminal S atoms of the staples and Au is at the bridging position of staples.[3,4] This unique arrangement of Au and S atoms was also found to exist in other thiol-stabilized Au MPCs.[5,6] Several studies suggested that this somewhat unexpected structural behavior leads to a highly stable architecture that is because of electronic rather than geometrical reasons.[7] Further proof of their remarkable stability has been shown by various oxidation and hydrogenation catalysis, where these MPCs were found to preserve their structural integrity after the catalytic processes.[8,9]

Herein we demonstrate that $Au_{25}L_{18}$ MPCs stabilized by several alkanethiols and phenylethanethiol can be employed for the reduction of 4-nitrophenol using $NaBH_4$ as a reducing agent. In our previous work we documented that $NaBH_4$ is a strong enough reducing agent to reductively desorb alkanethiol stabilizers from larger Au MPC surfaces and the Au cores tend to grow during the nitrophenol reduction reaction.[10] However in the present case, it was found that

$Au_{25}L_{18}$ clusters are stable during reduction catalysis and can be isolated with intact architectures and this enables high rates and recyclability of these MPCs.

2.3 Experimental

2.3.1 Materials

Tetraoctylammonium bromide (TOAB, 98%, Aldrich), Sodium borohydride ($NaBH_4$, 98%, EMD), Hydrogen tetrachloroaurate (III) trihydrate ($HAuCl_4.3H2O$, 99.9% on metal basis, Aldrich), 1-Dodecanethiol ($C_{12}H_{25}SH$, ≥ 98%, Aldrich), Phenylethanethiol (C_8H_9SH, 99%, Acros Organics), 1-Hexanethiol ($C_6H_{13}SH$, 97%, Alfa Aesar), 4-Nitrophenol ($C_6H_5NO_3$, 99%, Alfa Aesar). High purity THF and Acetonitrile were purchased from Fischer Scientific and 100% ethanol was purchased from Commercial Alcohols. 18 MΩ cm Milli-Q (Millipore, Bedford, MA) was used throughout.

2.3.2 Synthesis of Au_{25} MPCs

Alkanethiolate Au_{25} (hexanethiolate Au_{25} and dodecanethiolate Au_{25}) and phenylethanethiolate Au_{25} MPCs were prepared by modifying the literature procedure.[1] A typical synthesis is as follows: 50 mL solution of THF with 500 mg of $HAuCl_4{\cdot}3H_2O$ was mixed with 1.2 equiv. of TOAB and resulting solution was stirred for 10 minutes to ensure the complete formation of the $TOA^+AuX_4^-$ complex. After that, the stirring rate was decreased to 60 rpm and 5 eq of alkanethiol (hexanethiol, dodecanethiol) or phenylethanethiol was added dropwise and the solution was left under slow stirring until it became transparent. During the addition of thiol stabilizers, a slow stirring rate was maintained in order to avoid the formation of Au-thiolate polymers.[1] After getting a transparent solution, the stirring rate was increased to 1100 rpm and a solution of 10 eq of $NaBH_4$ in 10 mL ice cold water was added all at once and the final solution was left under high stirring for 4 days. After the reaction was over, the solvent was evaporated using a rotary evaporator and the reaction residue was sequentially washed with copious amounts of 75/25, 85/15 and 90/10 mixtures of ethanol/water. After washing, alkanethiolate Au_{25} MPCs were extracted with THF and phenylethanethiolate Au_{25} MPCs were extracted with acetonitrile.

2.3.3 Synthesis of $Au_{\sim 180}(SC_6H_{13})_{\sim 100}$ MPCs

A 25 ml solution of THF with 200 mg of $HAuCl_4 \cdot 3H_2O$ was mixed with 1.2 equiv. of TOAB and solution was stirred for 10 min. After stirring, 3 equiv. of hexanethiol was added and the solution was stirred until it became clear. To this clear solution, 10 equiv. of $NaBH_4$ in 5 ml ice cold water was added and the resulting solution was stirred for 2 hours. After the completion of the reaction, the solvent was evaporated and the residue was sequentially washed with the copious amount of water, ethanol and acetonitrile. The number of Au atoms and the number of ligands in the formula were calculated using a combination of TEM and TGA.[11]

2.3.4 Reduction Catalysis

The reduction of 4-nitophenol was studied using UV-Vis spectroscopy. The entire reaction was done under N_2 atmosphere. In a typical catalytic reaction, 7.0 mg of nitrophenol was dissolved in 25/5 mL mixture of THF/water. To this solution, Au MPCs (4.87×10^{-4} mM in Au) were added (alkanethiolate MPCs or phenylethanethiolate MPCs) and the solution was stirred under N_2 atmosphere. After stirring, 30 equiv. of $NaBH_4$ in ice cold water was added. Immediately after the addition of $NaBH_4$, UV-Vis spectra were recorded. The rate constant of the reduction process was determined by measuring the change in the absorbance of the initially observed peak at 400 nm for 4-nitrophenolate as a function of time. Control experiments were carried out at the same conditions without MPCs and no nitrophenol reduction was observed. Very short induction times (< 2 min) were observed because of the remnant oxygen and kinetic data were plotted after removing the induction time.

2.3.5 Treatment of Au MPCs with $NaBH_4$

Stability of Au_{25} MPCs and larger hexanethiolate Au MPCs towards $NaBH_4$ was studied with UV-Vis spectroscopy. In a typical procedure; to a solution of Au_{25} MPCs or larger hexanethiolate Au MPCs, 37500 equiv. of $NaBH_4$ was added and immediately after the addition of $NaBH_4$, UV-Vis spectra were recorded over the period of 30 minutes.

2.3.6 Characterization

Absorption spectra were recorded on a Varian Cary 50 Bio UV-Vis spectrometer with an optical path length of 1 cm. A transmission electron micrograph before catalysis was obtained with a Philips 410 microscope operating at 100 kV and a micrograph after catalysis was obtained with a Philips CM10 Microscope operating at 60 kV. Mass spectral analysis was done on an Applied Biosystems 4800 MALDI-TOF/TOF instrument (Frederic, MD, USA) operating in linear positive ion mode using DCTB (trans-2-[3-(4-tert-Butylphenyl)-2-methyl-2-propenylidene]malononitrile) as the matrix. A mixture of insulin and ubiquitin was used as an external standard.[12]

2.4 Results and Discussion

$Au_{25}L_{18}$ MPCs were synthesized with slight modifications of the literature procedure.[1] In short; $HAuCl_4 \cdot 3H_2O$ was mixed with 1.2 molar equivalent of TOAB (tetraoctylammonium bromide) with respect to Au salt in THF. Next, 5 molar equivalent of thiol (phenylethanethiol, hexanethiol and dodecanethiol) with respect to Au salt was added to this solution and the solution was stirred until it became colorless. To this clear solution, 10 molar equivalent of $NaBH_4$ with respect to Au salt in cold water was added all at once under high stirring and the progress of the reaction was monitored by UV-Vis spectroscopy. This solution was allowed to undergo oxidative etching under air for 4 days. It was found that such etching does not take place in the absence of air and thus low yields of Au_{25} MPCs are formed under inert conditions. After the completion of the reaction, Au_{25} MPCs were purified and analyzed by UV-Vis spectroscopy, TEM, and Matrix-Assisted Laser Desorption Ionization Time of Flight (MALDI-TOF) mass spectrometry. As-synthesized Au_{25} MPCs were characterized by using UV-Vis spectroscopy (Figure 2.1) and matrix-assisted laser desorption ionization time of flight (MALDI-TOF) mass spectrometry (Figure 2.2 and Table 2.1). UV-Vis spectra show three major absorption features characteristic of $Au_{25}(SR)_{18}^-$ clusters. The major peak is at ca. 680 nm and two minor peaks are at ca. 400 nm and ca. 450 nm. These absorption features have been assigned to various HOMO-LUMO transitions present within $Au_{25}(SR)_{18}^-$ clusters.[4] Mass spectrometric data show the molecular ion peaks and fragment ion peaks in all three cases. Observed peaks are in very good agreement with the theoretical peaks and are within instrumental error specifications.

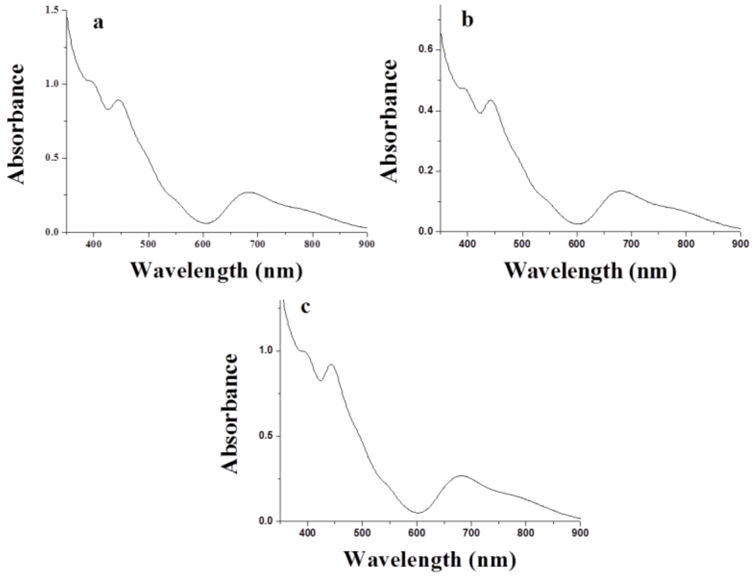

Figure 2.1. UV-Vis spectra of a) phenylethanethiolate Au_{25}, b) dodecanethiolate Au_{25} and c) hexanethiolate Au_{25} MPCs.

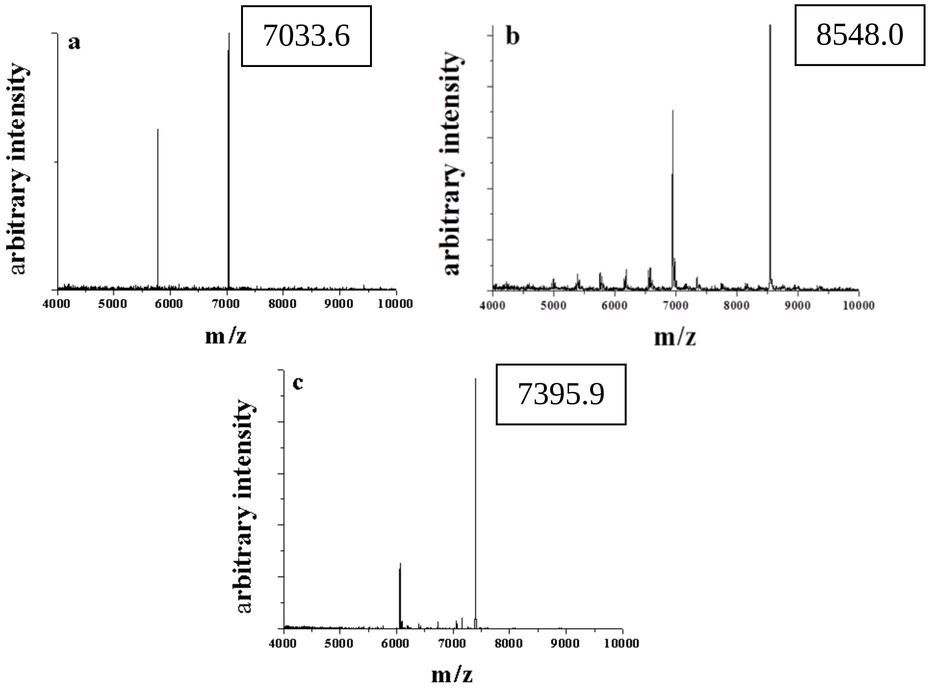

Figure 2.2. MALDI/TOF spectra of a) hexanethiolate Au_{25}, b) dodecanethiolate Au_{25} and c) phenylethanethiolate Au_{25} MPCs.

Table 2.1. Experimental and theoretical masses of Au_{25} MPCs.

Catalyst	Theoretical mass (m/z)	Experimental mass (m/z)	Error (Da)
$Au_{25}(SC_6H_{13})_{18}$	7034.4	7033.6	-0.8
$Au_{25}(SC_8H_9)_{18}$	7394.1	7395.9	1.8
$Au_{25}(SC_{12}H_{25})_{18}$	8549.2	8548.0	-1.2

Table 2.2 shows the pseudo-first order rate constants for the reduction of 4-nitrophenol for various MPCs. Pseudo-first order reaction kinetics was used. Here, the $NaBH_4$ concentration (30 molar equivalent with respect to Au salt) was assumed to be constant during the course of the reaction. A_0 is the absorbance of substrate (4-nitrophenol) at time zero, and A_t is the absorbance at time t. Rate constants were derived by monitoring the change in the absorbance of the 4-nitrophenolate ion at 400 nm during the reaction. A new band is also seen at 312 nm because of the formation of 4-aminophenol product (Figure 2.3). Reduction in the substrate absorption peak rather than enhancement in product absorption peak was followed in order to deduce rate constant values. This was done because of the fact that absorption peak of product (4-aminophenol) was too weak to be used for kinetic analysis, possibly due to the absorption of product molecules on the surface of catalyst. For the $Au_{25}L_{18}$ MPCs, the rate constant was found to vary with chain length and composition of the chain, with the highest value observed in the case of $Au_{25}(SC_8H_9)_{18}$ MPCs, followed by $Au_{25}(SC_6H_{13})_{18}$ MPCs and then $Au_{25}(SC_{12}H_{25})_{18}$ MPCs. Such a decrease in the rate constant with an increase in chain length suggests that it would be easier for the substrate molecules to access the surface in the case of short chain thiolate molecules. Pseudo-first order rate plots and fitting parameters are shown in Figure 2.4 and Table 2.3 respectively.

Table 2.2. Pseudo first order rate constant for MPC-catalyzed reduction of 4-nitrophenol.

Entry	**Catalyst**	**Rate constant (min^{-1})**
1	$Au_{25}(SC_8H_9)_{18}$	0.51 ± 0.10
2	$Au_{25}(SC_6H_{13})_{18}$	0.12 ± 0.01
2a	$Au_{25}(SC_6H_{13})_{18}$	0.25 ± 0.03
3	$Au_{25}(SC_{12}H_{25})_{18}$	0.08 ± 0.03
4	$Au_{\sim 180}(SC_6H_{13})_{\sim 100}$	0.30 ± 0.03

Conditions: $NaBH_4$: substrate 30 : 1; [Au] : substrate 1 : 105

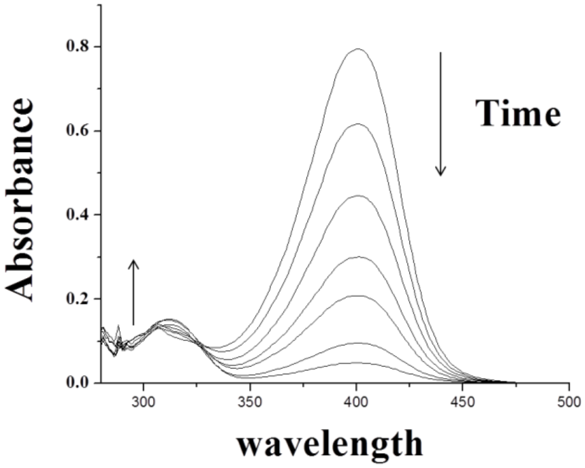

Figure 2.3. Representative UV-Vis spectra of the reduction of 4-nitrophenolate to 4- aminophenol over dodecanethiolate Au_{25} MPCs. Conditions: BH_4^- : total Au: substrate: 37500:1:105.

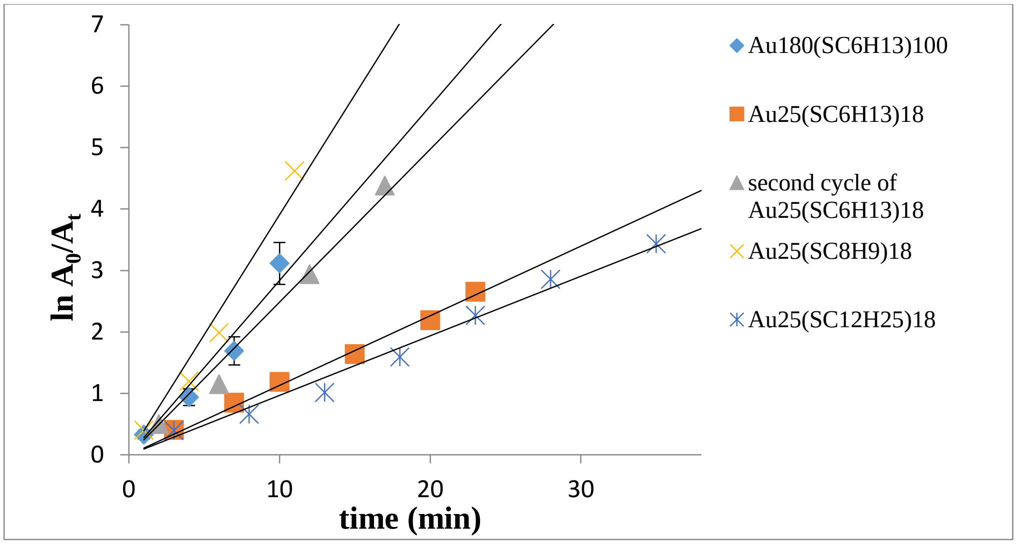

Figure 2.4. Kinetic pseudo-first order rate plots of the nitrophenolate absorption peak at 400 nm vs. time during reduction reactions using various Au MPCs.

Table 2.3. Fitting parameters deduced from pseudo-first order kinetic analysis of 4-nitrophenol reduction using various Au MPCs catalysts.

catalyst	**R^2 value**	**Induction time (min)**	**slope**
~ $Au_{180}(SC_6H_{13})_{100}$	.959	0	.30±.03
$Au_{25}(SC_8H_9)_{18}$	.964	2	.51±.10
second cycle of $Au_{25}(SC_8H_9)_{18}$	.996	2	.49±.05
$Au_{25}(SC_6H_{13})_{18}$	.994	2	.12±.01
Second cycle of $Au_{25}(SC_6H_{13})_{18}$	.994	2	.25±.03
$Au_{25}(SC_{12}H_{25})_{18}$	.983	2	.08±.03

After catalysis the MPCs were isolated and re-characterized by UV-Vis spectroscopy, TEM and MALDI-TOF. TEM data indicates the presence of clusters below 2 nm and absence of any large particles, but because of the limitation of the resolving power of TEM, exact distinction of cluster size before and after catalysis was difficult (Figure 2.5). However UV-Vis and MALDI-TOF (Figure 2.6) data clearly indicate that the integrity of the $Au_{25}L_{18}$ MPCs is preserved after the catalytic process. Extra fine features were observed in the mass-spectrum after catalysis (Figure 2.6 D) after catalysis. However, these were likely caused by extensive fragmentation of clusters during mass-spec analysis.

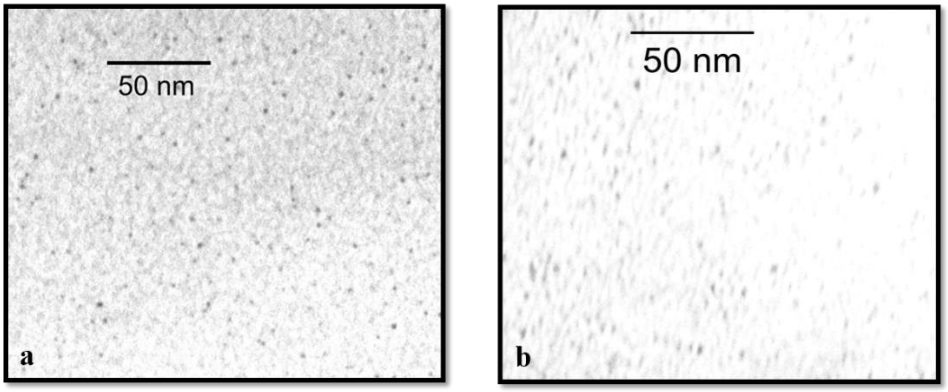

Figure 2.5. TEM images of hexanethiolate Au_{25} MPCs a) before catalysis and b) after catalysis.

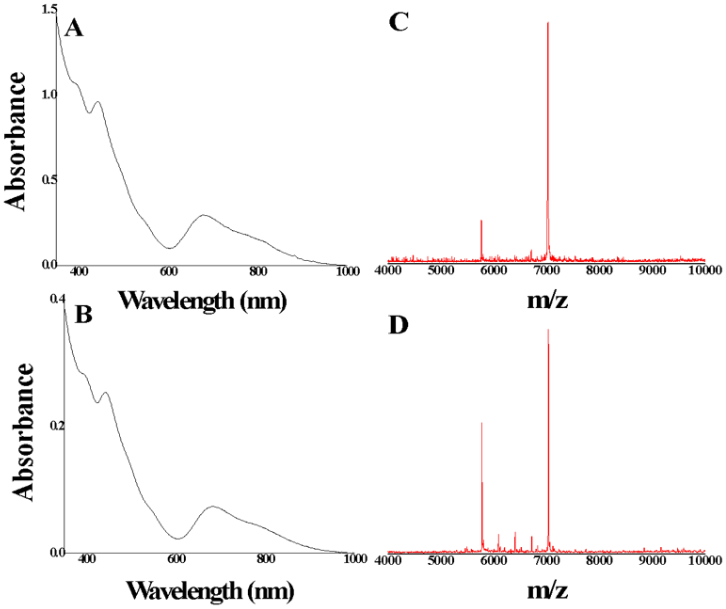

Figure 2.6. UV-Vis spectra of $Au_{25}(SC_6H_{13})_{18}$ MPCs before and (B) after catalysis, (C) MALDI-TOF spectrum of $Au_{25}(SC_6H_{13})_{18}$ clusters before and (D) after catalysis.

The high stability of these MPCs under the reaction conditions enabled a study of the recyclability. After recycling the rate constant was found to be higher than the original catalyst in the case of hexanethiolate Au_{25} MPCs, and was similar in the case of phenylethanethiolate Au_{25} MPCs (Figure 2.4), while no catalytic activity was observed in the case of dodecanethiolate Au_{25} MPCs. The higher rate constant for the $Au_{25}(SC_6H_{13})_{18}$ MPCs may be because of the fact that after first catalytic cycle and washing partial thiol removal took place from some Au_{25} MPCs, which would make more surface area available for catalysis. At this point in time we are uncertain as to why the more-sterically hindered $Au_{25}(SC_{12}H_{25})_{18}$ MPCs are not readily recyclable. In the case of larger $Au_{\sim180}(SC_6H_{13})_{\sim100}$ MPCs, the rate constant was found to be higher than hexanethiolate Au_{25} MPCs, but these larger MPCs were not stable and could not be recycled. This result suggests that the transient state responsible for catalysis is not stable in the case of larger MPCs. To gain insight into the stability of the Au MPCs towards $NaBH_4$, the effect of the addition of $NaBH_4$ to these MPCs was investigated using UV-Vis spectroscopy (Figure 2.7). No changes in the absorption pattern of $Au_{25}L_{18}$ MPCs after the addition of sodium borohydride were observed. However in the case of larger $Au_{\sim180}(SC_6H_{13})_{\sim100}$ MPCs, a rapid change was observed and the baseline was found to increase because of the formation of a precipitate. This result suggests that Au_{25} MPCs are more stable towards $NaBH_4$ treatment.

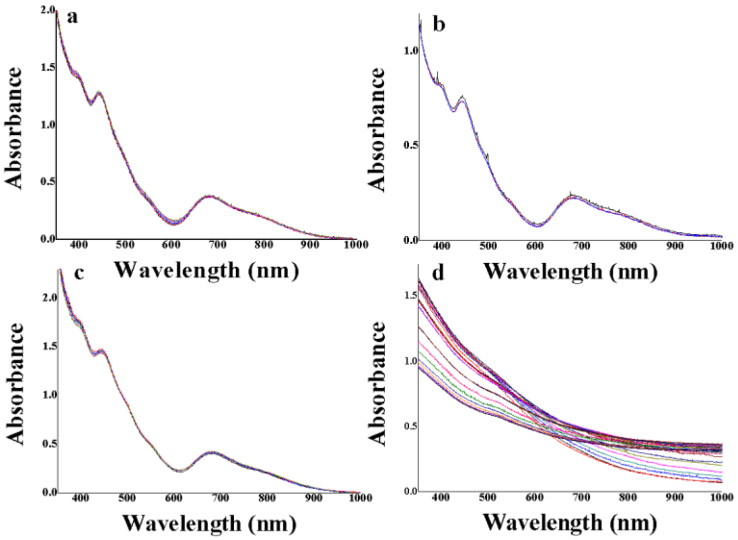

Figure 2.7. UV-Vis spectra showing the effect of the addition of 37500 equiv. of $NaBH_4$ to a) hexanethiolate Au_{25} MPCs, b) phenylethanethiolate Au_{25} MPCs, c) dodecanethiolate Au_{25} and d) larger hexanethiolate Au MPCs.

These results beg the question as to why the $Au_{25}L_{18}$ MPCs are more stable than their larger counterparts? Desorption of thiol monolayers from 2D Au facets using BH_4^- can be an energetically favourable process, where thiol desorption takes place at a potential of –1.0 V to -1.3 V (vs. NHE)[13,14] and the standard oxidation potential for BH_4^- is 1.24 V vs. NHE in basic conditions.[15] Indeed, we have shown that for larger Au MPCs, thiolate removal occurs in the presence of $NaBH_4$ which leads to the growth of MPCs and eventually precipitation of the MPCs during catalytic reductions.[10] However, preferential thiolate desorption at lower potentials from Au {111} is often seen compared to Au {100} and Au {110} facets in electrochemical studies.[16] Unlike larger Au MPCs, $Au_{25}L_{18}$ MPCs do not possess such {111} fcc facets and thus thiol desorption should not be as energetically favourable.[17] In addition, the high curvature of the $Au_{25}L_{18}$ clusters should allow for substrate access to the surface and thus incomplete ligand passivation of the clusters; thus thiolate removal may not be a necessary step for activation of the clusters. Jin et al. proposed a similar rationale for the catalytic oxidation of α,β-unsaturated ketones and aldehydes.[18] Also, we note that oxygen tends to quench the reduction reaction by scavenging electrons, which suggests facile O_2 access to the surface; a result similar to that of Jin et al. who suggested that that electron transfer takes place from $Au_{25}L_{18}$ clusters to oxygen.[18]

2.5 Conclusion

In summary, we have shown that Au_{25} MPCs are more stable towards $NaBH_4$ treatment than larger $Au_{\sim180}(SC_6H_{13})_{\sim100}$ MPCs. Further proof of the stability is provided by isolating hexanethiolate Au_{25} MPCs after the catalysis from the reaction mixture and characterizing them with UV-Vis, TEM, and MALDI-TOF techniques. However in the case of larger Au MPCs, such isolation was not possible because of the instability of these MPCs and no recyclability was observed. In the future, we will work towards immobilizing Au_{25} MPCs on support materials and studying their catalytic activity for nitrophenol reduction catalysis.

Acknowledgements

We acknowledge the very helpful assistance of Dr. Mahdi Hesari and Dr. Mark Workentin at Western University with $Au_{25}L_{18}$ synthesis and purification, and financial assistance from the National Sciences and Engineering Research Council of Canada (NSERC).

2.6 References

1. Zhu, M.; Garg, N.; Bier, M. E.; Jin, R., Kinetically Controlled High-Yield Synthesis of Au_{25} Clusters. *J. Am. Chem. Soc*. **2008**, *130* (4), 1138–1139.

2. Qian, H. F.; Zhu, M. Z.; Andersen, U. N.; Jin, R., Facile, Large Scale Synthesis of Dodecanethiol-Stabilized Au_{38} Clusters. *J. Phys. Chem. A* **2009**, *113* (16), 4281–4284.

3. Jadzinsky, P. D.; Calero, G.; Ackerson, C.; J.; Bushnell, D.; A.; Kornberg, R.; D., Structure of a Thiol Monolayer-Protected Gold Nanoparticle at 1.1 Angstrom Resolution. *Science* **2007**, *318* (5849), 430–433.

4. Zhu, M.; Aikens, C. M.; Hollander, F. J.; Schatz, G. C.; Jin, R., Correlating the Structure of A Thiol-Protected Au_{25} Cluster and Optical Properties. *J. Am. Chem. Soc*. **2008**, *130* (18), 5883–5885.

5. Qian, H. F.; Eckenhoff, W. T.; Zhu, Y.; Pintauer, T.; Jin, R., Total Structure Determination of Thiolate-Protected Au_{38} Nanoparticles. *J. Am. Chem. Soc.* **2010**, *132* (24), 8280–8281.

6. Lopez-Acevedo, O.; Akola, J.; Whetten, R. L.; Gronbeck, H.; Hakkinen, H., Structure and Bonding in the Ubiquitous Icosahedral Metallic Gold Cluster $Au_{144}(SR)_{60}$. *J. Phys. Chem. C* **2009**, *113* (13), 5035–5038.

7. Maity, P.; Xie, S. H.; Yamauchi, M.; Tsukuda, T., Stabilized Gold Clusters: from Isolation Toward Controlled Synthesis. *Nanoscale*, **2012**, *4* (14), 4027–4037.

8. Zhu, Y.; Qian, H. F.; Zhu, M. Z.; Jin, R., Thiolate-Protected Aun Nanoclusters as Catalysts for Selective Oxidation and Hydrogenation Process. *Adv. Mater*. **2010**, *22* (17), 1915–1920.

9. Nie, X. T.; Qian, H. F.; Ge, Q. J.; Xu, H. Y.; Jin, R., CO Oxidation Catalyzed by Oxide-Supported $Au_{25}(SR)_{18}$ Nanoclusters and Identification of Perimeter Sites as Active Centers. *ACS Nano* **2012**, *6* (7), 6014–6022.

10. Dasog, M.; Hou, W.; Scott, R. W. J., Controlled Growth and Catalytic Activity of Gold Monolayer Protected Clusters in Presence of Borohydride Salts. *Chem. Commun*. **2011**, *47* (30), 8569–8571.

11. Hou, W. B.; Dasog, M.; Scott, R. W. J., Probing the Relative Stability of Thiolate- and Dithiolate-Protected Au Monolayer-Protected Clusters. *Langmuir* **2009**, *25* (22), 12954-12961.

12. Dass, A.; Stevenson, A.; Dubay, G. R.; Tracy, J. B.; Murray, R. W., Nanoparticle MALDI-TOF Mass Spectrometry without Fragmentation: $Au_{25}(SCH_2CH_2Ph)_{18}$ and Mixed Monolayer $Au_{25}(SCH_2CH_2Ph)_{18-x}(L)_x$. *J. Am. Chem. Soc*. **2008**, *130* (18), 5940-5946.

13. Yang, D. F.; Wilde, C. P.; Morin, M., Electrochemical Desorption and Adsorption of Nonyl Mercaptan at Gold Single Crystal Electrode Surfaces. *Langmuir* **1996**, *12* (26), 6570–6577.

14. Yang, D. F.; Wilde, C. P.; Morin, M., Studies of the Electrochemical Removal and Efficient Re-Formation of a Monolayer of Hexadecanethiol Self-Assembled at an Au(111) Single Crystal in Aqueous Solutions. *Langmuir* **1997**, *13* (2), 243–249.

15. *CRC Handbook of Chemistry and Physics*, CRC Press, Cleveland, OH, 91st edition, 2010.

16. Arihara, K.; Ariga, T.; Takashima, N.; Arihara, K.; Okajima, T.; Kitamura, F.; Tokuda, K.; Ohsaka, T., Multiple Voltammetric Waves for Reductive Desorption of Cysteine and 4-Mercaotpbenzoic Acid Monolayers Self-Assembled on Gold Substrates. *Phys. Chem. Chem. Phys*. **2003**, *5* (17), 3758–3761.

17. Heaven, M. W.; Dass, A.; White, P. S.; Holt, K. M.; Murray, R. W., Crystal structure of the gold nanoparticle $[N(C_8H_{17})_4][Au_{25}(SCH_2CH_2Ph)_{18}]$. *J. Am. Chem. Soc.* **2008**, *130* (12), 3754–3755.

18. Zhu, Y.; Qian, H. F.; Drake, B. A.; Jin, R., Atomically Precise $Au_{25}(SR)_{18}$ Nanoparticles as Catalysts for the Selective Hydrogenation of α,β-unsaturated ketones and aldehydes *Angew. Chem., Int. Ed.* **2010**, *49* (7), 1295–1298.

Chapter 3

3. Isolation of Carboxylic Acid-Protected Au_{25} Clusters Using a Borohydride Purification Strategy

This work has been published in *Langmuir*. This work describes the synthesis of Au_{25} clusters protected with carboxylic acid terminated thiol stabilizers using the knowledge obtained on the stability of $Au_{25}(SR)_{18}^-$ clusters from the previous study (Chapter 2). Here, 11-mercatodecanoic acid and 16-hexadecanoic protected $Au_{25}L_{18}$ clusters were isolated from a polydisperse Au cluster solution by adding the controlled amount of $NaBH_4$. The entire process of the isolation of $Au_{25}L_{18}^-$ clusters was followed by TEM and UV-Vis spectroscopy. Finally, as synthesized 11-mercaptodecanoic acid protected Au_{25} clusters were characterized by using mass spectrometry and ^1H NMR spectroscopy.

This work has been published in *Langmuir* **2015**, *31* (5), 1835–1841. The author would like to acknowledge the contributions of Lisa Wang, who at the time was a first year undergraduate student, for assisting in the synthesis of 11-mercaptoundecanoic acid-protected Au_{25} clusters, UV-Vis study, and NMR data collection. The author's contributions to this manuscript include: synthesis of carboxylic acid-protected Au_{25} clusters, characterization (UV-Vis and mass-spectrometry study), data interpretation, and in the preparation of the manuscript. This manuscript was revised by Dr. Robert Scott prior to publication.

Isolation of Carboxylic Acid-Protected Au_{25} Clusters Using a Borohydride Purification Strategy

Atal Shivhare, Lisa Wang, and Robert W. J. Scott*

Department of Chemistry, University of Saskatchewan, 110 Science Place, Saskatoon,
Saskatchewan S7N 5C9, Canada

3.1 Abstract

We report the synthesis of 11-mercaptoundecanoic acid (11-MUA) and 16-mercaptohexadecanoic acid (16-MHA) protected Au_{25} clusters with moderate yields (∼15%) using a $NaBH_4$ purification strategy. UV−Vis spectroscopy, transmission electron microscopy (TEM), and matrix-assisted laser desorption/ ionization (MALDI) mass spectrometry were employed to study the entire process of the isolation of 11-MUA-protected Au_{25} clusters from a polydisperse Au cluster solution. UV−Vis and TEM data clearly show the formation of a polydisperse mixture, which upon the addition of $NaBH_4$ leads to the growth and precipitation of non-Au_{25} clusters, leaving the Au_{25} clusters behind. MALDI MS shows the molecular ion peak for the 11-MUA-protected Au_{25} cluster. 11-MUA-protected Au_{25} clusters in THF were purified by slowly increasing the pH of the solution, which leads to the complete deprotonation of carboxyl groups on the surface and eventually precipitation of Au_{25} clusters. Further protonation of these clusters by acetic acid leads to their solubilization in THF. These results show that, owing to the inherent stability of Au_{25} clusters, a $NaBH_4$ purification strategy can be used to isolate Au_{25} clusters with surface carboxylic acid functionalities from a polydisperse Au cluster solution.

3.2 Introduction

Recently, Au monolayer protected clusters (MPCs) have been used for a variety of applications, mainly because of the synthetic methodologies developed by various groups that allow for the synthesis of Au MPCs of various sizes and chemical compositions.[1−10] Many of these methodologies are the modifications of the original biphasic Brust and Schiffrin synthesis,[11] though many single-phase synthesis protocols now exist. Typically in these syntheses, stable and isolable Au MPCs are synthesized by reducing $HAuCl_4$ using $NaBH_4$ in the presence of thiol stabilizers. Au MPCs prepared by this approach are stable and can be isolated and redissolved in common organic solvents without any decomposition. Recently, many groups have shown that this approach can be used to synthesize highly monodisperse Au MPCs with distinct HOMO−LUMO electronic transitions, and the exact atomic composition of these clusters can be analyzed by mass spectrometry.[12−15] In most of these cases, monodispersity was achieved by using a top-to-bottom size-focusing approach where the initially formed polydisperse Au MPC solution was allowed to undergo oxidative etching for several hours.[16] This leads to the oxidation of unstable clusters and only stable clusters survive, which can be easily separated from the reaction mixture. The basic principle behind controlling the size of Au MPCs in all these approaches has been the fast reduction step, where the instantaneous addition of a large amount of reducing agent leads to the higher concentration of Au nuclei in solution.[17] These nuclei then oxidatively ripen into smaller MPCs, and these small MPCs can be size focused to a particular size. There are particularly very few examples of monodisperse Au clusters with functionalizable terminal groups using direct synthetic routes,[18,19] though other ligand exchange routes exist.[20−22] Growth dynamics of Au nuclei become completely different when functional-group-terminated (e.g., −COOH, −OH, and $-NH_2$) thiol stabilizers are used, perhaps because of the relatively strong interparticle interactions between these functional groups.[18,19] In particular, Yuan *et al*. have shown that slowing down the kinetics of Au MPC nucleation by NaOH addition to $NaBH_4$ can allow isolation of functionalizable Au clusters.[18]

Both ourselves[23,24] and others[25,26] have reported that BH_4^- reducing agents can reductively desorb thiol stabilizers from the surface of Au MPCs. Zhang and co-workers found that $NaBH_4$ can desorb many ligands from Au nanoparticle surfaces, including halides and thiolate stabilizers, and noted via computational work that hydrides derived from $NaBH_4$ had strong binding affinities to Au.[25] Das *et al*. recently showed that thiolates could be reductively desorbed off Au clusters and thus activated on solid oxide supports for oxidation catalysis.[26] We showed that BH_4^- can be used to open up catalytically active sites of Au MPCs for p-nitrophenol reduction reactions.[23] During the catalytic reaction, Au MPCs were found to grow in size because of BH_4^- induced thiol desorption. Recently, we employed Au_{25} MPCs as a catalyst to study the p-nitrophenol reduction reaction using $NaBH_4$ reducing agent.[24] We found that Au_{25} MPCs were considerably more stable to $NaBH_4$ than their larger counterparts and could be used as recyclable catalysts for p-nitrophenol reduction.

These interesting findings suggested to us that Au_{25} MPCs could be isolated from a polydisperse Au MPC reaction mixture using a novel BH_4^- purification strategy, where larger MPCs are prone to growth and precipitation because of BH_4^- induced thiolate removal. We used this approach in the present study and found that by carefully tuning the amount of BH_4^-, 11-mercaptoundecanoic acid (11-MUA) and 16-mercaptohexadecanoic acid (16-MHA) protected Au_{25} MPCs can be size separated from a polydisperse Au MPC solution. In the case of 11-MUA-protected Au_{25} MPCs, the separation process and resulting MPCs have been characterized by transmission electron microscopy (TEM), ultraviolet−visible (UV−vis) spectroscopy, and matrix-assisted laser desorption/ionization (MALDI) mass spectrometry. Finally, we show that purified 11-MUA-protected Au_{25} MPCs can be dissolved in water and THF both by changing the pH of the solution because of the presence of carboxyl-terminated thiol stabilizers. The present study demonstrates the stability of Au_{25} MPCs toward $NaBH_4$ and present a way to isolate Au_{25} MPCs protected with carboxyl-terminated thiol stabilizers from a polydisperse Au MPC mixture.

3.3 Experimental

3.3.1 Materials

Hydrogen tetrachloroaurate(III) trihydrate ($HAuCl_4 \cdot 3H_2O$, 99.9% on a metal basis, Aldrich), tetraoctylammonium bromide (TOAB, 98%, Aldrich), sodium borohydride ($NaBH_4$, 98%, Fisher Scientific), 11-mercaptoundecanoic acid (11-MUA, $HS(CH_2)10CO_2H$, 95%, Aldrich), and 16-mercaptohexadecanoic acid (16-MHA, 90%, Aldrich) were used as received. High-purity tetrahydrofuran (THF), methanol (≥99.8%), and acetic acid (≥99.7%) were purchased from Fisher Scientific. Milli-Q (Millipore, Bedford, MA) deionized water (18 MΩ cm) was used throughout. Deuterium oxide (D_2O, 99.9% atom D) was purchased from Aldrich, and dimethyl sulfoxide-d_6 (DMSO-d_6, 99.9% atom D) was purchased from the Cambridge Isotope Laboratory.

3.3.2 Synthesis of 11-MUA-Protected Au_{25} MPCs

11-Mercaptoundecanoic acid-protected Au_{25} monolayer protected clusters were produced using a typical synthesis as follows: 200 mg of $HAuCl_4{\cdot}3H_2O$ was dissolved in 20 mL of THF and mixed with 1.2 equiv of TOAB. The resulting solution was stirred at a moderate speed for 10 min, until it became reddish-orange in color. Then, the stirring rate was slowed and a mixture of 5 equiv of 11-mercaptoundecanoic acid in 5 mL of THF was added dropwise to the solution. The resulting solution was left to stir slowly until it became colorless. The stirring rate of the solution was again increased to a high speed and the solution was cooled in an ice bath. Another solution containing 4 equiv. of $NaBH_4$ in 2 mL of ice-cold water was added slowly dropwise at a rate of 2 drops per second (2 drops ~ 0.01 mL) to the Au solution until small features for Au_{25} MPCs started to appear, as monitored by UV−vis spectroscopy. After that, the ice bath was removed, and the solution was allowed to stir for 30 min, followed by the addition of 2 drops of $NaBH_4$. Successive spectra were collected at intervals of 30 min, and the amount of $NaBH_4$ added in between each spectrum was 2 drops. Completion of the reaction was determined by monitoring the UV−Vis spectra. In a completed reaction, the absorbance spectrum showed the typical peaks for Au_{25} MPCs and also showed that no further changes to the spectrum were occurring. When the MPCs were fully formed, the brown solution containing the Au_{25} MPCs was separated from the dark precipitate and collected using filtration

3.3.3 Synthesis of 16-MHA-Protected Au_{25} MPCs

16-Mercaptohexadecanoic acid-protected Au_{25} monolayer protected clusters were produced using a typical synthesis as follows: 53 mg of $HAuCl_4{\cdot}3H_2O$ was dissolved in 10 mL of THF and mixed with 1.2 equiv of TOAB. The resulting solution was stirred at a moderate speed for 10 min, until it became reddish-orange in color. Then, the stirring rate was slowed and a mixture of 5 equiv. of 11-mercaptoundecanoic acid in 5 mL of THF was added dropwise to the solution. The resulting solution was left to stir slowly until it became colorless. The stirring rate of the solution was again increased to a high speed and the solution was cooled in an ice bath. Another solution containing 10 equiv. of $NaBH_4$ in 2 mL of ice-cold water was added slowly dropwise at a rate of 2 drops per second (2 drops ~ 0.01 mL) to the Au solution until small features for Au_{25}

MPCs started to appear, as monitored by UV−Vis spectroscopy. After that, the ice bath was removed and the solution was allowed to stir for 15 min, followed by the addition of 2 drops of $NaBH_4$. Successive spectra were collected at intervals of 15 min, and the amount of $NaBH_4$ added in between each spectrum was 2 drops. Completion of the reaction was determined by monitoring the UV−Vis spectra. In a completed reaction, the absorbance spectrum showed the typical peaks for Au_{25} MPCs and also showed that no further changes to the spectrum were occurring.

3.3.4 Purification of 11-MUA-Protected Au_{25} MPCs

The solution containing 11-MUA-protected Au_{25} MPCs was purified using a multiple-step procedure. The Au_{25} solution in THF was cooled in an ice bath and stirred vigorously while a fresh solution of 1.5 equiv. of $NaBH_4$ in 2 mL of ice-cold water was added slowly dropwise. The $NaBH_4$ was added until a fine, brown precipitate was observed suspended in solution and the solution became colorless. The solid was collected using centrifugation and washed twice with fresh THF. After washing, the solid was dissolved in methanol to selectively extract the Au_{25} MPCs. The Au_{25} solution was collected and placed within a flask, and then the methanol was evaporated using a rotary evaporator. The yield of Au_{25} MPCs obtained after purification was ca. 15%. After being dried, the Au_{25} solid was dissolved in a minimal amount of deionized water, forming a brown-colored solution. A diluted acetic acid solution with an approximate pH of 3 was prepared and added to the solution dropwise in order to acidify it. After the addition of a few drops of acetic acid, the Au_{25} MPCs slowly precipitated out of the mixture to form a brown solid suspended within a colorless solution. The solid was collected using centrifugation, and the Au_{25} MPCs were dissolved in THF. To store the Au_{25} MPCs, the THF solvent and any remaining water was removed using a rotary evaporator. Then, the MPCs were redissolved in fresh THF and stored in a sealed flask under cooled conditions.

3.3.5 Characterization

UV−Vis absorption spectra were recorded using a Varian Cary Bio UV−vis spectrometer with an optical path length of 1 cm. Transmission electron micrographs (TEM) were taken with a HT7700 TEM operating at 100 kV. TEM grids were prepared by placing a drop of the Au MPC solution in THF onto a carbon-coated 400 mesh Cu TEM grid (Electron Microscopy Sciences). Mass spectrometry was performed on an Applied Biosystems 4800 MALDITOF/TOF instrument (Frederick, MD) operating in linear negative ion mode using a matrix of DIT (anthracene-1,8,9-

triol). ^{1}H nuclear magnetic resonance (NMR) was obtained with a Bruker 500 MHz Avance spectrometer, with D_2O as the solvent.

3.4 Results and Discussion

Figure 3.1a is the UV−vis spectra showing the formation of 11-MUA-protected Au_{25} MPCs during the dropwise addition of $NaBH_4$ at a rate of 2 drops per second.. After the addition of the first few drops of $NaBH_4$, an almost featureless absorption spectrum with very small absorption peaks characteristic of Au_{25} MPCs was observed. The spectra indicates the presence of Au MPCs with less than 2 nm size[27] along with the small population of Au_{25} clusters. Further addition of $NaBH_4$ leads to the formation of a small amount of precipitate, along with a sharpening of features in the visible region. Dropwise addition of $NaBH_4$ was continued until absorption features characteristic of $Au_{25}L_{18}$ MPCs were observed at ca. 400, 450, and 690 nm.[28] Figure 3.1b shows the formation of 16-MHA-protected Au_{25} MPCs during the dropwise addition of $NaBH_4$. Here, during the dropwise addition of $NaBH_4$, absorption features characteristic of Au_{25} MPCs were observed. These features, upon further addition of $NaBH_4$, were intensified, and the overall absorption was also increased, as shown by the black arrow. Addition of $NaBH_4$ was continued until the black spectrum representative of 16-MHA-protected Au_{25} MPCs was observed as a result of the precipitation of all non-Au_{25} MPCs, as shown by the green arrow. Different UV−Vis trends observed in two different systems are attributed to the increase in chain length as well as the difference in solubility between larger Au MPCs and Au_{25} MPCs in the case of two different stabilizers. In the case of 11- MUA, larger Au MPCs were unstable in solution and immediately precipitated out of the solution, as shown by the black arrow, which represents the formation of precipitate during the addition of $NaBH_4$ (Figure 3.1a).

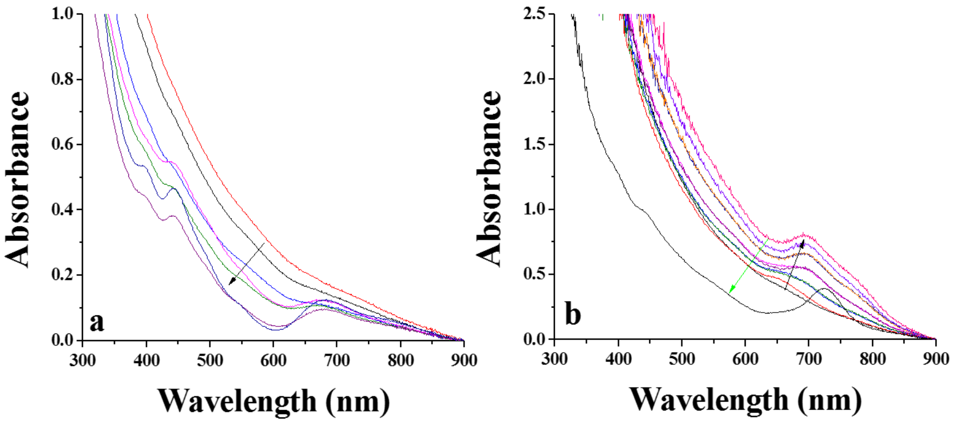

Figure 3.1. Normalized UV−vis spectra showing the formation of (a) 11-MUA-protected Au_{25} MPCs and (b) 16-MHA-protected Au_{25} MPCs during dropwise addition of $NaBH_4$. Spectra have been normalized at 900 nm to remove scattering artifacts because of hydrogen bubbles and heterogeneous precipitates.

In the case of 16-MHA, larger Au MPCs were relatively more stable and remained in solution. This leads to the increase in overall absorption during the addition of $NaBH_4$, as shown by the black arrow (Figure 3.1b). Attempts were also made to use this methodology with a more conventional hydrophobic ligand (dodecanethiol) and 1-mercapto-1-undecanol, but it was not successful in either case (data not shown). In the case of dodecanethiol, very weak features similar to those of Au_{25} MPCs were observed during the initial period of the addition of $NaBH_4$, but clusters could not readily be separated from larger Au MPCs. This may be attributed to very small solubility differences between larger dodecanethiol-stabilized Au MPC and Au_{25} MPCs. No cluster features were seen in the case of 1- mercapto-1-undecanol. Thus, this technique seems to be more specific toward carboxylic acid-terminated MPCs. Nevertheless, as synthesis of Au clusters from carboxylic acid-terminated ligands has been challenging by conventional oxidative Au cluster size-focusing strategies, this represents an appealing strategy for the synthesis of such clusters. While the UV−Vis is strongly suggestive of that Au_{25} MPCs are formed, TEM and MALDI MS evidence below gives more evidence for the composition of the MPCs.

The 11-MUA system was chosen for further characterization. Figure 3.2 shows the formation of precipitate and 11-MUA-protected Au_{25} MPCs from the initially formed polydisperse solution on the left side. The first few drops of $NaBH_4$ lead to the formation of polydisperse Au

MPCs. These MPCs do not readily grow into large nanoparticles, as no surface plasmon band was observed in the UV−vis spectra at any time. Attempts to form 11-MUA- or 16-MHA-protected $Au_{25}L_{18}$ MPCs via oxidative ripening failed (e.g., aging in air); typically, complete precipitation of the Au MPCs was seen over time. Further addition of $NaBH_4$ leads to the growth and precipitation of larger Au MPCs. We believe that this occurs via thiol desorption and MPC growth in the presence of excess $NaBH_4$,[23–26] and that the larger MPCs also become insoluble in THF because of the higher density of carboxylate groups on their surfaces (carboxylate groups likely form at high $NaBH_4$ excesses, leading to anionic surfaces). We have found that fast addition of excess $NaBH_4$ leads to nearly complete precipitation of all Au MPCs.

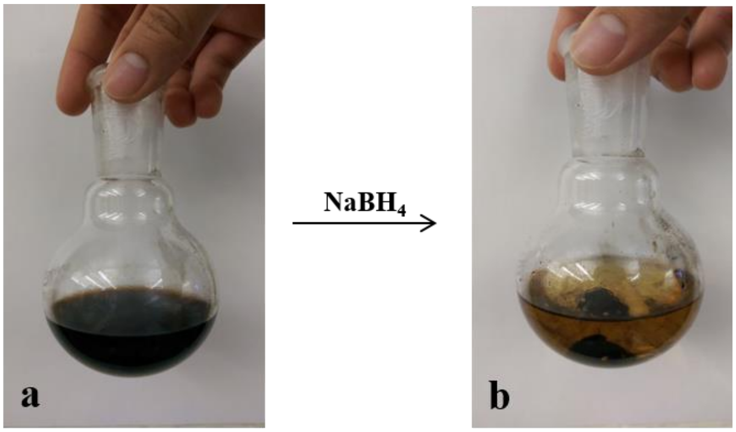

Figure 3.2. Pictorial presentation of the 11-MUA-protected (a) polydisperse Au MPC solution and (b) formation of Au_{25} clusters after $NaBH_4$ addition.

Figure 3.3 shows the TEM images of 11-MUA-protected Au MPCs during the progress of the reaction. After the addition of the first few drops of $NaBH_4$, a polydisperse solution was observed, which is clearly evident from Figure 3.3a.

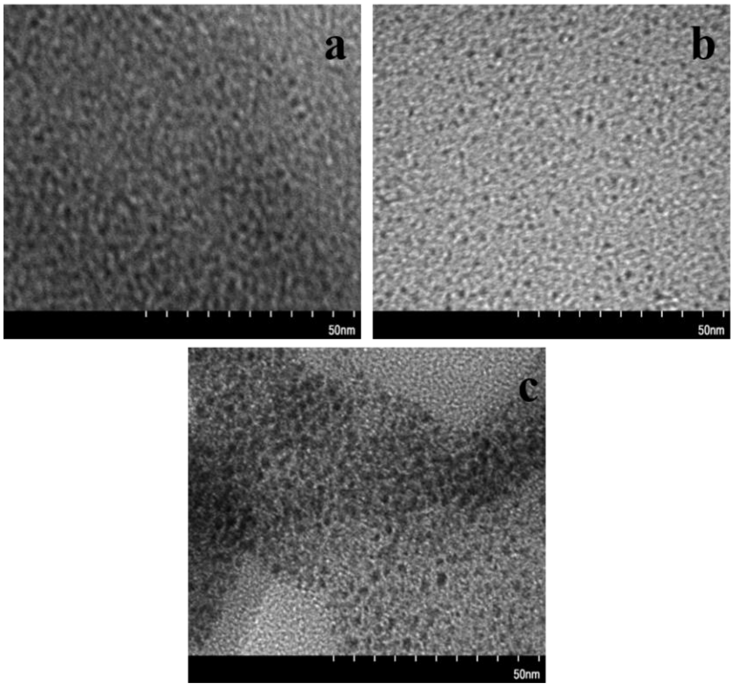

Figure 3.3. TEM images of 11-MUA-protected (a) polydisperse Au MPCs, (b) Au_{25} MPCs, and (c) water-soluble precipitate.

At this stage, the average size of MPCs was 1.4 ± 0.4 nm, which is in agreement with the featureless spectrum seen by UV−Vis spectroscopy.[27] After the complete addition of $NaBH_4$, both the precipitate and solution were sampled. Figure 3.3b shows a TEM image of 11-MUA-protected Au_{25} MPCs that remain in solution, which have an average size of 1.1 ± 0.2 nm. Figure 3.3c shows the TEM image of the water-soluble fraction of the precipitate; MPCs are clearly larger (with an average particle size of 1.8 ± 0.3 nm). The TEM image of the water-insoluble fraction of the precipitate showed much larger Au aggregates (not shown). Thus, the TEM investigation clearly shows that the Au_{25} MPCs were size-separated from larger MPCs via selective growth/precipitation of the larger MPCs. Because of the inherent stability of Au_{25} MPCs, addition of more $NaBH_4$ only led to the growth and eventual precipitation of non-Au_{25} clusters.

A mass spectroscopic investigation of the 11-MUA-protected Au_{25} MPCs (Figure 3.4) clearly shows the presence of the highest molecular ion peak at 8834.20 amu. This value is 1.23 amu less than the MW for singly deprotonated $Au_{25}(SC_{11}H_{21}O_2)_{18}$ MPCs (8835.43 amu).

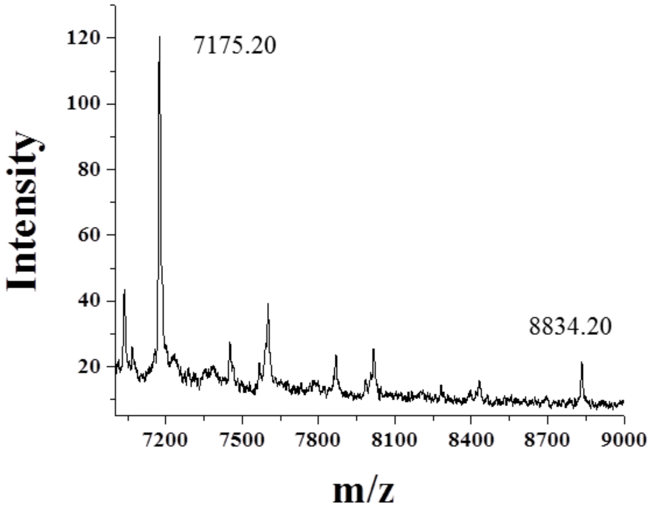

Figure 3.4. MALDI mass spectroscopy spectra of $Au_{25}(SC_{11}H_{21}O_2)_{18}$ MPCs.

This difference in values likely can be attributed to small calibration errors. A major fragmentation peak was found at 7175.20 amu. This peak is attributed to the formation of $Au_{21}(SC_{11}H_{21}O_2)_{14}$ species by the dissociation of a $Au_4(SC_{11}H_{21}O_2)_4$ unit from $Au_{25}(SC_{11}H_{21}O_2)_{18}$ MPCs.[24] This type of fragmentation has been seen previously in the case of thiol-protected Au_{25} MPCs during laser exposure under mass spectrometric analysis. The m/z value of fragmented species is several amu less than the molecular weight (7178.17 amu). Many other smaller peaks are also present, but they have not been assigned. It should be noted that unlike in alkanethiolate and or phenylethanethiolate $Au_{25}L_{18}$ systems, the presence of the carboxylate groups will lead to the formation of thousands of putative species (multianions + adducts), which can make mass spectrometric analyses quite difficult.

11-MUA-protected Au_{25} MPCs were purified from the reaction mixture by separating the THF phase containing MPCs followed by the dropwise addition of $NaBH_4$ at low temperature. Addition of more aqueous $NaBH_4$ further deprotonates carboxyl groups and causes the $Au_{25}(SC_{11}H_{21}O_2)_{18}$ MPCs to become insoluble in THF. This precipitate can be dissolved in water; the reprotonation of carboxylate groups by acetic acid in water again leads to the precipitation of the Au_{25} MPCs. We have found that by increasing or decreasing the pH of the solution, 11-MUA-protected Au_{25} MPCs can be dissolved in both water and THF. Figure 3.5 shows the UV−Vis spectra of the Au_{25} MPCs in each of these solvents. Absorption features are much broader in H_2O

than in THF; this is a reversible effect that may be because of the changes in the dielectric constant or H-bonding ability of the solvent.

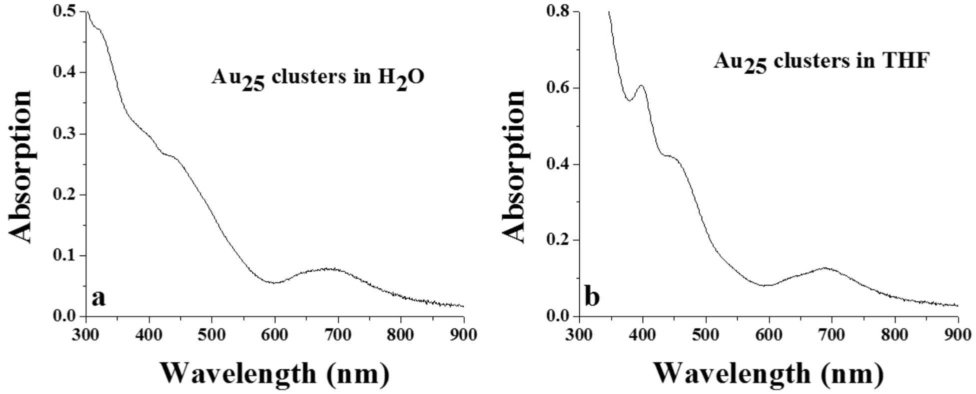

Figure 3.5. UV−Vis spectra showing the features of 11-MUA-protected Au_{25} MPCs (a) in water and (b) in THF.

It should be noted that during the purification step, leftover 11-MUA was not precipitated out of the solution after $NaBH_4$ addition. Evidence of this is seen by ^1H NMR of the Au_{25} MPCs in D_2O. NMR spectra (Figure 3.6) clearly show that $Au_{25}(SC_{11}H_{21})_{18}$ MPCs did not have the contamination of free thiol, as no sharp peak was detected at ∼2.5 ppm. The NMR also shows that the proton peak for the α-methylene proton off the thiol has disappeared, likely because of the broadening as a result of slow rotation in solution.[29] We do note that a small amount of disulfide impurity [formed in the original Au(III) reaction with MUA] is still present after purification. The yield of $Au_{25}(SC_{11}H_{21}O_2)_{18}$ MPCs was ca. 15% after drying the precipitate. The low yield of Au_{25} MPCs is because of the sacrificial nature of the methodology, which relies on the precipitation of all non-Au_{25} MPCs as a means to separate Au_{25} MPCs from a polydisperse Au MPC mixture. Oxidative size focusing strategies for hydrophobic ligands typically give maximum yields of 30−40%,[16] but that strategy involves oxidizing larger clusters downward, which can increase the total population of Au clusters. Combining this $NaBH_4$ purification approach with alternative reducing agents (such as $NaBH_4$/ NaOH or CO),[18,30] which can yield larger amounts of clusters at synthesis, could be effective in producing higher yields of Au clusters with carboxyl ligands in the future.

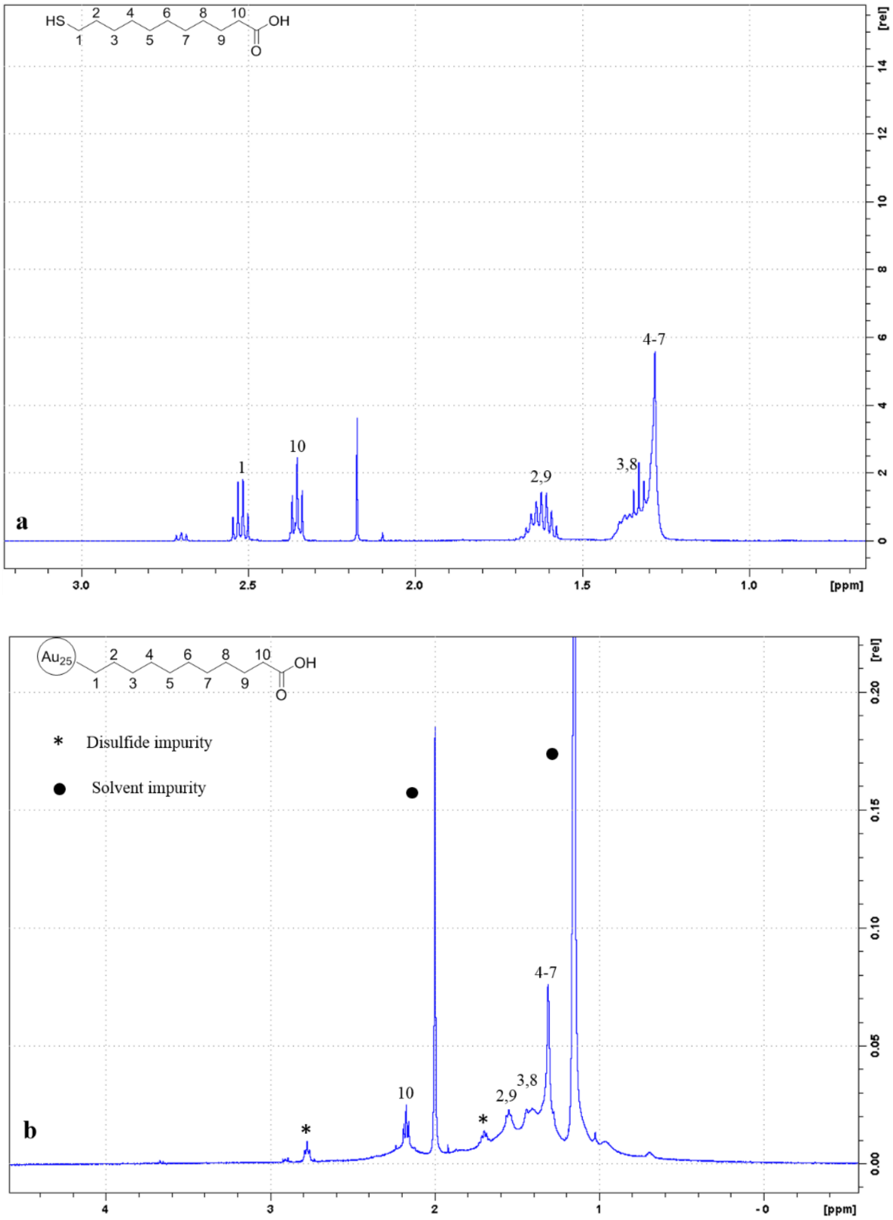

Figure 3.6. ^{1}H NMR spectrum of (a) 11-MUA in $CDCl_3$ and (b) 11-MUA-protected Au_{25} MPCs in D_2O.

3.5 Conclusion

In summary, we have shown a new route for the isolation of 11-MUA- and 16-MHA-protected Au_{25} MPCs from a polydisperse Au MPC solution. Our study shows that the $NaBH_4$ reducing agent can potentially be used to separate intrinsically stable carboxylic acid-terminated Au_{25} MPCs from a polydisperse Au MPC reaction mixture. While this is a promising pathway toward the isolation of functionalizable Au_{25} MPCs, yields by this process are moderate at best (ca. 15%). We have shown the generality of this methodology in the case of thiol stabilizers terminated with carboxyl groups.

Acknowledgements

We acknowledge financial assistance from the National Sciences and Engineering Research Council of Canada (NSERC). We also acknowledge R. Purves and the National Research Council (NRC) Canada for providing access to mass spectrometry facilities.

3.6 References

1. Bauld, R.; Hesari, M.; Workentin, M. S.; Fanchini, G. Tessellated gold nanostructures from $Au_{144}(SCH_2CH_2Ph)_{60}$ molecular precursors and their use in organic solar cell enhancement. *Nanoscale* **2014**, *6* (13), 7570−7575.

2. Chen, Y. S.; Kamat, P. V. Glutathione-capped gold nanoclusters as photosensitizers. Visible light-induced hydrogen generation in neutral water. *J. Am. Chem. Soc.* **2014**, *136* (16), 6075−6082.

3. Kumara, C.; Zuo, X. B.; Ilavsky, J.; Chapman, K. W.; Cullen, D. A.; Dass, A. Super-stable, highly monodisperse plasmonic faradaurate- 500 nanocrystals with 500 gold atoms: $Au_{\sim500}(SR_{)\sim120}$. *J. Am. Chem. Soc.* **2014**, *136* (20), 7410−7417.

4. Xie, S. H.; Tsunoyama, H.; Kurashige, W.; Negishi, Y.; Tsukuda, T. Enhancement in aerobic alcohol oxidation catalysis of Au_{25} clusters by single Pd atom doping. *ACS Catal.* **2012**, *2* (7), 1519−1523.

5. Nimmala, P. R.; Yoon, B.; Whetten, R. L.; Landman, U.; Dass, A. $Au_{67}(SR)_{35}$ nanomolecules: Characteristic size-specific optical, electrochemical, structural properties and first-principles theoretical analysis. *J. Phys. Chem. A* **2013**, *117* (2), 504−517.

6. Shivhare, A.; Chevrier, D. M.; Purves, R. W.; Scott, R. W. J. Following the thermal activation of $Au_{25}(SR)_{18}$ clusters for catalysis by X-ray absorption spectroscopy. *J. Phys. Chem. C* **2013**, *117* (39), 20007−20016.

7. Marjomakia, V.; Lahtinen, T.; Martikainen, M.; Koivisto, J.; Malola, S.; Salorinne, K.; Pettersson, M.; Hakkinen, H. Site-specific targeting of enterovirus capsid by functionalized monodisperse gold nanoclusters. *Proc. Natl. Acad. Sci. U. S. A.* **2014**, *111* (4), 1277−1281.

8. Mathew, A.; Natarajan, G.; Lehtovaara, L.; Hakkinen, H.; Kumar, R. M.; Subramanian, V.; Jaleel, A.; Pradeep, T. Supramolecular functionalization and concomitant enhancement in properties of Au_{25} clusters. *ACS Nano* **2014**, *8* (1), 139−152.

9. Antonello, S.; Hesari, M.; Polo, F.; Maran, F. Electron transfer catalysis with monolayer protected Au_{25} clusters. *Nanoscale* **2012**, *4* (17), 5333−5342.

10. Fields-Zinna, C. A.; Parker, J. F.; Murray, R. W. Mass spectrometry of ligand exchange chelation of the nanoparticle $[Au_{25}(SCH_2CH_2C_6H_5)_{18}]^{-1}$ by $CH_3C_6H_3(SH)_2$. *J. Am. Chem. Soc.* **2010**, *132* (48), 17193−17198.

11. Brust, M.; Walker, M.; Bethell, D.; Schiffrin, D. J.; Whyman, R. Synthesis of thiol-derivatized gold nanoparticles in a 2-phase liquid− liquid system. *J. Chem. Soc. Chem. Commun.* **1994**, No. *7*, 801−802.

12. Zhu, M.; Lanni, E.; Garg, N.; Bier, M. E.; Jin, R. Kinetically controlled, high-yield synthesis of Au_{25} clusters. *J. Am. Chem. Soc.* **2008**, *130* (4), 1138−1139.

13. Kim, J.; Lema, K.; Ukaigwe, M.; Lee, D. Facile preparative route to alkanethiolate-coated Au_{38} nanoparticles: Postsynthesis core size evolution. *Langmuir* **2007** *23* (14), 7853-7858.

14. Kumara, C.; Dass, A. $Au_{329}(SR)_{84}$ nanomolecules: Compositional assignment of the 76.3 kDa plasmonic faradaurates. *Anal. Chem.* **2014**, *86* (9), 4227−4232.

15. Ackerson, C. J.; Jadzinsky, P. D.; Kornberg, R. D. Thiolate ligands for synthesis of water-soluble gold clusters. *J. Am. Chem. Soc.* **2005**, *127* (18), 6550−6551.

16. Jin, R. C.; Qian, H. F.; Wu, Z. K.; Zhu, Y.; Zhu, M. Z.; Mohanty, A.; Garg, N. Size focusing: A methodology for synthesizing atomically precise gold nanoclusters. *J. Phys. Chem. Lett.* **2010**, *1* (19), 2903− 2910.

17. Finney, E. E.; Finke, R. G. Nanocluster nucleation and growth kinetic and mechanistic studies: A review emphasizing transition-metal nanoclusters. *J. Colloid Interface Sci.* **2008**, *317* (2), 351−374.

18. Yuan, X.; Zhang, B.; Luo, Z. T.; Yao, Q. F.; Leong, D. T.; Yan, N.; Xie, J. P. Balancing the rate of cluster growth and etching for gramscale synthesis of thiolate-protected Au_{25} nanoclusters with atomic precision. *Angew. Chem., Int. Ed.* **2014**, *53* (18), 4623−4627.

19. Levi-Kalisman, Y.; Jadzinsky, P. D.; Kalisman, N.; Tsunoyama, H.; Tsukuda, T.; Bushnell, D. A.; Kornberg, R. D. Synthesis and characterization of $Au_{102}(p\text{-}MBA)_{44}$ nanoparticles. *J. Am. Chem. Soc.* **2011**, *133* (9), 2976−2982.

20. Woehrle, G. H.; Brown, L. O.; Hutchison, J. E. Thiol functionalized, 1.5-nm gold nanoparticles through ligand exchange reactions: Scope and mechanism of ligand exchange. *J. Am. Chem. Soc.* **2005**, *127* (7), 2172−2183.

21. Shibu, E. S.; Muhammed, M. A. H.; Tsukuda, T.; Pradeep, T. Ligand exchange of $Au_{25}SG_{18}$ leading to functionalized gold clusters: Spectroscopy, kinetics, and luminescence. *J. Phys. Chem. C* **2008**, *112* (32), 12168−12176.

22. Liu, X.; Worden, J. G.; Dai, Q.; Zou, J. H.; Wang, J. H.; Huo, Q. Monofunctional gold nanoparticles prepared via a noncovalentinteraction-based solid-phase modification approach. *Small* **2006**, *2* (10), 1126−1129.

23. Dasog, M.; Hou, W.; Scott, R. W. J. Controlled growth and catalytic activity of gold monolayer protected clusters in presence of borohydride salts. *Chem. Commun.* **2011**, *47* (30), 8569−8571.

24. Shivhare, A.; Ambrose, S. J.; Zhang, H. X.; Purves, R. W.; Scott, R. W. J. Stable and recyclable Au_{25} clusters for the reduction of 4- nitrophenol. *Chem. Commun.* **2013**, *49* (3), 276−278.

25. Ansar, S. M.; Arneer, F. S.; Hu, W. F.; Zou, S. L.; Pittman, C. U.; Zhang, D. M. Removal of molecular adsorbates on gold nanoparticles using sodium borohydride in water. *Nano Lett.* **2013**, *13* (3), 1226− 1229.

26. Das, S.; Goswami, A.; Hesari, M.; Al-Sharab, J. F.; Mikmekova, E.; Maran, F.; Asefa, T. Reductive deprotection of monolayer protected nanoclusters: An efficient route to supported ultrasmall Au nanocatalysts for selective oxidation. *Small* **2014**, *10* (8), 1473− 1478.

27. Alvarez, M. M.; Khoury, J. T.; Schaaff, T. G.; Shafigullin, M. N.; Vezmar, I.; Whetten, R. L. Optical absorption spectra of nanocrystal gold molecules. *J. Phys. Chem. B* **1997**, *101* (19), 3706−3712.

28. Zhu, M.; Aikens, C. M.; Hollander, F. J.; Schatz, G. C.; Jin, R. Correlating the crystal structure of a thiol-protected Au_{25} cluster and optical properties. *J. Am. Chem. Soc.* **2008**, *130* (18), 5883−5885.

29. Hasan, M.; Bethell, D.; Brust, M. The fate of sulfur-bound hydrogen on formation of self-assembled thiol monolayers on gold: ^{1}H NMR spectroscopic evidence from solutions of gold clusters. *J. Am. Chem. Soc.* **2002**, *124* (7), 1132−1133.

30. Yu, Y.; Chen, X.; Yao, Q.; Yu, Y.; Yan, N.; Xie, J. Scalable and Precise Synthesis of Thiolated Au_{10-12}, Au_{15}, Au_{18}, and Au_{25} Nanoclusters via pH Controlled CO Reduction. *Chem. Mater.* **2013**, *25* (6), 946−952.

CHAPTER 4

4. Following the Thermal Activation of $Au_{25}(SR)_{18}$ Clusters for Catalysis by X-ray Absorption Spectroscopy

This work has been published in *J. Phys. Chem. C.* Our previous study showed that the catalytic activity of $Au_{25}(SR)_{18}^-$ clusters in solution was directly related to the steric bulk of thiol stabilizers. Based on this, we envisioned that complete removal of thiol stabilizers from the surface of these clusters will further improve the catalytic activity of these clusters. This work describes the effect of the removal of thiol stabilizers from mesoporous carbon supported $Au_{25}(SR)_{18}$ clusters on 4-nitrophenol reduction catalysis. Here, activation of these clusters (removal of thiol stabilizers) was studied by using TEM and EXAFS spectroscopy. EXAFS data show that complete removal of thiol stabilizers takes place at ca. 200^{o}C. Removal of thiol stabilizers was found to be associated with an enhancement in catalytic activity. Further increases in temperature beyond 200^{o}C leads to the sintering of these clusters and this eventually leads to decrease in catalytic activity.

This work has been published in *J. Phys. Chem. C* **2013,** *117* (39), 20007-20016. The author would like to acknowledge the contributions of Daniel M. Chevrier for assisting in extended X-ray absorption fine structure spectroscopy (EXAFS) data interpretation and Dr. Randy W. Purves for assisting in mass spectrometry data collection. The author’s contributions to this article include: synthesis and characterization of various monolayer-protected Au clusters, synthesis of mesoporous carbon supported Au_{25} clusters, EXAFS data collection and interpretation, catalysis experiments, kinetic study, and in the preparation of the manuscript. This manuscript was revised by Dr. Robert Scott prior to publication.

Following the Thermal Activation of $Au_{25}(SR)_{18}$ Clusters for Catalysis by X-ray Absorption Spectroscopy

Atal Shivhare,[1] Daniel M. Chevrier,[2] Randy W. Purves,[3] Robert W. J. Scott[1*]

[1]Department of Chemistry, University of Saskatchewan, 110 Science Place, Saskatoon, SK S7N 5C9, Canada

[2]Department of Chemistry, Dalhousie University, Halifax, NS, Canada

[3]National Research Council of Canada, 110 Gymnasium Place, Saskatoon, SK S7N 0W9, Canada

4.1 Abstract

We show the thermal activation of phenylethanethiolate (L = SC_8H_9) and hexanethiolate (L = SC_6H_{13}) $Au_{25}L_{18}$ monolayer protected clusters (MPCs) on carbon black supports, followed by characterization with extended X-ray absorption fine structure (EXAFS) spectroscopy and transmission electron microscopy (TEM). EXAFS analysis shows that the thiolate stabilizers can be partially removed from the surface under mild heating conditions without significant changes in the cluster size. The resulting clusters are shown to be catalytically active for the reduction catalysis of 4-nitrophenol. EXAFS and TEM data show that thermal treatment under air at 200°C leads to nearly complete removal of all of the thiolate stabilizers with little to no growth in cluster size, while cluster sintering was seen at higher calcination temperatures. The maximum catalytic activity for $Au_{25}(SC_8H_9)_{18}$ MPCs was seen at 250°C activation conditions. These results are consistent with results reported earlier for $Au_{25}(SR)_{18}$ clusters on ceria by Jin *et al.*, who suggested that cluster integrity was maintained during mild activation conditions. Here, EXAFS data unambiguously show that while the cluster size does not grow significantly, such mild heating conditions do lead to nearly complete removal of the thiolate stabilizers.

4.2 Introduction

Achievements in the solution phase synthesis and structural characterization of stable and monodisperse Au monolayer protected clusters (Au_{25}, Au_{38}, Au_{55}, Au_{102}, and Au_{144} MPCs) have been vital for understanding the physical and chemical properties of Au in the nanometer size regime.[1–5] These clusters have been isolated in good yields and have been shown to act as catalysts for a large number of oxidation, reduction, hydrogenation, and electron transfer catalytic reactions.[6–12] Recent single crystal structure studies of thiolate protected Au_{25} and Au_{102} clusters have shown that these clusters have a core-shell type structure, with a highly symmetrical core made up of Au atoms and a shell composed of a small variety of Au-thiolate staple motifs containing alternating Au and S atoms.[13-15] In subsequent studies other clusters were also found to have similar atomic arrangements.[16,17] Theoretical studies attribute the stability of these clusters to superatom electronic theory, where the total number of electrons in these clusters is the number required to form a closed electronic shell, and this eventually results in stable architecture.[18] Several experimental studies suggest that thiolate protected Au_{25} clusters do not lose their structural integrity under exposure to mild oxidative and reductive conditions.[6,11] Other studies have shown that Au_{25} and Au_{55} clusters can survive oxidative etching conditions and remain intact while other clusters decompose under similar conditions.[19,20] There have been reports in the literature on the thermal activation of $Au_{25}(SR)_{18}$ MPCs for benzyl alcohol, carbon monoxide oxidation, and other catalytic reactions.[9,21,22] These interesting findings clearly suggest that there is an exciting opportunity to further explore the use of $Au_{25}(SR)_{18}$ MPCs (and other MPCs) as precursors for the development of near-monodisperse supported-Au nanoparticle catalysts. However, as thiols are thought to passivate the surface of supported-Au catalysts because of the strong bonding between Au and S, more needs to be known about the exact mechanisms upon which thiolates can be removed from MPCs with little or no growth in the underlying core size. Herein, we present an EXAFS study on the thermal activation of $Au_{25}(SC_8H_9)_{18}$ and $Au_{25}(SC_6H_{13})_{18}$ MPCs on mesoporous carbon and show that thiolate removal begins at temperatures as low as 125°C, and nearly complete thiolate removal can be achieved at temperatures beyond 200°C. Remarkably, EXAFS and TEM results show that cluster growth because of sintering is negligible under such mild calcination conditions. Immobilization of nanoparticle catalysts on support materials is important in order to prevent them from sintering, which often leads to a decrease in the catalytic activity. In addition, it is often easier to separate supported catalysts from the reaction mixture after the reaction is over. For example, Jin and coworkers synthesized oxide supported $Au_{25}L_{18}$ MPC catalysts for the chemoselective hydrogenation of α,β unsaturated aldehydes and ketones to unsaturated alcohols.[6] Complete selectivity (100%) was observed with both oxide supported and unsupported catalysts, but higher conversion was obtained in the case of the oxide supported catalyst.[6] Recently it was shown that different oxide supported phenylethanethiolate $Au_{25}L_{18}$ MPCs can be used as a catalyst for carbon monoxide oxidation catalysis where the highest catalytic activity was found in the case of cerium oxide supported catalysts activated at 150°C in an oxygen atmosphere. Experimental data suggested that thiolate stabilizers remained on the surface of Au_{25} clusters and oxidation took place on intact clusters.[21] Tsukuda and coworkers showed that hydroxyapatite supported $Au_{25}L_{18}$ clusters activated at 300°C can be used for the selective oxidation of styrene to styrene epoxide with 100% conversion and 92% selectivity using tert-butyl hydroperoxide as an oxidant.[8] In related work, Gaur *et al.* studied the effect of the thermal treatment on titania-supported dodecanethiolate $Au_{38}SR_{24}$ MPCs and found via EXAFS, TEM, X-ray photoelectron spectroscopy (XPS), and infrared spectroscopy (IR) techniques that thermal treatment at 400°C led to the complete removal of thiolate stabilizers, and subsequently, the catalyst became active for carbon monoxide oxidation catalysis.[12] While complete thiolate removal was observed at 400°C, the effect of low temperature heating on the integrity and catalytic behavior of the Au_{38} clusters was not presented. There have been few studies where an attempt has been made to address the stability of the Au-thiolate bond. Jin and co-workers showed by NMR spectroscopy and mass spectrometry (MS) that two different sulfur-binding modes in glutathione protected Au_{25} MPCs have different oxidative and thermal stability.[23] Especially above a certain temperature, binding mode-1 which is made up of 12-SR ligands that directly attach to 12 atoms gold core was more stable than binding mode-2 in which 6-SR ligands are only attached to 12 atoms gold shell. MS revealed $[Au_{25}SR_{12}]^-$ intermediates as a prominent species during thermal treatment. Data suggested that this $[Au_{25}SR_{12}]^-$ intermediate would form by the loss of 6 thiol molecules which were the part of binding mode-2. Cliffel *et al.* showed with the help of MS that in the case of tiopronin-protected MPCs, cyclic Au-thiolate tetramers ($Au_4(SR)_4$) were seen; this may likely be a decomposition product from similar Au MPC staples (although it was not identified as such in the paper).[24] Other studies have also shown the loss of $Au_4(SR)_4$ units during mass spectrometric analysis.[11,25] These studies suggest that it would be possible to activate $Au_{25}L_{18}$ MPCs for catalysis by removing surface staple motifs and Au cluster growth can be controlled by immobilizing them on support materials before activation.

Herein we show a detailed investigation on the thermal activation of several $Au_{25}(SR)_{18}$ MPCs at various temperatures on mesoporous carbon supports. EXAFS results show that catalytic activation begins at 125°C under air by partially removing thiolate stabilizers from the surface. EXAFS and TEM results show that mild Au cluster sintering is seen at temperatures between 125 and 200°C, while above 200°C rapid Au cluster sintering is seen. We studied nitrophenol reduction catalysis as a model reaction to show that $Au_{25}(SC_8H_9)_{18}$ MPCs supported on mesoporous carbon can be activated for catalysis under mild heating conditions. Catalytic results for the reduction of nitrophenol with sodium borohydride show that the catalytic rate constant increases after 125°C calcination and plateaus at ∼200°C, followed by a decrease in activity for sintered catalysts calcined at 350°C.

4.3 Experimental

4.3.1 Materials

Hydrogen tetrachloroaurate(III) trihydrate ($HAuCl_4 \cdot 3H_2O$, 99.9% on metal basis, Alfa Aesar), tetraoctylammonium bromide (TOAB, 98%, Aldrich), phenylethanethiol (C_8H_9SH, 99%, Acros Organics), 1-hexanethiol ($C_6H_{13}SH$, 97%, Alfa Aesar), sodium borohydride ($NaBH_4$, 98%, EMD), and 4-nitrophenol ($C_6H_5NO_3$, 99%, Alfa Aesar) were used as received. Vulcan XC-72R carbon was purchased from Fuel Cell Store. High purity THF (tetrahydrofuran) and acetonitrile were purchased from Fischer Scientific, and 100% ethanol was purchased from Commercial Alcohols. 18 MΩ cm Milli-Q (Millipore, Bedford, MA) deionized water was used throughout.

4.3.2 Synthesis of Phenylethanethiolate and Hexanethiolate $Au_{25}(SR)_{18}$ MPCs

$Au_{25}(SR)_{18}$ MPCs were synthesized according to the procedure reported previously.[11] Briefly, to the solution of 500 mg of $HAuCl_4 \cdot 3H_2O$ in 50 mL of THF, 1.2 equiv. of TOAB was added. The resulting solution was stirred for 10 min followed by the addition of 5 equiv. of phenylethanethiol or hexanethiol dropwise. This mixture was stirred until the solution became transparent, and then 10 equiv. of $NaBH_4$ in 5 mL of ice cold water was added all at once. The resulting mixture was stirred in air for 4 days. After 4 days the reaction was stopped, and the solvent was evaporated completely. The resulting solid was then washed with a mixture of ethanol/water several times to remove excess leftover thiol, and finally the residue was dried using a rotary evaporator. $Au_{25}(SC_6H_{13})_{18}$ MPCs were extracted with THF, while $Au_{25}(C_8H_9)_{18}$ MPCs were extracted with acetonitrile.

4.3.3 Synthesis of Carbon-Supported $Au_{25}(SR)_{18}$ MPCs

For EXAFS, TGA, and TEM analysis, carbon supported $Au_{25}(SC_8H_9)_{18}$ and $Au_{25}(SC_6H_{13})_{18}$ MPCs were prepared by supporting 3% by metal weight of $Au_{25}(SC_8H_9)_{18}$ and $Au_{25}(SC_6H_{13})_{18}$ MPCs on Vulcan XC-72R carbon. For 4-nitrophenol reduction catalysis the metal loading was maintained at 0.3% by metal weight. A detailed procedure is as follows: first, 100 mg of Vulcan XC-72R carbon was suspended in 25 mL of THF, and the resulting suspension was sonicated for 10 min. To the above suspension, the required amount of $Au_{25}(SR)_{18}$ MPCs in THF was added dropwise, and the resulting mixture was left for stirring under air for 2 h. $Au_{25}(SR)_{18}^-$ clusters from solution get absorbed onto the carbon support because of the presence of hydrophobic stabilizers on the surface of the clusters. After 2 h, the solvent was evaporated first by using a rotary evaporator and finally using a Schlenk line vacuum to ensure complete removal of THF.

4.3.4 Thermal Treatment of Carbon-Supported Au_{25} Clusters

Vulcan XC-72R carbon-supported $Au_{25}(SC_8H_9)_{18}$ and $Au_{25}(SC_6H_{13})_{18}$ MPCs were thermally treated at 125, 150, 200, 250, and 350°C under air for 1.5 h using a Lindberg/Blue M furnace. Heating and cooling rates were maintained at 10°C/ min.

4.3.5 4-Nitrophenol Reduction Catalysis

All reactions were done under a N_2 atmosphere. In a typical catalytic reaction, 7 mg of 4-nitrophenol was dissolved in 25/5 mL mixture of THF/water. To this solution, 7 mg of carbon-supported $Au_{25}(SR)_{18}$ MPCs was added, and the resulting mixture was purged with N_2 for 15 min while stirring. After purging with N_2, 30 equiv. of $NaBH_4$ in 3 mL of ice cold water was added, and immediately after the addition of $NaBH_4$, UV-Vis spectra were recorded. The rate constant of the reaction process was determined by measuring the change in the absorbance of the initially observed peak at 400 nm for 4-nitrophenolate as a function of time. Each reaction was done two times to ensure reproducibility. A control experiment was also carried out with just Vulcan XC-72R carbon, and no catalytic activity was observed.

4.3.6 EXAFS Analysis

EXAFS measurements were conducted at HXMA beamline 061D-1 (energy range 5−30 keV; resolution, 1×10^{-4} ΔE/E) at the Canadian Light Source (CLS, 2.9 GeV storage ring, 250 mA current). All samples were pressed into pellets and measured in transmission mode at room temperature. A double-crystal Si(111) monochromator was employed for energy selection Au L_3-edge (11919 eV). Higher harmonics were eliminated by detuning double-crystal Si(111) by using a Rh-coated 100 nm long KB mirror. The incident and transmission X-ray intensities were detected by ion chambers filled with helium−nitrogen mixtures that were installed in front of and behind of the sample cell. The WinXAS 3.2 software package was used to fit the data. Uncertainties in EXAFS fitting results were computed from off-diagonal elements of the correlation matrix, which were weighted by the square root of the reduced chi-squared value obtained for each simulated fit.[47] The amount of experimental noise was also taken into consideration for each FT-EXAFS spectrum.[47] For the data analysis the amplitude reduction factor (S_0^2) was determined from Au foil and fixed at 0.89 for all remaining fits. For data fitting the k-range was chosen from 3.0 to 12.5 $Å^{-1}$. A $Au_{25}(SC_8H_9)_{18}$ MPCs model was used for the analysis of as synthesized carbon black supported $Au_{25}(SC_8H_9)_{18}$ and $Au_{25}(SC_6H_{13})_{18}$ MPCs,[14] and for thermally activated samples Au-S and Au-Au models were used based on Au_2S and fcc Au unit cell dimensions.[28] Theoretical phase and scattering amplitudes used in EXAFS fitting were obtained for the aforementioned models using the FEFF8.2 program code.[48]

4.3.7 TEM/MALDI/UV−Vis/TGA Analyses

Transmission electron micrographs of original $Au_{25}(SC_8H_9)_{18}$ MPCs and after calcination at 125, 150, 200, and 250°C were obtained on Philips 410 microscope operating at 100 kV, and TEM images of of $Au_{25}(SC_8H_9)_{18}$ MPCs calcined at 350°C were obtained on Philips CM-10 microscope operating at 80 kV. Typically ∼100 nanoparticles were measured to determine average particles sizes. Mass spectrometry analysis was done on an Applied Biosystems 4800 MALDI-TOF/TOF instrument (Frederic, MD) operating in linear positive ion mode using DCTB (trans-2-[3-(4-tert-butylphenyl)-2-methyl-2-propenylidene]malononitrile) as a matrix. A mixture of ubiquitin and insulin was used as an external standard. Absorption spectra were recorded on a Varian Cary 50 Bio UV-Vis spectrometer with an optical path length of 1 cm. Thermal gravimetric analyses (TGA) were performed using a TA Instruments TGA Q5000IR under air flow. Samples were run from 25 to 500°C with a heating rate of 5°C/min.

4.4 Results and Discussion

$Au_{25}(SR)_{18}$ MPCs were characterized by UV-Vis spectroscopy and MS techniques (Figure 4.1). UV-Vis spectra show three major peaks which have been assigned to negatively charged Au_{25} clusters.[26] Mass spectra show molecular ion peaks along with the fragmented peaks and confirm the fact that these clusters are monodisperse MPCs. The second largest fragment peak has been assigned as $Au_{21}(SR)_{14}$, which forms with the loss of Au_4SR_4 unit. According to the literature Au_4SR_4 units exist as a cyclic tetramer but the mechanism behind its formation is unclear.[23]

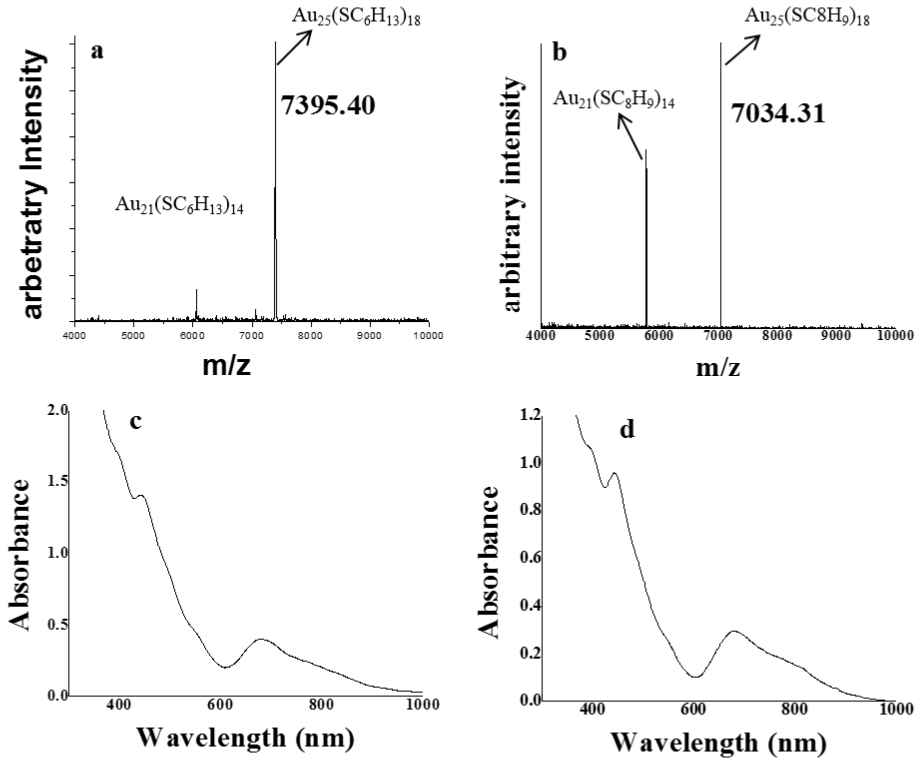

Figure 4.1. UV−Vis and mass spectra of (a, c) phenylethanethiolate and (b, d) hexanethiolate $Au_{25}(SR)_{18}$ MPCs.

4.4.1 EXAFS Analysis of Mesoporous Carbon-Supported Phenylethanethiolate and Hexanethiolate $Au_{25}(SR)_{18}$ MPCs.

A detailed procedure for the synthesis of carbon-supported $Au_{25}(SC_8H_9)_{18}$ and $Au_{25}(C_6H_{13})_{18}$ MPCs is described in the Experimental Section. An inspection of the $Au_{25}(SC_8H_9)_{18}$ crystal structure reveals that Au_{25} cluster is composed of an Au_{13} icosahedron core where the central Au atom is surrounded by 12 gold atoms.[14] This icosahedron core is surrounded by six –S-A-S-Au-S- staple motifs, where sulfur atoms of the staple motifs are directly attached to the 12 gold atoms of the icosahedron core.[14] EXAFS analysis of these supported clusters was done on the Hard X-ray Microanalysis (HXMA) beamline of Canadian Light Source (CLS) via measurements at the Au L_3-edge. We used a multishell fitting approach to fit Au−S and different Au−Au contributions using phenylethanethiolate $Au_{25}L_{18}$ MPCs as a model compound following previously published protocols.[27] In this multishell fitting approach all Au−Au coordination numbers were fixed (using values from calculated coordination numbers)[27] along with the amplitude reduction factor (determined from a Au foil standard), which was fixed at 0.89. Figure 4.2 shows the experimental Fourier transformed EXAFS (FT-EXAFS) and simulated EXAFS fit for as-synthesized $Au_{25}(SC_8H_9)_{18}$ and $Au_{25}(SC_6H_{13})_{18}$ MPCs.

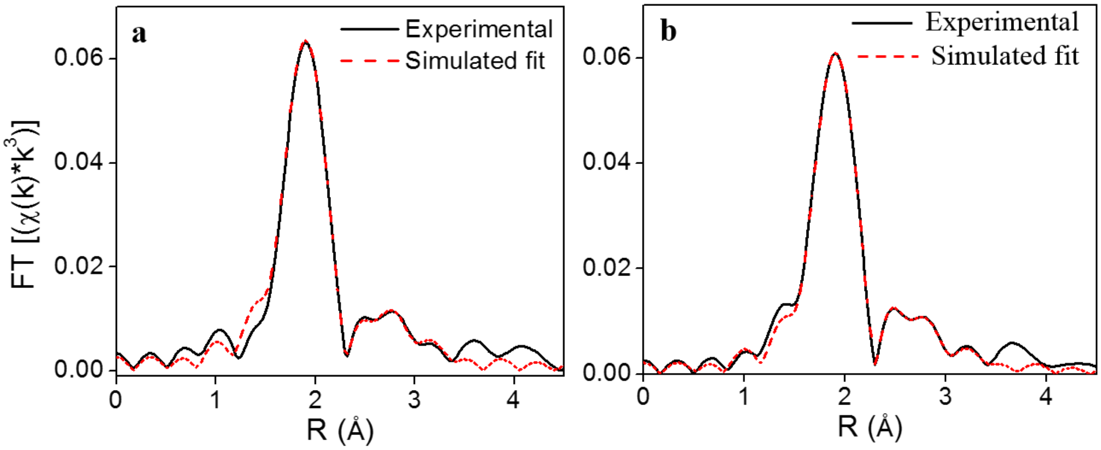

Figure 4.2. Au L_3-edge EXAFS fitting in R-space of as-synthesized (noncalcined) (a) phenylethanethiolate and (b) hexanethiolate $Au_{25}(SR)_{18}$ MPCs on carbon.

The peaks at ca. 1.9 Å show the Au−S contribution, and the following three peaks at approximately 2.4, 2.8, and 3.2 Å show Au-Au contributions in different bonding environments (not phase corrected).[27] EXAFS fitting parameters for $Au_{25}(SC_8H_9)_{18}$ and $Au_{25}(SC_6H_{13})_{18}$ MPCs are shown in Tables 4.1 and 4.2, respectively. The Au−S bond lengths obtained after a two-shell fit were 2.32 and 2.315 Å for $Au_{25}(SC_8H_9)_{18}$ and $Au_{25}(SC_6H_{13})_{18}$ MPCs, respectively. These match very well with literature values of 2.28-2.39 Å.[14] After fitting the Au-S shell separately using two-shell fit, the Au-S parameters were fixed during multishell Au-Au fitting.[27]

Table 4.1. EXAFS Fitting Parameters of As-Synthesized Phenylethanethiolate $Au_{25}(SR)_{18}$ MPCs on Carbon.

	CN	**R/Å**	**σ^2/Å^2**	**E_0 shift/eV**
Au-S	2.0	2.32	0.0053	-0.2
Au-Au (core)	1.44	2.76(2)	0.0079(5)	3(3)
Au-Au (surf)	1.98	3.01(3)	0.0154(2)	3(3)
Au-Au (staple)	2.88	3.3(1)	0.025(5)	3(3)

Table 4.2. EXAFS Fitting Parameters of As-Synthesized Hexanethiolate $Au_{25}(SR)_{18}$ MPCs on Carbon.

	CN	**R/Å**	**σ^2/Å^2**	**E_0 shift/eV**
Au-S	1.8	2.315	0.0044	-0.47
Au-Au (core)	1.44	2.805(4)	0.0072(2)	5.3(7)
Au-Au (surf)	1.98	3.02(1)	0.0129(5)	5.3(7)
Au-Au (staple)	2.88	3.32(2)	0.023(1)	5.3(7)

Au-Au bond lengths of 2.76 Å [$Au_{25}(SC_8H_9)_{18}$ MPCs] and 2.80 Å [$Au_{25}(SC_6H_{13})$ MPCs] arise from the bonding between the central Au atom of the icosahedron core and surrounding 12 surface gold atoms and also the bond lengths between six short Au-Au pairs which exist in the 12 surface gold atoms of icosahedron. Au-Au bond lengths of 3.01 Å (phenylethanethiolate $Au_{25}L_{18}$

MPCs) and 3.02 Å (hexanethiolate $Au_{25}L_{18}$ MPCs) represent the second set of Au-Au pairs present between the 12 surface gold atoms of the icosahedron core with slightly higher bond lengths than the first pair. The third Au-Au bond lengths of 3.3 Å (phenylethanethiolate $Au_{25}L_{18}$ MPCs) and 3.32 Å (hexanethiolate $Au_{25}L_{18}$ MPCs) represent the distance between the surface gold atoms and the staple gold atoms. These values are in very good agreement with the literature values reported for $Au_{25}(SC_8H_9)_{18}$ MPCs.[27] Our multishell EXAFS analysis suggests that $Au_{25}(SC_8H_9)_{18}$ and $Au_{25}(SC_6H_{13})_{18}$ MPCs were successfully transferred from solution to solid carbon supports, and they retained their structural integrity before calcination.

4.4.2 Thermal Treatment of Carbon-Supported Phenylethanethiolate and Hexanethiolate Protected $Au_{25}(SR)_{18}$ MPCs.

$Au_{25}(SC_8H_9)_{18}$ and $Au_{25}(SC_6H_{13})$ MPCs supported on carbon black were thermally treated at different temperatures to study their thermal stability and activation for catalysis. Figure 4.3 shows the Au L_3-edge FT-EXAFS data at calcination temperatures ranging from 125 to 250°C. Beyond 125°C thermal treatments, isolation of different Au-Au bonding environments was not possible via the multishell fitting approach described in the previous section. This is likely because of the fact that Au-thiolate staples start to be removed from the surface and the structural integrity of the $Au_{25}(SR)_{18}$ MPCs was no longer preserved. Thus, only two-shell fits were conducted using 1 Au-Au and 1 Au-S shell using fcc Au and Au_2S as structural models.[28] Simulated EXAFS fits for $Au_{25}(SC_8H_9)_{18}$ MPCs are shown at each temperature in Figure 4.4 with corresponding fit parameters for $Au_{25}(SC_8H_9)_{18}$ and $Au(SC_6H_{13})_{18}$ in Tables 4.3 and 4.4, respectively. For carbon-supported $Au_{25}(SC_8H_9)_{18}$ MPCs, the Au-Au contribution was still very low after heating at 125°C, with a CN of 6.3(5), while the Au-S contribution dropped to 1.11(9) from a value of 2.0 for the pristine $Au_{25}L_{18}$ cluster No significant changes in the EXAFS were seen at calcination temperatures below 125°C; thus, this seems to be the transition temperature where thiolate removal from the gold starts to take place.

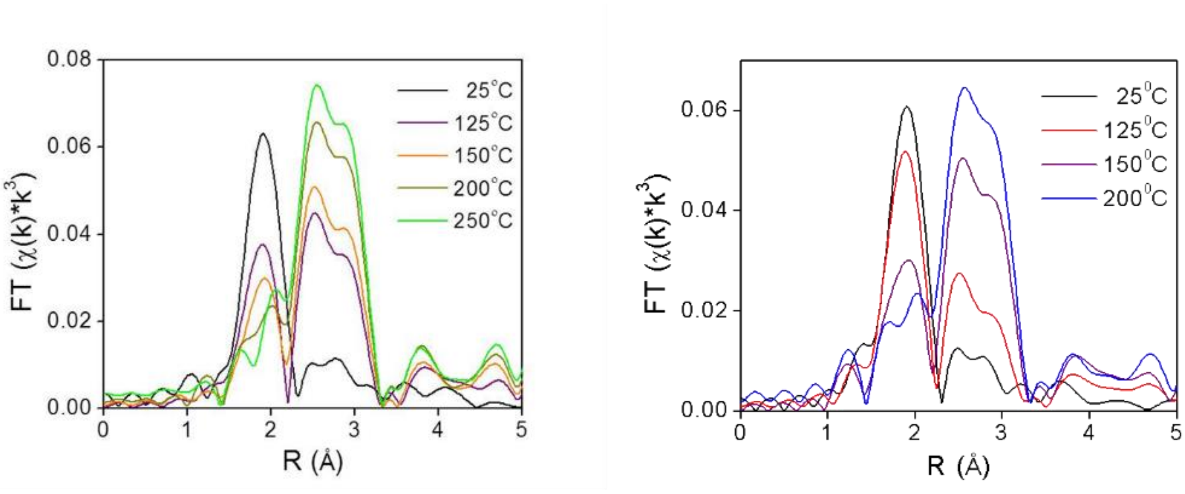

Figure 4.3. Au L_3-edge EXAFS data in R-space of the carbon-supported phenylethanethiolate and hexanethiolate Au_{25} clusters thermally treated at different temperatures: (a) $Au_{25}(SC_8H_9)_{18}$ and (b) $Au_{25}(SC_6H_{13})_{18}$ MPCs.

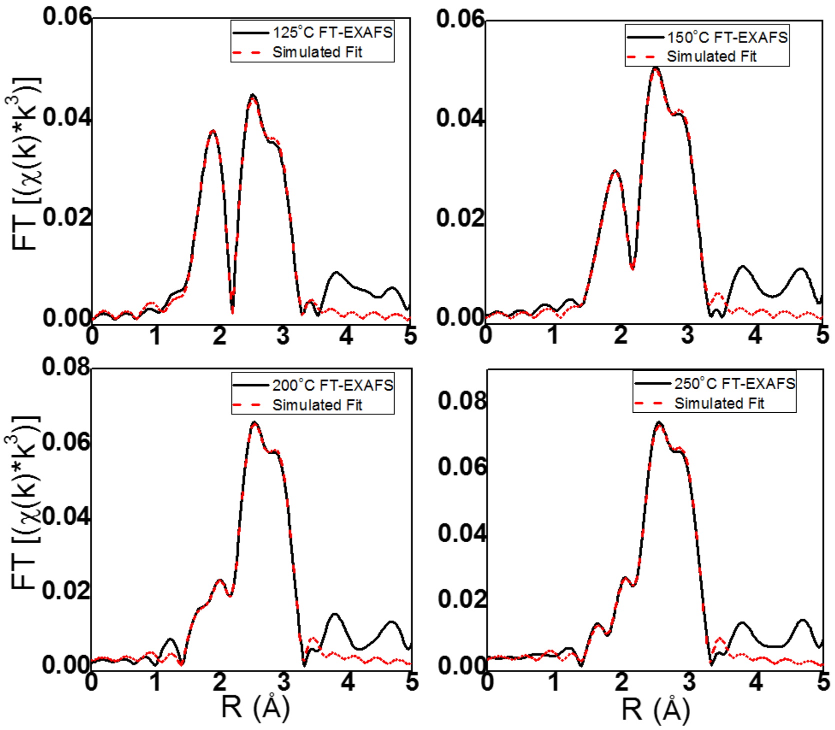

Figure 4.4. EXAFS fitting of carbon-supported $Au_{25}(SC_8H_9)_{18}$ MPCs calcined at (a) 125°C, (b) 150°C, (c) 200°C, and (d) 250°C.

Table 4.3. EXAFS Fitting Parameters of Carbon-Supported Phenylethanethiolate $Au_{25}(SR)_{18}$ MPCs Thermally Treated at Different Temperatures.

T/°C	**CN (Au−S)**	**R/Å (Au−S)**	**σ^2/Å^2 (Au−S)**	**E_0 shift/eV (Au−S)**	**CN (Au−Au)**	**R/Å (Au−Au)**	**σ^2/Å^2 Au−Au)**	**E_0 shift/eV (Au−Au)**
125	1.11(9)	2.325(4)	0.0034(4)	2(1)	6.3(5)	2.848(4)	0.0089(5)	−1.8(7)
150	0.75(9)	2.331(5)	0.0029(7)	0(1)	7.3(8)	2.852(3)	0.0089(5)	−1.8(7)
200	0.63(8)	2.342(8)	0.0043(7)	1(1)	9.3(3)	2.855(2)	0.0088(2)	−0.4(3)
250	0.5(1)	2.33(2)	0.005(2)	3(3)	10.1(5)	2.855(2)	0.0086(3)	−0.5(4)

Table 4.4. EXAFS Fitting Parameters of Carbon Black Supported Hexanethiolate $Au_{25}L_{18}$ MPCs Thermally Treated at Different Temperatures.

T/°C	**CN (Au−S)**	**R/Å (Au−S)**	**σ^2/Å^2 (Au−S)**	**E_0 shift/eV (Au−S)**	**CN (Au−Au)**	**R/Å (Au−Au)**	**σ^2/Å^2 Au−Au)**	**E_0 shift/eV (Au−Au)**
125	1.58(6)	2.315(2)	0.0042(3)	0.2(4)	3.6(3)	2.855(3)	0.0091(5)	0.2(4)
150	1.0(1)	2.329(6)	0.0046(8)	2(1)	6.7(4)	2.857(5)	0.0084(3)	0(1)
200	0.8(2)	2.32(2)	0.007(2)	1(4)	9.0(7)	2.851(5)	0.0085(5)	−1(1)

At a similar calcination temperature, the hexanethiolate MPCs had a significantly lower Au-Au CN of 3.6(3) and a Au-S CN of 1.58(6), which seems to suggest a slightly more thermally stable Au−S bond for this ligand. This data suggests that the Au-S bonds are very vulnerable to decomposition even at low temperature heating, and calcination temperatures of 300°C or beyond are not necessary for catalytic activation of these clusters.[12] A further increase in temperature to 150°C brought further changes in Au-Au and Au-S contributions, and it was found that the Au-S contribution dropped significantly in both cases to 0.75(9) and 1.0(1) for $Au_{25}(SC_8H_9)_{18}$ and

$Au_{25}(SC_6H_{13})_{18}$ MPCs, respectively, while the Au-Au contribution further increased to 7.3(8) and 6.7(4), respectively. The increase in Au-Au contribution suggests that the partial removal of thiolate stabilizer from the Au core took place followed by partial sintering. Further increases in temperature resulted in further increases in the Au-Au contributions and decreases in the Au-S contributions, as the removal of thiolate leads to particle sintering. In addition, a small increase in the Au-S bond lengths upon increasing calcination temperature is seen in both cases, although this increase is not large and may not be significant. In addition, the Debye-Waller parameter (σ^2) increases with higher calcination temperatures for the Au-S bond in both systems, indicating a larger degree of disorder for the samples calcined at higher temperatures. There is little to no increase in the Au-Au bond distance. These results suggest that the structure of $Au_{25}(SR)_{18}$ cluster is very vulnerable to mild heating and thiolate stabilizers can be partially removed with minimal sintering at low temperature.

A TGA analysis of the $Au_{25}(SC_8H_9)_{18}$ MPCs on carbon in air is shown in Figure 4.5. The TGA results show that no significant mass loss is seen from the sample until temperatures of ~150°C, with a major mass loss because of the phenylethanethiol ligands from 150 to 350°C, followed by a second mass loss at temperatures beyond 350°C. The first mass loss is in general agreement with the work of Nie et al.,[21] who showed that although $Au_{25}(SC_8H_9)_{18}$ MPCs on ceria were activated for CO oxidation at temperatures below 150°C, no significant mass loss was seen at these temperatures. However, EXAFS results above definitively show that although the phenylethanethiol is not being removed from the sample at such temperatures, ligands are being removed from the Au clusters; they do not remain completely intact. At this time we believe the second mass loss beyond 350°C is because of the Au-nanoparticle catalyzed oxidation of the carbon support; pure carbon support samples show no significant mass loss in air until temperatures beyond 500°C.

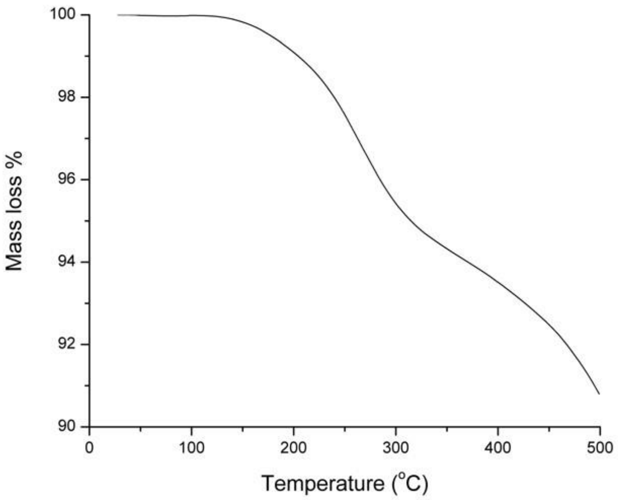

Figure 4.5. TGA analysis of carbon-supported $Au_{25}(SC_8H_9)_{18}$ MPCs in air.

TEM analyses of the samples were performed to monitor cluster size growth and correlate size with EXAFS CN values, as shown in Figure 4.6. It should be noted that it is very difficult to image the clusters at low calcination temperatures and that the limit of resolution (TEM resolution ca. 1 nm) may lead to overestimations of particle sizes. Figure 4.6a shows the TEM image of $Au_{25}(SC_8H_9)_{18}$ MPCs supported on carbon black with the cluster size of 1.3 ± 0.1 nm. After calcining these MPCs at 125°C (Figure 4.6b) the size increased to 1.5 ± 0.2 nm, and was 1.9 ± 1.1 nm at 250°C and eventually 2.1 ± 0.9 nm at 350 °C calcination temperatures. For each sample 20-25 particles were counted. TEM results suggest that fairly constant growth in cluster size occurs when the temperature is increased, which is accompanied by the removal of thiols, as previously revealed from our EXAFS analysis. TEM cluster size analysis suggests that the standard deviations of particle sizes are small at intermediate calcination temperatures, thus suggesting a partial removal of thiols followed by growth as opposed to a more heterogeneous system in which some clusters decompose/sinter while others remain intact. However, we do note that given the resolution limits of TEM, no definitive statements can be made about the absence of un-sintered clusters in any of the samples.

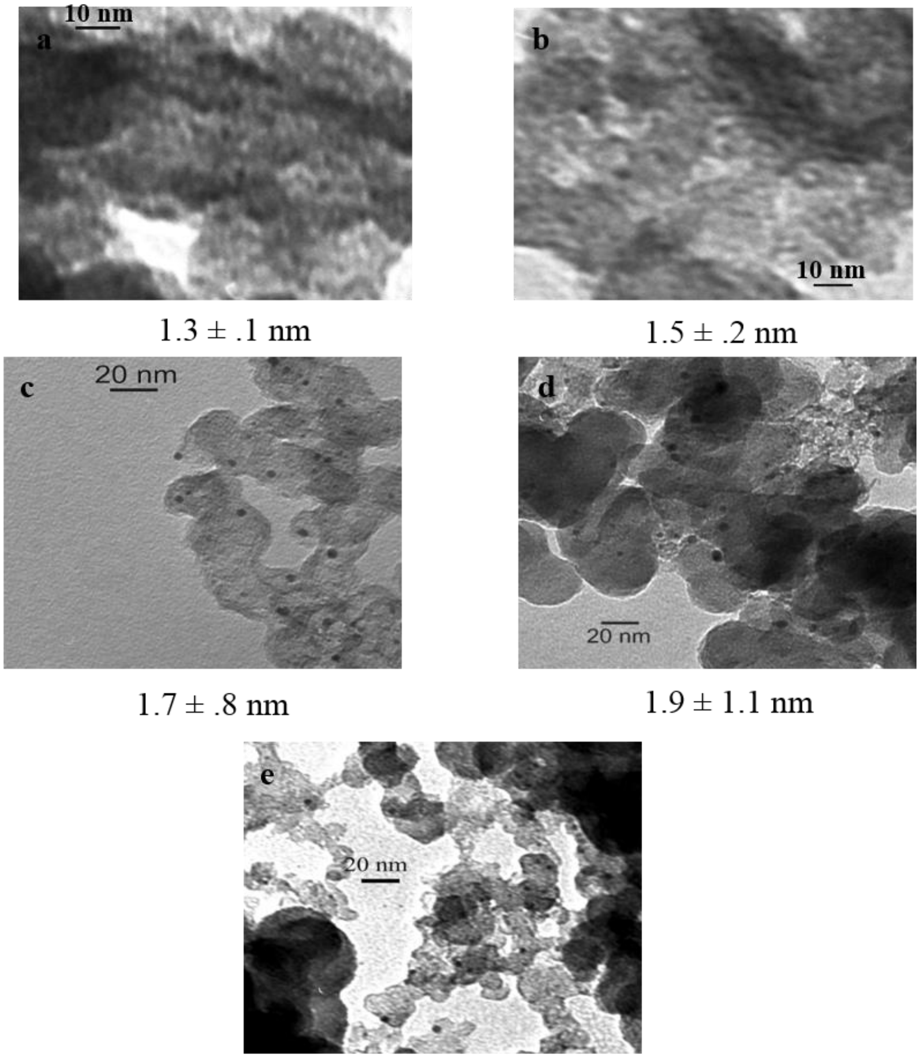

1.3 ± .1 nm

1.5 ± .2 nm

1.7 ± .8 nm

1.9 ± 1.1 nm

2.1 ± .9 nm

Figure 4.6. TEM images of carbon-supported $Au_{25}(SC_8H_9)_{18}$ MPCs: (a) as synthesized and (b) thermally treated at 125, (c) 200, (d) 250, and (e) 350°C.

Figure 4.7 shows the correlation between the number of atoms in the clusters and the average first shell coordination number for different geometries determined using studies reported earlier.[29–31] Analysis of the number of atoms in the clusters using these equations is limited to clusters with closed shells. For clusters with incomplete shells, exact determination of the number of atoms as a function of the coordination number may not be possible, but a general idea about the number of atoms can be obtained by interpolation. It can be seen from Figure 4.7 that there is a constant growth in number of atoms as a function of first shell coordination number. By comparing these values with the CNs obtained from EXAFS fitting results (Tables 4.3 and 4.4), we can say that there is a constant growth in number of atoms and would result in constant growth in the size as revealed by TEM analysis. After 125°C calcination of $Au_{25}(SC_8H_9)_{18}$ and $Au_{25}(SC_6H_{13})_{18}$ MPCs, coordination values obtained from EXAFS analysis were 6.3(5) and 3.6(3), respectively. After correlating these CN values with the number of atoms in the clusters (Figure 4.7), this suggests that the $Au_{25}(SC_8H_9)_{18}$ clusters consist of 15−30 Au atoms after calcination at 125°C.

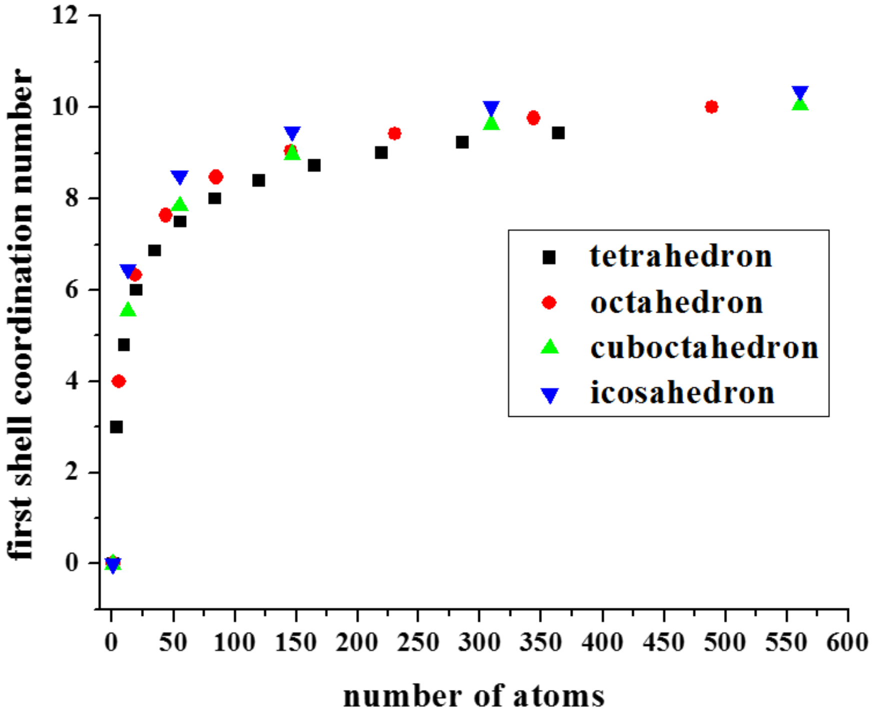

Figure 4.7. Number of atoms in a given cluster as a function of first shell coordination number for different geometries. Data were obtained from refs 29−31.

These low values (particularly that for $Au_{25}(SC_6H_{13})_{18}$) suggest that there may be some Au sample heterogeneity at such intermediate calcination temperatures; further studies are needed to explain if there is any formation of low coordinated Au sites (i.e., from staples which have been removed from the clusters) which leads to low CN values. After heating at 150°C, increases in the Au-Au CN for $Au_{25}(SC_8H_9)_{18}$ MPCs and a significant jump in the Au-Au CN value for $Au_{25}(SC_6H_{13})_{18}$ MPCs were observed. These values suggest further growth in the cluster size as revealed by TEM analysis. Based on the Au−Au CN values obtained at this temperature, the number of atoms in a particle with these CN values could vary from 40 to 80 (Figure 4.7) depending on the shape it adopts. After heating to 200 and 250°C, clusters further grew and eventually started to reflect bulk Au nanoparticles with 500 or more atoms in the particles. These results agree well with TEM results in Figure 4.6 and suggest that the sintering of these MPCs starts to take place beyond ∼200°C because of the fact that surface stabilizers were nearly completely removed from the surface. The combination of EXAFS and TEM data suggests that it is possible to partially remove thiolate stabilizers from the surface of Au_{25} with minimal sintering.

4.4.3 4-Nitrophenol Reduction Catalysis

In 1989, Haruta et al. showed that Au in the nanometer size regime (less than 5 nm) can be used for room temperature carbon monoxide oxidation catalysis.[32] Since then there have been many studies focusing on controlling the size of Au nanoparticles in order to study their size dependent catalytic activity for different oxidation and reduction catalytic reactions.[33−35] Different stabilizers have been used to control the size of gold in nanometer size regime.[36−39] Of all the stabilizers used, alkanethiols have been commonly used because of very strong bonding between gold and sulfur.[38,1−5] However, this strong bonding is also believed to passivate the surface of Au and hence leaves little surface area available for the catalysis to take place.[40,41] This problem can be addressed to some extent by either decreasing the size of the Au MPCs or by using less bulky thiol stabilizers.[6,11] In our previous study we showed that the catalytic activity of thiolate protected Au MPCs for the reduction catalysis of 4-nitrophenol was dependent on the chain length of the thiolate and found that $Au_{25}(SC_8H_9)_{18}$ MPCs had the highest catalytic activity while $Au_{25}(SC_{12}H_{25})_{18}$ MPCs showed the lowest activity.[11]

These results suggested that the access of nitrophenolate to the Au surface was a crucial step, and this was somewhat hindered in the case of larger stabilizers. To further increase the accessibility of nitrophenolate to the surface of Au, we examined the carbon-supported calcined samples described above. We used phenylethanethiolate as a protecting ligand because it gave us the highest catalytic activity in the previous study.[11] The catalyst was prepared by supporting 0.3% by metal weight $Au_{25}(SC_8H_9)_{18}$ MPCs on the carbon support (higher loadings of 3% were used for EXAFS analysis in order to obtain good EXAFS data). A detailed procedure for the preparation of the supported catalyst and the catalytic reaction is described in the Experimental Section. Figure

4.8a shows the UV−vis spectra showing the progress of the catalytic reaction. The peak at 400 nm corresponds to the nitrophenolate peak. This peak decreases with time because of the reduction of nitrophenolate, and a new peak appears at ∼320 nm because of the formation of aminophenol. This data were fit using the pseudo-first-order rate constant equation where time of the reaction was plotted against ln A_0/A, as shown in Figure 4.8b. Here A_0 was the absorbance at time zero and A was the absorbance at time t. Pseudo-first-order rate equation was used because the amount of $NaBH_4$ used in the reaction was in excess, and assumed to be constant during the course of the reaction. The reaction rate was derived by plotting the change in concentration of para-nitrophenol (which is proportional to the absorbance) against time.

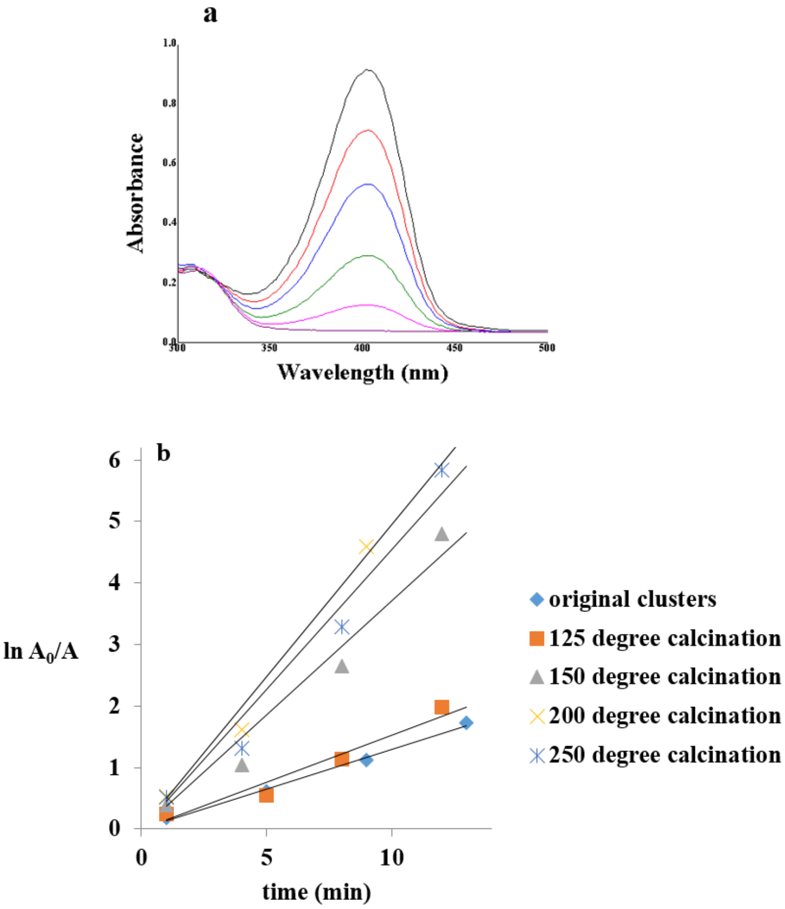

Figure 4.8. (a) Representative UV-Vis spectra showing the progress of the reduction on 4-nitrophenol by a carbon-supported $Au_{25}(SC_8H_9)_{18}$ catalyst and (b) pseudo-first-order rate fitting of the reduction of 4-nitrophenol by carbon-supported $Au_{25}(SC_8H_9)_{18}$ MPC catalysts thermally treated at different temperatures.

Figure 4.9 shows the value of pseudo-first-order rate constant as a function of calcination temperature of the catalyst. The as synthesized (uncalcined) particles on carbon do show some activity (rate constant ca. 0.1 min^{-1}), which is in agreement with previous work.[11] We note that the catalytic amounts in this work are ca. 10 times lower than that used for quasi-homogeneous reactions in early work; thus, the rate constant is somewhat lower.

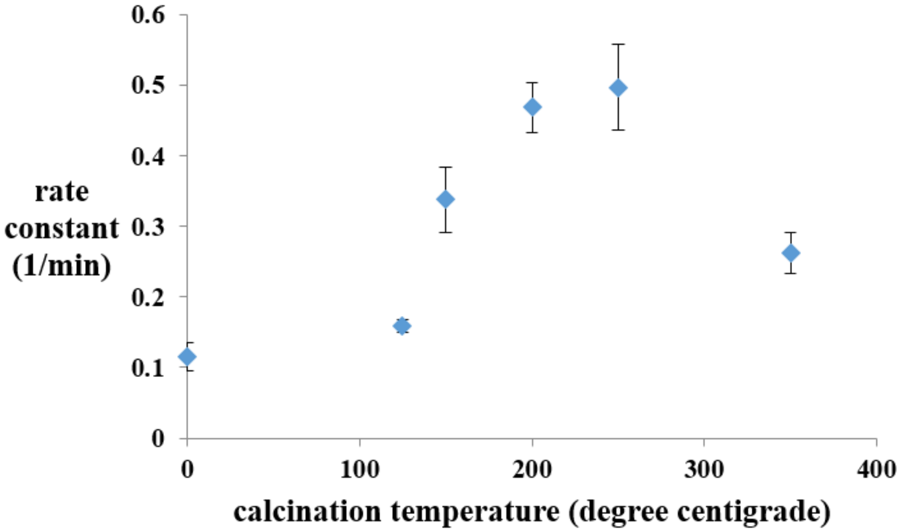

Figure 4.9. Rate constant for the reduction of 4-nitrophenol using carbon-supported $Au_{25}(SC_8H_9)_{18}$ MPC catalysts thermally treated at different temperatures.

Data show that after 125°C calcination the rate constant showed little to no change. A further increase in calcination temperature led to increases in catalytic rate constant, with maximum rate constants of ca. 0.5 min^{-1} seen for calcination at 250°C. Such rates are consistent with literature for unstabilized solid Au nanoparticles in which rates ranging from 0.1 to 1.0 min^{-1} have been reported.[42–46] Much lower rates were seen at the higher calcination temperature of 350°C, likely because of particle sintering occurring at this temperature. These results suggest that complete thiolate removal is not necessary for catalytic activity in this system. Data suggest that there are two factors that affect the catalytic activity: the first is the removal of the thiol, and the other is the growth of the clusters via sintering. Our previous study showed that as we increased the steric bulk around the Au_{25} clusters by increasing the chain length of the stabilizers, the catalytic rate constant decreased. It suggests that steric factors are an important factor to be taken into consideration when attempting to modify the catalytic activity. On the basis of this evidence, we can speculate that the enhancement in the catalytic activity would be mainly because of the removal of the thiolate stabilizers. This was further supported by a decrease in rate constant because of sintering when the catalyst was calcined at 350°C.

4.5 Conclusion

In summary, we have shown that $Au_{25}(SC_8H_9)_{18}$ and $Au_{25}(SC_6H_{13})_{18}$ MPCs can be supported on carbon supports and activated for catalysis without significantly affecting the structural integrity of the MPCs. These MPCs were thermally activated for 4-nitrophenol reduction catalysis by removing thiolate stabilizers from the surface. EXAFS analysis shows that the thiolate removal from the surface starts to take place at 125°C which was evident by the decrease in Au-S contribution, increase in Au-Au contribution, and nearly complete thiol removal at 250°C where the highest catalytic activity was observed. Further heating at 350°C led to a decrease in the rate constant because of Au cluster sintering. Data also indicated that thiolate removal was accompanied by minimal growth in the cluster size as supported by TEM and EXAFS studies. It also suggests that the access of the nitrophenolate species to the surface of the Au cluster is extremely important for the catalysis to take place, and that this can be achieved by partially removing thiolates at intermediate calcination temperatures. In the future, we will focus on studying the activation of these MPCs on oxide supports for oxidation and reduction catalysis, and correlating the activation conditions to the catalytic activity.

Acknowledgements

The authors acknowledge financial assistance from the National Sciences and Engineering Research Council of Canada (NSERC) and thank Ning Chen at the Canadian Light Source for assistance with XAS measurements. We also acknowledge the very helpful assistance of Mahdi Hesari and Mark Workentin at Western University with $Au_{25}L_{18}$ synthesis and purification. EXAFS experiments described in this paper was performed at the Canadian Light Source, which is supported by the Natural Sciences and Engineering Research Council of Canada, the National Research Council Canada, the Canadian Institutes of Health Research, the Province of Saskatchewan, Western Economic Diversification Canada, and the University of Saskatchewan.

4.6 References

1. Donkers, R. L.; Lee, D.; Murray, R. W., Synthesis and Isolation of the Molecule-like Cluster $Au_{38}(PhCH_2CH_2S)_{24}$. *Langmuir* **2004**, *20* (5), 1945−1952.

2. Lotz, A. R.; Froba, M., Synthesis and Characterization of Au_{55} Clusters Within Mesoporous Silica. *Z. Anorg. Allg. Chem.* **2005**, *631* (13-14), 2800−2805.

3. Zhu, M.; Lanni, E.; Garg, N.; Bier, M. E.; Jin, R., Kinetically Controlled, High-Yield Synthesis of Au_{25} Clusters. *J. Am. Chem. Soc.* **2008**, *130* (4), 1138−1139.

4. Levi-Kalisman, Y.; Jadzinsky, P. D.; Kalisman, N.; Tsunoyama, H.; Tsukuda, T.; Bushnell, D. A.; Kornberg, R. D., Synthesis and Characterization of $Au_{102}(p\text{-}MBA)_{44}$ Nanoparticles. *J. Am. Chem. Soc.* **2011**, *133* (9), 2976−2982.

5. Qian, H.; Jin, R., Ambient Synthesis of $Au_{144}(SR)_{60}$ Nanoclusters in Methanol. *Chem. Mater.* **2011**, *23* (8), 2209−2217.

6. Zhu, Y.; Qian, H.; Drake, B. A.; Jin, R., Atomically Precise $Au_{25}(SR)_{18}$ Nanoparticles as Catalysts for the Selective Hydrogenation of α,β-Unsaturated Ketones and Aldehydes. *Angew. Chem., Int. Ed.* **2010**, *49* (7), 1295−1298.

7. Gao, W.; Chen, X. F.; Li, J. C.; Jiang, Q., Is Au_{55} or Au_{38} Cluster a Threshold Catalyst for Styrene Epoxidation? *J. Phys. Chem. C* **2010**, *114* (2), 1148−1153.

8. Liu, Y.; Tsunoyama, H.; Akita, T.; Tsukuda, T., Efficient and Selective Epoxidation of Styrene with TBHP Catalyzed by Au_{25} Clusters on Hydroxyapatite. *Chem. Commun.* **2010**, *46* (4), 550−552.

9. Xie, S.; Tsunoyama, H.; Kurashige, W.; Negishi, Y.; Tsukuda, T., Enhancement in Aerobic Alcohol Oxidation Catalysis of Au_{25} Clusters by Single Pd Atom Doping. *ACS Catal.* **2012**, *2* (7), 1519−1523.

10. Antonello, S.; Hesari, M.; Polo, F.; Maran, F., Electron Transfer Catalysis with Monolayer Protected Au_{25} Clusters. *Nanoscale* **2012**, *4* (3), 5333−5342.

11. Shivhare, A.; Ambrose, S. J.; Zhang, H.; Purves, R. W.; Scott, R. W. J., Stable and Recyclable Au_{25} Clusters for the Reduction of 4- Nitrophenol. *Chem. Commun.* **2013**, *49* (3), 276−278.

12. Gaur, S.; Miller, J. T.; Stellwagen, D.; Sanampudi, A.; Kumar, C. S. S. R.; Spivey, J. J., Synthesis, Characterization, and Testing of Supported Au Catalysts Prepared from Atomically-Tailored $Au_{38}(SC_{12}H_{25})_{24}$ Clusters. *Phys. Chem. Chem. Phys.* **2012**, *14* (5), 1627− 1634.

13. Jadzinsky, P. D.; Calero, G.; Ackerson, C. J.; Bushnell, D. A.; Kornberg, R. D., Structure of a Thiol Monolayer-Protected Gold Nanoparticle at 1.1 Å Resolution. Science 2007, 318, 430−433.

14. Zhu, M.; Aikens, C. M.; Hollander, F. J.; Schatz, G. C.; Jin, R., Correlating the Crystal Structure of a Thiol-Protected Au_{25} Cluster and Optical Properties. *J. Am. Chem. Soc.* **2008**, *130* (18), 5883−5885.

15. Heaven, M. W.; Dass, A.; White, P. S.; Holt, K. M.; Murray, R. W., Crystal Structure of the Gold Nanoparticle $[N(C_8H_{17})_4]^+$ $[Au_{25}(SCH_2CH_2Ph)_{18}]^-$. *J. Am. Chem. Soc.* **2008**, *130* (12), 3754−3755.

16. MacDonald, M. A.; Zhang, P.; Chen, N.; Qian, H.; Jin, R., Solution-Phase Structure and Bonding of $Au_{38}(SR)_{24}$ Nanoclusters from X-Ray Absorption Spectroscopy. *J. Phys. Chem. C* **2011**, *115* (1), 65− 69.

17. Lopez-Acevedo, O.; Akola, J.; Whetten, R. L.; Grö nbeck, H.; Hakkinen, H., Structure and Bonding in the Ubiquitous Icosahedral¨Metallic Gold Cluster $Au_{144}(SR)_{60}$. *J. Phys. Chem. C* **2009**, *113* (13), 5035− 5038.

18. Walter, M.; Akola, J.; Lopez-Acevedo, O.; Jadzinsky, P. D.; Calero, G.; Ackerson, C. J.; Whetten, R. L.; Grönbeck, H.; Häkkinen, H., A Unified View of Ligand-Protected Gold Clusters as Superatom Complexes. *Proc. Natl. Acad. Sci. U. S. A.* **2008**, *105* (27), 9157−9162.

19. Shichibu, Y.; Negishi, Y.; Tsunoyama, H.; Kanehara, M.; Teranishi, T.; Tsukuda, T., Extremely High Stability of GlutathionateProtected Au_{25} Clusters Against Core Etching. *Small* **2007**, *3* (5), 835− 839.

20. Boyen, H. G.; Kastle, G.; Weigl, F.; Koslowski, B.; Dietrich, C.;¨Ziemann, P.; Spatz, J. P.; Riethmüller, S.; Hartmann, C.; Möller, M.; Schmid, G.; Garnier, M. G.; Oelhafen, P., Oxidation-Resistant Gold-55 Clusters. *Science* **2002**, *297* (5586), 1533−1536.

21. Nie, X.; Qian, H.; Ge, Q.; Xu, H.; Jin, R., CO Oxidation Catalyzed by Oxide-Supported $Au_{25}(SR)_{18}$ Nanoclusters and Identification of Perimeter Sites as Active Centers. *ACS Nano* **2012**, *6* (7), 6014−6022.

22. Gao, L.; Jin, R., Atomically Precise Gold Nanoclusters as New Model Catalyst. *Acc. Chem. Res.* **2013**, *46* (8), 1749−1758.

23. Wu, Z.; Jin, R., Stability of the Two Au-S Binding Modes in $Au_{25}(SG)_{18}$ Nanoclusters Probed by NMR and Optical Spectroscopy. *ACS Nano* **2009**, *3* (7), 2036−2042.

24. Gies, A. P.; Hercules, D. M.; Gerdon, A. E.; Cliffel, D. E., Electrospray Mass Spectrometry Study of Tiopronin Monolayer Protected Gold Nanoclusters. *J. Am. Chem. Soc.* **2007**, *129* (5), 1095− 1104.

25. Dass, A.; Stevenson, A.; Dubay, G. R.; Tracy, J. B.; Murray, R. W., Nanoparticle MALDI-TOF Mass Spectrometry Without Fragmentation: $Au_{25}(SCH_2CH_2Ph)_{18}$ and Mixed Monolayer $Au_{25}(SCH_2CH_2Ph)_{18-x}(L)_x$. J. Am. Chem. Soc. **2008**, *130* (18), 5940−5946.

26. Zhu, M.; Eckenhoff, W. T.; Pintauer, T.; Jin, R., Conversion of Anionic $[Au_{25}(SCH_2CH_2Ph)_{18}]^-$ Cluster to Charge Neutral Cluster via Air Oxidation. *J. Phys. Chem. C* **2008**, *112* (37), 14221−14224.

27. MacDonald, M. A.; Chevrier, D. M.; Zhang, P.; Qian, H.; Jin, R., The Structure and Bonding of $Au_{25}(SR)_{18}$ Nanoclusters from EXAFS: The Interplay of Metallic and Molecular Behavior. *J. Phys. Chem. C* **2011**, *115* (31), 15282−15287.

28. Simms, G. A.; Padmos, J. D.; Zhang, P., Structural and Electronic Properties of Protein/Thiolate-Protected Gold Nanocluster with “Staple” Motif: A XAS, L-DOS, and XPS Study. *J. Chem. Phys.* **2009**, *131* (21), 214703.

29. Fritsche, H. G.; Benfield, R. E., Exact Analytical Formulas for Mean Coordination Numbers in Clusters. *Z. Phys. D: At., Mol. Clusters* **1993**, *26*, S15−S17.

30. Jentys, A., Estimation of Mean Size and Shape of Small Metal Particles by EXAFS. *Phys. Chem. Chem. Phys.* **1999**, *1* (17), 4059−4063.

31. Benfield, R. E., Mean Coordination Numbers and the Nonmetal-Metal Transition in Clusters. *J. Chem. Soc., Faraday Trans.* **1992**, *88* (8), 1107−1110.

32. Haruta, M.; Yamada, N.; Kobayashi, T.; Iijima, S., Gold Catalysts Prepared by Coprecipitation for Low-Temperature Oxidation of Hydrogen and of Carbon-Monoxide. *J. Catal.* **1989**, *115* (2), 301−309.

33. Fenger, R.; Fertitta, E.; Kirmse, H.; Thünemann, A. F.; Rademann, K., Size Dependent Catalysis with CTAB-Stabilized Gold Nanoparticles. *Phys. Chem. Chem. Phys.* **2012**, *14* (26), 9343−9349.

34. Laoufi, I.; Saint-Lager, M.-C.; Lazzari, R.; Jupille, J.; Robach, O.; Garaudee, S.; Cabailh, G.; Dolle, P.; Cruguel, H.; Bailly, A., Size and´ Catalytic Activity of Supported Gold Nanoparticles: An in Operando Study During CO Oxidation. *J. Phys. Chem. C* **2011**, *115* (11), 4673−4679.

35. Valden, M.; Lai, X.; Goodman, D. W., Onset of Catalytic Activity of Gold Clusters on Titania with the Appearance of Nonmetallic Properties. *Science* **1998**, *281* (5383), 1647−1650.

36. Zhao, L.; Jiang, D.; Cai, Y.; Ji, X.; Xie, R.; Yang, W., Tuning the Size of Gold Nanoparticles in the Citrate Reduction by Chloride Ions. *Nanoscale* **2012**, *4* (16), 5071−5076.

37. Krommenhoek, P. J.; Wang, J.; Hentz, N.; Johnston-Peck, A. C.; Kozek, K. A.; Kalyuzhny, G.; Tracy, J. B., Bulky Adamantanethiolate and Cyclohexanethiolate Ligands Favor Smaller Gold Nanoparticles with Altered Discrete Sizes. *ACS Nano* **2012**, *6* (6), 4903−4911.

38. Debnath, D.; Kim, S. H.; Geckeler, K. E., The First Solid-Phase Route to Fabricate and Size-Tune Gold Nanoparticles at Room Temperature. *J. Mater. Chem.* **2009**, *19* (46), 8810−8816.

39. Wu, S.-H.; Tseng, C.-T.; Lin, Y.-S.; Lin, C.-H.; Hung, Y.; Mou, C.-Y., Catalytic Nano-Rattle of Au@hollow Silica: Towards a Poison Resistant Nanocatalyst. *J. Mater. Chem.* **2011**, *21* (3), 789−794.

40. Della Pina, C.; Falletta, E.; Rossi, M.; Sacco, A., Selective Deactivation of Gold Catalyst. *J. Catal.* **2009**, *263* (1), 92−97.

41. Huang, X.; Li, B.; Zhang, H.; Hussain, I.; Liang, L.; Tan, B., Facile Preparation of Size-Controlled Gold Nanoparticles Using Versatile and End-Functionalized Thioether Polymer Ligands. *Nanoscale* **2011**, *3* (4), 1600−1607.

42. Lee, J.; Park, J. C.; Song, H., A Nanoreactor Framework of a Au@SiO_2 Yolk/Shell Structure for Catalytic Reduction of p-Nitrophenol. *Adv. Mater.* **2008**, *20* (8), 1523−1528.

43. Rashid, M. H.; Mandal, T. K., Templateless Synthesis of Polygonal Gold Nanoparticles: An Unsupported and Reusable Catalyst with Superior Activity. *Adv. Funct. Mater.* **2008**, *18* (15), 2261− 2271.

44. Zeng, J.; Zhang, Q.; Chen, J.; Xia, Y. A., Comparison Study of the Catalytic Properties of Au-Based Nanocages, Nanoboxes, and Nanoparticles. *Nano Lett.* **2010**, *10* (1), 30−35.

45. Ismail, A. A.; Hakki, A.; Bahnemann, D. W., Mesostructure Au/TiO_2 Nanocomposites for Highly Efficient Catalytic Reduction of p-Nitrophenol. *J. Mol. Catal. A: Chem.* **2012**, *358*, 145−151.

46. Yamamoto, H.; Yano, H.; Kouchi, H.; Obora, Y.; Arakawa, R.; Kawasaki, H., N,N-Dimethylformamide-Stabilized Gold Nanoclusters as a Catalyst for the Reduction of 4-Nitrophenol. *Nanoscale* **2012**, *4* (14), 4148−4154.

47. Newville, M.; Boyanov, B. I.; Sayers, D. E., Estimation of Uncertainties in XAFS Data. *J. Synchrotron Radiat.* **1999**, *6*, 264−265.

48. Ankudinov, A. L.; Ravel, B.; Rehr, J. J.; Conradson, S. D., Real Space Multiple-Scattering Calculation and Interpretation of X-Ray Absorption Near-Edge Structure. *Phys. Rev. B* **1998**, *58* (12), 7565−7576.

CHAPTER 5

5. Following the Thermal and Chemical Removal of Thiolate Stabilizers from Supported Au Clusters using X-ray Absorption Spectroscopy

In the previous study, I studied the thermal activation of $Au_{25}(SR)_{18}$ clusters for 4-nitrophenol reduction catalysis. While $Au_{25}(SR)_{18}$ clusters were found to show maximum catalytic activity at 200^{o}C temperatures, further increases in calcination temperature led to cluster sintering and a decrease in catalytic activity. In the present study, we have studied the activation of Al_2O_3-supported $Au_{25}(SC_8H_9)_{18}$ clusters using alternative chemical routes with little to no growth in cluster size. Here, BH_4^- reducing agents were used in order to remove thiol stabilizers from the surface of Al_2O_3-supported $Au_{25}(SR)_{18}$ clusters. The resulting changes in cluster size and structure after BH_4^- treatments were studied by using TEM and EXAFS spectroscopy.

This chapter is a manuscript in preparation which will soon be submitted. All the experimental work in this paper has been done by myself along with the manuscript writing and editing.

Following the Thermal and Chemical Removal of Thiolate Stabilizers from Supported Au Clusters using X-ray Absorption Spectroscopy

Atal Shivhare and Robert W. J. Scott*

Department of Chemistry, University of Saskatchewan, 110 Science Place, Saskatoon, SK S7N 5C9, Canada

5.1 Abstract

Al_2O_3-supported $Au_{25}(SC_8H_9)_{18}$ clusters with various Au loadings were thermally and chemically treated in order to determine the most efficient method towards the removal of thiolate stabilizers while avoiding unwanted increases in cluster size because of agglomeration and sintering. X-ray absorption spectroscopy (XAS) and transmission electron microscopy (TEM) were used to investigate samples before and after thermal and chemical treatments. Results show that while 250°C thermal treatment leads to nearly complete removal of thiolate stabilizers, it comes with a concomitant increase in cluster size as sintering becomes problematic. In contrast, chemical reduction treatments using borohydride reducing agents does not lead to significant growth in cluster size, but only allows for partial thiolate removal. These results are important as many researchers look to determine optimal activation conditions for ultra-monodisperse Au and bimetallic clusters for use as model catalysts without altering their original structures.

5.2 Introduction

Au clusters, owing to their stability and well-defined structures, have recently emerged as an important class of materials in order to study the size and structure related properties of Au nanocatalysts.[1-3] Among all existing Au clusters, $Au_{25}(SR)_{18}$ clusters have gained special attention because of their high yield syntheses and exceptional stability.[4-6] Recently, several research groups have shown that $Au_{25}(SR)_{18}$ clusters in solution and on various support materials can act as catalysts for a variety of catalytic reactions such as CO oxidation, hydrogenation of nitrobenzene and its derivatives, styrene oxidation, semi-hydrogenation of terminal alkynes, and alcohol oxidation.[7-13] In many of these studies, the catalytic activity of Au clusters has been found to be affected by the steric bulk of the thiolate stabilizers, and a positive effect on the catalytic activity was found upon removal of the stabilizers. Removal of thiolate stabilizers has been mostly carried out by calcining these clusters at moderate temperatures, which leads to the partial or complete removal of thiolate stabilizers. For example; Tsukuda and coworkers found that thermal activation of porous carbon supported $Au_{25}(SR)_{18}$ clusters at 450^{o}C led to an enhancement in the catalytic activity and selectivity for benzyl alcohol oxidation.[7] Jin and coworkers found that CeO_2-supported Au_{25} clusters can be activated for CO oxidation catalysis by partially removing thiolate stabilizers at 150^{o}C.[11] Our group reported that mesoporous carbon-supported Au_{25} clusters can be thermally activated for p-nitrophenol reduction catalysis by removing thiolate stabilizers at temperatures as low as 125^{o}C.[10]

While the effect of temperature on the removal of thiolate stabilizers from supported Au_{25} clusters for catalysis has been studied by a number of groups, the effect of chemical reducing agents on the removal of thiolate stabilizers from supported Au clusters has not been studied much. This is despite the presence of literature reports suggesting that borohydride species can reductively desorb thiolate stabilizers from the surface of thiolate-protected Au nanoparticles in solution.[14-15] Recently Asefa and coworkers showed that BH_4^- treatment of supported thiolate-protected Au_{25} and Au_{144} clusters led to an enhancement in the catalytic activity for styrene oxidation and this enhancement was attributed to the partial removal of thiolate stabilizers after BH_4^- treatment.[12]

Herein, we document a detailed investigation of the removal of thiolate stabilizers from supported $Au_{25}(SC_8H_9)_{18}$ clusters with various Au loadings using thermal and chemical strategies using X-ray Absorption Spectroscopy (XAS) and TEM particle size analyses. Thermal treatment of supported $Au_{25}(SC_8H_9)_{18}$ clusters at 250°C leads to nearly complete removal of thiolate stabilizers, albeit with a concomitant growth in cluster size. Treatment using various hydride reducing agents; however, did not lead to significant growth in cluster size, but only leads to partial thiolate removal. Our data show that very distinct features in the X-ray absorption near edge (XANES) and extended X-ray absorption fine structure (EXAFS) spectra can be used to follow the thiolate removal process from supported $Au_{25}(SC_8H_9)_{18}^-$ clusters and associated changes in cluster size during thermal and chemical treatments. To the best of our knowledge, this is the first study showing EXAFS evidence of the removal of thiolate stabilizers from supported $Au_{25}(SC_8H_9)_{18}$ clusters using borohydride reducing agents.

5.3 Experimental

5.3.1 Materials

Hydrogen tetrachloroaurate(III) trihydrate ($HAuCl_4 \cdot 3H_2O$, 99.9% on metal basis, Alfa Aesar), tetraoctylammonium bromide (TOAB, 98%, Aldrich), phenylethanethiol (C_8H_9SH, 99%, Acros Organics), sodium borohydride ($NaBH_4$, 98%, EMD), and aluminum oxide (Al_2O_3, 58 Å, ~150 mesh) were used as received. High purity acetonitrile was purchased from Fischer Scientific. High purity tetrahydrofuran was purchased from EMD and 100% ethanol was purchased from Commercial Alcohols. 18 MΩ cm Milli-Q (Millipore, Bedford, MA) deionized water was used throughout.

5.3.2 Synthesis of $Au_{25}(SC_8H_9)_{18}^-$ clusters

Synthesis of $Au_{25}(SC_8H_9)_{18}$ clusters is reported elsewhere.[4] Briefly, 500 mg of $HAuCl_4 \cdot 3H_2O$ in 50 mL of THF was mixed with 1.2 equiv. of TOAB. To this solution, 5 equiv. of phenylethanethiol was added dropwise and the mixture was left for stirring till it became clear. Subsequently, 10 equiv. of $NaBH_4$ in 10 mL of ice cold water was added all at once. Resulting solution was stirred for four days. After four days, the reaction was stopped and the solvent was evaporated completely. The resulting solid was then washed with a mixture of ethanol/water several times to remove excess leftover thiol and disulfide species, and finally the residue was dried using a rotary evaporator. The resulting $Au_{25}(SC_8H_9)_{18}$ clusters were extracted with acetonitrile.

5.3.3 TEM analysis

Transmission electron micrographs (TEM) were taken with a HT7700 TEM operating at 100 kV. TEM grids were prepared by placing a drop of sample suspended in hexane on graphene-enhanced lacey carbon TEM grids (Electron Microscopy Sciences).

5.3.4 Sample preparation for EXAFS measurements

All samples used for EXAFS analysis were prepared by supporting phenylethanethiol-protected Au_{25} clusters with different loadings, 2.5%, 1.5%, 0.75%, and 0.2% by metal weight on Al_2O_3 support (58 Å, ~150 mesh) using a wetness impregnation approach.

5.3.5 Thermal and hydride treatment

200 mg of supported $Au_{25}(SC_8H_9)_{18}^-$ clusters with different metal loadings were treated at 250^oC under air atmosphere for 90 minutes. Treatment with $LiAlH_4$ and $LiBH_4$ was carried out by suspending 100 mg of supported samples in 5mL of hexane, followed by the addition of 70 equiv. of $LiAlH_4$ and $LiBH_4$ with respect to $Au_{25}(SC_8H_9)_{18}^-$ clusters. These solutions were stirred for 10 minutes and subsequently washed with hexane and water. Treatment with $NaBH_4$ was carried out by first intimately mixing 100 mg of supported samples and 3500 equiv. of $NaBH_4$ with respect to $Au_{25}(SC_8H_9)_{18}^-$ clusters. To this mixture was then added 5 mL of deionized water and resulting mixture was allowed to stir for 20 minutes. After that, the resulting solid was washed with excess of water and dried under vacuum.

5.3.6 EXAFS measurements and analysis

EXAFS measurements were conducted at the Hard X-ray MicroAnalysis (HXMA) beamline 061D-1 (energy range 5−30 keV; resolution, 1×10^{-4} ΔE/E) of the Canadian Light Source (CLS, 2.9 GeV storage ring, 250 mA current). Samples was pressed into pellets and measured in transmission (2.5% and 1.5% loadings by metal weight) and fluorescence (0.75 and 0.2% loadings by metal weight) modes by measuring the Au L_3-edge. A double-crystal Si (111) was employed for energy selection. Higher harmonics were eliminated by detuning double-crystal using a Rh coated KB mirrors for Au L_3-edge. The incident and transmission X-ray intensities were detected by ion chambers filled with helium−nitrogen mixtures for transmission measurements, and a 32 element detector was used for fluorescence measurements. The IFEFFIT software package was used for data processing.[16] For the data analysis, the amplitude reduction factor, S_0^2, was found from fitting Au foil and subsequently fixed at 0.90. For EXAFS data fitting, a standard $Au_{25}L_{18}$ crystal structure was using in order to fit the as-synthesized, $LiAlH_4$ and $LiBH_4$ treated samples,[10] Au face centered cubic (fcc) and AuS models were used to fit thermally-treated and $NaBH_4$-treated samples.

5.4 Result and Discussion

Figure 5.1 is the EXAFS fitting in *R*-space of Al_2O_3-supported $Au_{25}(SC_8H_9)_{18}$ clusters with 2.5% loading by Au weight in R space. The data shows one major peak at *ca*. 2 Å because of the scattering of photoelectrons from neighboring sulphur atoms along with three much smaller Au-Au peaks (~ 2.2-3.2 Å), which have been shown by Zhang and coworkers because of different Au-Au bonding pairs present within Au_{25} clusters.[10,17]

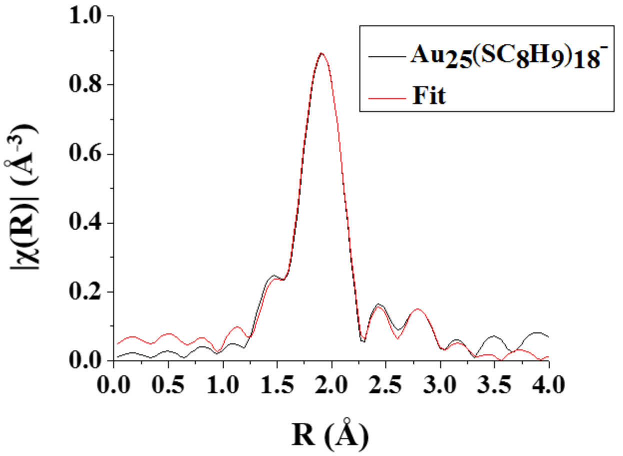

Figure 5.1. EXAFS fitting in R space of Al_2O_3-supported $Au_{25}(SC_8H_9)_{18}$ clusters with 2.5% loading by metal weight.

The first Au-Au (core) peak is because of the bonding between the central Au atom of the icosahedron core of the Au_{25} clusters and 12 neighboring Au atoms along with six short Au-Au pairs present on Au_{13} surface with an average Au-Au bond distance of 2.73 Å (designated Au-Au core contribution). The second Au-Au peak is because of the presence of larger Au-Au pairs on the surface of Au_{13} core with the Au-Au bond distance of 2.94 Å and is given the designation Au-Au surface contribution. The last Au-Au (staple) peak at is because of the bonding between Au atoms from staple motifs and Au atoms form the surface of the Au_{13} core with the Au-Au distance of 3.3 Å.[17] Because of the phase shift of the exited photoelectron, Au-Au bonding pairs in R-space data (Figure 5.1) are at lower R values compared to the bond distance values obtained from single crystal data.[18] In order to fit the EXAFS data, different Au-Au coordination numbers were fixed to that obtained from the literature crystal structures and rest of the parameters were allowed to vary (Table 5.1). Here, interestingly, we found that Au-S coordination number value of 1.4 (1) was lower than the value reported for intact $Au_{25}(SR)_{18}$ clusters by both ourselves and others (Au-S CN = 2.0).[10,17] This is a very interesting finding and we attribute it to the partial removal of thiolate groups after the immobilization of $Au_{25}(SC_8H_9)_{18}$ clusters on the oxide support.

Table 5.1. EXAFS fitting parameters of Al_2O_3-supported $Au_{25}(SC_8H_9)_{18}$ clusters with 2.5% loading by metal weight.

	CN	**R/Å**	**σ^2/Å^2**	**E_0 shift/eV**	***R*-factor**
Au-S	1.4 (1)	2.313 (5)	.001 (4)	2.2 (7)	0.0008
Au-Au (core)	1.44	2.732 (4)	.007 (1)	6.2 (1.2)	0.0008
Au-Au (surface)	1.92	2.94 (5)	.016 (5)	6.2 (1.2)	0.0008
Au-Au (staple)	2.88	3.30 (8)	.04 (2)	6.2 (1.2)	0.0008

Recently, various groups have reported that oxide supported $Au_{25}(SR)_{18}$ clusters show catalytic activity at moderate temperature without any high temperature thermal activation.[19-21] This finding provides a possible explanation to this by attributing the catalytic activity of these supported clusters to a decrease in Au-S coordination number, which opens up the active sites for catalysis. Figure 5.2 shows the EXAFS data in R space of Al_2O_3 supported $Au_{25}(SC_8H_9)_{18}$ clusters with 1.5% loading by Au weight after thermal (250°C) and chemical treatments. BH_4^- and thermal treatments led to a decrease in the Au-S contribution and increase in the Au-Au contribution. The decrease in the Au-S contribution shows removal of thiolate stabilizers from the surface of Au clusters, and the increase in the Au-Au contribution shows growth in cluster size. EXAFS fittings in R space after thermal and chemical treatment in shown in Figure 5.3. Full fitting parameters for each of the samples are found in Table 5.2.

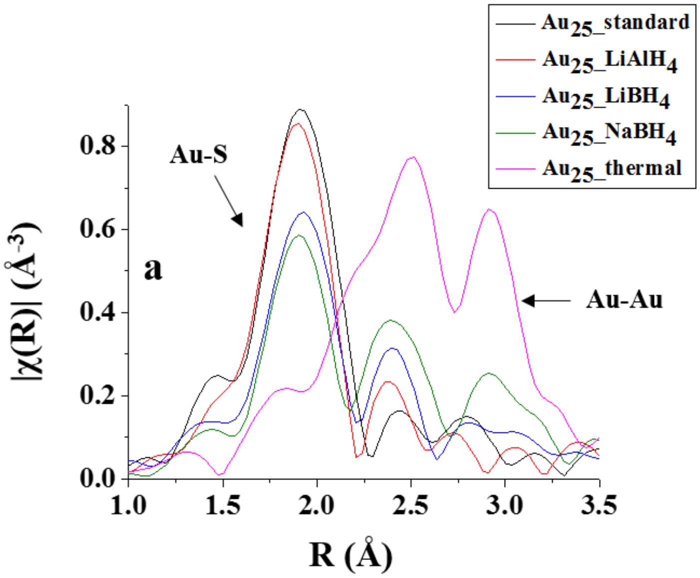

Figure 5.2. EXAFS data in R space of thermally and chemically treated Al_2O_3-supported $Au_{25}(SC_8H_9)_{18}$ clusters with 1.5% loading by metal weight.

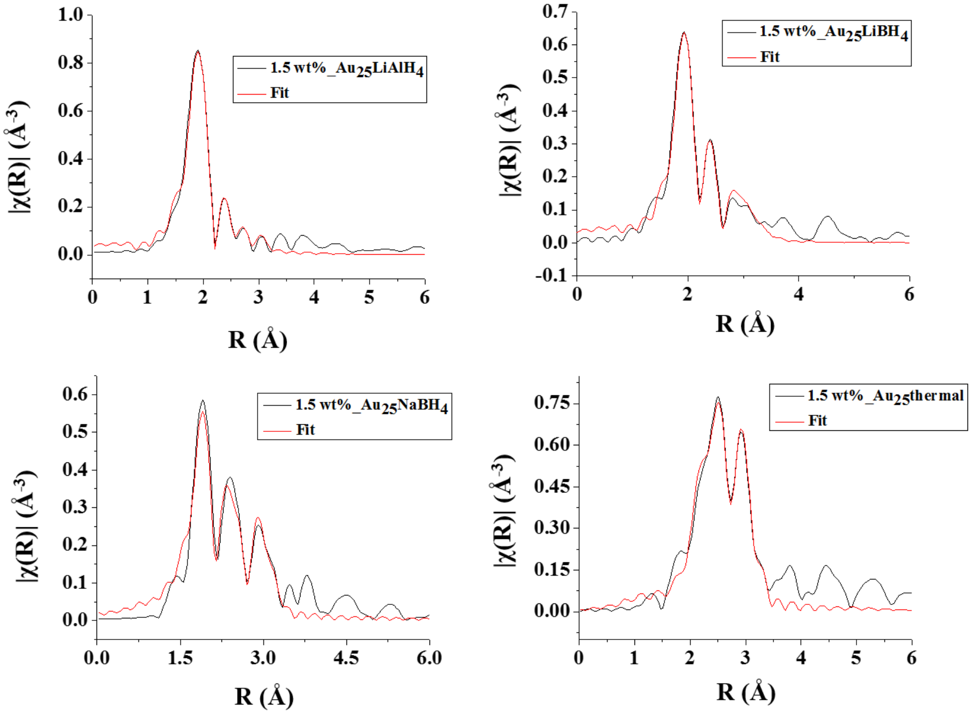

Figure 5.3. EXAFS fitting in R space of thermally and chemically treated Al_2O_3-supported $Au_{25}(SC_8H_9)_{18}$ clusters with 1.5% loading by metal weight.

Table 5.2. EXAFS fitting parameters of thermally and chemically treated Al_2O_3-supported $Au_{25}(SC_8H_9)_{18}$ clusters with 1.5% loading by metal weight.

LiAlH$_4$	**CN**	**R/Å**	**σ^2/Å^2**	**E$_0$ shift/eV**	***R*-factor**
Au-S	1.2 (1)	2.30 (2)	.0007 (8)	-1.1 (1.1)	0.005
Au-Au (core)	1.44	2.73 (2)	.007 (3)	2.25	0.005
Au-Au (surface)	1.92	2.89 (3)	.012 (5)	2.25	0.005
Au-Au (staple)	2.88	3.2 (1)	.05 (4)	2.25	0.005
LiBH$_4$	**CN**	**R/Å**	**σ^2/Å^2**	**E$_0$ shift/eV**	***R*-factor**
Au-S	0.8 (1)	2.319 (8)	.0004 (9)	0.96 (1.5)	0.006
Au-Au (core)	1.44	2.7 (3)	.007 (2)	0.8	0.006
Au-Au (surface)	1.92	2.85 (4)	.019 (8)	0.8	0.006
NaBH$_4$	**CN**	**R/Å**	**σ^2/Å^2**	**E$_0$ shift/eV**	***R*-factor**
Au-S	0.6 (1)	2.301 (7)	.001	4.2 (7)	0.013
Au-Au	6.1 (7)	2.83 (1)	.003 (1)	4.2 (7)	0.013
Thermal	**CN**	**R/Å**	**σ^2/Å^2**	**E$_0$ shift/eV**	***R*-factor**
Au-Au	9.7 (5)	2.846 (4)	.0095 (5)	4.9 (3)	0.004

Data show that the Au-S contribution below 2 Å decreases in intensity after treatment with different reducing agents and completely disappears after thermal treatment at 250°C. This agrees Chapter 4 results which showed that such moderate thermal treatments leads to nearly complete thiolate removal.[10] After $LiAlH_4$ treatment, the Au-Au contributions experienced very little change; however, significant changes were observed after treatment with $LiBH_4$ and $NaBH_4$. After $LiBH_4$ treatment, the Au-Au staple contribution could not be fit, which is likely because of the fact that borohydride reducing agent reacted with the thiolate stabilizers present in these staple motifs. This is evident by the decrease in Au-S coordination number from 1.4(1) in the case of Al_2O_3-

supported $Au_{25}(SC_8H_9)_{18}$ clusters to 0.8(1) after $LiBH_4$ treatment. Treatment of Al_2O_3-supported $Au_{25}(SC_8H_9)_{18}$ clusters with $NaBH_4$ led to significant changes in both the Au-S and Au-Au coordination number values, such that only one Au-Au first shell fcc contribution could be fit. The Au-S coordination number decreased to 0.6(1) and the Au-Au coordination number was found to be 6.1(7). The low Au-Au coordination number value after $NaBH_4$ treatment (6.1 ± 0.7) compared to thermal treatment (9.7 ± 0.5) shows very little growth in cluster size after $NaBH_4$ treatment. The correlation between coordination numbers obtained from EXAFS analysis and particle size (calculated theoretically using imperial formulae) suggests that cluster size changes from 25 Au atoms to ~ 30-40 Au atoms after $NaBH_4$ treatment; however, after thermal treatment cluster size changes to ~ 400 Au atoms.[10] It is important to note that the $NaBH_4$ studies were done at much higher concentrations than $LiBH_4$/$LiAlH_4$ studies in order to try to attempt to fully remove thiol stabilizers, and thus differences between $LiBH_4$ and $NaBH_4$ are likely mostly because of higher concentrations of $NaBH_4$ used.

We have also analyzed EXAFS data in R space for Al_2O_3-supported $Au_{25}(SC_8H_9)_{18}^-$ clusters with 2.5% loading by metal weight (Figure 5.4, Table 5.3), and data shows similar trends to the 1.5% by weight sample data.

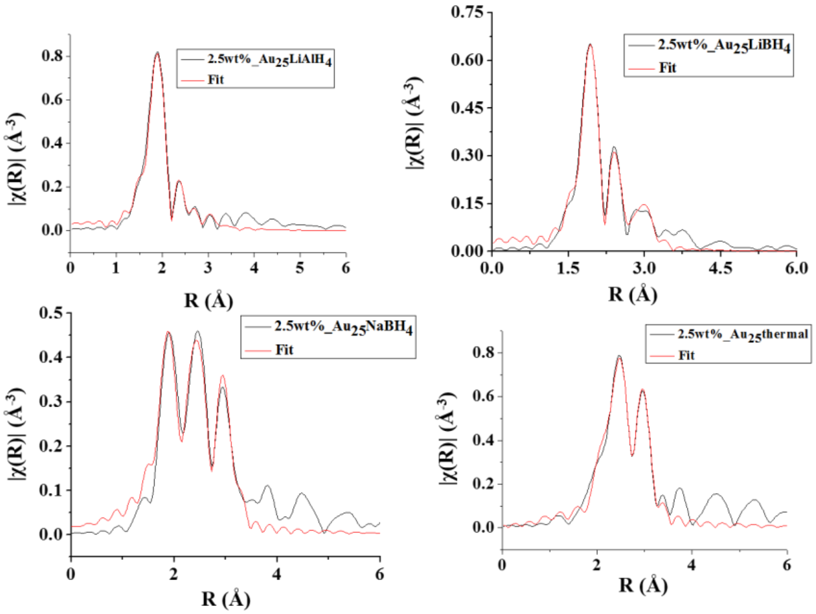

Figure 5.4. EXAFS fitting in R space of thermally and chemically treated Al_2O_3-supported $Au_{25}(SC_8H_9)_{18}$ clusters with 2.5% loading by metal weight.

Table 5.3. EXAFS fitting parameters of chemically and thermally treated Al_2O_3 supported $Au_{25}(SC_8H_9)_{18}^-$ clusters with 2.5% loading by metal weight.

$LiAlH_4$	**CN**	**R/Å**	**σ^2/Å^2**	**E_0 shift/eV**	***R*-factor**
Au-S	1.1 (1)	2.296 (8)	.0007 (9)	-3.3 (1.3)	0.008
Au-Au (core)	1.44	2.71 (3)	.007 (3)	0.1	0.008
Au-Au (surface)	1.92	2.87 (3)	.016 (7)	0.1	0.008
Au-Au (staple)	2.88	3.3 (1)	.02 (2)	0.1	0.008
$LiBH_4$	**CN**	**R/Å**	**σ^2/Å^2**	**E_0 shift/eV**	***R*-factor**
Au-S	0.9 (2)	2.32 (1)	.0005 (9)	1.0 (2.0)	0.008
Au-Au (core)	1.44	2.74 (4)	.005 (4)	1.3	0.008
Au-Au (surface)	1.92	2.86 (5)	.007 (5)	1.3	0.008
$NaBH_4$	**CN**	**R/Å**	**σ^2/Å^2**	**E_0 shift/eV**	***R*-factor**
Au-S	0.5 (1)	2.304 (7)	.011 (9)	5.2	0.008
Au-Au	6.4 (5)	2.840 (7)	.001 (1)	5.2	0.008
Thermal	**CN**	**R/Å**	**σ^2/Å^2**	**E_0 shift/eV**	***R*-factor**
Au-Au	9.4 (5)	2.847 (4)	.0091 (6)	5.2 (3)	0.004

TEM analysis (Figure 5.5) of the Al_2O_3-supported $Au_{25}(SC_8H_9)_{18}$ clusters was also carried out. The initial clusters are hard to discriminate from the Al_2O_3 support, but those measured have an average size of 1.0 ± 0.2 nm, which is consistent with their expected size. After thermal treatment at 250°C, the clusters grew to 1.8 ± 0.4 nm, while BH_4^- treatment led to a final size of 1.3 ± 0.3 nm. TEM data shows that while thermal treatment leads to significant growth in cluster size, borohydride treatments leads to almost negligible growth in size, which further corroborates our previous EXAFS findings.

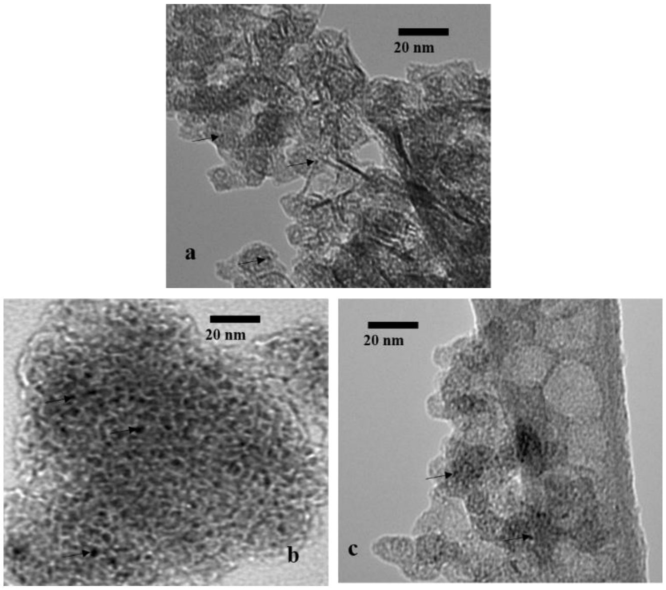

Figure 5.5. TEM images of a) as synthesized $Au_{25}(SC_8H_9)_{18}$ clusters with 1.5% loading by metal weight, b) thermally treated $Au_{25}(SC_8H_9)_{18}$ clusters with 1.5% loading by metal weight, and c) $NaBH_4$ treated $Au_{25}(SC_8H_9)_{18}$ clusters with 1.5% loading by metal weight.

Correlation of first-shell coordination number values obtained by EXAFS after thermal and $NaBH_4$ treatments with number of Au atoms obtained theoretically suggest that after $NaBH_4$ treatment, the cluster size grew from 25 Au atoms to ~30-40 Au atoms, and after thermal treatment, the number of Au atoms in the clusters grows significantly to ~450 Au atoms.[10]

Figure 5.6 shows the Au-L_3 XANES edges of Al_2O_3-supported $Au_{25}(SC_8H_9)_{18}$ clusters with 1.5% loading by Au weight before and after thermal and chemical treatments. Figure 5.6 shows the XANES edges for each of the samples. While there are only minimal differences at the white line (at *ca.* 11930 eV) suggesting no change in oxidation state, a clear trend can be seen beyond the white-line region (marked peaks), with a new peak growing at *ca.* 11950 eV as the clusters show greater thiolate removal. Comparing this data with the Fourier transformed EXAFS data in R space (Figure 5.3) suggests that these new features are related to the decrease in Au-S contribution and increase in Au-Au contribution, and thus increase in cluster size. We believe this 11950 eV peak is a multi-scattering peak, such that its' intensity is related to the number of shells around absorbing atoms; small Au clusters which do not have many upper-shell Au neighbours thus show a much lowered intensity.

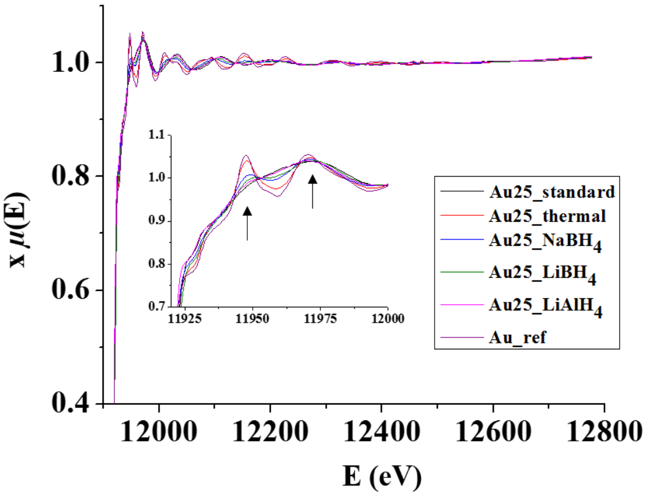

Figure 5.6. XANES data of thermally and chemically treated Al_2O_3-supported $Au_{25}(SC_8H_9)_{18}$ clusters with 1.5 % loading by metal weight.

The generality of these features was established by analyzing XANES data at various Au loadings (Figure 5.7); similar trends in the XANES were observed for various Au loadings. This is an important as it shows that XANES, as well, can be used to study small changes in the cluster size and structure during thiolate removal, which is sometimes very difficult to study with EXAFS data alone because of the poor quality of data at low Au loadings.[11]

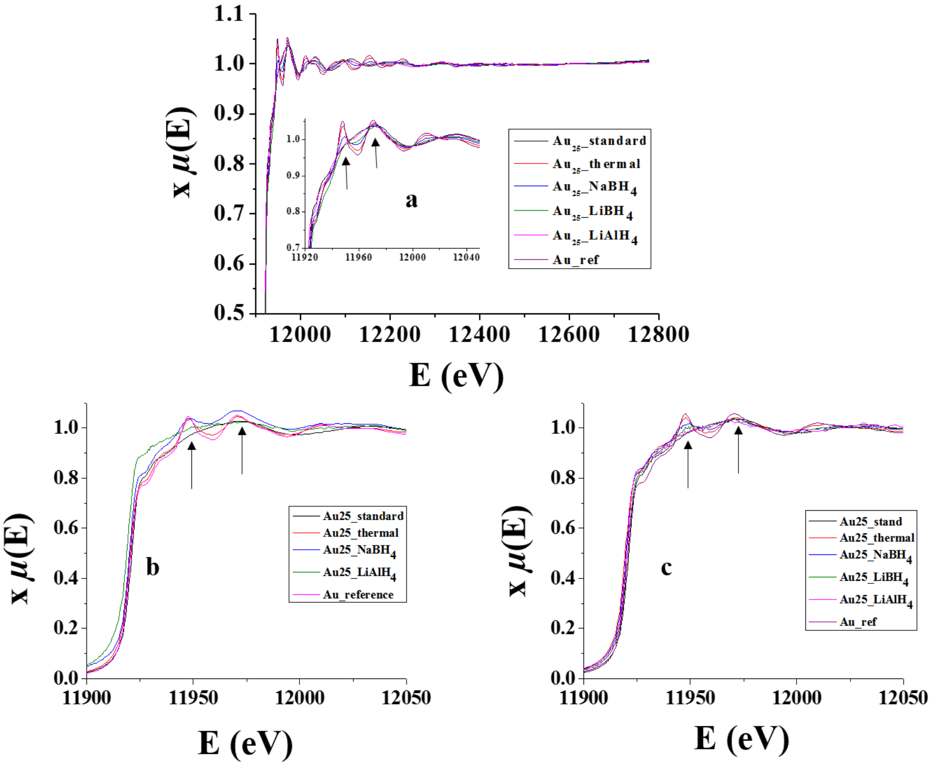

Figure 5.7. a) XANES data of thermally and chemically treated Al_2O_3-supported $Au_{25}(SC_8H_9)_{18}$ clusters with a) 2.5% loading by metal weight, b) 0.75% loading by metal weight, and c) 0.2% loading by metal weight.

It has been reported in the literature that desorption of two-dimensional thiolate self-assembled monolayer from Au surface takes place at a potential of *ca*. -1.0 V to -1.3 V (*vs*. NHE). $NaBH_4$ has a standard oxidation potential of 1.24 V vs. NHE in basic conditions, and therefore can desorb thiolate monolayers from Au surface.[22] For a planar Au surface covered with two-dimensional self-assembled thiolate monolayers, dissociation mechanism is rather simple and involves the reductive desorption of organic thiolates via one electron transfer.[23] However, in the case of $Au_{25}(SR)_{18}$ clusters, because of the presence of two spatially different thiolates in staple motifs, the exact determination of the point of cleavage is not clear. Asefa and coworkers have reported that thiolate desorption from $Au_{25}(SR)_{18}$ clusters occurs at a negative potential of *ca*. -1.5 V; however, no comment was made on the selectivity of thiolate removal.[12] Jin and coworkers showed using NMR spectroscopy that in the case of glutathione protected Au_{25} clusters; thiolates bonded with only staple Au atoms are more vulnerable to attack by $Ce(SO_4)_2$ than thiolates bonded with Au_{13} core directly.[24] In our study, in the case of $LiBH_4$ treatment suggests that Au_{13} core was completely preserved, as we were able to fit EXAFS data after fixing Au-Au (core) and Au-Au (surface) coordination numbers representative of Au_{13} core. However, inability to use Au-Au (staple) coordination number suggests that BH_4^- was perhaps reducing weaker thiolates bonded with only staple Au atoms. After $NaBH_4$ treatment, both types of thiolates were found to be mostly desorbed as the increase in Au-Au coordination number value because of the growth in cluster size was observed. In our previous study, we showed that $Au_{25}(SR)_{18}$ clusters were relatively more stable towards $NaBH_4$ in solution than their larger counterparts.[4] The present study however suggests that oxide supported $Au_{25}(SR)_{18}$ clusters are less stable towards $NaBH_4$ than the same clusters in solution, as some thiols are removed upon adsorption onto the oxide support. Our data also suggests that by varying the amount and the strength of the reducing agents, one can partially remove the thiolate stabilizers under relatively mild conditions (chemical treatments). This result shows promise towards developing strategies that allow for selectively accessing active sites for catalysis.

5.5 Conclusion

In summary, we have shown that thiolate stabilizers can be removed partially from oxide-supported Au_{25} clusters under milder conditions (using borohydride reducing agents) with particle sizes much smaller than that seen under harsher temperature treatments (250°C thermal treatment). TEM data suggest that thermal treatment leads to significant growth in cluster size; however, borohydride treatment leads to almost negligible growth in size during thiolate removal. EXAFS data suggests that partial desorption of thiolate stabilizers was observed after the immobilization of these clusters on oxide supports. This is an important finding, as it can help explain the catalytic activity of oxide supported $Au_{25}(SR)_{18}$ clusters before any thermal activation step. Finally we have shown that very distinct features in the XANES region can be used to follow this thiolate removal process and the concomitant growth in cluster size. This is particularly important in the case of low Au loadings, where it becomes very difficult to obtain high-quality EXAFS data.

Acknowledgements The authors acknowledge financial assistance from the National Sciences and Engineering Research Council of Canada (NSERC) and thank Ning Chen and Weifeng Chen at the Canadian Light Source for assistance with XAS measurements. EXAFS experiments described in this paper were performed at the Canadian Light Source, which is supported by the Natural Sciences and Engineering Research Council of Canada, the National Research Council Canada, the Canadian Institutes of Health Research, the Province of Saskatchewan, Western Economic Diversification Canada, and the University of Saskatchewan.

5.6 References

1. Li, G.; Jiang, D. E.; Kumar, S.; Chen, Y. X.; Jin, R. C., Size Dependence of Atomically Precise Gold Nanoclusters in Chemoselective Hydrogenation and Active Site Structure. *ACS Catal.* **2014,** *4* (8), 2463-2469.

2. Stamplecoskie, K. G.; Kamat, P. V., Size-Dependent Excited State Behavior of Glutathione-Capped Gold Clusters and Their Light-Harvesting Capacity. *J. Am. Chem. Soc.* **2014,** *136* (31), 11093-11099.

3. Zhu, Y.; Qian, H. F.; Das, A.; Jin, R. C., Comparision of the Catalytic Properties of 25-Atom Gold Nanospheres and Nanorods. *Chinese J. Catal.* **2011**, *32* (7), 1149-1155.

4. Shivhare, A.; Ambrose, S. J.; Zhang, H. X.; Purves, R. W.; Scott, R. W. J., Stable and Recyclable Au_{25} Clusters for the Reduction of 4-Nitrophenol. *Chem. Commun.* **2013**, *49* (3), 276-278.

5. Shichibu, Y.; Negishi, Y.; Tsunoyama, H.; Kanehara, M.; Teranishi, T.; Tsukuda, T., Extremely High Stability of Glutathione-Protected Au_{25} Clusters Against Core Etching. *Small* **2007**, *3* (5), 835-839.

6. Tofanelli, M. A.; Ackerson, C. J., Superatom Electron Configuration Predicts Thermal Stability of $Au_{25}(SR)_{18}$ Nanoclusters. *J. Am. Chem. Soc.* **2012**, *134* (41), 16937-16940.

7. Yoskamtorn, T.; Yamazoe, S.; Takahata, R.; Nishigaki, J.; Thivasasith, A.; Limtrakul, J.; Tsukuda, T., Thiolate-Mediated Selectivity Control in Aerobic Alcohol Oxidation by Porous Carbon-Supported Au_{25} Clusters. *ACS Catal.* **2014**, *4* (10), 3696-3700.

8. Fang, J.; Li, J. G.; Zhang, B.; Yuan, X.; Asakura, H.; Tanaka, T.; Teramura, K.; Xie, J. P.; Yan, N., The Support Effect on the Size and Catalytic Activity of Thiolated Au_{25} nanoclusters as Precatalysts. *Nanoscale* **2015** *7* (14), 6325-6333.

9. Liu, Y. M.; Tsunoyama, H.; Akita, T.; Tsukuda, T., efficient and Selective Epoxidation of Styrene with TBHP Catalyzed by Au_{25} Clusters on Hydroxyapatite. *Chem. Commun.* **2010**, *46* (4), 550-552.

10. Shivhare, A.; Chevrier, D. M; Purves, R. W.; Scott, R. W. J., Following the Thermal Activation of $Au_{25}(SR)_{18}$ Clusters for Catalysis by X-ray Absorption Spectroscopy. *J. Phys. Chem. C* **2013**, *117* (39), 20007-20016.

11 Wu, Zili.; Jiang, D-E.; Mann, A. K. P.; Mullins, D. R.; Qiao, Z-A.; Allard, L. F.; Zeng, C.; Jin, R.; Overbury, S. H., Thiolate Ligands as a Double-Edged Sword for CO Oxidation on CeO_2 Supported $Au_{25}(SCH_2CH_2Ph)_{18}$ Nanoclusters. *J. Am. Chem. Soc.* **2014,** *136* (16), 6111-6122.

12. Das, S.; Goswami, A.; Hesari, M.; Al-Sharab, J. F.; Mikmekova, E.; Maran, F.; Asefa, T., Reductive Deprotection of Monolayer Protected Nanoclusters: An Efficient Route to Supported Ultrasmall Au Nanocatalysts for Selective Oxidation. *Small* **2014**, *10* (8), 1473-1478.

13. Li, G.; Jin, R. C., Gold Nanocluster-Catalyzed Semihydrogenation: A Unique Activation Pathway for Terminal Alkynes. *J. Am. Chem. Soc.* **2014**, *136* (32), 11347-11354.

14. Yang, D. F.; Wilde, C. P.; Morin, M., Electrochemical Deposition And Adsorption of Nonytl Mercaptan at Gold Single Crystal Electrode Surface. *Langmuir* **1996**, *12* (26), 6570-6577.

15. Ansar, S. M.; Arneer, F. S.; Hu, W. F.; Zou, S. L.; Pittman, C. U.; Zhang, D. M., Removal of Molecular Adsorbates on Gold Nanoparticles Using Sodium Borohydride in Water. *Nano Lett.* **2013**, *13* (3), 1226-1229.

16. Newville, M. *IFEFFIT*: Interactive XAFS Analysis and *FEFF* Fitting. *J. Synchrotron Rad.* **2001**, 8, 322−324.

17. MacDonald, M. A.; Chevrier, D. M.; Zhang, P., The Structure and Bonding of $Au_{25}(SR)_{18}$ Nanoclusters from EXAFS: The Interplay of Metallic and Molecular Behavior. *J. Phys. Chem. C* **2011,** *115* (31), 15282-15287.

18. Gaur, A.; Shrivastava, B. D.; Nigam, H. L., X-ray Absorption Fine Structure (XAFS) Spectroscopy. *Proc. Indian. Natn. Sci. Acad.* **2013**, 921-966.

19. Zhu, Y.; Qian, H. F.; Drake, B. A.; Jin, R. C., Atomically Precise $Au_{25}(SR)_{18}$ Nanoparticles as Catalysts for the Selective Hydrogenation of Alpha, Beta-Unsaturated Aldehyde and Ketone. *Angew. Chem., Int. Edit.* **2010**, *49* (7), 1295-1298.

20. Nie, X. T.; Qian, H. F.; Ge, Q. J.; Xu, H. Y.; Jin, R. C., CO Oxidation Catalyzed by Oxide-Supported $Au_{25}(SR)_{18}$ Nanoclusters and Identification of Perimeter Sites as Active Center. *ACS Nano* **2012**, *6* (7), 6014-6022.

21. Liu, j.; Krishna, K.S.; Losovyj, Y. B.; Chattopadhyay, S.; Lozova, N.; Miller, J. T.; Spivey J. J.; Kumar, S. S. R.; Ligand stabilized and Atomically Precise Gold Nanocluster Catalysis: A case Study for Correlating Fundamental Electronic Properties with Catalysis. *Chem-Eur. J.* **2013**, *19* (31), 10201-10208.

22. Widrig, C. A.; Chung, C.; Porter, M. D., The Electrochemical Deposition of n-Alkanethiol Monolayers from Polycrystalline Au and Ag Electrodes. *J. Electroanal. Chem.* **1991**, *310* (1-2), 335-359.

23. Quinn, B. M.; Kontturi, K., Reductive Desorption of Thioolate from Monolayer Protected Gold Clusters. *J. Am. Chem. Soc.* **2004**, *126* (23), 7168-7169.

24. Wu, Z.; Gayathri, C.; Gil, R. R.; Jin, R., Probing the Structure and Charge State of Glutathione-Capped $Au_{25}(SG)_{18}$ Clusters by NMR and Mass Spectrometry. *J. Am. Chem. Soc.* **2009**, *131* (18), 6535-6542.

CHAPTER 6

6. Following the Reactivity of $Au_{25}(SC_8H_9)_{18}^-$ Clusters with Pd^{2+} and Ag^+ ions Using *in situ* X-ray Absorption Spectroscopy: A Tale of Two Metals

This work describes the synthesis and structural study of AuPd and AuAg bimetallic clusters. These clusters were synthesized by using previously synthesized $Au_{25}(SC_8H_9)_{18}^-$ clusters (Chapter 2) as starting precursors. The reactions between atomically precise $Au_{25}(SC_8H_9)_{18}^-$ clusters with Pd^{2+} and Ag^+ ions, and the resulting structures of the resulting bimetallic clusters were studied by using UV-Vis spectroscopy, TEM, and *in situ* XANES and EXAFS spectroscopy.

This chapter is based on manuscript which will be submitted for publication in the near future. The author would like to acknowledge the contributions of Dr. Kee Eun Lee for studying the reaction between $Au_{25}(SC_8H_9)_{18}^-$ clusters and Ag(I) salts using X-ray absorption near edge spectroscopy (XANES), TEM, and UV-Vis spectroscopy. The author would like to acknowledge the contribution of Dr. Yongfeng Hu for assisting in the XANES data collection. The author's contributions to this manuscript include: studying the reaction between $Au_{25}(SC_8H_9)_{18}^-$ clusters and Pd(II) salts using XANES, EXAFS, TEM, and UV-Vis spectroscopy, and in the preparation of the final manuscript.

Following the reactivity of $Au_{25}(SC_8H_9)_{18}^-$ clusters with Pd^{2+} and Ag^+ ions using *in situ* X-ray absorption spectroscopy: A tale of two metals

Atal Shivhare, Kee Eun Lee, Yongfeng Hu, and Robert W. J. Scott*

Department of Chemistry, University of Saskatchewan, 110 Science Place, Saskatoon, SK S7N 5C9, Canada

Canadian Light Source, University of Saskatchewan, Saskatoon, SK S7N 0X4, Canada

6.1 Abstract

This work examines the reaction between $Au_{25}(SC_8H_9)_{18}^-$ clusters with palladium acetate (Pd^{2+}) and silver nitrate (Ag^+) using UV-Vis, transmission electron microscopy (TEM), EXAFS, and *in situ* liquid cell X-ray absorption spectroscopy (XAS). UV-Vis results show that upon the addition of Pd^{2+} and Ag^+ salts to $Au_{25}(SC_8H_9)_{18}^-$ clusters, significant changes are seen in the optical properties of the clusters. In the case of Pd, there is little to no change in the size of the clusters evidenced by TEM, while for Ag systems, significant particle growth is seen. *in situ* XAS results show that Pd^{2+} reacts with the staple motifs of $Au_{25}(SC_8H_9)_{18}^-$ clusters and forms Pd(II) thiolate species, as shown by the Pd L_3- and Au L_3-edge data, as well as Pd K edge EXAFS results. However, Ag L_3-edge data suggest that Ag^+ reduces to Ag on the cluster core and does not form Ag(I) thiolate species. This work highlights the power of using *in situ* XANES to follow Au cluster transformations in liquid environments.

6.2 Introduction

Au clusters (typically defined as Au colloids <2 nm in size) have emerged in recent years as a new class of nanomaterials with well-defined structures and molecule-like electronic behavior.[1] Au clusters have been used as model compounds in order to study the size dependent chemical and physical properties of Au nanomaterials.[2] Recently, researchers have suggested that Au clusters with well-defined structures can be doped with various heteroatoms, such as Ag, Cu, Pd, and Pt either on the surface or inside the core, and this results in the formation of bimetallic clusters.[3-7] Literature reports suggest that doping by various heteroatoms can potentially be a way to systematically modify the chemical and physical properties of these clusters.[8-15] Doping by various heteroatoms has been either carried out by co-reduction methods or by the post-synthetic treatment of Au clusters with desired metal ions.[16] Co-reduction methods are more common, in which two metal salts are mixed in the presence of thiolate stabilizers, and the resulting mixture is reduced by the addition of reducing agent, followed by separation of bimetallic and/or metallic clusters. Using this method, various thiolate-protected bimetallic clusters, such as $Au_{25-x}Ag_x$, $Au_{25-x}Cu_x$, $Au_{25-x}Pt_x$, and $Au_{25-x}Pd_x$ have been synthesized.[9,12,17-19] It should be noted that, despite the exciting possibility of the incorporation of different number of heteroatoms into the various Au clusters, the co-reduction method typically suffers from low yields of specific bimetallic clusters because of difficult post-synthetic extractions of specific bimetallic clusters from the crude mixture, which limits their applications to mainly fundamental studies.

Post-synthetic treatment methods involve the treatment of pre-synthesized Au nanoclusters with various metal ions.[16] Treatment of anionic $Au_{25}L_{18}^-$ clusters with various metal ions, such as Ag^+, Pb^{2+}, and Cu^{2+} have been reported in the literature.[3,4,16,20] According to this method, upon the addition of metal ions, $Au_{25}L_{18}^-$ clusters get oxidized to $Au_{25}L_{18}$ while the added metal ions get reduced, and are incorporated into the $Au_{25}L_{18}$ cluster. For example, Wu *et al.* reported the synthesis of thiolate-protected Au_xAg_y bimetallic clusters synthesized from $[Au_{25}(SC_2H_4Ph)_{18}]^-$ and Ag nitrate and found using mass spectrometry (MS) and X-ray photoelectron spectroscopy that Ag was present in reduced form in the bimetallic cluster.[4] Murray *et al.* studied similar reactions with various metal ions, such as Ag^+, Pb^{2+}, and Cu^{2+} and found using UV-Vis spectroscopy, MS, electrochemistry, and fluorescence spectroscopy that anionic $[Au_{25}(SC_2H_4Ph)_{18}]^-$ clusters were oxidized while metal ions got reduced, resulting in the formation of bimetallic clusters.[3] Recently, Wu *et al.* reported the high yield synthesis of $Au_{25}Ag_2(SC_2H_4Ph)_{18}$ bimetallic clusters by using a post-synthetic treatment method, and predicted using experimental and density functional theory studies that two reduced Ag atoms formed bonds with the central Au_{13} core in the $Au_{25}(SC_8H_9)_{18}$ cluster.[20] Post-synthetic treatment methods are relatively simple in nature in terms of the small number of synthetic steps involved, and also offer the possibility of high yields of the resulting bimetallic clusters. However, the future development of this method for the synthesis of various bimetallic clusters requires mechanistic understanding of the reactions between metal ions and Au nanoclusters, and the final structures of the bimetallic clusters.

Our present study looks to address this issue by using *in situ* X-ray absorption spectroscopy (XAS). Herein, we show the reaction between highly monodisperse $Au_{25}(SC_8H_9)_{18}^-$ clusters with Pd^{2+} and Ag^+ ions using UV-Vis, TEM, EXAFS, and *in situ* liquid cell XAS. Our data indicates that Pd^{2+} species were incorporated into the staple motifs of $Au_{25}(SC_8H_9)_{18}^-$ clusters, and these staple motifs were still attached to the Au cluster surface, as no surface plasmon band or growth in cluster size (via TEM) was observed even after that addition of 6 equiv. of Pd^{2+}. EXAFS results confirm this *in situ* XANES assignments, and show only Pd-S bonding contributions. However, in the case of Ag^+ salts, data supports previous literature such that Ag^+ gets reduced to form zerovalent Ag species on the surface of the clusters. These results show the strength of using *in situ* X-ray absorption spectroscopy as a characterization technique for metal speciation for bimetallic cluster syntheses.

6.3 Experimental

6.3.1 Materials

Hydrogen tetrachloroaurate(III) trihydrate ($HAuCl_4 \cdot 3H_2O$, 99.9% on metal basis, Alfa Aesar), silver nitrate ($AgNO_3$, ≥99.0%, Aldrich), tetraoctylammonium bromide (TOAB, 98%, Aldrich), phenylethanethiol (C_8H_9SH, 99%, Acros Organics), sodium borohydride ($NaBH_4$, 98%, EMD), palladium(II) acetate, trimer (99.98% on metal basis, Alfa Aesar), polyvinylpyrrolidone (M.W., 8000, Aldrich), ethylene glycol (Aldrich), and aluminum oxide (Al_2O_3, 58Å, ~150 mesh) were used as received. High purity acetonitrile and methanol were purchased from Fischer Scientific. High purity tetrahydrofuran was purchased from EMD and 100% ethanol was purchased from Commercial Alcohols. 18 MΩ cm Milli-Q (Millipore, Bedford, MA) deionized water was used throughout.

6.3.2 Synthesis of $Au_{25}(SC_8H_9)_{18}^-$ clusters

Synthesis of $Au_{25}(SC_8H_9)_{18}^-$ clusters is reported elsewhere.[21] Briefly, 500 mg of $HAuCl_4 \cdot 3H_2O$ in 50 mL of THF was mixed with 1.2 equiv. of TOAB. To this solution, 5 equiv. of phenylethanethiol was added dropwise and the mixture was left for stirring until it became clear. Subsequently, 10 equiv. of $NaBH_4$ in 10 mL of ice cold water was added all at once. The resulting solution was stirred for 4 days. After 4 days, the reaction was stopped and the solvent was evaporated completely. The resulting solid was then washed with a mixture of ethanol/water several times to remove all excess leftover thiol and disulfide species, and finally the residue was dried using a rotary evaporator. The resulting $Au_{25}(SC_8H_9)_{18}^-$ clusters were extracted with acetonitrile and characterized using UV-Vis spectroscopy.

6.3.3 Synthesis of Ag Nanoparticles

Polyvinylpyrrolidinone (PVP, M.W., 8000) (4.0 g, 36 mmol) was mixed with ethylene glycol (EG) and heated in an oil bath at 130°C for 30 minutes. Then, $AgNO_3$ (0.60 g, 3.6 mmol) dissolved in EG/H_2O (0.4 mL/0.3 mL) was rapidly injected into the PVP solution and stirred for 30 minutes at 130°C. The resulting mixture was cooled down to room temperature, and subsequently washed with acetone several times followed by centrifugation. The obtained Ag nanoparticles were redispersed in ethanol.

6.3.4 Synthesis of Pd (II) dodecanethiolate

Pd (II) thiolate was prepared by reacting 1.0 mg of Pd acetate dissolved in THF with 10 equiv. of dodecanethiol to give a final 10 mM solution.

6.3.5 Reaction between $Au_{25}(SC_8H_9)_{18}^-$ clusters and palladium acetate

1 mg (136 nmol) of $Au_{25}(SC_8H_9)_{18}^-$ clusters in THF were reacted with 0.5 equiv. of Pd acetate dissolved in THF. The entire reaction was monitored by UV-Vis spectroscopy over 1 minute intervals. In the case of the higher amount of Pd acetate (6 equiv.), UV-Vis spectra were recorded before and after the addition of 6 equiv. of Pd acetate.

6.3.6 Reaction between $Au_{25}(SC_8H_9)_{18}^-$ clusters and silver nitrate

1.31 mg (178 nmol) $Au_{25}(SC_8H_9)_{18}^-$ clusters were reacted with different sub-stoichiometric amounts of Ag^+ and after each addition a UV-Vis spectrum was recorded.

6.3.7 Sample preparation for EXAFS measurements

All samples used for EXAFS analysis were prepared by supporting Au and AuPd bimetallic clusters on an Al_2O_3 support using a wetness impregnation approach. For $Au_{25}(SC_8H_9)_{18}^-$ clusters, the final metal loading was 3% by weight. In the case of AuPd bimetallic clusters, a 5% wt Au loading was maintained for the sample prepared by the addition of 0.5 equiv. of Pd^{2+} to the $Au_{25}(SC_8H_9)_{18}^-$ clusters and a 8% wt Au loading was maintained for the sample prepared by the addition of 6 equiv. of Pd^{2+} to the $Au_{25}(SC_8H_9)_{18}^-$ clusters.

6.3.8 UV-Vis and TEM measurements

Absorption spectra were recorded on a Varian Cary 50 Bio UV−Vis spectrometer with an optical path length of 1 cm. Transmission electron micrographs of $Au_{25}(SC_8H_9)_{18}^-$ clusters and after the addition of 6 equiv. of Pd^{2+} were obtained on a HT7700 TEM operating at 100 kV. Transmission electron micrographs of $Au_{25}(SC_8H_9)_{18}^-$ clusters after the addition of 1 equiv. of Ag^+ was obtained on Philips CM10 microscope operating at 100 kV. TEM grids for each samples were prepared by drop-casting one drop of each sample dissolved in THF on a carbon coated copper TEM grid followed by drying under air for several hours. For particle size measurements ~20-30 particles for each sample were counted.

6.3.9 EXAFS measurements and analysis

EXAFS measurements were conducted at the Hard X-ray MicroAnalysis (HXMA) beamline 061D-1 (energy range 5−30 keV; resolution, 1×10^{-4} $\Delta E/E$) of the Canadian Light Source (CLS, 2.9 GeV storage ring, 250 mA current). Samples were pressed into pellets and measured in transmission (Au L_3-edge) and fluorescence (Pd K-edge) modes at room temperature. A double-crystal monochromator housing two crystal pairs [Si (111) and Si (220)] was employed for energy selection. Higher harmonics were eliminated by detuning double-crystal using a Pt-coated KB mirror for Pd K-edge and Rh coated KB mirrors for Au L_3-edge. The incident and transmission X-ray intensities were detected by ion chambers filled with helium−nitrogen mixtures for Pd K-edge and pure helium for Au L_3-edge. The IFEFFIT software package was used for data processing.[22] For the data analysis, the amplitude reduction factor, S_0^2, was determined from foil data and was found to be a value of 0.90 for both Au L_3-edge and Pd K-edge data. For data fitting, the k-range was chosen from 2.0 to 11 $Å^{-1}$ for the Pd K-edge and 2-12.5 $Å^{-1}$ for Au L_3-edge. A Au_{25} model was used for fitting Au L_3-edge data and a PdS model was generated using FEFF 6 program and used to fit Pd K-edge data.[23]

6.3.10 *in situ* XANES measurements

in situ Pd L_3-edge and Ag L_3-edge data were collected at the SXRMB beamline of Canadian Light Source in fluorescence mode. The liquid cells used for XANES analysis were SPEX CertiPrep Disposable XRF X-Cell sample cups with 4 μm ultralene window film. All Pd and Ag L_3-edge and S K-edge data were collected in fluorescence mode under helium atmosphere to reduce beam loss and scattering. In the case of Pd acetate, *in situ* measurements were performed with a mixture of $Au_{25}(SC_8H_9)_{18}^-$ clusters and 0.5 equiv. of Pd acetate in THF in the liquid cell, while for Ag measurements, 0.5 equiv. of Ag nitrate dissolved in acetonitrile and Au_{25} clusters dissolved in THF were added to the liquid cell, followed by further addition of Ag nitrate between measurements.

6.4 Results and Discussion

$Au_{25}(SC_8H_9)_{18}^-$ clusters were synthesized with phenylethanethiol ligands as stabilizers using previously reported methodology.[21] The negative charge on these clusters was confirmed by UV-Vis spectra showing the characteristic features of negatively charged clusters.[24] Figure 6.1a shows the UV-Vis spectra of the reaction between $Au_{25}(SC_8H_9)_{18}^-$ clusters and 0.5 equiv. of Pd (II) acetate. Spectra were collected immediately after the addition of 0.5 equiv. of Pd^{2+} to the $Au_{25}(SC_8H_9)_{18}^-$ clusters, and every minute thereafter. The absorption features of $Au_{25}(SC_8H_9)_{18}^-$ clusters at ~670 nm and ~450 nm started to dampen over time, as shown by the direction of the arrows in Figure 6.1a, which suggests that $Au_{25}(SC_8H_9)_{18}^-$ clusters were losing their structural integrity.

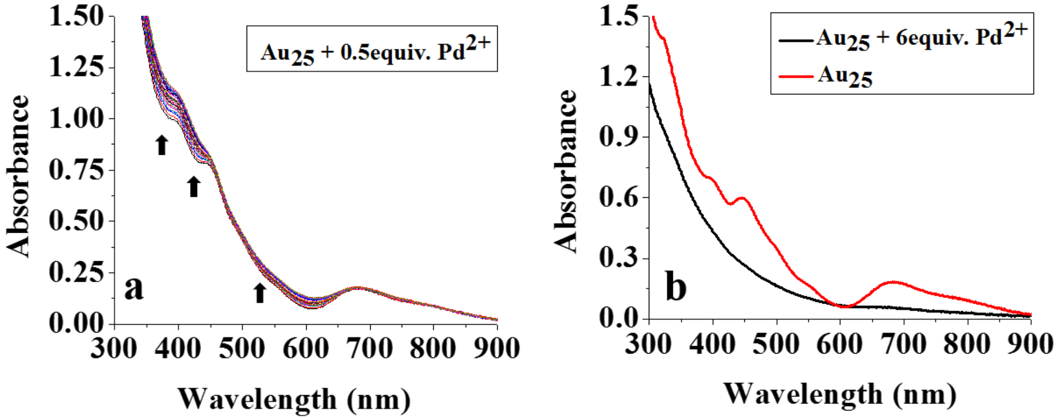

Figure 6.1. UV-Vis spectra of (a) progress of the reaction between $Au_{25}(SC_8H_9)_{18}^-$ clusters and 0.5 equiv. of Pd acetate, (b) spectra of $Au_{25}(SC_8H_9)_{18}^-$ clusters before and after the addition of 6 equiv. of Pd acetate.

The effect of the addition of 6 equiv. of Pd^{2+} to the $Au_{25}(SC_8H_9)_{18}^-$ clusters was also studied to see if these clusters would further react with more Pd^{2+}. As shown in Figure 6.1b, after the addition of 6 equiv. of Pd^{2+}, the absorption features of the $Au_{25}(SC_8H_9)_{18}^-$ clusters at ~670 nm and 450 nm completely disappear and thus the structural integrity of $Au_{25}(SC_8H_9)_{18}^-$ clusters was completely destroyed.

TEM was used to follow the possible changes in cluster size during the reaction. Figure 6.2a shows a TEM image of the original $Au_{25}(SC_8H_9)_{18}^-$ clusters; the Au clusters were difficult to image as they were beam sensitive at high electron fluxes, but faint clusters can be seen that have an average size of 1 nm which corresponds well to the expected $Au_{25}L_{18}$ cluster size. TEM data of clusters after the addition of 6 equiv. of Pd^{2+} (Figure 6.2b) showed no significant growth in size (cluster size 1.3 ± 0.2 nm), and no surface plasmon band because of the formation of larger Au nanoparticles (> ~ 2nm) was seen in either sample.

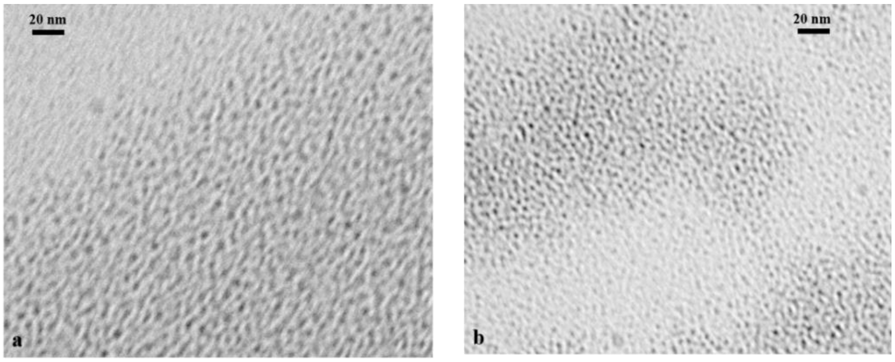

Figure 6.2. TEM images of (a) $Au_{25}(SC_8H_9)_{18}^-$ clusters and (b) $Au_{25}(SC_8H_9)_{18}^-$ clusters after the addition of 6 equiv. of Pd^{2+}.

In the case of Ag^+, we chose to study the incremental addition of Ag^+ to the $Au_{25}(SC_8H_9)_{18}^-$ clusters, since, unlike Pd^{2+}, reaction between $Au_{25}(SC_8H_9)_{18}^-$ clusters and Ag^+ was almost instantaneous and no spectral evolution was observed as found in the case of Pd^{2+}. UV-Vis data (Figure 6.3a) shows that as Ag^+ is added to the Au clusters, the peak at 670 nm shifts to lower wavelengths. Murray *et al*. reported similar shift in their study and attributed it to the oxidation of $Au_{25}(SC_8H_9)_{18}^-$ clusters to $Au_{25}(SC_8H_9)_{18}$ clusters.[3] A TEM image of the AuAg sample (Figure 6.3b) after the addition of 1 equiv. of Ag^+ to the $Au_{25}(SC_8H_9)_{18}^-$ clusters show the formation of much larger nanoparticles with an average size of 2.2 ± 0.5 nm. Thus TEM and UV-Vis data suggests that Ag^+ and Pd^{2+} react quite differently with the $Au_{25}(SC_8H_9)_{18}^-$ clusters.

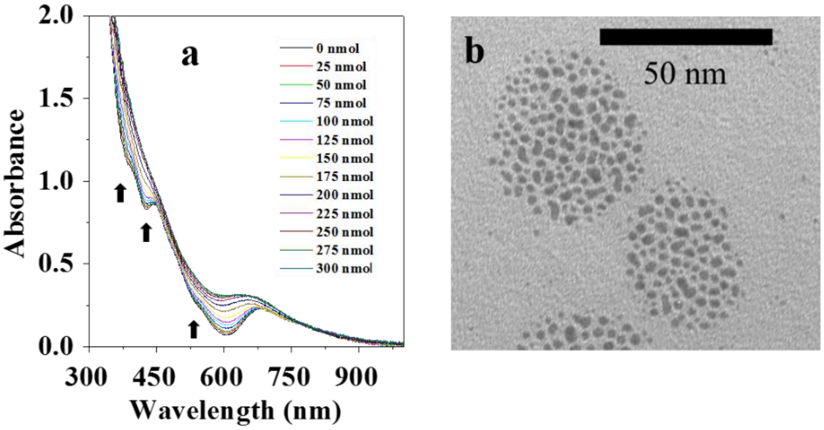

Figure 6.3. (a) UV-Vis spectra showing the progress of the reaction between 178 nmol of $Au_{25}(SC_8H_9)_{18}^-$ clusters and different amount of Ag^+ and (b) TEM image of $Au_{25}(SC_8H_9)_{18}^-$ clusters after the addition of 1 equiv. of Ag^+.

To gain further insight into the differing reactions between the $Au_{25}(SC_8H_9)_{18}^-$ clusters and Pd^{2+} and Ag^+ ions, we studied the chemical speciation of Ag and Pd during reactions with $Au_{25}(SC_8H_9)_{18}^-$ clusters by studying the Pd L_3-edge and Ag L_3-edge at the Soft X-ray Microcharacterization Beamline (SXRMB) at the Canadian Light Source (CLS). *In situ* X-ray absorption near edge structure (XANES) data was collected in fluorescence mode using a liquid cell setup used previously.[25-27] This cell was first filled with a solution of $Au_{25}(SC_8H_9)_{18}^-$ clusters and 0.5 equiv. of Pd^{2+} and was placed on a magnetic stirrer to ensure the constant mixing of the reaction mixture. Figure 6.4 shows the Pd L_3 edge data before and after the addition of 0.5 equivalent of Pd^{2+} to the $Au_{25}(SC_8H_9)_{18}^-$ clusters. As seen in the spectra, the white line for the Pd L_3 edge is initially very strong for Pd(II) acetate, and after reaction with Au_{25} clusters, the white line intensity drops significantly in intensity and shifts to the higher energy. To figure out the exact speciation of Pd after the addition of $Au_{25}(SC_8H_9)_{18}^-$ clusters, we compared the spectra with Pd(II) thiolate and Pd foil standards. As can be seen from the inspection of the data, the final spectra is closer in appearance to the Pd(II) thiolate spectra. This suggests that Pd^{2+} does not get reduced by $Au_{25}(SC_8H_9)_{18}^-$ clusters and remained in oxidized form at the end of the reaction. Rather, data suggests that Pd acetate was converted to Pd (II) thiolate species by reacting with the staple motifs of the $Au_{25}(SC_8H_9)_{18}^-$ clusters, as the six staple motifs (-S-Au-S-Au-S-) of Au_{25} clusters are made up of 12 Au atoms and connected with Au_{13} core through S atoms.[28] At this point, based on UV-Vis, TEM, and XANES results we believe that Pd^{2+} reacts with the staple motifs of Au_{25} clusters and displaces Au staple atoms.

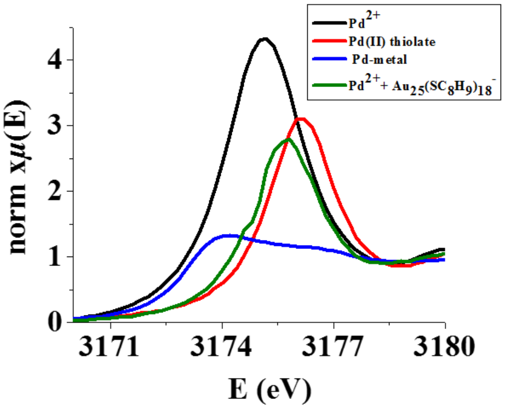

Figure 6.4. Pd L_3-edge XANES spectra after the addition of 0.5 equiv. of Pd^{2+} to the $Au_{25}(SC_8H_9)_{18}^-$ clusters.

More information about the possible outcome of the reactions between $Au_{25}(SC_8H_9)_{18}^-$ clusters and Pd^{2+} was obtained by analyzing Pd K-edge and Au L_3-edge EXAFS data collected at the Hard X-ray MicroAnalysis (HXMA) beamline at the CLS; note these measurements were not done *in situ* but rather as solid-support samples in order to obtain acceptable EXAFS spectra with sufficient signal-to-noise. Detailed procedures for the preparation of sample and data analysis is given in the Experimental section. Figure 6.5a shows the Pd K-edge EXAFS data and the EXAFS fit in R-space of the sample prepared by the addition of 0.5 equiv. of Pd^{2+} to the $Au_{25}(SC_8H_9)_{18}^-$ clusters. The EXAFS data shows only one peak in the range of 1.6-2.0 Å. This peak was attributed to the scattering of photoelectron from Pd absorbing atom by neighboring sulphur atoms, and was fitted using PdS model generated using the IFEFFIT program. EXAFS parameters obtained after fitting are shown in Table 6.1.

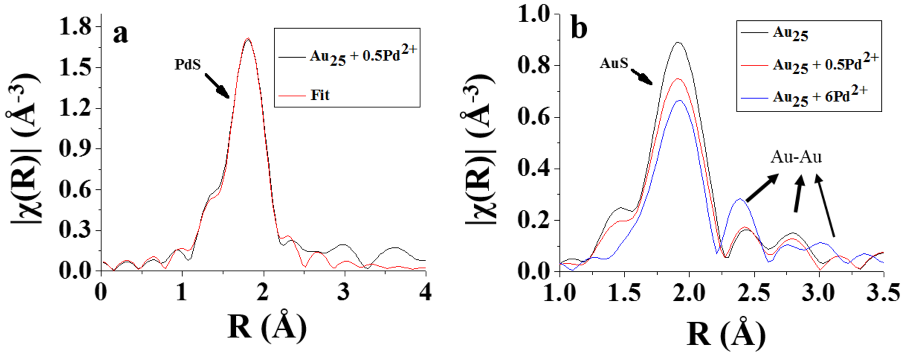

Figure 6.5. a) Pd K-edge EXAFS fitting in *R*-space and b) Au L_3-edge EXAFS spectra in *R*-space of Au_{25} clusters and after the addition of different amount of Pd^{2+}.

Table 6.1. Pd K-edge EXAFS fitting parameters of the sample prepared by the addition of 0.5 equivalents of Pd^{2+} to the $Au_{25}(SC_8H_9)_{18}^-$ clusters.

$Au_{25}(SC_8H_9)_{18}^-$ + 0.5 equiv. Pd^{2+}	**CN**	**R/Å**	**σ^2/Å^2**	**E_0 shift/eV**
PdS	3.64 (3)	2.337 (6)	0.0024 (9)	-0.9 (7)

The Pd-S coordination number value obtained from the fitting was 3.64 ± 0.03. This value is close to 4 and may represent cross-linking between Au clusters through Pd staple motifs; alternatively, it may suggest that some of the thiolates are being removed from Au clusters upon

Pd^{2+} reaction. We do not believe significant thiolate removal is occurring in this system as there is no significant change in the Au particle size via TEM after reaction (removal of thiolates often leads to Au particle growth and/or precipitation).[29] Figure 6.5b shows the Au L_3-edge EXAFS data in *R*-space of $Au_{25}(SC_8H_9)_{18}^-$ clusters before and after the addition of 0.5 and 6 equiv. of Pd^{2+}. Data shows that Au-S contribution at ~ 2Å has decreased in amplitude with an increase in the concentration of Pd^{2+}, which again supports Pd^{2+} replacing Au atoms in the staple motifs of the $Au_{25}(SC_8H_9)_{18}^-$ clusters. Small peaks above 2 Å in all samples (~ 2.2-3.2 Å) are attributed to the three different Au-Au bonding arrangements present within $Au_{25}(SC_8H_9)_{18}^-$ clusters.[31,32] Au L_3-edge EXAFS fittings in R space are quite good (Figure 6.6), and extracted fitting parameters are shows in Table 6.2. It should be noted that the AuS coordination number obtained from the fitting was 1.34 ± 0.10 (Table 6.2), which is slightly lower than the actual value of 2.0 seen previously.[31]The reason for this low coordination number is not clear, but it could be because of the partial desorption of thiol stabilizers form the surface after deposition on the Al_2O_3 support. After treatment with 0.5 equivalent of Pd^{2+}, EXAFS fitting parameters show that the AuS contribution has decreased from 1.34 ± .10 to 1.11 ± .07, which is in agreement with Pd^{2+} replacing Au sites in the staple motifs of $Au_{25}(SC_8H_9)_{18}^-$ clusters. After the addition of 6 equivalent of Pd^{2+}, the AuS coordination number further decreased to 0.73 ± .09. In addition, we could no longer fit a contribution from AuAu staple motifs because of the fact that Pd^{2+} reacted with $Au_{25}(SC_8H_9)_{18}^-$ clusters through the staple motifs. AuAu (surface) coordination numbers for the sample prepared by adding 6 equiv. of Pd^{2+} to the $Au_{25}(SC_8H_9)_{18}^-$ clusters were found to be significantly higher than the values observed for original clusters, with significantly shorter Au-Au bond lengths. We believe these changes are because of the fact that Pd^{2+} displaces Au atoms from the staple motifs, and these displaced Au atoms then are relocated onto the surface of the Au_{13} core.

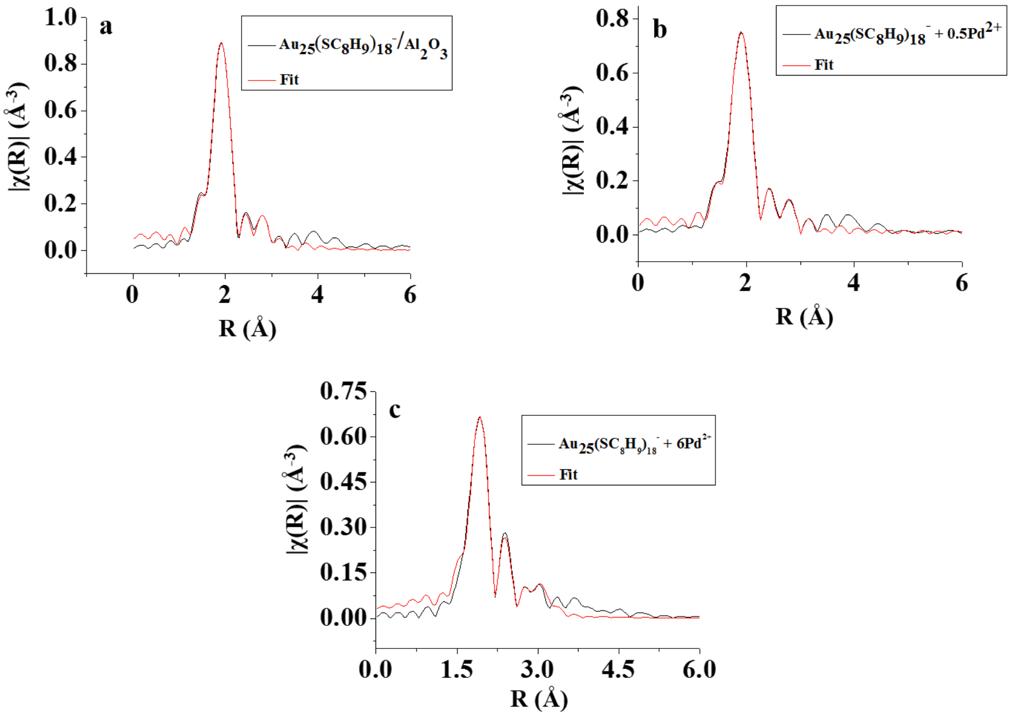

Figure 6.6. EXAFS fitting in *R*-space of (a) $Au_{25}(SC_8H_9)_{18}^-/Al_2O_3$, and $Au_{25}(SC_8H_9)_{18}^-$ clusters after the addition of b) 0.5 equiv. of Pd^{2+} following by deposition on Al_2O_3 and c) 6 equiv. of Pd^{2+} followed by deposition on Al_2O_3.

Table 6.2. Au L_3-edge EXAFS fitting parameters of $Au_{25}(SC_8H_9)_{18}^-$ clusters supported on Al_2O_3 support.

$Au_{25}(SC_8H_9)_{18}^-$	**CN**	**R/Å**	**σ^2/Å^2**	**E_0 shift/eV**
Au-S	1.34 (.10)	2.313 (5)	.0010 (3)	1.5 (7)
Au-Au (core)	1.44*	2.75 (2)	.012 (2)	6.4 (1.2)
Au-Au (surface)	1.92*	3.0 (4)	.012 (2)	6.4 (1.2)
Au-Au (staple)	2.88*	3.30 (6)	.03 (1)	6.4 (1.2)
$Au_{25}(SC_8H_9)_{18}^-$ + 0.5 equiv. Pd^{2+}	**CN**	**R/Å**	**σ^2/Å^2**	**E_0 shift/eV**
Au-S	1.11 (7)	2.313 (3)	.001 (1)	0.83 (1.14)
Au-Au (core)	1.44*	2.76 (1)	.012 (2)	4.4 (1.9)
Au-Au (surface)	1.92*	2.98 (3)	.014 (4)	4.4 (1.9)
Au-Au (staple)	2.88*	3.28 (5)	.03 (1)	4.4 (1.9)
$Au_{25}(SC_8H_9)_{18}^-$ + 6 equiv. Pd^{2+}	**CN**	**R/Å**	**σ^2/Å^2**	**E_0 shift/eV**
Au-S	0.73 (9)	2.311 (8)	.001	7.3 (1.5)
Au-Au (core)	1.2 (9)	2.72 (2)	.005 (4)	1.2 (1.5)
Au-Au (surface)	2.8 (9)	2.86 (2)	.012 (6)	1.2 (1.5)

*Au-Au coordination numbers were fixed, as discussed in ref [31, 32]

in situ liquid cell XANES data for Ag^+ addition to $Au_{25}(SC_8H_9)_{18}^-$ clusters was collected in the same manner as for Pd^{2+}. Figure 6.7 shows the Ag L_3-edge spectra after the addition of one equiv. of Ag^+ to the $Au_{25}(SC_8H_9)_{18}^-$ clusters. For comparison Ag(I) nitrate and Ag (I) thiolate standards were also collected. Data shows that unlike Pd^{2+}, Ag^+ was reduced to Ag after reacting with the $Au_{25}(SC_8H_9)_{18}^-$ clusters. Comparison with Ag(I) thiolate standard suggests that, Ag(I) nitrate does not convert into Ag(I) thiolate as seen in the Pd system above. There are differences in the spectra of Ag NPs vs. this AuAg cluster system, which is likely because of Ag-Au environment in the final clusters. The final spectrum for the AuAg system is shifted significantly to lower energy and no longer has a sharp white line feature ($2p_{3/2}$ to 4d transition) which is indicative of Ag(I) salts (while putatively a $4d^{10}$ species, s-p-d hybridization typically leads to a small white line at the Ag L_3-edge for Ag(I) salts).[32] Further increases in the concentration of $AgNO_3$ shows an increase in the white line intensity and suggests unreacted Ag^+ (not shown). Reduction of Ag^+ has been reported by various groups recently; however, absence of any Ag-S bonding contradicts suggestions that reduced Ag atoms has a Ag-S bond.[20] Unfortunately, because of the low Ag loadings, high quality EXAFS data could not be collected on these samples at the Ag K edge to further document Ag reduction and Ag-Au coordination numbers.

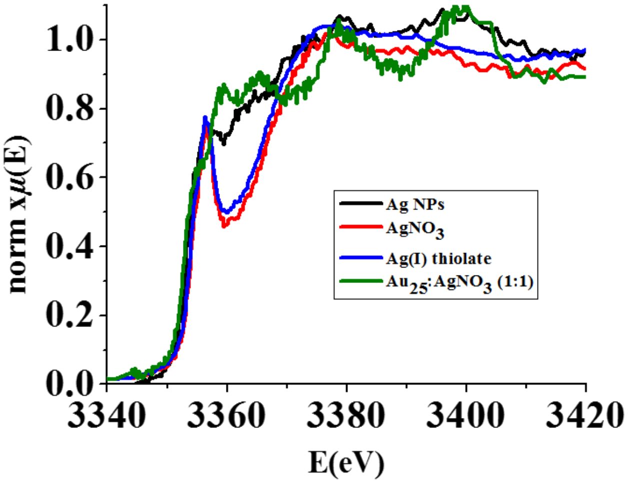

Figure 6.7. Ag L_3-edge XANES spectra after the addition of different amounts of Ag^+ to the $Au_{25}(SC_8H_9)_{18}^-$ clusters.

Finally, the question arises is why these two metal ions react differently with $Au_{25}(SC_8H_9)_{18}^-$ clusters? Based on standard redox potentials, Pd^{2+} (Pd^{2+}/Pd, $E^0 = 0.951$ V) requires a slightly higher potential to reduce than Ag^+ (Ag^+/Ag, $E^0 = 0.799$ V).[33] Another possible explanation could be the Ag-S vs Pd-S bond strengths; the Pd-S bond dissociation energy (398 $D^0_{298}/kJ/mol^{-1}$) is almost double of Ag-S bond dissociation energy (217.1 $D^0_{298}/kJ/mol^{-1}$).[33] Based on this, it seems that Pd^{2+} forms strong Pd-S bonds after reacting with $Au_{25}(SC_8H_9)_{18}^-$ clusters, and because of lower Ag-S bond energy, Ag^+ is more prone to reduction to Ag. Finally, as the $Au_{25}(SC_8H_9)_{18}^-$ clusters have a quantized -1 charge, it is possible that multiple clusters would be needed for full reduction of Pd^{2+} species.

6.5 Conclusion

A number of different characterization techniques, including *in situ* XAS, were used to investigate the reaction between $Au_{25}(SC_8H_9)_{18}^-$ clusters with Pd^{2+} and Ag^+ ions. Our study suggests that Pd^{2+} reacts with $Au_{25}(SC_8H_9)_{18}^-$ clusters through staple motifs and forms Pd(II) thiolate species which are anchored on the surface of Au clusters, as no significant growth or precipitation of Au clusters were observed during the reaction. In the case of Ag^+, it was observed that Ag^+ gets reduced to Ag metal as shown by XANES study. This agrees with results seen previously by other groups for reactions of $Au_{25}L_{18}^-$ clusters and Ag^+, Cd^{2+}, and Pb^{2+} ions.[3] TEM data also shows formation of larger AuAg nanoparticles after treatment with Ag^+, which could be because of the lower stability of the resulting AuAg clusters, which grow into larger nanoparticles. Finally, our study suggests that *in situ* XAS is an important tool in order to study reactions between $Au_{25}(SC_8H_9)_{18}^-$ clusters and various metal ions.

Acknowledgements. The authors acknowledge financial assistance from the National Sciences and Engineering Research Council of Canada (NSERC) and thank Ning Chen at the Canadian Light Source for assistance with XAS measurements. XANES and EXAFS experiments described in this paper were performed at the Canadian Light Source, which is supported by the Natural Sciences and Engineering Research Council of Canada, the National Research Council Canada, the Canadian Institutes of Health Research, the Province of Saskatchewan, Western Economic Diversification Canada, and the University of Saskatchewan.

6.6 References

1. Jin, R. C., Atomically precise metal nanoclusters: stable sizes and optical properties. *Nanoscale* **2015,** *7* (5), 1549-1565.

2. Li, G.; Jin, R. C., Atomically Precise Gold Nanoclusters as New Model Catalysts. *Acc. Chem. Res.* **2013,** *46* (8), 1749-1758.

3. Choi, J. P.; Fields-Zinna, C. A.; Stiles, R. L.; Balasubramanian, R.; Douglas, A. D.; Crowe, M. C.; Murray, R. W., Reactivity of $[Au_{25}(SCH_2CH_2Ph)_{(18)}]^-$ Nanoparticles with Metal Ions. *J. Phys. Chem. C* **2010,** *114* (38), 15890-15896.

4. Wu, Z. K., Anti-Galvanic Reduction of Thiolate-Protected Gold and Silver Nanoparticles. *Angew. Chem., Int. Edit.* **2012,** *51* (12), 2934-2938.

5. Negishi, Y.; Kurashige, W.; Kobayashi, Y.; Yamazoe, S.; Kojima, N.; Seto, M.; Tsukuda, T., Formation of a Pd@Au-12 Superatomic Core in $Au_{24}Pd_1(SC_{12}H_{25})_{18}$ Probed by Au-197 Mossbauer and Pd K-Edge EXAFS Spectroscopy. *J. Phys. Chem. Lett.* **2013,** *4* (21), 3579-3583.

6. Negishi, Y.; Igarashi, K.; Munakata, K.; Ohgake, W.; Nobusada, K., Palladium doping of magic gold cluster $Au_{38}(SC_2H_4Ph)_{24}$: formation of $Pd_2Au_{36}(SC_2H_4Ph)_{24}$ with higher stability than $Au_{38}(SC_2H_4Ph)_{24}$. *Chem. Commun.* **2012,** *48* (5), 660-662.

7. Qian, H. F.; Ellen, B.; Zhu, Y.; Jin, R. C., Doping 25-Atom and 38-Atom Gold Nanoclusters with Palladium. *Acta Phys.-Chim. Sin.* **2011,** *27* (3), 513-519.

8. Xie, S. H.; Tsunoyama, H.; Kurashige, W.; Negishi, Y.; Tsukuda, T., Enhancement in Aerobic Alcohol Oxidation Catalysis of Au_{25} Clusters by Single Pd Atom Doping. *ACS Catal.* **2012,** *2* (7), 1519-1523.

9. Negishi, Y.; Iwai, T.; Ide, M., Continuous modulation of electronic structure of stable thiolate-protected Au_{25} cluster by Ag doping. *Chem. Commun.* **2010,** *46* (26), 4713-4715.

10. Jin, R. C.; Nobusada, K., Doping and alloying in atomically precise gold nanoparticles. *Nano Res.* **2014,** *7* (3), 285-300.

11. Niihori, Y.; Kurashige, W.; Matsuzaki, M.; Negishi, Y., Remarkable enhancement in ligand-exchange reactivity of thiolate-protected Au_{25} nanoclusters by single Pd atom doping. *Nanoscale* **2013,** *5* (2), 508-512.

12. Negishi, Y.; Munakata, K.; Ohgake, W.; Nobusada, K., Effect of Copper Doping on Electronic Structure, Geometric Structure, and Stability of Thiolate-Protected Au_{25} Nanoclusters. *J. Phys. Chem. Lett.* **2012,** *3* (16), 2209-2214.

13. Wang, S. X.; Meng, X. M.; Das, A.; Li, T.; Song, Y. B.; Cao, T. T.; Zhu, X. Y.; Zhu, M. Z.; Jin, R. C., A 200-fold Quantum Yield Boost in the Photoluminescence of Silver Doped Ag_xAu_{25-x} Nanoclusters: The 13th Silver Atom Matters. *Angew. Chem., Int. Edit.* **2014,** *53* (9), 2376-2380.

14. Yang, H. Y.; Wang, Y.; Huang, H. Q.; Gell, L.; Lehtovaara, L.; Malola, S.; Hakkinen, H.; Zheng, N. F., All-thiol-stabilized Ag_{44} and $Au_{12}Ag_{32}$ nanoparticles with single-crystal structures. *Nat. Commun.* **2013,** *4*, 2422-2429.

15. Zhou, M.; Cai, Y. Q.; Zeng, M. G.; Zhang, C.; Feng, Y. P., Mn-doped thiolated Au-25 nanoclusters: Atomic configuration, magnetic properties, and a possible high-performance spin filter. *Appl. Phys. Lett.* **2011,** *98* (14), 143103-143105.

16. Yuan, X.; Dou, X.;Zheng, K.; Xie, J., Recent advances in the synthesis and applications of ultrasmall bimetallic nanoclusters. *Part. Part. Syst. Charact.* **2015**, DOI: 10.1002/ppsc.201400212.

17. Dou, X. Y.; Yuan, X.; Yao, Q. F.; Luo, Z. T.; Zheng, K. Y.; Xie, J. P., Facile synthesis of water-soluble $Au_{25-x}Ag_x$ nanoclusters protected by mono- and bi-thiolate ligands. *Chem. Commun.* **2014,** *50* (56), 7459-7462.

18. Fields-Zinna, C. A.; Crowe, M. C.; Dass, A.; Weaver, J. E. F.; Murray, R. W., Mass Spectrometry of Small Bimetal Monolayer-Protected Clusters. *Langmuir* **2009,** *25* (13), 7704-7710.

19. Qian, H. F.; Jiang, D. E.; Li, G.; Gayathri, C.; Das, A.; Gil, R. R.; Jin, R. C., Monoplatinum Doping of Gold Nanoclusters and Catalytic Application. *J. Am. Chem. Soc.* **2012,** *134* (39), 16159-16162.

20. Yao, C. H.; Chen, J. S.; Li, M. B.; Liu, L. R.; Yang, J. L.; Wu, Z. K., Adding Two Active Silver Atoms on Au_{25} Nanoparticle. *Nano. Lett.* **2015,** *15* (2), 1281-1287.

21. Shivhare, A.; Ambrose, S. J.; Zhang, H.; Purves, R. W.; Scott, R. W. J., Stable and Recyclable Au_{25} Clusters for the Reduction of 4-Nitrophenol. *Chem. Commun*. **2013**, *49* (3), 276-278.

22. Newville, M., *IFEFFIT* : interactive XAFS analysis and *FEFF* fitting. *J. Synchrotron Rad.* **2001**, *8*, 331-333.

23. MacDonald, M. A.; Chevrier, D. M.; Zhang, P.; Qian, H. F.; Jin, R. C., The Structure and Bonding of $Au_{25}(SR)_{18}$ Nanoclusters from EXAFS: The Interplay of Metallic and Molecular Behavior. *J. Phys. Chem. C* **2011**, *115* (31), 15282-15287.

24. Zhu, M.; Eckenhoff, W. T.; Pintauer, T,; Jin, R., Conversion of Anionic $[Au_{25}(SC_8H_9)_{18}]^-$ Cluster to Charge Neutral Cluster via Air Oxidation. *J. Phys. Chem. C* **2008,** *112* (37), 14221-14224.

25. MacLennan, A.; Banerjee, A.; Hu, Y.; Miller, J. T.; Scott, R. W. J., In Situ X-ray Absorption Spectroscopic Analysis of Gold-Palladium Bimetallic Nanoparticle Catalysts. *ACS Catal.* **2013,** 3 (6), 1411-1419.

26. Yao, Y.; Hu, Y.; Scott, R. W. J., Watching Iron Nanoparticles Rust: An *in Situ* X-ray Absorption Spectroscopic Study. *J. Phys. Chem. C* **2014,** *118* (38), 22317-22324.

27. Liu, L.; Burnyeat, C. A.; Lepsenyi, R. S.; Nwabuko, I. O.; Kelly, T. L., Mechanism of Shape Evolution in Ag Nanoprisms Stabilized by Thiol-Terminated Poly(ethylene glycol): An in Situ Kinetic Study. *Chem. Mater.* **2013**, *25* (21), 4206-4214.

28. Zhu, M.; Aikens, C. M.; Hollander, F. J.; Schatz, G. C.; Jin, R., Correlating the crystal structure of a thiol-protected Au_{25} cluster and optical properties. *J. Am. Chem. Soc.* **2008,** *130* (17), 5883-5885.

29. Dasog, M.; Hou, W.; Scott, R. W. J.; Controlling growth and catalytic activity of gold monolayer protected clusters in presence of borohydride salt. *Chem. Commun.* **2011,** *47* (30), 7459-7462.

30. MacDonald, M. A.; Chevrier, D. M.; Zhang, P.; Qian, H. F.; Jin, R. C., The Structure and Bonding of $Au_{25}(SR)_{18}$ Nanoclusters from EXAFS: The Interplay of Metallic and Molecular Behavior. *J. Phys. Chem. C* **2011,** *115* (31), 15282-15287.

31. Shivhare, A.; Chevrier, D. M.; Purves, R. W.; Scott, R. W. J., Following the Thermal Activation of $Au_{25}(SR)_{18}$ Clusters for Catalysis by X-ray Absorption Spectroscopy. *J. Phys. Chem. C* **2013,** *117* (39), 20007-20016.

32. Banerjee, A.; Theron, R.; Scott, R. W. J., Design, synthesis, catalytic application, and strategic redispersion of plasmonic silver nanoparticles in ionic liquid media. *J. Mol. Catal. a-Chem.* **2014**, *393*, 105-111.

33. *CRC Handbook of Chemistry and Physics*, CRC Press, Cleveland, OH, 91 edn, 2010.

CHAPTER 7

7. Au_{25} Clusters as Precursors for the Synthesis of AuPd Bimetallic Nanoparticles with Isolated Atomic Pd Surface Sites

This chapter describes the synthesis of oxide-supported AuPd bimetallic nanoparticles using previously synthesized AuPd bimetallic clusters as starting precursors (Chapter 6). The structure of as-synthesized, oxide-supported AuPd bimetallic nanoparticles was studied by using TEM and EXAFS spectroscopy. This structural study shows the formation of AuPd bimetallic nanoparticles with isolated atomic Pd sites on the surface. Finally, these bimetallic nanoparticles were used for allyl alcohol hydrogenation catalysis and the structure-property relationship was studied.

This chapter is based on a manuscript in preparation. All the experiments in this manuscript were solely performed by the author. The manuscript was solely written by the author.

Au_{25} Clusters as Precursors for the Synthesis of AuPd Bimetallic Nanoparticles with Isolated Atomic Pd Surface Sites

Atal Shivhare[1] and Robert W. J. Scott[1*]

[1] Department of Chemistry, University of Saskatchewan, 110 Science Place, Saskatoon, SK S7N 5C9, Canada

*Corresponding author, E-mail: robert.scott@usask.ca, voice: 306-966-2017

7.1. Abstract

This study documents synthesis of Al_2O_3-supported AuPd bimetallic nanoparticles using $Au_{25}(SC_8H_9)_{18}^-$ clusters as starting precursors. $Au_{25}(SC_8H_9)_{18}^-$ clusters were used as starting precursors followed by Pd(II) salt addition to form AuPd bimetallic clusters. Extended X-ray absorption fine structure (EXAFS) analysis shows that thermal and $LiBH_4$ treatments of thiolate protected AuPd bimetallic clusters results in the formation of AuPd bimetallic nanoparticles with isolated atomic Pd-sites on the surface. EXAFS data also show that Pd atoms present on the surface were still bonded with thiolate stabilizers, which keeps these bimetallic nanoparticles from growing during thermal and $LiBH_4$ treatments. Finally, these AuPd catalysts were tested for the selective hydrogenation of allyl alcohol and were shown to have excellent activities and selectivities for the hydrogenation reaction.

7.2 Introduction

Bulk Au had long been considered inactive for catalysis until the seminal discovery by Haruta *et al*. in 1980 showing that oxide supported, well-dispersed Au nanoparticles (less than 5 nm) can act as a catalyst for low temperature CO oxidation reactions.[1] Since then, a plethora of research articles have been published showing the catalytic activity of supported Au nanoparticles for a wide range of reactions, such as oxidation of alcohols and alkenes, hydrogenation of alkenes and nitroaromatics, and the chemoselective hydrogenation of unsaturated aldehydes and ketones.[2-9] Various groups have shown that alloying Au with Pd leads to a significant enhancement in the catalytic activity and selectivity for various industrially important reactions, such as the oxidation of primary C-H bonds, direct H_2O_2 synthesis from hydrogen and oxygen, vinyl acetate synthesis, and the selective oxidation of alcohols.[10-14] The catalytic activity and selectivity of these AuPd bimetallic nanoparticles can be attributed to the two main factors: 1) modulation in electronic structure upon mixing two metal components,[15-18] and 2) a dilution effect; leading to the formation of catalytically active, isolated atomic Pd sites on the surface of AuPd bimetallic nanoparticles.[19-22] While the effect of modulation in the electronic structure has been very well explored, very little research has been reported on the effect of isolated atomic Pd sites on the surface of AuPd bimetallic nanoparticles towards catalytic activity and selectivity. This is apparently because of the lack of facile synthetic methodologies available for the design of AuPd bimetallic nanoparticles with isolated atomic Pd sites on the surface.

The importance of having catalytically active isolated atomic Pd sites has been discussed by a number of groups.[19-26] For example, Goodman *et al*. have shown that the pair of isolated Pd sites were essential for the acetoxylation of ethylene resulting in the formation of vinyl acetate.[19] Here, the role of two suitably spaced Pd-sites was to facilitate the coupling between surface acetate and ethylene species and to suppress the formation of undesirable reaction byproducts. Sykes and coworkers have shown that isolated atomic Pd sites on Cu (111) surfaces enhances the selectivity of styrene and acetylene hydrogenation reactions towards ethyl benzene and ethane, respectively, by prohibiting the decomposition of these substrates.[20] Meyer and coworkers have shown that the isolation of active surface Pd atoms on inactive Zn cores was responsible for the exclusive dehydrogenation of propane to propylene, and indicated that the competing hydrogenolysis of propane did not take place because the latter reaction requires a contiguous Pd surface.[21] Zhang and coworkers demonstrated the synthesis of Au alloyed Pd single-atom catalyst with an ion-exchange-$NaBH_4$ reduction method and showed that the resulting catalyst exhibit exceptional activity and durability for Ullman reactions of aryl halides.[22]

Atomically-precise, thiolate-protected Au clusters have recently emerged as an important class of materials because of their monodispersity and well-defined structures.[27] These clusters have been used by a number of groups in order to synthesize supported Au catalysts. Both ourselves and others have shown that supported Au clusters can be activated for a number of catalytic reactions by removing thiol stabilizers from the surface either thermally or chemically using BH_4^- reducing agents.[28] For example; we previously reported that mesoporous carbon-supported $Au_{25}(SC_8H_9)_{18}^-$ clusters can be activated for p-nitrophenol reduction catalysis by removing thiol stabilizers at ca. 200°C (Chapter 4).[28] Thermal treatment beyond 200°C led to catalyst deactivation because of sintering. Jin and co-workers reported that CeO_2-supported $Au_{25}(SC_8H_9)_{18}^-$ clusters can be activated for CO oxidation catalysis by thermally removing thiol stabilizers from the interface between CeO_2 and Au clusters at ca. 250°C.[29] Asefa and co-workers reported the activation of SBA-15 supported $Au_{25}(SC_8H_9)_{18}^-$ clusters using BH_4^- reducing agent for styrene oxidation reactions.[30] BH_4^- can reductively eliminate thiol stabilizers from the surface of monolayer protected Au clusters and therefore open-up the catalytically active sites.[31-32] We have recently contrasted the removal of thiol stabilizers from the surface of Al_2O_3-supported $Au_{25}(SC_8H_9)_{18}^-$ clusters by calcining these clusters at 250°C and by treating these clusters using BH_4^- reducing agents (Chapter 5). EXAFS and TEM study showed that BH_4^- treatments led to negligible growth in cluster size while-thermal treatments led to the significant growth in size.[33]

A number of groups have suggested that atomically precise Au_{25} clusters can be used as starting precursors for the synthesis of bimetallic clusters.[34-35] In our previous study, we found that Pd(II) salts react with $Au_{25}(SC_8H_9)_{18}^-$ clusters through surface staple motifs to form Pd(II) thiolate species (Chapter 6).[36] These Pd(II) thiolate species were thought to be anchored on the surface of these clusters leading to the formation of thiolate protected AuPd bimetallic clusters.[36] This present study is an extension of our previous work. Here, using extended X-ray absorption fine structure (EXAFS) spectroscopy, we have shown that thermal and $LiBH_4$ treatments of thiolate-protected AuPd bimetallic clusters on oxide supports lead to the formation of AuPd bimetallic nanoparticles with isolated atomic Pd-sites on the surface. Our data suggests that surface Pd atoms were still bonded with thiolate stabilizers, which may partially constrain growth of these bimetallic alloy nanoparticles during thermal and $LiBH_4$ treatments. The salient features of the present study are as follows: 1) since we are starting with highly monodisperse $Au_{25}(SC_8H_9)_{18}^-$ clusters as starting precursors, better control over the final PdAu nanoparticle compositions can be obtained, and 2) the ability to tune the number of catalytically active atomic Pd-sites on the surface of Au particles can be achieved by simply varying the Au_{25} to Pd^{2+} ratio during bimetallic cluster syntheses, followed by thermal or chemical activation.

7.3 Experimental

7.3.1 Materials

Hydrogen tetrachloroaurate(III) trihydrate ($HAuCl_4 \cdot 3H_2O$, 99.9% on metal basis, Alfa Aesar), tetraoctylammonium bromide (TOAB, 98%, Aldrich), phenylethanethiol (C_8H_9SH, 99%, Acros Organics), sodium borohydride ($NaBH_4$, 98%, EMD), palladium(II) acetate, trimer (99.98% on metal basis, Alfa Aesar), aluminum oxide (Al_2O_3, 58 Å, ~150 mesh), $LiBH_4$ (1M in THF, Sigma Aldrich), and deuterated chloroform ($CDCl_3$, D-99.8%, Cambridge Isotope Laboratories) were used as received. High purity acetonitrile (HPLC grade, submicron filtered) and methanol (HPLC, 0.2 micron filtered) were purchased from Fischer Scientific. High purity tetrahydrofuran was purchased from EMD (HPLC grade) and 100% ethanol was purchased from Commercial Alcohols. 18 MΩ cm Milli-Q (Millipore, Bedford, MA) deionized water was used throughout.

7.3.2 Synthesis of $Au_{25}(SC_8H_9)_{18}^-$ clusters

Synthesis of $Au_{25}(SC_8H_9)_{18}^-$ clusters is reported elsewhere.[37] Briefly, 500 mg of $HAuCl_4 \cdot 3H_2O$ in 50 mL of THF was mixed with 1.2 equiv. of TOAB. To this solution, 5 equiv. of phenylethanethiol was added dropwise and the mixture was left for stirring until it became clear. Subsequently, 10 equiv. of $NaBH_4$ in 10 mL of ice cold water was added all at once. The resulting solution was stirred for 4 days. After 4 days, the reaction was stopped and the solvent was evaporated completely. The resulting solid was then washed with a mixture of ethanol/water several times to remove excess leftover thiol, and finally the residue was dried using a rotary evaporator. The resulting $Au_{25}(SC_8H_9)_{18}^-$ clusters were extracted with acetonitrile and analyzed using UV-Vis spectroscopy.

7.3.3 Sample preparation for EXAFS measurements

Sample B was prepared by mixing 8 mg of $Au_{25}(SC_8H_9)_{18}^-$ clusters with 0.5 equiv. of Pd acetate in THF and stirring the resulting solution overnight. The clusters were then immobilized on 100 mg of an Al_2O_3 support using a wetness impregnation approach and the obtained solid was dried by purging the sample using N_2 gas. Thermal treatment of sample B was done by calcining the obtained powder at 250°C for 90 minutes first under air followed by 90 minutes thermal treatment under H_2 atmosphere. $LiBH_4$ treatment of sample B was done by adding 0.1 mL of $LiBH_4$ (1M in THF) dropwise to the 100 mg of sample A suspended in hexane. The resulting solution was stirred for 10 minutes and subsequently washed with hexane and dried by purging the resulting solid using N_2 gas. Sample A was similarly prepared by mixing 13 mg of $Au_{25}(SC_8H_9)_{18}^-$ clusters with 6 equiv. of Pd acetate in THF and stirring the resulting solution overnight. Thermal and $LiBH_4$ treatments of sample A were done exactly in the same manner as done for sample B.

7.3.4 EXAFS measurements and analysis

EXAFS measurements were conducted at the Hard X-ray MicroAnalysis (HXMA) beamline 061D-1 (energy range 5−30 keV; resolution, 1×10^{-4} ΔE/E) of the Canadian Light Source (CLS, 2.9 GeV storage ring, 250 mA current). Samples was pressed into pellets and measured in transmission mode (sample A, Au L_3-edge, Pd K-edge and sample B, Au L_3-edge) and fluorescence mode (sample B, Pd K-edge) modes at room temperature. A double-crystal Si (111) monochromator was employed for energy selection at both Au L_3-edge and Pd K-edge. Higher harmonics were eliminated by detuning double-crystal monochromator housing two crystal pairs [Si (111) and Si (220)] using a Pt-coated KB mirror for Pd K-edge and Rh coated KB mirrors for Au L_3-edge. The incident and transmission X-ray intensities were detected by ion chambers filled with helium−nitrogen mixtures for Pd K-edge and pure helium for L_3-edge Au L_3-edge. IFEFFIT software package was used for data processing.[38-39] For the data analysis, the amplitude reduction factor, S_0^2, was found to be 0.90 for both the Au L_3-edge and Pd K-edge; these values was determined via fitting of Au and Pd foil data. Simultaneous fits was carried out by using a AuPd alloy model generated using Au fcc and Pd fcc models. For Au L_3-edge data, the AuPd alloy model was created by replacing few Au atoms in the first coordination shell by Pd atoms (depending on the initial Au_{25} to Pd ratio). For Pd K-edge data, a PdAu alloy model was created by replacing few Pd atoms in the first coordination shell by Au atoms (depending on the initial Au_{25} to Pd ratio).

7.3.5 TEM analysis and sample preparation

Transmission electron micrographs of all samples were obtained on Philips CM10 microscope operating at 100 kV. TEM grids for each samples were prepared by drop-casting one drop of each sample suspended in hexane on carbon coated copper grid followed by drying under air for several hours. For particle size measurements ~20-30 particles for each samples were counted.

7.3.6 Allyl alcohol hydrogenation catalysis

A typical procedure for the hydrogenation reaction is as follows: 13 mg of supported catalyst with 1% loading by Au metal weight was suspended in 6 mL of deionized water. The resulting suspension was purged with H_2 gas for ~20 minutes. After that flask was sealed and a balloon filled with H_2 gas was attached to the flask through the septum. Subsequently 0.030 mL of allyl alcohol was introduced into the reaction mixture through a syringe and the resulting solution was stirred for 20 minutes. Finally, the solid catalyst was separated from reaction mixture via centrifugation and the leftover reactants and formed products were extracted in deuterated chloroform for ^1H NMR analysis.

7.4 Result and Discussion

Synthesis of thiolate-protected AuPd bimetallic clusters starting from $Au_{25}(SC_8H_9)_{18}^-$ clusters as precursors and their characterization using UV-Vis, transmission electron microscopy (TEM), and X-ray absorption spectroscopy (XAS) have been reported in a previous study (Chapter 6).[36] We showed that Pd^{2+} reacts with $Au_{25}(SC_8H_9)_{18}^-$ clusters through surface staple motifs and forms Pd (II) thiolate species. These Pd(II) thiolate species were found to be anchored on the surface of Au clusters by replacing Au species in the staple motifs, leading to the formation of thiolate-protected AuPd bimetallic clusters as evidenced by UV-Vis, TEM, and XAS data. In the present study, we further support these bimetallic clusters onto an Al_2O_3 support and subject them to thermal treatment at 250°C under air and H_2 atmosphere or chemical treatments using $LiBH_4$ reducing agents. Thermal treatment at 250°C was done in order to activate these clusters by removing thiol stabilizers as reported in our previous study (Chapter 4).[28]

Two samples were analyzed; the first sample was prepared by mixing 6 equiv. of Pd^{2+} to $Au_{25}(SC_8H_9)_{18}^-$ clusters in THF followed by deposition on Al_2O_3 support (sample A) and the second sample was prepared by mixing 0.5 equiv. of Pd^{2+} to $Au_{25}(SC_8H_9)_{18}^-$ clusters in THF followed by deposition on Al_2O_3 support (sample B). Figure 7.1 shows the Pd K-edge EXAFS data in k space for samples A and B after thermal treatment. EXAFS waves for both samples show similar amplitudes, which is much lower than that of bulk Pd metal. The data for sample B is much noisier because of the much lower Pd content of this sample. Bulk Pd metal has a face centered cubic (fcc) structure with the first shell coordination number value of ~12. Compared to bulk Pd metal, both samples show much lower amplitude and hence have fewer first shell neighboring atoms.

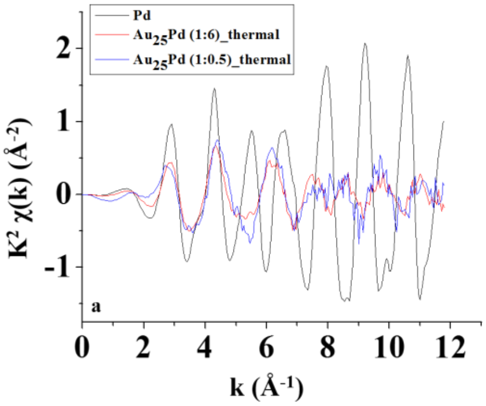

Figure 7.1. Pd K-edge EXAFS spectra in k-space for pure Pd metal, sample A, and sample B after thermal treatment.

Data in k-space also shows a significant shift in the periodicity of the EXAFS wave for both samples. This shift is because of a significant change in the average Pd-X bond lengths in these samples from Pd-Pd bond lengths seen for pure Pd metal. Figures 7.2a and 7.2b are the Pd K-edge EXAFS fittings in R space with the EXAFS fitting parameters shown in Table 7.1.

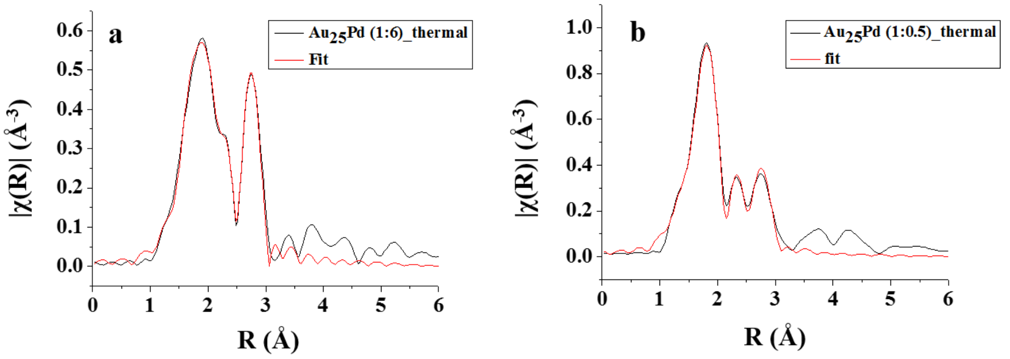

Figure 7.2. Pd K-edge EXAFS fitting in *R*-space for sample A and sample B after thermal treatment.

Table 7.1. Pd K-edge and Au L_3-edge EXAFS fitting parameters of samples A and B after thermal treatment at 250°C.

Sample A	**CN**	**R/Å**	**σ^2/Å^2**	**E$_0$ shift/eV**	***R*-factor**
Pd-S	1.2 (6)	2.30 (2)	0.01 (1)	-3.7(1.2)	0.006
Pd-Au	7.7 (1.2)	2.81 (1)	0.012 (3)	-3.7 (1.2)	0.006
Sample B	**CN**	**R/Å**	**σ^2/Å^2**	**E$_0$ shift/eV**	***R*-factor**
Pd-S	2.2 (5)	2.30 (3)	0.004 (6)	-1.2 (3.3)	0.009
Pd-Au	3.6 (1.7)	2.83 (4)	.007 (8)	-1.2 (3.3)	0.009
Sample A	**CN**	**R/Å**	**σ^2/Å**	**E$_0$ shift/eV**	***R*-factor**
Au-Au	7.6 (4)	2.831 (3)	0.0089 (5)	4.7 (0.2)	0.006
Au-Pd	1.3 (3)	2.81 (1)	0.010 (2)	4.7 (0.2)	0.006
Sample B	**CN**	**R/Å**	**σ^2/Å**	**E$_0$ shift/eV**	***R*-factor**
Au-Au	9.5 (3)	2.845 (2)	0.0091 (4)	5.7 (2)	0.009

Table 7.1 shows Pd-S and Pd-Au coordination number values for both samples after thermal treatment at 250°C. The Pd-Au coordination number was higher for sample A than for

sample B, however both samples had lower first shell coordination number values compared to fcc Pd (CN = 12), and therefore suggest a significant number of surface Pd atoms after thermal treatment.[40-41] Data also suggest that after thermal treatment, Pd comes in direct contact with Au as suggested by the Pd-Au contributions in both samples. Evidence for the surface enrichment of Pd is further supported by the presence of Pd-S contributions for both samples, which is possible only if Pd is present on the surface. The absence of any Pd-Pd contribution for both samples also suggests atomically dispersed Pd-sites on the surface.[22] The Pd-Au bond distance values for both samples were found to be in-between pure Au-Au and pure Pd-Pd bond length values for fcc Au and Pd metals, and best fits were found for only Pd-Au bonding, with no Pd-Pd bonding present. Intermediate bond length values can also suggest the formation of AuPd alloy nanoparticles.[18,40-41]

Figure 7.3 shows the Au L_3-edge EXAFS data in k-space for both samples after thermal treatment. Smaller shifts in the periodicity of the EXAFS wave was observed for both samples, which is consistent with the shift observed in Pd K-edge data (Figure 1a); *i.e.* it is consistent with the formation of Au-Pd bonds. Interestingly, sample A experienced a great shift in the periodicity of the EXAFS wave than sample B; this is because of the fact that in sample A, more Pd was present compared to sample B. Another interesting feature in the Au L_3-edge EXAFS data is the lower amplitude of the EXAFS wave for sample A compared to sample B, which indicates that the incorporation of more Pd atoms in the final particles seems to constrain the growth of the nanoparticles during thermal treatment.

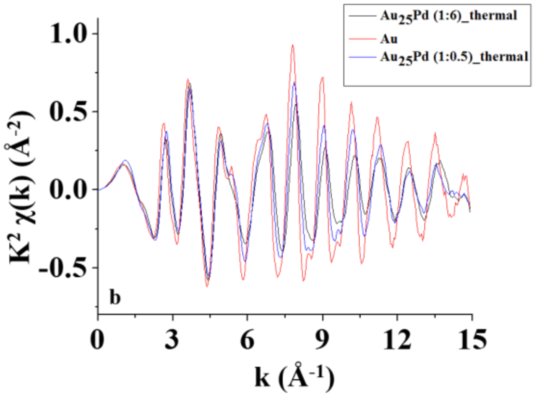

Figure 7.3. Au L_3-edge EXAFS data in k-space for pure Au metal, sample A, and sample B after thermal treatment.

Figures 7.4a and 7.4b are the Au L3-edge EXAFS fittings in R space with the EXAFS fitting parameters shown in Table 7.1.

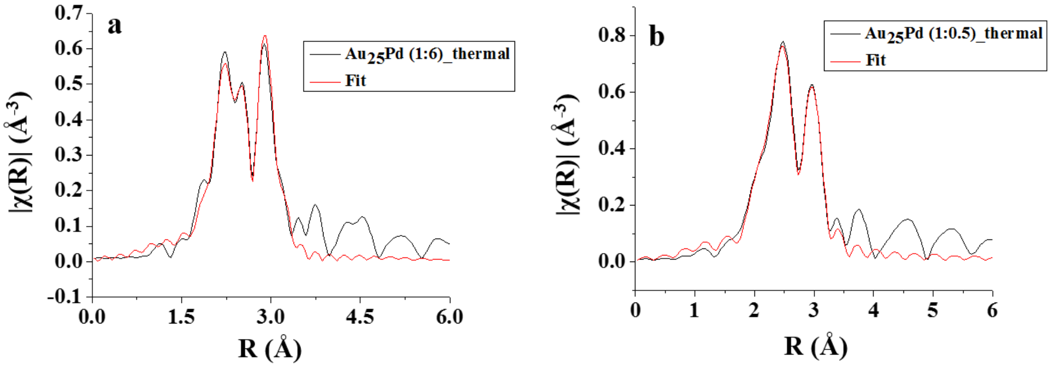

Figure 7.4. Au L3-edge EXAFS fitting in *R*-space for sample A and sample B after thermal treatment.

The sizes of the bimetallic nanoparticles after thermal treatment are also reflected in the Au-Au and Au-Pd coordination numbers (Table 7.1). Au-M first shell coordination numbers (Au-Au + Au-Pd) were found to be lower for sample A than for sample B, which suggest lower nanoparticle size for sample A than for sample B.[42] EXAFS fitting parameters for sample A (Table 7.1) also show a low Au-Pd coordination number value of 1.3 ± 0.3. This low value supports the presence of isolated atomic Pd-sites.

It was not possible to extract any Au-Pd contribution from Au L3-edge data of sample B, possibly because of the very small amount of Pd present in sample B compared to sample A. It is important to note that no remaining Au-S interactions were seen for either sample. Both Au L3-edge and Pd K-edge data suggest the formation of AuPd bimetallic bonds in the nanoparticles with isolated atomic Pd-sites on the surface. TEM analysis (Figure 7.5) further supports these results and show smaller particle size for sample A (3.6 ± 0.9 nm), compared to sample B (5.4 ± 1.0 nm).

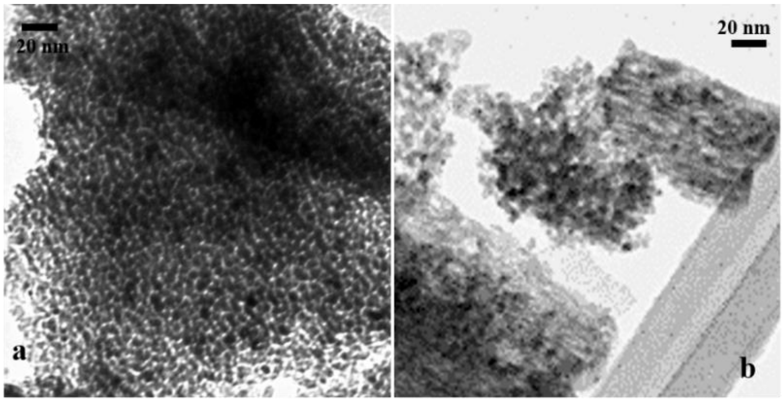

Figure 7.5. TEM images of a) sample B after thermal treatment, b) sample A after thermal treatment.

It should be noted here that particle sizes calculated from TEM are significantly higher than what is expected based on EXAFS coordination number values. This is likely because of the fact that larger particles are easier to locate using TEM than smaller ones; TEM sizes are likely overestimating the average particle size.

It has been reported in the literature that borohydride anions (BH_4^-) can reductively desorb thiolate stabilizers form monolayer protected Au nanoparticles.[32,43] In our previous study, we showed that borohydride reducing agents can be used in order to remove thiolate stabilizers from Al_2O_3 supported $Au_{25}(SC_8H_9)_{18}^-$ clusters.[33] We found that, while the thermal treatment of Al_2O_3-supported $Au_{25}(SC_8H_9)_{18}^-$ clusters at 250°C under air led to the significant growth in cluster size, very little growth was observed after borohydride treatment, albeit this treatment only gave partial thiolate removal. In the present study, we further explored the use of borohydride reducing agent to reduce thiolate protected AuPd bimetallic clusters.

Figure 7.6 shows the Pd K-edge EXAFS data in k-space for both samples after $LiBH_4$ treatment.

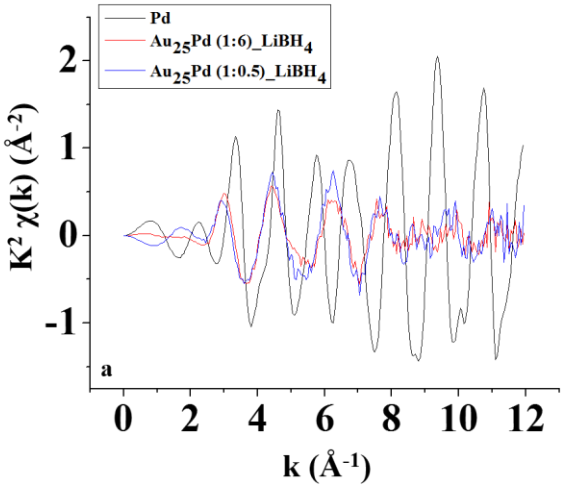

Figure 7.6. Pd K-edge EXAFS spectra in k-space for pure Pd metal, sample A, and sample B after $LiBH_4$ treatment.

Similar features were observed as in the case of thermally treated samples (lower amplitude than pure Pd metal and shift in the periodicity of waves), which indicates that Pd-Au bonds have been formed in this system as well. Pd K-edge EXAFS fittings for both samples are shown in Figure 7.7, and EXAFS fitting parameters for both samples are shown in Table 7.2.

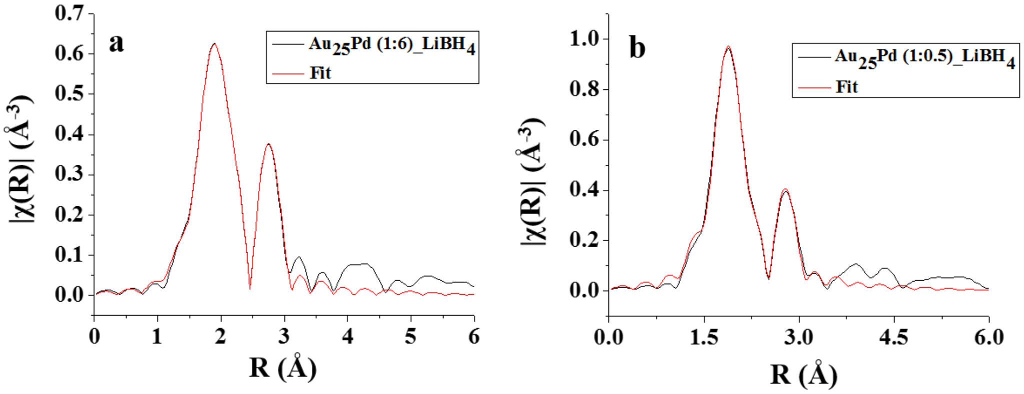

Figure 7.7. Pd K-edge EXAFS fitting in *R*-space for sample A, and sample B after $LiBH_4$ treatment.

Table 7.2. Pd K-edge and Au L_3-edge EXAFS fitting parameters of samples A and B after $LiBH_4$ treatment.

Sample A	**CN**	**R/Å**	**σ^2/Å**	**E_0 shift/eV**	***R*-factor**
Pd-S	0.9 (0.3)	2.29 (3)	0.004 (.017)	-2.7 (1.6)	0.006
Pd-Pd	0.3 (0.3)	2.72 (6)	0.002 (.02)	-2.7 (1.6)	0.006
Pd-Au	7.0 (1.4)	2.77 (1)	0.01 (1)	-2.7 (1.6)	0.006
Sample B	**CN**	**R/Å**	**σ^2/Å**	**E_0 shift/eV**	***R*-factor**
Pd-S	1.5 (3)	2.32 (2)	0.003 (6)	-2.5 (2.6)	0.015
Pd-Au	8.7 (1.8)	2.77 (2)	0.014 (5)	-2.5 (2.6)	0.015
Sample A	**CN**	**R/Å**	**σ^2/Å**	**E_0 shift/eV**	***R*-factor**
Au-S	0.21 (6)	2.31 (1)	0.001 (2)	3.8 (6)	0.006
Au-Au	6.3 (2)	2.809 (3)	0.011 (1)	3.8 (3)	0.006
Au-Pd	1.1 (2)	2.77 (1)	.013 (6)	3.8 (3)	0.006
Sample B	**CN**	**R/Å**	**σ^2/Å**	**E_0 shift/eV**	***R*-factor**
Au-S	0.68 (5)	2.298 (5)	0.001 (1)	3.9 (8)	0.015
Au-Au	5.3 (3)	2.798 (6)	0.014 (2)	3.9 (8)	0.015

Low Pd-Au coordination numbers and the presence of Pd-S contributions in both samples suggest the enrichment of the surface with Pd. Sample A has Pd-S, weak Pd-Pd, and Pd-Au contributions; however, sample B shows only Pd-S and Pd-Au contributions, which supports atomic dispersion of Pd on the surface of the Au nanoparticles. Figure 7.8 shows the Au L_3-edge EXAFS data in k-space for both samples after $LiBH_4$ treatment. EXAFS k-space data show a reduction in amplitude and shift in the periodicity of the wave, which is consistent with Pd-Au bond formation as shown in the case of thermally treated samples.

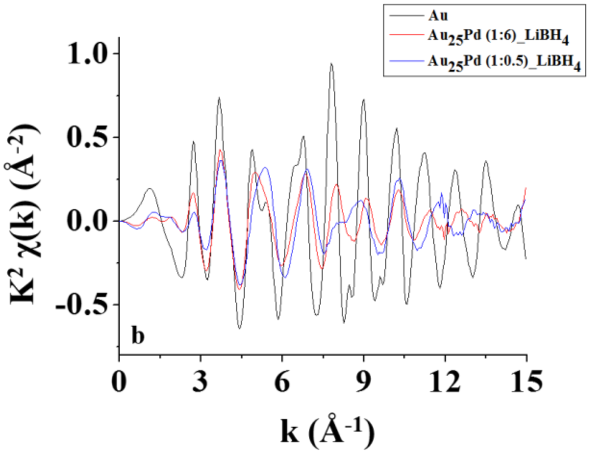

Figure 7.8. Au L_3-edge EXAFS data in k-space for pure Au metal, sample A, and sample B after $LiBH_4$ treatment.

EXAFS fittings of these samples are shown in Figure 7.9 and EXAFS fitting parameters are shown in Table 7.2. Here, significant Au-S contributions are seen in for both samples, which contrasts with thermally treated samples in which no Au-S contributions were observed. These values were slightly lower than the value observed previously for Al_2O_3-supported $Au_{25}(SC_8H_9)_{18}^-$ clusters after $LiBH_4$ treatment (CN = 0.8 ± 0.1), particularly for sample A.[33] The Au-S coordination number for sample A (CN = 0.21 ± 0.06) was lower than the value observed for sample B (CN = 0.68 ± 0.05), which suggests higher loadings of Pd lead to improved removal of thiolates from the Au surface. This is an interesting observation, and it may indicate that some of the original $Au_{25}(SC_8H_9)_{18}^-$ clusters in sample B did not incorporate Pd, and thus $LiBH_4$ treatment led to only partial removal of thiolate stabilizers from sample B because of the inherent stability of leftover $Au_{25}(SC_8H_9)_{18}^-$ clusters present in the sample.[37] The Au-Pd coordination number of 1.1 ± 0.2 for sample A seems to suggest that after $LiBH_4$ treatment, isolated atomic Pd sites were formed on the surface of the particle. Enrichment of the surface with Pd is supported by the presence of Pd-S contributions for both samples.

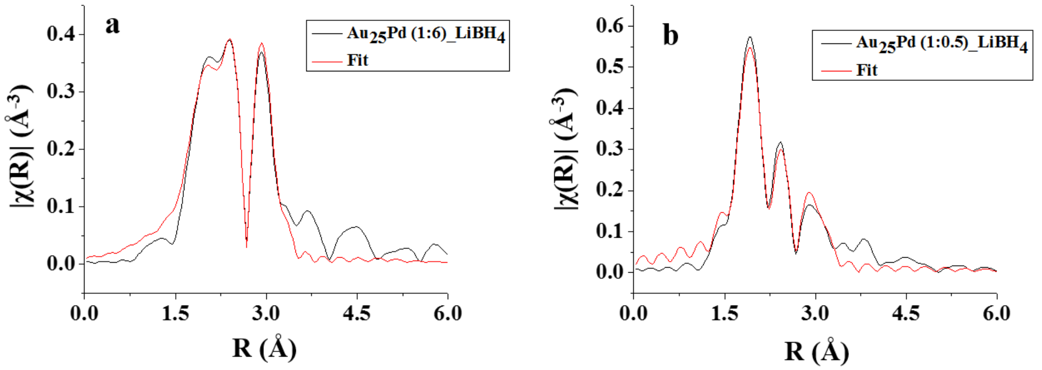

Figure 7.9. Au L_3-edge EXAFS fitting in *R*-space for sample A and sample B after $LiBH_4$ treatment.

Figure 7.10 shows the Au-L_3 EXAFS data in k-space for the borohydride-treated and thermally treated samples. A significantly lower amplitude was seen for sample A after $LiBH_4$ treatment compared to the amplitude of the wave for the same sample after thermal treatment. Also, the shift in the periodicity of EXAFS wave was more pronounced after $LiBH_4$ treatment than after thermal treatment.

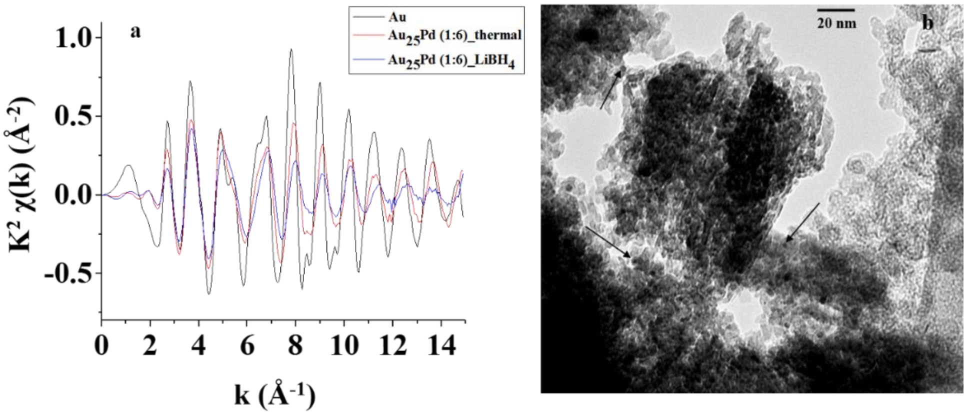

Figure 7.10. a) Au L_3-edge EXAFS data in k-space for pure Au metal and sample A after thermal and $LiBH_4$ treatments and b) TEM image of sample A after $LiBH_4$ treatment.

This is an interesting finding as it suggests significant growth in the size of bimetallic nanoparticles after thermal treatments compared to $LiBH_4$ treatment. Lower Au-Au bond distance values observed for $LiBH_4$ treated samples compared to thermally treated samples further suggest the formation of smaller bimetallic nanoparticles after $LiBH_4$ treatment. This suggests the beneficial role of $LiBH_4$ in controlling the size of AuPd bimetallic nanoparticles. Formation of smaller bimetallic nanoparticles after $LiBH_4$ treatment was also supported by the TEM analysis which shows much smaller nanoparticle sizes (2.0 ± 0.3 nm) compared to thermally treated samples.

Finally, allyl alcohol hydrogenation was used as model reaction in order to test the activity of these supported bimetallic nanoparticles.[44-46] Table 7.3 describes the Turnover Frequency (TOF) of various supported catalysts and product selectivity. TOFs were calculated by considering the number of moles of Pd as active sites for catalysis. In the case of pure Pd nanoparticles, TOFs of 3960 h^{-1} with higher selectivity for propanol was obtained. In the case of the $Au_{25}Pd$ (1:6)_standard (without thermal or $LiBH_4$ treatments) catalyst, TOF and selectivity were slightly reduced compared to pure Pd nanoparticles. It should be noted that in this case, Pd atoms were the part of staple motifs and were bonded with thiolate stabilizers. This may be the possible explanation for reduced activity compared to pure Pd nanoparticles. After thermal treatment of the same catalyst [$Au_{25}Pd$ (1:6)_thermal], the TOF was significantly enhanced compared to pure Pd nanoparticles and standard AuPd nanoparticles [$Au_{25}Pd$ (1:6)_standard]. This enhanced activity after thermal treatment supports the presence of active Pd sites on the surface of AuPd alloy nanoparticles and also supports previous EXAFS results. The higher activity than the as-synthesized pre-calcination standard indicates that after thermal treatment most of the thiol stabilizers were removed and thus active sites for catalysis were readily available.

Table 7.3. Allyl alcohol hydrogenation catalysis using various supported catalysts.

Catalysts	**TOF (h^{-1})**	**Propanol (%)**	**Propionaldehyde (%)**
Pd	3960	68	31
$Au_{25}Pd$ (1:6)_standard	2901	60	39
$Au_{25}Pd$ (1:6)_thermal	7845	61	38
$Au_{25}Pd$ (1:6)_$LiBH_4$	4794	63	36

No significant enhancement in the selectivity was observed after thermal treatment. This indicates that AuPd alloy formation after thermal treatment did not affect the selectivity of the reaction. A $LiBH_4$ treated sample [$Au_{25}Pd$ (1:6)_$LiBH_4$] was also tested. Here, a much lower TOF was observed compared to thermally treated sample, however; both samples show similar selectivity for propanol. We are not certain as to why lower activities are seen for the $LiBH_4$ samples; this may be partially because of additional thiolates attached to Au sites near the Pd sites, which leads to greater mass transfer issues for catalysis at the Pd sites.

7.5 Conclusion

In summary, we have shown the synthesis of AuPd bimetallic nanoparticles using $Au_{25}(SC_8H_9)_{18}^-$ clusters as starting precursors. Our data suggest the formation of isolated atomic Pd-sites on the surface of bimetallic alloy nanoparticles. EXAFS data indicate that Pd atoms present on the surface were bonded with thiolate stabilizers, which keep these bimetallic nanoparticles from significantly sintering during thermal and $LiBH_4$ treatments. Bimetallic nanoparticles prepared with 6 equiv. of Pd^{2+} were found to be lower in size than the sample prepared with 0.5 equiv. of Pd^{2+}. This is attributed to the enrichment of the surface with Pd and therefore the presence of more thiolate stabilizers on the surface. These catalysts also showed significantly higher activities for hydrogenation catalysis compared to $LiBH_4$-treated samples.

Acknowledgements

The authors acknowledge financial assistance from the National Sciences and Engineering Research Council of Canada (NSERC) and thank Ning Chen at the Canadian Light Source for assistance with XAS measurements. EXAFS experiments described in this paper was performed at the Canadian Light Source, which is supported by the Natural Sciences and Engineering Research Council of Canada, the National Research Council Canada, the Canadian Institutes of Health Research, the Province of Saskatchewan, Western Economic Diversification Canada, and the University of Saskatchewan.

7.6 References

1. Haruta, M.; Kobayashi, T.; Sano, H.; Yamada, N., Novel Gold Catalysts for the Oxidation of Carbon-Monoxide at a Temperature Far Below 0-Degrees-C. *Chem. Lett.* **1987,** (2), 405-408;

2. Ketchie, W. C.; Murayama, M.; Davis, R. J., Promotional effect of hydroxyl on the aqueous phase oxidation of carbon monoxide and glycerol over supported Au catalysts. *Top. Catal.* **2007,** *44* (1-2), 307-317.

3. Prati, L.; Rossi, M., Gold on carbon as a new catalyst for selective liquid phase oxidation of diols. *J. Catal.* **1998,** *176* (2), 552-560.

4. Carrettin, S.; McMorn, P.; Johnston, P.; Griffin, K.; Hutchings, G. J., Selective oxidation of glycerol to glyceric acid using a gold catalyst in aqueous sodium hydroxide. *Chem. Commun.* **2002,** (7), 696-697.

5. Alshammari, H.; Miedziak, P. J.; Davies, T. E.; Willock, D. J.; Knight, D. W.; Hutchings, G. J., Initiator-free hydrocarbon oxidation using supported gold nanoparticles. *Catal. Sci. Technol.* **2014,** *4* (4), 908-911.

6. McEwan, L.; Julius, M.; Roberts, S.; Fletcher, J. C. Q., A review of the use of gold catalysts in selective hydrogenation reactions. *Gold Bull.* **2010,** *43* (4), 298-306.

7. Li, G.; Jiang, D. E.; Kumar, S.; Chen, Y. X.; Jin, R. C., Size Dependence of Atomically Precise Gold Nanoclusters in Chemoselective Hydrogenation and Active Site Structure. *ACS Catal.* **2014,** *4* (8), 2463-2469.

8. Ide, M. S.; Hao, B.; Neurock, M.; Davis, R. J., Mechanistic Insights on the Hydrogenation of alpha,beta-Unsaturated Ketones and Aldehydes to Unsaturated Alcohols over Metal Catalysts. *ACS Catal* **2012,** *2* (4), 671-683.

9. Mertens, P. G. N.; Poelman, H.; Ye, X.; Vankelecom, I. F. J.; Jacobs, P. A.; De Vos, D. E., Au-0 nanocolloids as recyclable quasihomogeneous metal catalysts in the chemoselective hydrogenation of alpha,beta-unsaturated aldehydes and ketones to allylic alcohols. *Catal. Today* **2007,** *122* (3-4), 352-360.

10. Kesavan, L.; Tiruvalam, R.; Ab Rahim, M. H.; bin Saiman, M. I.; Enache, D. I.; Jenkins, R. L.; Dimitratos, N.; Lopez-Sanchez, J. A.; Taylor, S. H.; Knight, D. W.; Kiely, C. J.; Hutchings, G. J., Solvent-Free Oxidation of Primary Carbon-Hydrogen Bonds in Toluene Using Au-Pd Alloy Nanoparticles. *Science* **2011,** *331* (6014), 195-199.

11. Edwards, J. K.; Carley, A. F.; Herzing, A. A.; Kiely, C. J.; Hutchings, G. J., Direct synthesis of hydrogen peroxide from H_2 and O_2 using supported Au-Pd catalysts. *Faraday Discuss.* **2008,** *138*, 225-239.

12. Han, Y. F.; Wang, J. H.; Kumar, D.; Yan, Z.; Goodman, D. W., A kinetic study of vinyl acetate synthesis over Pd-based catalysts: kinetics of vinyl acetate synthesis over Pd-Au/SiO_2 and Pd/SiO_2 catalysts. *J. Catal.* **2005,** *232* (2), 467-475.

13. Wittstock, A.; Zielasek, V.; Biener, J.; Friend, C. M.; Baumer, M., Nanoporous Gold Catalysts for Selective Gas-Phase Oxidative Coupling of Methanol at Low Temperature. *Science* **2010,** *327* (5963), 319-322.

14. Enache, D. I.; Edwards, J. K.; Landon, P.; Solsona-Espriu, B.; Carley, A. F.; Herzing, A. A.; Watanabe, M.; Kiely, C. J.; Knight, D. W.; Hutchings, G. J., Solvent-free oxidation of primary alcohols to aldehydes using Au-Pd/TiO_2 catalysts. *Science* **2006,** *311* (5759), 362-365.

15. Wang, R.; Wu, Z.; Chen, C.; Qin, Z.; Zhu, H.; Wang, G.; Wang, H.; Wu, C.; Dong, W.; Fan, W.; Wang, J., Graphene-supported Au-Pd bimetallic nanoparticles with excellent catalytic performance in selective oxidation of methanol to methyl formate. *Chem. Commun.* **2013,** (49), 8250-8252.

16. Zhang, Z.; Wang, Y.; Li, X.; Dai, W-L., Synergistic effect on Au-Pd bimetallic catalyst during oxidation of benzyl alcohol to sodium benzoate. *Chinese J. Catal*. **2014**, *35* (11), 1846-1853.

17. Su, Ren.; Tiruvalam, R.; Logsdail, A. J.; He, Q.; Downing, C. A.; Jensen, M. T.; Dimitratos, N.; Kesavan, L.; Wells, P. P.; Bechstein, R.; Jensen, M. T.; Wendt, S.; Catlow. C. R. A.; Kiely, C. J.; Hutchings, G. J.; Besenbacher, F., Designer titania-supported Au-Pd nanoparticles for efficient photocatalytic hydrogen production. *ACS Nano* **2014**, *8* (4), 3490-3497.

18. Liu, F.; Wechsler, D.; Zhang, P., Alloy-structure-dependent electronic behaviour and surface properties of Au-Pd nanoparticles. *Chem. Phys. Lett.* **2008**, *461* (4), 254-259.

19. Chen, M. S.; Kumar, D.; Yi, C. W.; Goodman, D. W., The promotional effect of gold in catalysis by palladium-gold. *Science* **2005,** *310* (5746), 291-293.

20. Kyriakou, G.; Boucher, M. B.; Jewell, A. D.; Lewis, E. A.; Lawton, T. J.; Baber, A. E.; Tierney, H. L.; Flytzani-Stephanopoulos, M.; Sykes, E. C. H., Isolated Metal Atom Geometries as a Strategy for Selective Heterogeneous Hydrogenations. *Science* **2012,** *335* (6073), 1209-1212.

21. Childers, D. J.; Schweitzer, N. M.; Shahari, S. M. K.; Rioux, R. M.; Miller, J. T.; Meyer, R. J., Modifying structure-sensitive reactions by addition of Zn to Pd. *J. Catal.* **2014,** *318*, 75-84.

22. Zhang, L.; Wang, A.; Miller, J. T.; Liu, X.; Yang, X.; Wang, W.; Li, L.; Huang, Y.; Mou, C. Y.; Zhang, T., Efficient and Durable Au Alloyed Pd Single-Atom Catalyst for the Ullmann Reaction of Aryl Chlorides in Water. *ACS Catal.* **2014,** *4* (5), 1546-1553.

23. Aich, P.; Wei, H.; Basan, B.; Kropf, A. J.; Schweitzer, N. M.; Marshall, C. L.; Miller, J. T.; Meyer, R., Single Atom Alloy Pd-Ag Catalysts for Selective Hydrogenation of Acrolein. *J. Phys. Chem. C, J. Phys. Chem. C,* **2015**, *119* (32), 18140-18148.

24. Pei, G, X.; Liu, X. Y.; Wang, A.; Lee, A. F.; Isaacs, M. A.; Li, L.; Pan, X.; Yang, X.; Wang, X.; Tai, Z.; Wilson, K.; Zhang, T., Ag Alloyed Pd Single-Atom Catalysts for Efficient Selective Hydrogenation of Acetylene to Ethylene in Excess Ethylene. *ACS Catal.* **2015**, *5* (6), 3717–3725.

25. X, Cao.; Q, Fu.; Y, Luo., Catalytic Activity of Pd-Doped Cu Nanoparticles for Hydrogenation as a Single-Atom-Alloy Catalyst. *Phys. Chem. Chem. Phys.* **2014**, *16* (18), 8367-8375.

26. Calver, C. F.; Dash, P.; Scott, R. W. J., Selective Hydrogenations with Ag-Pd Catalysts Prepared by Galvanic Exchange Reactions. *ChemCatChem* **2011**, *3* (4), 695-697.

27. Li, G.; Jin, R. C., Atomically Precise Gold Nanoclusters as New Model Catalysts. *Acc. Chem. Res.* **2013,** *46* (8), 1749-1758.

28. Shivhare, A.; Chevrier, D. M.; Purves, Scott, R. W. J., Following the Thermal Activation of $Au_{25}(SR)_{18}$ Clusters for Catalysis by X-Ray Absorption Spectroscopy. *J. Phys. Chem. C*, **2013**, *117* (39), 20007–20016.

29. Wu, Zili.; Jiang, D-E.; Mann, A. K. P.; Mullins, D. R.; Qiao, Z-A.; Allard, L. F.; Zeng, C.; Jin, R.; Overbury, S. H., Thiolate Ligands as a Double-Edged Sword for CO Oxidation on CeO_2 Supported $Au_{25}(SCH_2CH_2Ph)_{18}$ Nanoclusters. *J. Am. Chem. Soc.* **2014,** *136* (16), 6111-6122.

30. Das, S.; Goswami, A.; Hesari, M.; Al-Sharab, J. F.; Mikmekova, E.; Maran, F.; Asefa, T., Reductive Deprotection of Monolayer Protected Nanoclusters: An Efficient Route to Supported Ultrasmall Au Nanocatalysts for Selective Oxidation *Small* **2014**, *10* (8), 1473-1478.

31. Quinn, B. M.; Kontturi, K., Reductive Desorption of Thioolate from Monolayer Protected Gold Clusters. *J. Am. Chem. Soc.* **2004**, *126* (23), 7168-7169.

32. Widrig, C. A.; Chung, C.; Porter, M. D., The Electrochemical Deposition of n-Alkanethiol Monolayers from Polycrystalline Au and Ag Electrodes. *J. Electroanal. Chem.* **1991**, *310* (1-2), 335-359.

33. Shivhare, A.; Scott, R. W. J., Following the thermal and chemical removal of thiolate stabilizers from supported Au clusters using X-ray absorption spectroscopy (unpublished work).

34. Choi, J. P.; Fields-Zinna, C. A.; Stiles, R. L.; Balasubramanian, R.; Douglas, A. D.; Crowe, M. C.; Murray, R. W., Reactivity of $[Au_{25}(SCH_2CH_2Ph)_{18}]^{1-}$ Nanoparticles with Metal Ions. *J. Phys. Chem. C* **2010,** *114* (38), 15890-15896.

35. Wu, Z. K., Anti-Galvanic Reduction of Thiolate-Protected Gold and Silver Nanoparticles. *Angew. Chem., Int. Edit.* **2012,** *51* (12), 2934-2938.

36. Shivhare, A.; Lee, K. E.; Hu, Y.; Scott R. W. J., Following the reactivity of $Au_{25}(SC_8H_9)_{18}^{-}$ clusters with Pd^{2+} and Ag^{+} using X-ray absorption spectroscopy (unpublished work).

37. Shivhare, A.; Ambrose, S. J.; Zhang, H.; Purves, R. W.; Scott, R. W. J., Stable and recyclable Au_{25} clusters for the reduction of 4-nitrophenol. *Chem. Commun.* **2013**, (49) 276-278.

38. Newville, M. J., *IFEFFIT* : interactive XAFS analysis and *FEFF* fitting. *J. Synchrotron Radiat*. **2001**, *8*, 322−324.

39. Stern, E. A.; Newville, M.; Ravel, B.; Yacoby, Y.; Haskel, D., The UWXAFS analysis package: philosophy and details. *Physica B* **1995**, *208,* 117.

40. Balcha, T.; Strobl, J. R.; Fowler, C.; Dash, P.; Scott, R. W. J., Selective Aerobic Oxidation of Crotyl Alcohol Using AuPd Core-Shell Nanoparticles. *ACS Catal.* **2011,** *1* (5), 425-436.

41. Maclennan, A.; Banerjee, A.; Hu, Y. F.; Miller, J. T.; Scott, R. W. J., In Situ X-ray Absorption Spectroscopic Analysis of Gold-Palladium Bimetallic Nanoparticle Catalysts. *ACS Catal.* **2013,** *3* (6), 1411-1419.

42. Bus, E.; van Bokhoven, J. A., Electronic and geometric structures of supported platinum, gold, and platinum - Gold catalysts. *J. Phys. Chem. C* **2007,** *111* (27), 9761-9768.

43. Ansar, S. M.; Arneer, F. S.; Hu, W. F.; Zou, S. L.; Pittman, C. U.; Zhang, D. M., Removal of Molecular Adsorbates on Gold Nanoparticles Using Sodium Borohydride in Water. *Nano Lett.* **2013,** *13* (3), 1226-1229.

44. Dash, P.; Dehm, N. A.; Scott, R. W. J., Bimetallic PdAu Nanoparticles as Hydrogenation Catalysts in Imidajolium Ionic Liquids. *J. Mol. Catal. A: Chem.* **2008**, 286 (1-2), 114-119.

45. Wilson, O. M.; Knecht, M. R.; Garcia-Martinez, J. C.; Crooks, R. M., Effect of Pd Nanoparticles Size on the Catalytic Hydrogenation of Allyl Alcohol. *J. Am. Chem. Soc.* **2006**, *128* (14), 4510-4511.

46. Sadeghmoghaddam, E.; Gu, Hanmo.; Shon, Y-S., Pd Nanoparticle-Catalyzed Isomerization vs Hydrogenation of Allyl Alcohol: Solvent-Dependent Regioselectivity. *ACS Catal.* **2012**, *2* (9), 1838–1845

CHAPTER 8

8.1 Summary and Conclusions:

The first objective of this thesis was to study the catalytic activity and stability of $Au_{25}(SR)_{18}^-$ clusters in solution. $Au_{25}(SR)_{18}^-$ clusters in the presence of $NaBH_4$ reducing agent were found to be active catalysts for the reduction of 4-nitrophenol (Chapter 2). Here, the catalytic activity was found to be dependent on the chain length of thiol stabilizers. The highest catalytic activity was observed in the case of the lowest chain length stabilizer (2-phenylethanethiol) and the smallest catalytic activity was observed in the case of the longest chain length stabilizer (dodecanethiol). The stability of these clusters under experimental conditions was studied by using UV-Vis spectroscopy and mass spectrometry. After one catalytic cycle, 1-hexanethiol-protected Au_{25} clusters were isolated from the reaction mixture and characterized by UV-Vis spectroscopy and mass spectrometry. Data showed that these clusters were completely preserved and catalysis took place on intact clusters. The relative stability of these clusters compared to larger thiol-protected $Au_{\sim180}$ clusters against $NaBH_4$ was also studied by UV-Vis spectroscopy. Data showed that $Au_{25}(SR)_{18}^-$ clusters remained intact, as no significant changes in the UV-Vis absorption features were observed during the addition of $NaBH_4$, while $Au_{\sim180}$ clusters precipitated out of the solution.

The second objective of this thesis was to synthesize Au_{25} clusters protected with –carboxylate group-terminated thiol stabilizers (Chapter 3). We knew from our previous study (Chapter 2) that $Au_{25}(SC_8H_9)_{18}^-$ clusters were more stable against $NaBH_4$ than their larger counterparts. We used this knowledge in the present case and size separated 11-mercaptoundecanoic acid and 16-mercaptohexadecanoic acid protected Au_{25} clusters from a polydisperse thiol-protected Au cluster mixture by carefully adding $NaBH_4$. Addition of $NaBH_4$ led to the growth and eventually precipitation of non-Au_{25} clusters leaving Au_{25} clusters behind in solution. The separation process was followed by TEM and UV-Vis spectroscopy. The polydisperse Au cluster solution showed a featureless absorption spectrum, which is typical of polydisperse Au clusters in the ~ 2nm size range. After the addition of $NaBH_4$, absorption features characteristic of Au_{25} clusters started to appear, which upon further addition of $NaBH_4$, became intensified and the color of the solution changed from dark brown to reddish-orange indicating the removal of non-Au_{25} clusters from the solution. As-synthesized 11-mercaptoundecanoic acid protected Au_{25} clusters were characterized by using mass spectrometry and were assigned as $Au_{25}(SR)_{18}^-$ clusters (SR = 11-mercaptoundecanoic acid). These clusters could be solubilized in both THF and water by simply changing the pH of the solution. In the basic pH range, carboxylic groups on the surface were deprotonated and resulting clusters were found to be soluble in water. In the acidic pH range, carboxylate groups were protonated and the resulting clusters were found to be soluble in THF. A drawback of this work is the low yield (*ca*. 15%) of $Au_{25}(SR)_{18}^-$ clusters.

In the subsequent study (Chapter 4), we immobilized $Au_{25}(SC_8H_9)_{18}^-$ clusters on mesoporous carbon supports, and studied their thermal activation for 4-nitrophenol reduction catalysis using TEM and EXAFS spectroscopy. The structural integrity of $Au_{25}(SC_8H_9)_{18}^-$ clusters after their immobilization on mesoporous carbon support was maintained as shown by EXAFS spectroscopy. These supported clusters were calcined under air at different temperatures and after each calcination step, these clusters were used as catalysts for the 4-nirtrophenol reduction reaction. The highest catalytic activity was observed after 200°C thermal treatment and further increases in calcination temperature led to a decrease in catalytic activity. EXAFS and TEM studies indicated that enhancement in the catalytic activity was directly related to the removal of thiol stabilizers from the surface of these clusters during thermal treatment. At ~200°C, most of the thiol stabilizers were removed as shown by the EXAFS study and therefore the highest catalytic activity was observed. Further increases in calcination temperature led to a decrease in catalytic activity because of sintering.

Our studies show that $Au_{25}(SR)_{18}^-$ clusters are active catalysts both in solution as well as on support materials for the reduction reaction. Both these studies show that the activity of catalyst was dependent on the possibility of interaction between the Au catalyst surface and 4-nitrophenol. Increase in the bulkiness of the stabilizers weakens the interaction between 4-nitrophenol and the catalyst surface and thus less catalytic activity was observed. Catalysts on mesoporous carbon support was found be more active than in solution. However, here too, an increase in catalytic activity was observed upon removal of thiol stabilizers via calcination. This again signifies the importance of the interaction between 4-nitrophenol and catalyst surface. The major drawback of supported Au clusters was their sintering at high calcination temperature leading to the decrease in catalytic activity.

The next objective of this thesis was to activate supported $Au_{25}(SC_8H_9)_{18}^-$ clusters under mild conditions with minimal sintering. I found from our previous study (Chapter 4) that in order to activate supported $Au_{25}(SR)_{18}^-$ clusters for catalysis, removal of thiol stabilizers was necessary by calcining these clusters at ca. 200^{o}C under air. Calcination of supported clusters resulted in sintering and further calcination at higher temperature resulted in the loss of catalytic activity (Chapter 4).

In Chapter 5, I supported $Au_{25}(SC_8H_9)_{18}^-$ clusters on Al_2O_3 supports and studied their activation by subjecting them to thermal treatments in air and chemical treatments using BH_4^- reducing agents (Chapter 5). BH_4^- has been shown to have the ability to reductively remove thiol stabilizers from the surface of Au MPCs in solution.[1,2] In the present study, we used BH_4^- in order to study the removal of thiol stabilizers from supported $Au_{25}(SC_8H_9)_{18}^-$ clusters. Supported clusters after thermal and chemical treatments were characterized by using TEM and EXAFS spectroscopy. Both EXAFS and TEM data showed that treatment with BH_4^- led to the partial removal of thiolate stabilizers from the surface of supported $Au_{25}(SC_8H_9)_{18}^-$ clusters with little to no growth in cluster size. Thermal treatments on the other hand led to the complete removal of thiolate stabilizers with significant sintering of Au clusters. Yoskamtorn *et al*. have recently shown that partial removal of thiol stabilizers from the surface of supported $Au_{25}(SC_8H_9)_{18}^-$ via calcination was necessary in order to activate these clusters for selective oxidation of benzyl alcohol.[3] Our study provides an alternative route towards the activation of supported $Au_{25}(SC_8H_9)_{18}^-$ clusters for selective catalysis via relatively milder BH_4^- treatment approach.

The fourth objective of this thesis was to study the synthesis of AuPd and AuAg bimetallic clusters using $Au_{25}(SR)_{18}^-$ clusters as starting precursors (Chapter 6). Our study was motivated by the earlier work from Murray and Xie groups.[4-5] They showed that $Au_{25}(SC_8H_9)_{18}^-$ clusters react with metal ions through galvanic exchange. Here, metal ions get reduced and $Au_{25}(SC_8H_9)_{18}^-$ clusters get oxidized to $Au_{25}(SC_8H_9)_{18}$ clusters. Reduced metal atoms were found to be incorporated within Au clusters as shown by mass spectrometry. In the present study, we studied the reaction between $Au_{25}(SC_8H_9)_{18}^-$ clusters with Pd^{2+} and Ag^+ ions using EXAFS spectroscopy and *in situ* XANES spectroscopy, and elucidated the structures of the resulting bimetallic clusters. Spectroscopic data showed that Pd^{2+} reacts with the surface staple motifs of $Au_{25}(SC_8H_9)_{18}^-$ clusters and form Pd(II) thiolate species. These Pd thiolate species were found to be anchored on the surface of Au clusters as no growth and precipitation of Au clusters was observed by TEM even after the addition of 6 equiv. of Pd^{2+}. EXAFS data indicated that palladium was replacing Au atoms from the surface staple motifs and the replaced Au atoms were becoming the part of Au core. Pd K-edge EXAFS data indicated towards the possible crosslinking between clusters through Pd atoms, as the Pd-S coordination number was close to 4. This is possible only when sulphur atoms from more than one cluster are involved in bonding with Pd atom. *In situ* XANES data in the case of Ag showed that unlike Pd^{2+}, Ag^+ got reduced to Ag and did not form Ag(I) thiolate species. These findings were very similar to the study from Xie group where they showed that Ag^+ reacts with $Au_{25}(SC_8H_9)_{18}^-$ clusters through galvanic exchange and form $Au_{25}Ag_2$ adduct. The difference in the reactivity between Pd^{2+} and Ag^+ ions with $Au_{25}(SC_8H_9)_{18}^-$ clusters was explained on the basis of the Pd-S vs Ag-S bond strengths. The Pd-S bond strength is much higher compared to Ag-S bond strength. This may be the reason that Pd^{2+} would prefer to form bond with sulphur, while Ag^+ because of lower Ag-S bond strength would be prone to reduction.

Finally, aforementioned AuPd bimetallic clusters (Chapter 6) were used as starting precursors for the synthesis of AuPd bimetallic nanoparticles (Chapter 7). Various groups have shown that AuPd bimetallic nanoparticles are much more efficient catalysts for a variety of industrially important reactions than their monometallic counterparts.[6-8] However, the determination of the exact structure of these bimetallic nanoparticles has been challenging because of their polydispersity and therefore the study of the structure-property relationships has been difficult. In the present study, we used previously synthesized highly monodisperse, well-characterized AuPd bimetallic clusters (Chapter 6) as starting precursors in order to synthesize AuPd bimetallic nanoparticles. AuPd bimetallic clusters were immobilized on Al_2O_3 supports and subjected to thermal treatment at 250°C first under air and then under H_2 atmospheres or chemical treatment using BH_4^- reducing agents. Thermal treatment at 250°C and chemical treatments were done in order to remove thiol stabilizers as shown in our previous studies (Chapter 3 and 4). The resulting bimetallic nanoparticles were characterized by using TEM and EXAFS spectroscopy. Data showed that both thermal and chemical treatments led to the synthesis of AuPd bimetallic nanoparticles via removal of thiol stabilizers. After thermal and BH_4^- treatments, Pd atoms from the surface staple motifs came in direct contact with Au cores, resulting in the formation of AuPd bimetallic nanoparticles. Data also indicated that while thermal treatments led to the complete removal of thiol stabilizers, BH_4^- treatments led to only partial thiolate removal. After BH_4^-

treatment, the Au-S contribution was completely disappeared but Pd atoms on the surface were still bonded with thiol stabilizers as shown by EXAFS spectroscopy. TEM particle size analysis showed that significant sintering took place in thermally treated samples as compared to BH_4^- treated samples. This agrees with results of our previous study (Chapter 5) where we showed that BH_4^- treatment can be used in order to remove thiol stabilizers form the surface of $Au_{25}(SC_8H_9)_{18}^-$ clusters with little to no growth in cluster size. These well-characterized nanoparticles were used for allyl alcohol hydrogenation catalysis. AuPd bimetallic nanoparticles were shown to have higher catalytic activity than pure Pd nanoparticles. The high catalytic activity was attributed to the presence of isolated atomic Pd sites on the surface.

Finally, the major findings which we have learnt from this work are as follows. 1) $Au_{25}(SR)_{18}^-$ clusters are more stable against $NaBH_4$ than their larger counterparts and this fact can be used in the synthesis of Au_{25} clusters protected with functional group-terminated thiol stabilizers; 2) $Au_{25}(SR)_{18}^-$ clusters are active for reduction catalysis and their activity can be improved by thermally calcining these cluster at ca. 200°C; 3) $Au_{25}(SR)_{18}^-$ clusters can be used as template for the synthesis of AuPd and AuAg bimetallic clusters, and AuPd bimetallic nanoparticles; and 4) because of the highly monodisperse nature of these clusters, X-ray absorption spectroscopy (particularly EXAFS) can be used in order to gain an atomic level understanding of their structures while transforming these clusters into supported Au catalysts, AuPd and AuAg bimetallic clusters, and AuPd bimetallic nanoparticles. Also based on these studies, two major disadvantages of $Au_{25}(SR)_{18}^-$ clusters are as follows. 1) While $Au_{25}(SR)_{18}^-$ clusters can be activated under mild conditions for room temperature reduction reactions, use of these clusters for high temperature catalytic reactions such as methane combustion will be problematic because of sintering; and 2) $Au_{25}(SR)_{18}^-$ clusters can be used as a template for the synthesis of AuPd bimetallic nanoparticles with isolated atomic Pd sites on the surface. However, because of the ultrasmall size (~1 nm) of these clusters, these atomic Pd atoms on the surface can be prone to agglomeration during high temperature catalytic reactions. Minimizing these sites on the surface can be an alternative route to avoid agglomeration, however; it will at the same time affect the catalytic activity for reactions where Pd is an active metal.

8.2 Outlook and Future Work:

8.2.1 Sinter-Resistant $Au_{25}@SiO_2$ Nanoparticles for CH_4 Oxidation:

The long held belief of the inability of Au metal to act as catalyst was challenged in 1989 by Haruta *et al*., who showed that oxide supported Au nanoparticles (less than 5 nm in diameter) can catalyze the low temperature oxidation of CO.[9] Since then, supported Au nanoparticles have been used as catalysts for various reactions such as propylene oxidation, the water gas shift reaction, alcohols oxidations, and hydrogenation of unsaturated aldehydes and ketones.[9,10-13] According to the literature, the active Au particles in these catalytic reactions should be less than 5 nm in diameter. Despite the high catalytic activity of Au nanoparticles in this size regime, the major drawback of using Au nanoparticles as catalysts has been their sintering because of the low melting point of Au nanoparticles, and thus the high mobility of Au atoms at intermediate temperatures.[14] This usually prevents the use of Au nanocatalysts for high temperature catalytic reactions.[15-17]

Various strategies have been described in the literature such as the use of high surface area porous oxide supports, including the encapsulation of nanoparticles within oxide shells, and the synthesis of yolk-shell nanoparticles in order to stabilize Au nanoparticles against sintering during catalysis at high temperature.[18-23] While these strategies can prevent the sintering of Au nanoparticles during catalysis, the exact study of the size and structure dependent catalytic activity remains challenging mainly because of the polydispersity of Au nanoparticle starting materials. In most of these studies, electron microscopy has been used in order to study the changes in Au nanoparticles sizes during catalysis. However, small changes in Au nanoparticle sizes are difficult to monitor by using electron microscopy alone especially in the case of polydisperse Au clusters.

In the Chapter 3 of this thesis, I developed a methodology for the synthesis of highly monodisperse and structurally well-characterized 11-mercaptoundecanoic acid protected Au_{25} clusters. The surface of these clusters is terminated with carboxylic groups, therefore a SiO_2 shell can be built around these clusters as reported in the literature for larger particles.[24-25] This will result in the formation of $Au_{25}@SiO_2$ core-shell nanoparticles. Because of the presence of SiO_2 shells sintering of these clusters can be prevented. The thermal stability of these core-shell nanoparticles will be studied at various temperatures and finally these clusters can be used for high temperature CH_4 oxidation reaction. Before carrying out the CH_4 oxidation reaction, room temperature 4-nitrophenol reduction reaction can also be studied. In Chapter 2 and 4, the catalytic activity of $Au_{25}(SR)_{18}^-$ clusters in solution and on mesoporous carbon supports was discussed. Clusters were found to be active at room temperature without any thermal activation. We have begun to do the same room-temperature 4-nitrophenol reduction reaction using $Au_{25}@SiO_2$ nanoparticles as catalysts. This will help us to gain insight into the diffusion of reactant molecules through SiO_2 shell at room temperature. After this, these core-shell nanoparticles will be used as catalysts for high temperature CH_4 oxidation reaction. Because of the monodispersity of these clusters, their size and structure dependent catalytic activity will be studied by using TEM and EXAFS spectroscopy as discussed in Chapter 4.

8.2.1.1 Synthesis and Characterization of $Au_{25}@SiO_2$ Nanoparticles: Synthesis of $Au_{25}@SiO_2$ core-shell nanoparticles can be carried out by using a literature reported procedure used for larger Au nanoparticles.[25] Briefly, first, 11-mercaptodecanoic acid protected Au_{25} clusters is dissolved in water. Then, to this mixture, tetraethoxysilane pre-dissolved in ethanol is added followed by the addition of ammonia. The resulting solution is left stirring at room temperature for several hours, and the progress of the reaction is monitored by TEM. Below is a TEM image of $Au_{25}@SiO_2$ nanoparticles, synthesized by my colleague Sudheesh Veeranmaril who is following up this area up and provided the image (Figure 8.1).

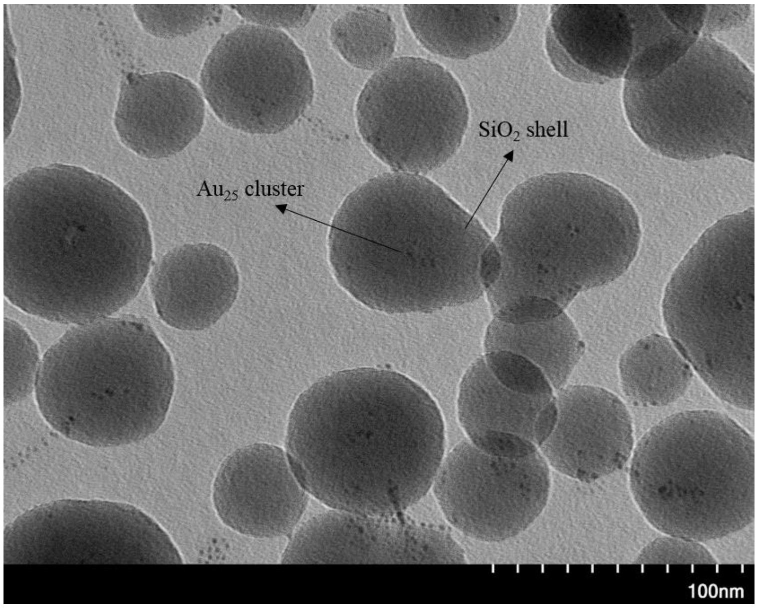

Figure 8.1. TEM image showing $Au_{25}@SiO_2$ nanoparticles.

As-synthesized $Au_{25}@SiO_2$ core-shell can be characterized by using TEM and EXAFS spectroscopy. While TEM can help study the size of Au clusters and number of Au clusters inside the SiO_2 shell, EXAFS spectroscopy can give us insight into the structural integrity of Au_{25} clusters encapsulated within SiO_2 shells. These nanoparticles will be calcined at different temperatures in order to study the removal of thiol stabilizers and associated sintering. The concomitant changes in size and structure will be studied by using TEM and EXAFS spectroscopy. Finally, these core-shell nanoparticles will be used for 4-nitrophenol reduction and methane oxidation reactions. These reactions will be done by using catalysts calcined at different temperatures, and structure-catalytic-activity relationships will be aided by using TEM and EXAFS spectroscopy characterization of the clusters.

8.2.2 AuPd Bimetallic Nanoparticles for Selective Catalysis: Various groups have suggested that alloying Au with Pd significantly improves the activity and selectivity of the resulting AuPd bimetallic nanoparticles catalysts for various reactions such as CO oxidation, vinyl acetate synthesis, H_2O_2 synthesis, acetylene trimerization, and hydrodesulfurization reactions.[26] Enhancement in activity and selectivity has been mainly attributed to two effects, namely ligand effects and ensemble effects. While ligand effects are based on the modification in electronic structure upon mixing two metal components, ensemble effect are because of the presence of a particular arrangement of active metal ensembles on the surface of bimetallic nanoparticles. In some of these studies, structure-property assignments have been made using single crystal surfaces of either Au or Pd metal, followed by sequentially deposition of the second metal and annealing at different temperatures. By controlling the annealing temperature, the surface structure of resulting bimetallic species can be controlled for a particular catalytic reaction. For example; Lambert *et al*. showed that the Au_6Pd ensemble was responsible for the production of benzene from 3 acetylene molecules.[27] Here, the surface composition was controlled by annealing Pd(111)/Au surfaces at different temperatures. Goodman *et al*. studied the formation of vinyl acetate on AuPd bimetallic surfaces.[28] Here, Pd was deposited on Au(111) and Au(100) surfaces and the resulting samples were annealed at different temperatures. After annealing, Pd atoms were found to be isolated on the surface of Au and higher catalytic activity was observed for Pd deposited on Au (111) surfaces. Based on a series of spectroscopic measurements, this was assigned to the lower distance between atomic Pd sites on Au(111) surfaces after annealing than on Au(100) surfaces. Gao *et al*. tested AuPd(100) surfaces for CO oxidation reaction and found that at low CO pressure, the reaction rate was very low.[29] However, at higher CO pressure (~ atmospheric pressure), the rate of CO oxidation was enhanced multifold. This rate enhancement was attributed to the formation of surface Pd ensembles at higher CO pressure compared to isolated Pd sites at lower CO pressure. CO has a very high binding affinity with Pd, which resulted in the surface segregation of Pd at higher CO pressure.

The study of structure-property relationships using AuPd catalysts synthesized using solution routes is rare. This is apparently because of the lack of solution-based synthesis methodologies available in order to design monodisperse, well-characterized AuPd catalysts. In most of the cases, AuPd catalysts prepared through solution based routes are polydisperse in nature and this results in a wide gap between the predicted catalytic activity based on singe crystal surfaces and catalytic activity observed using AuPd catalysts synthesized through solution based routes for practical applications.

In Chapter 6 of this thesis, the synthesis of AuPd bimetallic nanoparticles using highly monodisperse and well-characterized $Au_{25}(SC_8H_9)_{18}^-$ clusters has been discussed. These well-characterized nanoparticles were shown to have Au cluster core and atomic dispersion of Pd atoms on the surface. Because of their well-characterized structures, these nanoparticles will be used as model catalysts for vinyl acetate synthesis.

Vinyl Acetate Synthesis: Acetoxylation of ethylene on bimetallic Au-Pd surface is a well-established route for the synthesis of vinyl acetate (Scheme 8.1). Side reactions are the combustion of reactants and products.[29]

$$CH_3COOH + C_2H_4 + 0.5O_2 \longrightarrow CH_3COOCHCH_2 + H_2O \qquad (1)$$

Scheme 8.1. Synthesis of vinyl acetate using acetic acid and ethylene.

Compared to pure Pd nanoparticle catalysts, AuPd bimetallic nanoparticle catalysts have been shown to have higher activity and improved selectivity for vinyl acetate formation. Studies have shown that in AuPd bimetallic catalysts, because of weaker binding of reactant molecules, side reactions can be prevented to a large extent.[29] Furthermore, catalytic studies on single crystal Pd/Au(111) and Pd/Au(100) surfaces demonstrated that atomic dispersion of Pd on Au(111) surface leads to the higher activity and selectivity for vinyl acetate synthesis. This was attributed to the shorter distance between atomic Pd sites on Au(111) surface, which was suitable for the coupling between reactant molecules.[30]

In future, we plan to use AuPd bimetallic nanoparticles discussed in Chapter 7 for vinyl acetate synthesis reactions. These well-characterized AuPd bimetallic nanoparticles were shown to have Au cores and atomic Pd sites on the surface. The methodology reported for the synthesis of AuPd nanoparticles has potential to tune the dispersion and therefore distance between Pd atoms by tuning the size of Au core and/or the Pd:Au ratio used to make the bimetallic clusters. Correlation between the dispersion of Pd atoms on the surface of the Au core will be made with the activity and selectivity for vinyl acetate formation.

8.3 References:

1. Quinn, B. M.; Kontturi, K., Reductive Desorption of Thioolate from Monolayer Protected Gold Clusters. *J. Am. Chem. Soc.* **2004**, *126* (23), 7168-7169.

2. Widrig, C. A.; Chung, C.; Porter, M. D., The Electrochemical Deposition of n-Alkanethiol Monolayers from Polycrystalline Au and Ag Electrodes. *J. Electroanal. Chem.* **1991**, *310* (1-2), 335-359.

3. Yoskamtorn, T.; Yamazoe, S.; Takahata, R.; Nishigaki, J.; Thivasasith, A.; Limtrakul, J.; Tsukuda, T., Thiolate-Mediated Selectivity Control in Aerobic Alcohol Oxidation by Porous Carbon-Supported Au_{25} Clusters. *ACS Catal.* **2014,** *4* (10), 3696-3700.

4. Choi, J. P.; Fields-Zinna, C. A.; Stiles, R. L.; Balasubramanian, R.; Douglas, A. D.; Crowe, M. C.; Murray, R. W., Reactivity of $[Au_{25}(SCH_2CH_2Ph)_{18}]^{1-}$ Nanoparticles with Metal Ions. *J. Phys. Chem. C* **2010,** *114* (38), 15890-15896.

5. Wu, Z. K., Anti-Galvanic Reduction of Thiolate-Protected Gold and Silver Nanoparticles. *Angew. Chem., Int. Edit.* **2012,** *51* (12), 2934-2938.

6. Gao, F.; Goodman, D. W., Pd-Au bimetallic catalysts: understanding alloy effects from planar models and (supported) nanoparticles. *Chem. Soc. Rev.* **2012,** *41* (24), 8009-8020.

7. Edwards, J. K.; Freakley, S. J.; Carley, A. F.; Kiely, C. J.; Hutchings, G. J., Strategies for Designing Supported Gold-Palladium Bimetallic Catalysts for the Direct Synthesis of Hydrogen Peroxide. *Accounts. Chem. Res.* **2014,** *47* (3), 845-854.

8. Kesavan, L.; Tiruvalam, R.; Ab Rahim, M. H.; bin Saiman, M. I.; Enache, D. I.; Jenkins, R. L.; Dimitratos, N.; Lopez-Sanchez, J. A.; Taylor, S. H.; Knight, D. W.; Kiely, C. J.; Hutchings, G. J., Solvent-Free Oxidation of Primary Carbon-Hydrogen Bonds in Toluene Using Au-Pd Alloy Nanoparticles. *Science* **2011,** *331* (6014), 195-199.

9. Haruta, M.; Yamada, N.; Kobayashi, T.; Iijima, S., Gold Catalysts Prepared by Coprecipitation for Low-Temperature Oxidation of Hydrogen and of Carbon-Monoxide. *J. Catal.* **1989,** *115* (2), 301-309.

10. Hayashi, T.; Tanaka, K.; Haruta, M., Selective vapor-phase epoxidation of propylene over Au/TiO_2 catalysts in the presence of oxygen and hydrogen. *J. Catal.* **1998,** *178* (2), 566-575.

11. Sinha, A. K.; Seelan, S.; Tsubota, S.; Haruta, M., Catalysis by gold nanoparticles: epoxidation of propene. *Top. Catal.* **2004,** *29* (3-4), 95-102.

12. Fu, Q.; Weber, A.; Flytzani-Stephanopoulos, M., Nanostructured Au-CeO_2 catalysts for low-temperature water-gas shift. *Catal. Lett.* **2001,** *77* (1-3), 87-95.

13. Milone, C.; Crisafulli, C.; Ingoglia, R.; Schipilliti, L.; Galvagno, S., A comparative study on the selective hydrogenation of alpha,beta unsaturated aldehyde and ketone to unsaturated alcohols on Au supported catalysts. *Catal. Today* **2007,** *122* (3-4), 341-351.

14. Walther, G.; Cervera-Gontard, L.; Quaade, U. J.; Horch, S., Low temperature methane oxidation on differently supported 2 nm Au nanoparticles. *Gold. Bull.* **2009,** *42* (1), 13-19.

15. Yang, F.; Chen, M. S.; Goodman, D. W., Sintering of Au Particles Supported on TiO_2(110) during CO Oxidation. *J. Phys. Chem. C* **2009,** *113* (1), 254-260.

16. Herzing, A. A.; Kiely, C. J.; Carley, A. F.; Landon, P.; Hutchings, G. J., Identification of active gold nanoclusters on iron oxide supports for CO oxidation. *Science* **2008,** *321* (5894), 1331-1335.

17. Yang, C. M.; Kalwei, M.; Schuth, F.; Chao, K. J., Gold nanoparticles in SBA-15 showing catalytic activity in CO oxidation. *Appl. Catal. A-Gen.* **2003,** *254* (2), 289-296.

18. Bore, M. T.; Pham, H. N.; Switzer, E. E.; Ward, T. L.; Fukuoka, A.; Datye, A. K., The role of pore size and structure on the thermal stability of gold nanoparticles within mesoporous silica. *J. Phys. Chem. B* **2005,** *109* (7), 2873-2880.

19. Chen, C.; Shi, M. X.; Cargnello, M.; Fornasiero, P.; Murray, C. B.; Gorte, R. J., Au@TiO_2 Core-Shell Nanostructures with High Thermal Stability. *Catal. Lett.* **2014,** *144* (11), 1939-1945.

20. Wei, Y. C.; Zhao, Z.; Yu, X. H.; Jin, B. F.; Liu, J.; Xu, C. M.; Duan, A. J.; Jiang, G. Y.; Ma, S. H., One-pot synthesis of core-shell Au@CeO_2-delta nanoparticles supported on three-dimensionally ordered macroporous ZrO_2 with enhanced catalytic activity and stability for soot combustion. *Catal. Sci. Technol.* **2013,** *3* (11), 2958-2970.

21. Chen, J. C.; Zhang, R. Y.; Han, L.; Tu, B.; Zhao, D. Y., One-pot synthesis of thermally stable gold@mesoporous silica core-shell nanospheres with catalytic activity. *Nano Res.* **2013,** *6* (12), 871-879.

22. Wang, Z. H.; Li, L.; Han, D. M.; Gu, F. B., CO oxidation on Au@CeO_2 yolk-shell nanoparticles with high catalytic stability. *Mater. Lett.* **2014,** *137*, 188-191.

23. Lee, I.; Joo, J. B.; Yin, Y. D.; Zaera, F., A Yolk@Shell Nanoarchitecture for Au/TiO_2 Catalysts. *Angew. Chem., Int. Edit.* **2011,** *50* (43), 10208-10211.

24. Muhammed, M. A. H.; Pradeep, T., Au_{25}@SiO_2: Quantum Clusters of Gold Embedded in Silica. *Small* **2011,** *7* (2), 204-208.

25. Gangishetty, M. K.; Lee, K. E.; Scott, R. W. J.; Kelly, T. L., Plasmonic Enhancement of Dye Sensitized Solar Cells in the Red-to-near-Infrared Region using Triangular Core Shell Ag@SiO_2 Nanoparticles. *ACS Appl. Mater. Inter.* **2013,** *5* (21), 11044-11051.

26. Gao, F.; Goodman, D. W., Pd-Au Bimetallic Catalysts: Understanding Alloy Effects from Planar Models and (Supported) Nanoparticles. *Chem. Soc. Rev.* **2012**, *41* (24), 8009-8020.

27. Baddeley, C. J.; Tikhov, M.; Hardacre, T. C.; Lomas, J. R.; Lambert, R. M., Ensemble Effects in the Coupling of Acetylene to Benzane on a Bimetallic Surface: A Study with Pd(111)/Au. *J. Phys. Chem.* **1996**, *100* (6), 2189-2194.

28. Chen, M. S.; Luo, K.; Wei, T.; Yan, Z.; Kumar, D.; Yi, C. W.; Goodman, D. W., The Nature of the Active Site for Vinyl Acetate Synthesis Over Pd-Au. *Catal. Today* **2006**, *117* (1-3), 37-45.

29. Han, Y. F.; Wang, J. H.; Kumar. D.; Yan, Z.; Goodman, D. W., A KInetic Study of Vinyl Acetate Synthesis Over Pd-Based Catalysts- Kinetics of VA Synthesis Over Pd-Au/SiO_2 and Pd/SiO_2 Catalysts. *J. Catal.* **2005**, *232* (2), 467-475.

30. Chen, M. S.; Kumar, D.; Yi, C. W.; Goodman, D. W., *Science* **2005**, *310* (5746), 291-293.